Bert Schädlich

A Multilaminate Constitutive Model for Stiff Soils

Dissertation

Eingereicht an der Fakultät für Bauingenieurwissenschaften

Technische Universität Graz

Begutachter:

Ao.Univ.-Prof. Dipl.-Ing. Dr.-techn. Helmut F. Schweiger, M.Sc

Institute for Soil Mechanics and Foundation Engineering
Graz University of Technology, Austria

Prof. David M. Potts, B.Sc., Ph.D., D.Sc. (London), C.Eng., FICE

Imperial College London, UK

Graz, April 2012

Acknowledgements

This Dissertation would not have been possible without the continuous support and advice of Ao.Univ.-Prof. Dipl.-Ing. Dr.techn. Helmut F. Schweiger. I thank Helmut for giving me the opportunity to work in his research group and for providing the resources and the academic environment essential for performing the work summarized in this thesis. I very much enjoyed working in the Computational Geotechnics Group at Graz University of Technology, and I am very grateful for being given the opportunity to attend various conferences and to present my research at an international level.

I am grateful to Prof. David M. Potts of Imperial College London for reviewing this thesis.

O.Univ.-Prof. Dipl.-Ing. Dr.techn. Stephan Semprich as the Head of the Institute for Soil Mechanics and Foundation Engineering at Graz University of Technology made the facilities of the institute available for me, which I gratefully acknowledge.

I thank all colleagues at the Institute for Soil Mechanics and Foundation Engineering for the very pleasant working environment and the many fruitful discussions, research related or otherwise. In particular I would like to thank Franz Tschuchnigg, Christian Lackner, Gregor Supp, Ali Nasekhian, Ikhya and Indra Hamdhan.

The financial support by the Austrian Science Fund (FWF) is gratefully acknowledged.

Graz, April 2012 Bert Schädlich

Kurzfassung

Numerische Berechnungsverfahren sind in den letzten Jahren ein gängiges Hilfsmittel in der geotechnischen Ingenieurspraxis geworden, sowohl für die Prognose von Bodenverformungen, als auch für die Bewertung von Standsicherheitsproblemen. Für eine sichere und erfolgreiche Anwendung derartiger Berechnungsverfahren sind jedoch neben einer sorgfältigen Beschreibung der Bodeneigenschaften auch hoch entwickelte Stoffmodelle erforderlich, die das komplexe mechanische Materialverhalten des Bodens abbilden können.

In dieser Arbeit wird ein multilaminates Stoffgesetz für Finite Elemente Berechnungen vorgestellt, in dem anisotrope Steifigkeiten bei sehr kleinen Dehnungen und das Entfestigungsverhalten steifer, überkonsolidierter Tonböden berücksichtigt werden können. Plastische Dehnungen werden in multilaminaten Stoffgesetzen auf voneinander unabhängigen sogenannten Integrationsebenen berechnet, wodurch Anisotropie infolge plastischer Verformungen in einer physikalisch plausiblen Form abgebildet werden kann. Es wird gezeigt, dass der gewählte Ansatz zur Modellierung anisotroper elastischer Steifigkeit die Bandbreite physikalisch möglicher Parameter abdeckt. Die Anwendbarkeit des Stoffgesetzes wird mit numerischen Simulationen von Elementversuchen an verschiedenen Böden demonstriert. Zur Bewertung des Einflusses anisotroper Steifigkeit im Bereich kleiner Dehnungen in geotechnischen Problemstellungen wurden numerische Simulationen eines Baugrubenaushubs und eines Streifenfundaments durchgeführt.

Die Scherfestigkeit und das Entfestigungsverhalten überkonsolidierter Tonböden werden im Modell durch eine zusätzliche Hvorslev-Fließfläche auf den Integrationsebenen gesteuert. Dilatantes Materialverhalten ist ein Resultat der Überkonsolidierung und erfordert keine zusätzlichen Materialparameter. Berechnungsergebnisse mit diesem Modell werden mit experimentellen Daten von undrainierten Triaxialversuchen an zwei überkonsolidierten Tonböden verglichen. Zur Vermeidung von Netzabhängigkeit und numerischer Instabilität durch die Reduzierung der Scherfestigkeit wird ein nichtlokales Kontinuum für die Entfestigungsvariable verwendet. Am Beispiel numerischer Berechnungen von Biaxialversuchen wird gezeigt, dass diese Methode in der Lage ist, numerische Ergebnisse weitestgehend unabhängig vom verwendeten Finite Elemente Netz zu liefern.

Abstract

Numerical calculation methods have become a common design tool in geotechnical practice in recent years, both for the prediction of deformations at working load conditions and the evaluation of ultimate limit states. Successful application of these methods does not only require careful characterization of soil properties, but also depends on the availability of advanced constitutive models, which are able to reproduce the complex mechanical behaviour of soil.

In this thesis a multilaminate constitutive model for application in finite element analysis is presented, in which anisotropic soil stiffness at small strains and the strain softening behaviour of stiff, overconsolidated clay can be taken into account. Due to the multilaminate framework, plastic strains are calculated independently on a number of so-called integration planes, which allows the simulation of strain induced anisotropy in a mechanically meaningful manner. The chosen approach to model anisotropic elastic stiffness in the multilaminate concept is shown to cover the full range of physically possible parameters. Numerical simulations of element tests on various soils demonstrate the validity of the model and its predictive capabilities. To evaluate the influence of anisotropic stiffness in the small strain range in geotechnical problems, numerical simulations of an excavation problem and of a strip footing have been performed.

The shear strength and strain softening behaviour of heavily overconsolidated clays is governed by an additional Hvorslev yield surface at the integration plane level. Dilatancy evolves as a function of overconsolidation without additional input parameters. Model predictions are compared with undrained triaxial test data of two overconsolidated clays. So-called non-local strain regularization is employed to overcome mesh dependency and numerical instability in the strain softening post-peak range. The effectiveness of the non-local approach to obtain virtually mesh independent results is demonstrated in biaxial test simulations.

Table of contents

List of symbols

The symbols used in this thesis are listed in alphabetical order. Additional explanation is provided in the text at first appearance. Units and abbreviations are not included in this list.

Small letters

a_{II}	constant for determination of mobilised dilatancy angle
b_{II}	constant for determination of mobilised dilatancy angle
a_v	power index for stress dependency of vertical stiffness
a_{hh}, a_{vh}	power index for stress dependency of shear stiffness
b_h	power index for stress dependency of horizontal stiffness
b_{hh}, b_{vh}	power index for stress dependency of shear stiffness
c'	effective cohesion
c_{II}	constant for determination of mobilised dilatancy angle
c'_{HV}	cohesion intercept of Hvorslev surface in τ- σ'-diagram, normalised with σ'_{ne}
c'_{pe}	cohesion intercept of Hvorslev surface in τ- σ'-diagram, normalised with p'_e
c'_{ve}	cohesion intercept of Hvorslev surface in τ- σ'-diagram, normalised with σ'_{ve}
d_{II}	constant for determination of mobilised dilatancy angle
d_{50}	mean grain size
e	void ratio
e_0	initial void ratio
e_{max}	maximum void ratio
e_{min}	minimum void ratio
f	yield function
f_{cap}	volumetric part of yield function
f_{cone}	deviatoric part of yield function
f_{HV}	Hvorslev yield function
f_i	yield function for plane i
f_{tens}	yield function in tension (tension cut-off)
f_i^{trial}	value of yield function at elastic trial stress for plane i
g	plastic potential function
g_{cap}	plastic potential function, volumetric part
g_{cone}	plastic potential function, deviatoric part
g_h	cohesion intercept of Hvorslev surface in normalised p'-q-diagram

g_{HV}	plastic potential function, Hvorslev surface
g_i	plastic potential function for plane i
h_{soft}	softening parameter for Hvorslev surface
i	index number of sampling plane
k	iteration number
k_{II}	gradient of mobilised dilatancy at $\varphi'_m=\varphi'$
l	internal length
l_{cal}	internal length used in the calculation
m	power index, controlling stress dependency of stiffness
m	number of eigenvalues of global compliance matrix
m_H	inclination of Hvorslev surface in normalised p'-q-diagram
m_{SP}	number of stress points within radius of $2l$ around current stress point
m_t, m_r	stiffness recovery parameters in intergranular strain concept
n	number of integration planes
$n_{1,i}$, $n_{2,i}$, $n_{3,i}$	components of vector perpendicular to integration plane
$\mathbf{n}_i$	vector perpendicular to integration plane
n_v	vertical component of $\mathbf{n}_i$
n_{vh}, n_{hh}, n_{hv}	power index for stress dependency of shear stiffness
p'	mean effective stress
p'_0	initial mean effective stress
p'_c	isotropic pre-consolidation stress
p'_e	equivalent stress on isotropic normal compression line
p_{ref}	reference stress
p_w	pore water pressure
q	Roscoe deviatoric stress invariant
$s_{1,i}$, $s_{2,i}$, $s_{3,i}$	components of vector parallel to integration plane
$\mathbf{s}_i$	vector parallel to integration plane
$StepSize$	max. deviation from yield curve for next calculation step
s_v	vertical component of $\mathbf{s}_i$
$t_{1,i}$, $t_{2,i}$, $t_{3,i}$	components of vector parallel to integration plane
$\mathbf{t}_i$	vector parallel to integration plane
t_v	vertical component of $\mathbf{t}_i$
u	pore water pressure
w	specific weight of beam elements
w_i	weight coefficient for plane i
x, y, z	Cartesian coordinates

Capital letters

A_i	area of influence of integration plane
A_{sphere}	surface area of unit sphere
A_{mat}	deviatoric hardening parameter
A_r	anisotropy ratio
$A_{r,Cn}$	anisotropy ratio for normal compliance C_n
$A_{r,Ct}$	anisotropy ratio for tangential compliance C_t
B_{CS}	auxiliary parameter defining the position of the critical state line
$\mathbf{C}$	elastic compliance matrix of the soil mass
$\mathbf{C}_i$	elastic compliance matrix of plane i
C_d	deviatoric compliance on integration plane
C_n	normal compliance on integration plane
C_{n0}	mean normal compliance on integration plane
C_t	tangential compliance on integration plane
C_{t0}	mean tangential compliance on integration plane
C_{ts}	tangential compliance on integration plane in **s**-direction
C_{tt}	tangential compliance on integration plane in **t**-direction
C_v	volumetric compliance on integration plane
$\mathbf{D}^{\mathbf{e}}$	elastic stiffness matrix of the soil mass
E	Young’s modulus
$E_{50,ref}$	deviatoric hardening modulus in Hardening Soil model at reference pressure
E_0	isotropic Young’s modulus at very small strains
EA	axial stiffness
E_d	second deviatoric strain invariant
E'_{h}	elastic modulus in horizontal direction
E'_{h0}	small strain elastic modulus in horizontal direction
$E'_{h0,ref}$	small strain elastic modulus in horizontal direction at reference pressure
EI	flexural rigidity
$\mathbf{E}_m$	idempotent matrices of $\mathbf{C}$
E_{mean}	average Young’s modulus of cross-anisotropic elastic material
E_{oed}	actual stiffness for primary oedometer loading
$E_{oed,ref}$	reference stiffness for primary oedometer loading
E_{ur}	stiffness for un- and reloading at actual stress
$E_{ur,ref}$	stiffness for un- and reloading at reference stress
E'_{v}	elastic modulus in vertical direction
E'_{v0}	small strain elastic modulus in vertical direction
$E'_{v0,ref}$	small strain elastic modulus in vertical direction at reference pressure

G	shear modulus
G_0	initial isotropic shear modulus at small strains
$G_{0,ref}$	initial isotropic shear modulus at small strains at reference pressure
G_{eq}	equivalent shear modulus
$G_{eq,0}$	equivalent shear modulus at small strains
G_{hh}	shear modulus within isotropic plane of cross-anisotropic material
G_{tan}	tangential shear modulus
G_{ur}	unloading/reloading shear modulus at large strains
G_{vh}	independent shear modulus of cross-anisotropic material
G_{vh0}	independent small strain shear modulus
$G_{vh0,ref}$	independent small strain shear modulus at reference pressure
I_D	relative density
J	second deviatoric stress invariant
K'	drained elastic bulk modulus
K'	drained lateral stress ratio
K_0	lateral earth pressure coefficient at rest
K_{0nc}	lateral earth pressure coefficient at rest for normally consolidated conditions
K_e	equivalent bulk modulus of the pore fluid
K_u	undrained bulk modulus for the soil
L_{11}, L_{22}	Koiter coefficients
L_{12}, L_{21}	Koiter coefficients
L_{el}	maximum length of element in the FE-mesh
M_{com}	inclination of Mohr-Coulomb failure line in triaxial compression in p'-q-space
M_{CP}	shape factor determining the shape of the volumetric part of the yield curve
M_{CS}	inclination of critical state line in p'-q-space
M_{ext}	inclination of Mohr-Coulomb failure line in triaxial extension in p'-q-space
M_{yield}	inclination yielding line in triaxial extension
OCR	over-consolidation ratio
POP	pre-overburden pressure
R_f	failure ratio
S	surface area of unit sphere
S_h	axial stiffness parameter in horizontal direction
S_{hh}	shear stiffness parameter
SSS_{gl}	macroscopic small strain stiffness degradation indicator
S_v	axial stiffness parameter in vertical direction
S_{vh}	shear stiffness parameter (cross-anisotropic material)

$\mathbf{T}_i$	transformation matrix of plane *i*
V_w	weighted volume
W_{macro}	macroscopic virtual work
W_{micro}	virtual work on integration plane

Small Greek letters

α	parameter defining the shape of the cap yield function
α_0	mean value of anisotropic quantatity
α_i	orientation angle of integration plane
α_{non}	over-nonlocal parameter
α_u	any material property at direction of unit vector **u**
β_i	orientation angle of integration plane
γ	bulk unit weight of soil
$\gamma_{0.7}$	reference shear strain in Hardening Soil model
γ^p_{cone}	plastic shear strain on integration plane from deviatoric yield surface
γ^e_s, γ^e_t	local elastic shear strains on integration plane
γ^p_s, γ^p_t	local plastic shear strains on integration plane
γ_s, γ_t	local shear strains on integration plane
γ_{s1}	local shear strains in **s**-direction, resulting from global axial strains
γ_{s2}	local shear strains in **s**-direction, resulting from global shear strains
γ_{sat}	bulk unit weight of soil below ground water table
$\gamma_{s,centre}$	centre of local deviatoric strain history contour, shear component in **s**-direction
γ_{t1}	local shear strains in **t**-direction, resulting from global axial strains
γ_{t2}	local shear strains in **t**-direction, resulting from global shear strains
$\gamma_{t,centre}$	centre of local deviatoric strain history contour, shear component in **t**-direction
γ_{unsat}	bulk unit weight of soil above ground water table
γ_{xy}, γ_{yz}, γ_{xz}	global engineering shear strains
$\boldsymbol{\varepsilon}$	global strain tensor
ε_1, ε_2, ε_3	major, intermediate and minor principal strain
ε^*	non-local strain
$\boldsymbol{\varepsilon}^e$	elastic part of the strain tensor
ε_d	local damage strain on the level of stress point
ε_{di}	local damage strain on integration plane level
ε^*_{di}	non-local damage strain on integration plane level
ε^*_d	non-local damage strain on the level of stress point

ε_{deg}	local degradation strain
$\varepsilon_{deg,1}$, $\varepsilon_{deg,1}$	local degradation strains defining onset of stiffness degradation and transition to large strains
$\varepsilon_{di,peak}$	local damage strain on integration plane level at peak strength
$\varepsilon^{*}_{di,peak}$	non-local damage strain on integration plane level at peak strength
$\boldsymbol{\varepsilon}_{i}$	plastic strain tensor on integration plane
$\boldsymbol{\varepsilon}_{i}^{dev}$	deviatoric strain tensor on integration plane
$\boldsymbol{\varepsilon}_{i}^{e}$	elastic strain tensor on integration plane
$\boldsymbol{\varepsilon}_{i,m}$	spectral stress modes of $\boldsymbol{\varepsilon}_{i}$
$\boldsymbol{\varepsilon}_{i}^{p}$	strain tensor on integration plane
$\boldsymbol{\varepsilon}_{i}^{vol}$	volumetric strain tensor on integration plane
ε_{h}	horizontal strain
ε_{n}	local normal strain on integration plane
ε_{nd}	deviatoric part of local normal strain
$\varepsilon_{nd,centre}$	centre of local deviatoric strain history contour, deviatoric normal component
ε_{nv}	volumetric part of local normal strain
$\boldsymbol{\varepsilon}^{p}$	plastic part of the strain tensor
ε^{p}_{n}	plastic normal strain on integration plane from all yield sufaces
$\varepsilon^{p}_{n,cap}$	plastic normal strain from the cap yield surface
$\varepsilon^{p}_{n,cone}$	plastic normal strain from the cone yield surface
$\varepsilon^{p}_{n,HV}$	plastic normal strain from the Hvorslev yield surface
ε_{v}	vertical strain
ε_{vol}	volumetric strain
θ	Lode’s angle
θ	shear band inclination
κ	slope of the swelling line in ln(p')-ν-plane (swelling index)
λ	slope of the normal compression line in ln(p')-ν-plane (compression index)
λ_{m}	eigenvalues of global compliance matric
ν	specific volume (1+e)
ν', ν'_{ur}	drained Poisson’s ratio at large strains
ν'_{hh}	Poisson’s ratio within isotropic plane
ν'_{hh0}	initial Poisson’s ratio within isotropic plane
ν'_{vh}, ν'_{hv}	cross-anisotropic Poisson’s ratios
$\nu'_{vh,iso}$	cross-anisotropic Poisson’s ratio at isotropic stress state
ν'_{vh0}, ν'_{hv0}	initial cross-anisotropic Poisson’s ratios
$\boldsymbol{\sigma}'$	effective stress tensor
σ^{*}	non-local stress
$\boldsymbol{\sigma}'_{0}$	initial effective stress state

σ'_1, σ'_2, σ'_3	major, intermediate and minor principal stress
σ'_h	horizontal effective stress
σ'_{h0}	initial horizontal effective stress
$\boldsymbol{\sigma}'_i$	effective stress vector in terms of micro level components of plane *i*
$\boldsymbol{\sigma}'^{dev}_i$	deviatoric stress tensor on integration plane
$\boldsymbol{\sigma}'_{i,m}$	spectral stress modes of $\boldsymbol{\sigma}'_i$
$\boldsymbol{\sigma}'_{i,trial}$	auxiliary trial stress vector on integration plane i
$\boldsymbol{\sigma}'^{vol}_i$	volumetric stress tensor on integration plane
$\boldsymbol{\sigma}'_m$	spectral stress modes of $\boldsymbol{\sigma}'$
σ'_n, $\sigma'_{n,i}$	effective normal stress on integration plane
σ'_{nc}	local effective normal preconsolidation stress on integration plane
σ'^*_{nc}	non-local effective normal preconsolidation stress on integration plane
$\sigma'_{nc,0}$	initial effective normal preconsolidation stress on integration plane
$\sigma'_{nc,k}$	effective normal preconsolidation stress in step *k*
$\sigma'_{nc,k+1}$	effective normal preconsolidation stress in step $k+1$
σ'_{nd}	deviatoric part of effective normal stress on integration plane
σ'_{ne}	equivalent normal stress on local normal consolidation line
σ'_{nv}	volumetric part of effective normal stress on integration plane
$\boldsymbol{\sigma}'_{previous}$	previous state of stress
σ'_t	tensile strength
$\boldsymbol{\sigma}'_{trial}$	global auxiliary trial stress vector
σ'_v	vertical effective stress
σ'_{v0}	initial vertical effective stress
σ'_{ve}	equivalent vertical stress on 1D normal consolidation line
τ	shear stress on sampling plane
τ_s	local shear stresses in **s**-direction
τ_{s1}	local shear stresses in **s**-direction, resulting from global axial stresses
τ_{s2}	local shear stresses in **s**-direction, resulting from global shear stresses
τ_t	local shear stresses in **t**-direction
τ_{t1}	local shear stresses in **t**-direction, resulting from global axial stresses
τ_{t2}	local shear stresses in **t**-direction, resulting from global shear stresses
τ_{xy}, τ_{yz}, τ_{xz}	global shear stresses
φ'_0	initial mobilised effective friction angle
φ'_{cs}	effective friction angle at critical state
φ'_e	inclination of Hvorslev surface in τ- σ'-diagram

φ'_{m}	mobilised friction angle
$\varphi'_{m}{}^{*}$	mobilised friction angle at minimum mobilised dilatancy
φ'_{max}	maximum effective friction angle at peak strength
φ'_{mod}	modified friction angle
ψ	ultimate dilatancy angle in basic model
ψ_{m}	mobilised dilatancy angle
ψ_{max}	maximum dilatancy angle in Hvorslev surface model
$\psi_{mob,min}$	minimum of mobilised dilatancy angle
ω	Gaussian error function
ω'	error function according to Galavi (2007)

Capital Greek letters

K	hardening parameter
Λ_{i}	plastic multiplier of plane *i*

1 Introduction

1.1 Motivation

The prediction of ground movements, bearing capacity and stability of geotechnical structures is a key task in geotechnical engineering. The applicability of analytical methods to practical problems is in general limited, as the large variation in geometry and boundary conditions can hardly be taken into account in analytical solutions. As a consequence, numerical methods like the finite element method, in which the boundary value problem is solved in an approximate manner, have gained widespread application in the last decades.

Numerical methods are, however, not a priori a suitable tool for the design of geotechnical structures. The mechanical behaviour of geomaterials is significantly more complex than that of most materials encountered in structural engineering. Soils deform plastically long before failure, their stiffness and strength depends on stress state, loading history and physical grain properties, and material response often changes with the direction of loading. Additionally, natural soils are characterized by considerable heterogeneity and spatial variability of material properties. If realistic predictions are to be obtained by numerical simulations, careful investigation of in-situ soil properties as well as advanced constitutive models are required. Still, no generally accepted soil model, which is able to reproduce all the relevant characteristics of soil with physically meaningful material parameters, prevailed so far.

In this thesis a novel constitutive model is presented, which can account for two phenomena commonly observed in heavily overconsolidated, stiff clays and dense sands: Anisotropic stiffness in the range of very small strains, and the strain softening behaviour after peak strength has been mobilised.

It is well known that many natural soils exhibit anisotropy in both stiffness and strength, and thus the material response depends on the direction of loading. In the last 20 years much research has been devoted to investigate anisotropic properties of geomaterials. However, in surprisingly few cases these experimental results have been utilized in numerical simulations. This thesis focusses on anisotropy in the high initial stiffness at very small strains, which in many cases is the relevant strain level under working load conditions. Besides providing a tool for future application in numerical simulations, a major aim of this research was to obtain a better understanding of the influence of small strain stiffness anisotropy in geotechnical problems. In most engineering projects the anisotropic stiffness of the soil may not be known, or an anisotropic constitutive model may not be available. In these cases, estimating the range of material parameters and their influence on calculation results can still provide a better prediction of soil behaviour.

The second part of the thesis deals with the behaviour of stiff clays close to and beyond failure. These materials are known to possess much higher shear strength than their soft counterparts at the same stress level. After reaching peak strength, further deformations tend to concentrate in narrow shear bands, and the overall load bearing capacity of the soil body decreases due to loosening of the material. Such behaviour, however, diminishes at high stress levels. In conventional numerical analysis, peak strength is usually accounted for by increasing friction angle and cohesion, which fails to consider the stress dependency of peak strength as well as the reduction of soil strength in strain softening.

Application of strain softening constitutive models in numerical analysis is hindered by significant mesh-dependency, if no regularization technique is employed. A modified non-local approach is adopted here, in which reduction of soil strength is governed by a weighted average of strains in the vicinity of the numerical shear band.

The constitutive model is formulated within the multilaminate framework, as first introduced for soils by Pande & Sharma (1983). Material behaviour is defined by yield and plastic potential functions on so-called integration planes of predefined orientation. Plastic strains and strain hardening of yield surfaces are allowed to develop independently on these planes, thus accounting for strain induced anisotropy and rotation of principle stresses in a straightforward way. Recent developments at TU Graz, namely the work of Galavi (2007) and Scharinger (2007), form the basis of the current multilaminate model. Anisotropic shear strength as implemented by Galavi (2007) has been incorporated, but is not considered in this thesis.

1.2 Outline of thesis

A brief introduction to the concept of the multilaminate framework, which forms the basis of the constitutive model, and its historical development is given at the beginning of this thesis. The mathematical formulations and their underlying mechanical and geometric meaning are discussed. The principle of virtual work is shown to deliver mechanically sound micro-macro relations between local strains on integration planes and macroscopic strains. Applying the principle to isotropic elastic material, micro-macro relations for elastic parameters are established. Different assumptions with regard to the split of local stresses and their consequences for local strain distributions are discussed.

The basic version of the multilaminate model is presented in chapter 3. The yield criteria, hardening rules and plastic potential functions are explained. The stress point return algorithm is described only briefly, with a more detailed description provided in Appendix B. The numerical algorithm of the basic model has been modified to increase calculation speed and numerical robustness. It is shown that these improvements do not influence the accuracy of calculation results.

Anisotropic soil stiffness at very small strains is considered in chapter 4. Experimental data of anisotropic small strain stiffness are reviewed and inconsistencies in the experimental results are discussed. Focus is set on inherent and stress induced anisotropy. Two approaches for modelling anisotropic stiffness in the multilaminate framework are compared with respect to their capability to cover the range of experimental data. The formulations adopted in the anisotropic small strain model to account for stress dependency of stiffness, stiffness degradation and dependency on load history are presented. The model is validated by comparing model predictions with element test data of various soils, both in the small strain and large strain range.

The influence of anisotropic small strain stiffness in boundary value problems is investigated in chapter 5. Two simplified geotechnical problems, the excavation of a construction pit supported by a sheet pile wall and a shallow strip footing, are simulated numerically assuming various combinations of anisotropic small strain stiffness parameters.

Chapter 6 starts with a discussion of the mechanical behaviour of heavily overconsolidated clays and dense sands. The enhancement of the basic model to account for peak strength and strain softening of these materials is based on the critical state framework. The mathematical formulations of a Hvorslev yield surface on integration plane level, the corresponding softening rule and plastic potential are given. The capability of the model to predict pre-peak deformation behaviour is shown in simulations of undrained triaxial tests on Pietrafitta clay and Vallericca clay at different stress levels. Different regularization techniques to overcome mesh dependency in strain softening analysis are briefly explained. The non-local approach is discussed in more detail, as this method is employed in the model in the post-peak range. Numerical simulations of biaxial tests demonstrate that mesh independent results can be obtained. The impact of employing non-local strain regularization in the pre-peak range on the mechanical behaviour and the evolution of shear bands is discussed at the end of this chapter.

Chapter 7 summarizes the most significant findings of this work and gives some recommendations for further research on multilaminate models. References are provided in Chapter 8.

In order to focus on modelling aspects in the main part of the thesis, details of implementation are provided in appendices. Appendix A gives the eigenvalues and idempotent matrices of the cross-anisotropic elastic compliance matrix, required in the spectral decomposition method. Appendix B explains the implementation of the model as a user-defined subroutine in the finite element code PLAXIS 2D 2010. Partial derivatives of yield and plastic potential functions are also given there. The mathematical derivation of the Hvorslev yield function from the normalized formulation of the Hvorslev surface is shown in Appendix C. Appendix D contains the source code of the model, written in the programming language FORTRAN.

2 Multilaminate framework

2.1 Concept

The multilaminate framework is based on the concept, that the macro-mechanical behaviour of materials can be related to processes at the micro-mechanical scale. This approach dates back to the slip theory of Taylor (1938), who described sliding phenomena in metals by considering contact planes of various orientations. The concept is particularly attractive for describing the behaviour of granular materials like soils. If such materials are considered as an assemblage of discrete, solid particles, elastic deformations can be assigned to the particles, and plastic deformation can be attributed to inter-particle sliding. Macroscopic deformation of the soil body can be obtained by summation of all the micro-mechanical deformations.

A stringent variant of such an approach is found in the discrete element method (Cundall & Strack 1979), which models the interaction of all the individual particles. However, numerical analysis of practical boundary value problems using this approach suffers from the massive computational effort caused by the large number of particles. Application of the method is further hampered by the difficulty in obtaining appropriate micro-mechanical parameters.

To overcome these limitations, a major simplification is introduced in the multilaminate framework: Instead of modelling individual particles, soil is considered as a continuum with an infinite number of potential sliding planes of varying orientation. Elastic deformations are obtained from the continuum, and plastic deformations are derived from the sliding of planes once a predefined ratio of normal and shear stresses on the plane is exceeded. In numerical calculations, an infinite number of planes is obviously not feasible and a finite number of planes with predefined orientations is introduced. In this study these planes are called “integration planes”. A weighting factor is assigned to each integration plane in order to account for the area of influence represented by the respective plane.

2.2 Development of multilaminate models

The slip theory of Taylor (1938), which already comprised basic elements of the multilaminate framework, was further developed by Batdorf & Budiansky (1949) and Sanders (1955) to describe plastic straining of metal crystals. The first application to geomaterials dates back to Zienkiewicz & Pande (1977), who modelled rock joints of fixed orientation as planes of weakness within an elastic continuum and introduced the term “multilaminate model”. Assuming that an infinite number of slip planes are present in the material, the concept was extended for modelling of sands and clays by Pande & Sharma (1983) and Sadrnejad & Pande (1989). The novel idea was to use integration planes as a representation of continuum plasticity rather than a modelling tool for discrete joints. They used the model to investigate strain induced anisotropy and rotation of principal axis during loading.

An extensive comparison with predictions of standard invariant formulations has been given by Sharma (1980) and Varadarajan et al. (1990). Krajewski (1986) used a multilaminate model with volumetric and deviatoric strain hardening yield surfaces to back-calculate the load-displacement curves and bearing capacity of pile model tests. A summary on modelling elastoplastic material behaviour within the multilaminate framework was provided by Pietruszczak & Pande (1987).

A rate-independent multilaminate model has also been applied by Karstunen (1999) to study strain localization in dense sand, using a homogenisation technique to mitigate mesh dependency in the post-peak range. More recently, Schuller (2000) used a viscoplastic model based on the multilaminate framework for plane strain analysis of strain localization. His model employed deviatoric strain hardening in the pre-peak range and strain softening for post-peak behaviour, but no strain regularization was taken into account.

Wiltafsky (2003) developed the Multilaminate Model for Clay, which utilizes a deviatoric and a volumetric strain hardening yield surface. His model has been implemented into the finite element code PLAXIS (Brinkgreve et al. 2006) for the analysis of normally and slightly overconsolidated Scandinavian clays. The latest developments have been achieved by Scharinger (2007), who implemented inherently isotropic small strain stiffness and a new deviatoric plastic potential function, and by Galavi (2007), who added anisotropic shear strength, destructuration and strain softening with non-local strain regularization to Wiltafsky’s model.

At the beginning of the 1980ies, another class of conceptually similar models has been developed by Bažant and co-workers (Bažant & Oh 1983, Bažant 1984, Bažant & Prat 1988). Originally proposed for modelling fracturing and softening of concrete, these so-called “microplane” models employ the kinematic constraint (strains on integration planes are the projection of macroscopic strains) rather than the static constraint (stresses on integration planes are the projection of macroscopic stresses) used in multilaminate type models. In the first microplane models the material behaviour was described by explicit stress-strain curves, which were hard to compare to e.g. Mohr-Coulomb type failure criteria known in soil mechanics. Even though more recent developments introduced classical plasticity concepts (Carol & Bazant 1997, Kuhl & Ramm 2000, Sanchez & Prat 2008), application of microplane models to geotechnical boundary value problems is still rare.

2.3 Mathematical formulation

Multilaminate constitutive models are based on the concept that the global three-dimensional stress state can be represented by the sum of local, two-dimensional stress states at planes of varying orientation. The macroscopic strain corresponding to a global stress increment is obtained by integration of the local strains over all orientations, which are calculated according to the constitutive model defined locally.

Except for very basic material models and simple stress states, such integration cannot be carried out analytically. Therefore a predefined number of orientations is taken into account, and the integration over all orientations is replaced by the summation over these integration planes. Each plane represents a sector of a virtual sphere of unit radius around the stress point and is assigned a weight factor according to the proportion of its sector with regard to the volume of the unit sphere.

The orientation of plane *i* is fully defined by its normal vector $\mathbf{n}_i$, whose orientation with respect to the global coordinate system *x*, *y*, *z* is given by the angles α_i and β_i. The stress-strain behaviour is formulated locally in terms of local stresses and strains. In order to uniquely define the direction of the local stresses and strains parallel to the integration plane, local unit vectors $\mathbf{s}_i$ and $\mathbf{t}_i$ are introduced, with $\mathbf{n}_i$, $\mathbf{s}_i$ and $\mathbf{t}_i$ forming a system of mutually orthogonal local axes. While the choice of $\mathbf{s}_i$ and $\mathbf{t}_i$ is in principle arbitrary (provided they are mutually orthogonal), it is convenient to choose $\mathbf{s}_i$ and $\mathbf{t}_i$ parallel to the dip and strike direction of plane *i*, respectively.

$$\mathbf{n}_i = \begin{bmatrix} n_{1,i} \\ n_{2,i} \\ n_{3,i} \end{bmatrix} = \begin{bmatrix} \cos\alpha_i \\ \sin\alpha_i \cdot \sin\beta_i \\ \sin\alpha_i \cdot \cos\beta_i \end{bmatrix} \tag{1}$$

$$\mathbf{s}_i = \begin{bmatrix} s_{1,i} \\ s_{2,i} \\ s_{3,i} \end{bmatrix} = \begin{bmatrix} -\sin\alpha_i \\ \cos\beta_i \cdot \cos\alpha_i \\ \sin\beta_i \cdot \cos\alpha_i \end{bmatrix}, \quad \mathbf{t}_i = \begin{bmatrix} t_{1,i} \\ t_{2,i} \\ t_{3,i} \end{bmatrix} = \begin{bmatrix} 0 \\ -\sin\beta_i \\ \cos\beta_i \end{bmatrix} \tag{2}$$

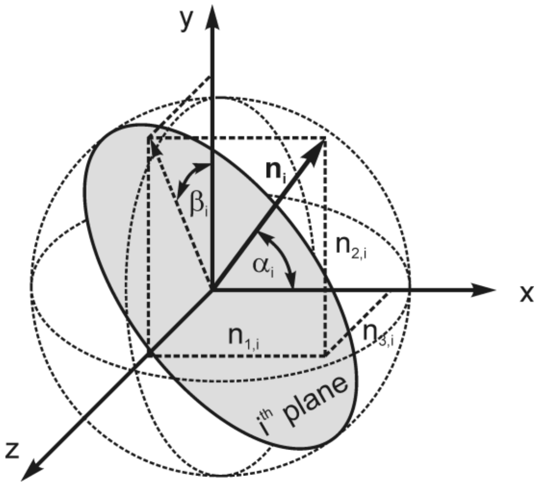

Fig. 1: Definition of integration plane orientation

The stress-strain state varies from plane to plane for all non-isotropic loading paths. If an elastoplastic strain hardening constitutive model is used, anisotropic hardening induced by plastic strains is automatically taken into account in the framework. Local stress increments $\mathbf{d\sigma}'_i$ are a projection of the global stresses, which is a fundamental assumption in multilaminate constitutive models and known as the static constraint. The global stress increment $\mathbf{d\sigma}'$, defined by 6 components and written as a vector in Equation 3, is projected on integration plane i by the transformation matrix $\mathbf{T}_i$.

$$\mathbf{d\sigma}' = \begin{pmatrix} d\sigma'_{xx} & d\sigma'_{yy} & d\sigma'_{zz} & d\tau_{xy} & d\tau_{yz} & d\tau_{xz} \end{pmatrix}^T \tag{3}$$

$$\mathbf{d\sigma}'_i = (\mathbf{T}_i)^T \cdot \mathbf{d\sigma}' = \begin{pmatrix} d\sigma'_n & d\tau_s & d\tau_t \end{pmatrix}^T \tag{4}$$

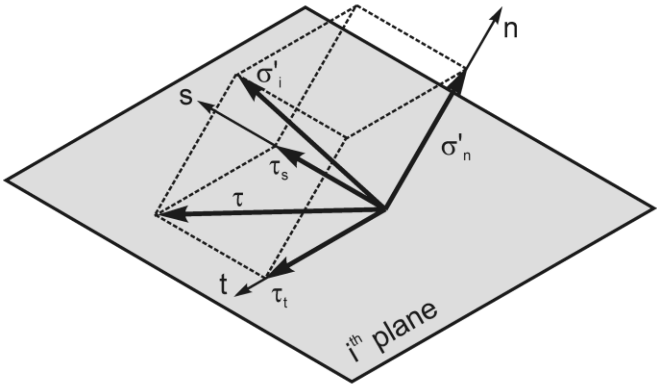

Fig. 2: Definition of local stress components

The transformation matrix $\mathbf{T}_i$ contains the derivatives of the local stress components with respect to the global axes, represented by the direction cosine of $\mathbf{n}_i$, $\mathbf{s}_i$ and $\mathbf{t}_i$.

$$\mathbf{T}_i = \frac{\partial \boldsymbol{\sigma}'_i}{\partial \boldsymbol{\sigma}'} = \begin{bmatrix} n_{1,i}^2 & n_{1,i} \cdot s_{1,i} & n_{1,i} \cdot t_{1,i} \\ n_{2,i}^2 & n_{2,i} \cdot s_{2,i} & n_{2,i} \cdot t_{2,i} \\ n_{3,i}^2 & n_{3,i} \cdot s_{3,i} & n_{3,i} \cdot t_{3,i} \\ 2n_{1,i} \cdot n_{2,i} & n_{1,i} \cdot s_{2,i} + n_{2,i} \cdot s_{1,i} & n_{1,i} \cdot t_{2,i} + n_{2,i} \cdot t_{1,i} \\ 2n_{2,i} \cdot n_{3,i} & n_{3,i} \cdot s_{2,i} + n_{2,i} \cdot s_{3,i} & n_{3,i} \cdot t_{2,i} + n_{2,i} \cdot t_{3,i} \\ 2n_{1,i} \cdot n_{3,i} & n_{3,i} \cdot s_{1,i} + n_{1,i} \cdot s_{3,i} & n_{3,i} \cdot t_{1,i} + n_{1,i} \cdot t_{3,i} \end{bmatrix} \tag{5}$$

Local strain increments are calculated according to the local constitutive model. If an elasto-plastic constitutive model is employed, the local strain increment $\mathbf{d\varepsilon}_i$ can be decomposed into elastic and inelastic contributions:

$$\mathbf{d\varepsilon}_i = \left(d\varepsilon_n \quad d\gamma_s \quad d\gamma_t \right)^T = \mathbf{d\varepsilon}_i^e + \mathbf{d\varepsilon}_i^p . \tag{6}$$

The local elastic strain increment $\mathbf{d\varepsilon}^e{}_i$ is obtained as

$$\mathbf{d\varepsilon}_i^e = \left(d\varepsilon_n^e \quad d\gamma_s^e \quad d\gamma_t^e \right)^T = \mathbf{C}_i \cdot \mathbf{d\sigma}'_i . \tag{7}$$

$\mathbf{C}_i$ is the local compliance matrix, which in the case of isotropic linear elastic material is equal for all planes. For non-linear elasticity (small strain stiffness), $\mathbf{C}_i$ depends on the strain history of each plane and therefore differs from plane to plane, resulting in anisotropic global behaviour, even though initially the material was isotropic. Further explanation regarding the structure and elements of $\mathbf{C}_i$ is given in subsequent chapters. The local plastic strain increment of the ith integration plane is calculated according to plasticity theory by

$$\mathbf{d\varepsilon}_i^p = \left(d\varepsilon_n^p \quad d\gamma_s^p \quad d\gamma_t^p \right)^T = d\Lambda_i \cdot \frac{\partial g_i}{\partial \boldsymbol{\sigma}'_i} . \tag{8}$$

$d\Lambda_i$ is the increment of the local plastic multiplier, which is obtained from the derivatives of local yield functions f_i, plastic potential functions g_i and the value of the yield function at the elastic trial stress, f_i^{trial}. Further details on the calculation of plastic strains are given in Appendix B.

$$d\Lambda_i = \frac{f_i^{trial}}{\frac{\partial f_i}{\partial \boldsymbol{\sigma}'_i} \cdot \mathbf{C}_i^{-1} \cdot \frac{\partial g_i}{\partial \boldsymbol{\sigma}'_i} - \frac{\partial f_i}{\partial \boldsymbol{\varepsilon}_i^p} \cdot \frac{\partial g_i}{\partial \boldsymbol{\sigma}'_i}} \tag{9}$$

Micro-macro relations between local and global strains can be established by enforcing the equivalence of virtual work at the macro- and micro-scale for small variations of the stress state $\delta\boldsymbol{\sigma}'$ and $\delta\boldsymbol{\sigma}'_i$ (Bažant & Gambarova 1984). At the macroscale, virtual work δW_{macro} is taken over the volume of a unit sphere, while the sum of microscopic virtual work δW_{micro} equals the integral over the surface S of a unit sphere.

$$\delta W_{macro} = \frac{4\Pi}{3} \cdot \delta\boldsymbol{\sigma}' \cdot \mathbf{d\varepsilon} = \int_S \delta W_{micro} dS = \int_S \left(\delta\boldsymbol{\sigma}'_i \cdot \mathbf{d\varepsilon}_i\right) dS \tag{10}$$

Following the static constraint, small local stress variations $\delta\boldsymbol{\sigma}'_i$ are projections of the macroscopic stress variation $\delta\boldsymbol{\sigma}'$.

$$\delta\boldsymbol{\sigma}'_i = \mathbf{T}_i^T \cdot \delta\boldsymbol{\sigma}' \tag{11}$$

Substituting Equation 11 into Equation 10 and taking $\delta\boldsymbol{\sigma}'$ (which is independent of plane orientation) out of the integral, a straightforward relation between macroscopic and local strain increments is obtained.

$$\frac{4\Pi}{3} \cdot \delta\boldsymbol{\sigma}' \cdot \mathbf{d\varepsilon} = \int_S \left[\left(\mathbf{T}_i^T \cdot \delta\boldsymbol{\sigma}'\right) \cdot \mathbf{d\varepsilon}_i\right] dS = \delta\boldsymbol{\sigma}' \cdot \int_S \left(\mathbf{T}_i \cdot \mathbf{d\varepsilon}_i\right) dS \tag{12}$$

$$0 = \delta\boldsymbol{\sigma}' \cdot \left[\int_S \left(\mathbf{T}_i \cdot \mathbf{d\varepsilon}_i\right) dS - \frac{4\Pi}{3} \cdot \mathbf{d\varepsilon}\right] \tag{13}$$

$$\mathbf{d\varepsilon} = \frac{3}{4\Pi} \cdot \int_S \left(\mathbf{T}_i \cdot \mathbf{d\varepsilon}_i\right) dS = \frac{3}{4\Pi} \int_{\alpha=0}^{\Pi} \int_{\beta=0}^{2\Pi} \left(\mathbf{T}_i \cdot \mathbf{d\varepsilon}_i\right) \cdot \sin\alpha \cdot d\beta \cdot d\alpha \tag{14}$$

In Equation 14 the infinitesimal surface area dS of the unit sphere is expressed in terms of the infinitesimal angles $d\alpha$ and $d\beta$. If the full integration is replaced by a numerical summation over a distinct number of predefined planes, with each plane representing a sector of the unit sphere, the infinitesimal angles $d\alpha$ and $d\beta$ turn into finite values $\Delta\alpha$ and $\Delta\beta$. The weight factors w_i are defined as the share of the surface area of each sector with respect to the total surface area of the unit sphere.

$$w_i = \frac{A_i}{A_{sphere}} = \frac{1^2 \cdot \sin\alpha \cdot \Delta\alpha \cdot \Delta\beta}{4\Pi \cdot 1^2} = \frac{\sin\alpha \cdot \Delta\alpha \cdot \Delta\beta}{4\Pi} \tag{15}$$

$$\mathbf{d\varepsilon} = \begin{pmatrix} d\varepsilon_{xx} & d\varepsilon_{yy} & d\varepsilon_{zz} & d\gamma_{xy} & d\gamma_{yz} & d\gamma_{xz} \end{pmatrix}^T \approx 3 \cdot \sum_i \left(\mathbf{T}_i \cdot \mathbf{d\varepsilon}_i \cdot w_i \right) \tag{16}$$

The weight factors w_i depend on the chosen integration rule and thus on the number and distribution of planes used for approximating the full integration over the sphere. While increasing the number of integration planes leads to more accurate results, and thus a higher number of planes would be favourable, for large boundary value problems the number of planes is limited by the computational effort required. Previous studies have shown that an integration rule based on 2 × 33 planes balances reasonably well between accuracy and computational effort (Bažant and Oh 1986, Scharinger 2007, Ehret et al. 2010). The direction cosines and corresponding weight factors are listed in Table 1 for this integration rule, which is used in the numerical simulations presented in this study.

Tab. 1: Direction cosines $n_{1,i}$, $n_{2,i}$, $n_{3,i}$ and weighting factors w_i of the integration planes for the symmetric 2 x 33-plane integration rule (Bazant & Oh 1986)

i	$n_{1,i}$	$n_{2,i}$	$n_{3,i}$	w_i
1	1	0	0	0.00985353993
2	0	1	0	0.00985353993
3	0	0	1	0.00985353993
4	0.7071067811	0.7071067811	0	0.01629696858
5	0.7071067811	-0.7071067811	0	0.01629696858
6	0.7071067811	0	0.7071067811	0.01629696858
7	0.7071067811	0	-0.7071067811	0.01629696858
8	0	0.7071067811	0.7071067811	0.01629696858
9	0	0.7071067811	-0.7071067811	0.01629696858
10	0.9338989563	0.3575370459	0	0.01347888440
11	0.9338989563	-0.3575370459	0	0.01347888440
12	0.3575370459	0.9338989563	0	0.01347888440
13	0.3575370459	-0.9338989563	0	0.01347888440
14	0.9338989563	0	0.3575370459	0.01347888440
15	0.9338989563	0	-0.3575370459	0.01347888440
16	0.3575370459	0	0.9338989563	0.01347888440
17	0.3575370459	0	-0.9338989563	0.01347888440
18	0	0.9338989563	0.3575370459	0.01347888440
19	0	0.9338989563	-0.3575370459	0.01347888440
20	0	0.3575370459	0.9338989563	0.01347888440
21	0	0.3575370459	-0.9338989563	0.01347888440
22	0.4372636760	0.4372636760	0.7858759158	0.01757591298
23	0.4372636760	0.4372636760	-0.7858759158	0.01757591298
24	0.4372636760	-0.4372636760	0.7858759158	0.01757591298
25	0.4372636760	-0.4372636760	-0.7858759158	0.01757591298
26	0.4372636760	0.7858759158	0.4372636760	0.01757591298
27	0.4372636760	0.7858759158	-0.4372636760	0.01757591298
28	0.4372636760	-0.7858759158	0.4372636760	0.01757591298
29	0.4372636760	-0.7858759158	-0.4372636760	0.01757591298
30	0.7858759158	0.4372636760	0.4372636760	0.01757591298
31	0.7858759158	0.4372636760	-0.4372636760	0.01757591298
32	0.7858759158	-0.4372636760	0.4372636760	0.01757591298
33	0.7858759158	-0.4372636760	-0.4372636760	0.01757591298

2.4 Micro-macro relations for isotropic elasticity

An important issue in multilaminate, microplane and micromechanical models is consistency between local and global material parameters, which are often referred to as micro-macro-relations (Carol et al. 1992). For plastic material behaviour such relations can only be established for rather simple elastic-perfectly plastic constitutive models based on Drucker-Prager, Tresca or Von Mises failure criteria (Leukart 2005). The global stress-strain behaviour of more advanced, multilaminate strain hardening models is a result of formulating yield surfaces and hardening rules on local level rather than by direct input. Accordingly, there is limited benefit to relate local hardening parameters to parameters used in other models which are formulated macroscopically.

However, establishing micro-macro-relations is much more relevant for elastic material behaviour, as in that case the stress-strain behaviour is unambiguously defined on global level. Any local constitutive model should not only deliver exactly the desired elastic stress-strain behaviour, but furthermore the local strains should be mechanically meaningful, if local parameters are supposed to vary with local strains.

In order to enforce consistency between local and global elastic stiffness parameters, micro-macro-relations can be determined analytically by comparing local and macroscopic strain increments for a general macroscopic stress increment. As the integration over all local orientations can be carried out analytically, no error is induced by assuming a numerical integration rule.

The global compliance matrix **C** for an isotropic elastic material is defined by two parameters, the Young's modulus *E* and Poisson's ratio ν' (Equation 17), while the local normal and shear compliance C_n and C_t form the local compliance matrix $\mathbf{C}_i$. It should be noted, that the diagonal structure of $\mathbf{C}_i$ (Equation 18) already involves the assumption, that on the local level elastic normal and shear deformations are decoupled and only caused by the respective normal and shear stresses.

$$\mathbf{C} = \frac{1}{E} \cdot \begin{bmatrix} 1 & -\nu' & -\nu' & 0 & 0 & 0 \\ -\nu' & 1 & -\nu' & 0 & 0 & 0 \\ -\nu' & -\nu' & 1 & 0 & 0 & 0 \\ 0 & 0 & 0 & 2\cdot(1+\nu') & 0 & 0 \\ 0 & 0 & 0 & 0 & 2\cdot(1+\nu') & 0 \\ 0 & 0 & 0 & 0 & 0 & 2\cdot(1+\nu') \end{bmatrix} \tag{17}$$

$$\mathbf{C}_i = \begin{pmatrix} C_n & 0 & 0 \\ 0 & C_t & 0 \\ 0 & 0 & C_t \end{pmatrix} \tag{18}$$

Equating the macroscopic strain increment **dε** with the integral over all local strain increments (Equation 19) delivers a unique relationship between local and global compliance (Equation 21).

$$\mathbf{d\varepsilon} = \mathbf{C} \cdot \mathbf{d\sigma}' = \frac{3}{4\Pi} \cdot \int\limits_{\alpha}\int\limits_{\beta} \left(\mathbf{T}_i \cdot \mathbf{d\varepsilon}_i\right) \cdot \sin\alpha \cdot d\beta \cdot d\alpha \tag{19}$$

$$\mathbf{d\varepsilon}_i = \mathbf{C}_i \cdot \mathbf{d\sigma}'_i = \mathbf{C}_i \cdot \left(\mathbf{T}_i^T \cdot \mathbf{d\sigma}'\right) \tag{20}$$

$$\mathbf{C} \cdot \mathbf{d\sigma}' = \frac{3}{4\Pi} \cdot \int\limits_{\alpha}\int\limits_{\beta} \left(\mathbf{T}_i \cdot \mathbf{C}_i \cdot \left(\mathbf{T}_i^T \cdot \mathbf{d\sigma}'\right)\right) \cdot \sin\alpha \cdot d\beta \cdot d\alpha \tag{21}$$

As the global stress increment **dσ′** is independent of plane orientation, it can be taken out of the integral and omitted from Equation 21. A direct relationship linking **C** and **C**$_i$ is obtained, and local parameters C_n and C_t are found by equating the elements of **C** in Equation 23 to those in Equation 17.

$$\mathbf{C} = \frac{3}{4\Pi} \cdot \int\limits_{\alpha}\int\limits_{\beta} \left(\mathbf{T}_i \cdot \mathbf{C}_i \cdot \mathbf{T}_i^T\right) \cdot \sin\alpha \cdot d\beta \cdot d\alpha \tag{22}$$

$$\mathbf{C} = \frac{1}{5} \cdot \left[\begin{matrix} 3C_n + 2C_t & C_n - C_t & C_n - C_t \\ C_n - C_t & 3C_n + 2C_t & C_n - C_t \\ C_n - C_t & C_n - C_t & 3C_n + 2C_t \\ 0 & 0 & 0 \\ 0 & 0 & 0 \\ 0 & 0 & 0 \end{matrix}\right. \cdots$$

$$\left.\begin{matrix} 0 & 0 & 0 \\ 0 & 0 & 0 \\ 0 & 0 & 0 \\ 4C_n + 6C_t & 0 & 0 \\ 0 & 4C_n + 6C_t & 0 \\ 0 & 0 & 4C_n + 6C_t \end{matrix}\right] \tag{23}$$

$$C_n = \frac{1-2\nu'}{E}; \quad C_t = \frac{1+3\nu'}{E} \tag{24}$$

If the kinematic constraint is utilized, a different set of local parameters are obtained (Carol & Bažant 1997), which shows that the proposed split of local stresses in normal and tangential components (N-T-split) does not fulfil the double constraint (i.e. both static and kinematic constraint). Although this is not strictly necessary for formulating multilaminate material models, by fulfilling the double constraint thermodynamic inconsistency and spurious energy dissipation can be avoided (Carol et al. 2001).

However, it is not straightforward to define a local elastic compliance matrix which satisfies the double constraint. Introducing some sort of coupling between local shear and normal strains leads to a non-diagonal local compliance matrix, and requires at least one additional local parameter. As in this case three local parameters are employed, these may not be uniquely related to the two global elastic parameters E and ν' anymore.

Another, more promising approach is to introduce a different split of the local stresses and strains, as first proposed for microplane models by Bažant & Prat (1988) and later derived theoretically by Kuhl & Ramm (2000) and Leukart (2005). Macroscopic elastic stress-strain behaviour can be split into a volumetric (p', ε_{vol}) and deviatoric (q, E_d) part, with each part being governed by one corresponding material parameter, bulk modulus K' and shear modulus G (Potts and Zdravković 1999).

$$\begin{pmatrix} \Delta p' \\ \Delta J \end{pmatrix} = \begin{pmatrix} K' & 0 \\ 0 & G \end{pmatrix} \cdot \begin{pmatrix} \Delta\varepsilon_v \\ \Delta E_d \end{pmatrix} \tag{25}$$

$$K' = \frac{E'}{2\cdot(1-2\nu')}; \quad G = \frac{E'}{2\cdot(1+\nu')} \tag{26}$$

The same can be achieved on local level by projecting both the macroscopic volumetric and deviatoric stress components separately into the plane coordinate system. Doing so delivers local volumetric and deviatoric stresses, $\boldsymbol{\sigma}'^{vol}_i$ and $\boldsymbol{\sigma}^{dev}_i$.

$$\boldsymbol{\sigma}'^{vol}_i = \begin{pmatrix} \sigma'_{nv} \\ 0 \\ 0 \end{pmatrix} = p' \cdot \begin{pmatrix} 1 \\ 0 \\ 0 \end{pmatrix}. \tag{27}$$

$$\boldsymbol{\sigma}_i^{dev} = \begin{pmatrix} \sigma_{nd} \\ \tau_s \\ \tau_t \end{pmatrix} = \mathbf{T}_i^T \cdot (\boldsymbol{\sigma}' - p' \cdot \mathbf{1}) = \mathbf{T}_i^T \cdot \left(\begin{bmatrix} \sigma'_{xx} \\ \sigma'_{yy} \\ \sigma'_{zz} \\ \tau_{xy} \\ \tau_{yz} \\ \tau_{xz} \end{bmatrix} - p' \cdot \begin{bmatrix} 1 \\ 1 \\ 1 \\ 0 \\ 0 \\ 0 \end{bmatrix} \right). \tag{28}$$

As local stresses are split into components according to their origin in macroscopic volumetric and deviatoric stresses, this approach is known as the volumetric-deviatoric split or V-D split (Leukart 2005). The volumetric component is independent of plane orientation and equals the macroscopic mean stress p', while the deviatoric normal component is obtained as $\sigma_{nd} = \sigma'_n - \sigma'_{nv}$. Local stresses are rearranged according to Equation 29 in order to retain the local stress-strain relationship $\boldsymbol{\varepsilon}_i = \mathbf{C}_i \cdot \boldsymbol{\sigma}'_i$. It should be noted, that the first two components σ'_{nv} and σ_{nd} have the same spatial orientation.

$$\boldsymbol{\sigma}'_i = \begin{pmatrix} \sigma'_{nv} & \sigma_{nd} & \tau_s & \tau_t \end{pmatrix}^T \tag{29}$$

$$\mathbf{C}_i = \begin{pmatrix} C_v & 0 & 0 & 0 \\ 0 & C_d & 0 & 0 \\ 0 & 0 & C_d & 0 \\ 0 & 0 & 0 & C_d \end{pmatrix} \tag{30}$$

As the shear stresses τ_s and τ_t and the deviatoric normal stress σ_{nd} are projections of the macroscopic deviatoric stress, the same local compliance C_d can be assigned to these local stress components. Following the same procedure as for the N-T-split, local elastic compliance parameters are found for the V-D-split as

$$C_v = \frac{1}{K'} = \frac{1-2\nu'}{E}; \quad C_d = \frac{1}{2G} = \frac{1+\nu'}{E} \tag{31}$$

The same set of micro-macro-relations is obtained with the kinematic constraint as demonstrated by Carol and Bažant (1997), thus indicating that the V-D-split fulfils the double constraint for linear elastic material.

Local elastic compliance must be strictly positive to be physically meaningful. As C_t becomes negative for $\nu' < -1/3$ in the N-T-split, and C_n and C_v become zero for $\nu' = 0.5$ in the N-T and V-D-split, respectively, this condition is not fulfilled for the full range of mechanically possible Poisson’s ratios ($-1 \leq \nu' \leq 0.5$).

However, negative isotropic Poisson's ratios (i.e. horizontal contraction in vertical compression) are typically not encountered in geomaterials. A Poisson's ratio $\nu' = 0.5$ is only relevant in undrained total stress analysis, in which case a value of $0.495 \leq \nu' < 0.5$ can be chosen, as suggested by Potts and Zdravković (1999). Consequently, no restrictions on the applicability of N-T and V-D-split in geotechnical problems are imposed by the limits of ν'.

N-T and V-D split differ in the distribution of local strains for macroscopic deviatoric loading, which is illustrated by the following example. The response of an isotropic elastic material (E = 10 MPa, $\nu' = 0.2$) to an isotropic stress increment of $\Delta\sigma'_v = \Delta\sigma'_h = -100$ kPa and to a triaxial stress increment of $\Delta\sigma'_h = 0$, $\Delta\sigma'_v = -100$ kPa is examined. For these simple cases the distribution of local strains can be worked out analytically using Equations 1, 2, 4 and 6.

Figure 3 and Figure 4 show local strain distributions over the plane orientation angle α, with $\alpha = 0$ denoting a horizontal plane and $\alpha = 90°$ a vertical plane. For the V-D-split the volumetric and deviatoric normal strains have been summed up to obtain the local normal strain $\Delta\varepsilon_n$. As the triaxial stress increment is symmetric to the vertical axis, local stresses and resulting elastic strains are independent of the orientation angle β.

Both N-T and V-D-split deliver identical macroscopic strain increments of $\Delta\varepsilon_v$ = -1.0%, $\Delta\varepsilon_h$ = 0.2%. However, local normal and shear strain distributions differ considerably. The V-D split delivers local normal strains $\Delta\varepsilon_n \neq 0$ for a vertically orientated plane (even though $\Delta\sigma'_n = 0$ on that plane), as the deviatoric normal strain (expansion) outweighs the contribution of the volumetric normal strain (compression). The N-T split delivers $\Delta\varepsilon_n = 0$ in that direction, as plane normal strain exclusively depends on plane normal stress $\Delta\sigma'_n$, which does not change for a vertically orientated plane. The difference in the local strains between N-T and V-D split becomes larger with increasing deviation from the isotropic stress state.

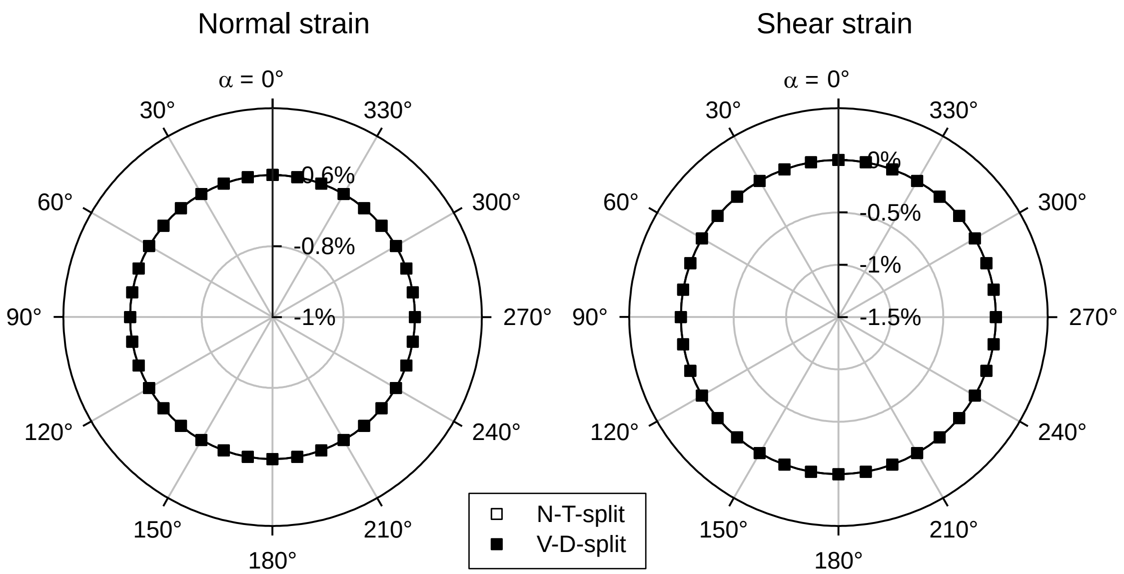

Normal strain

Shear strain

Fig. 3: Distribution of local strains in isotropic compression

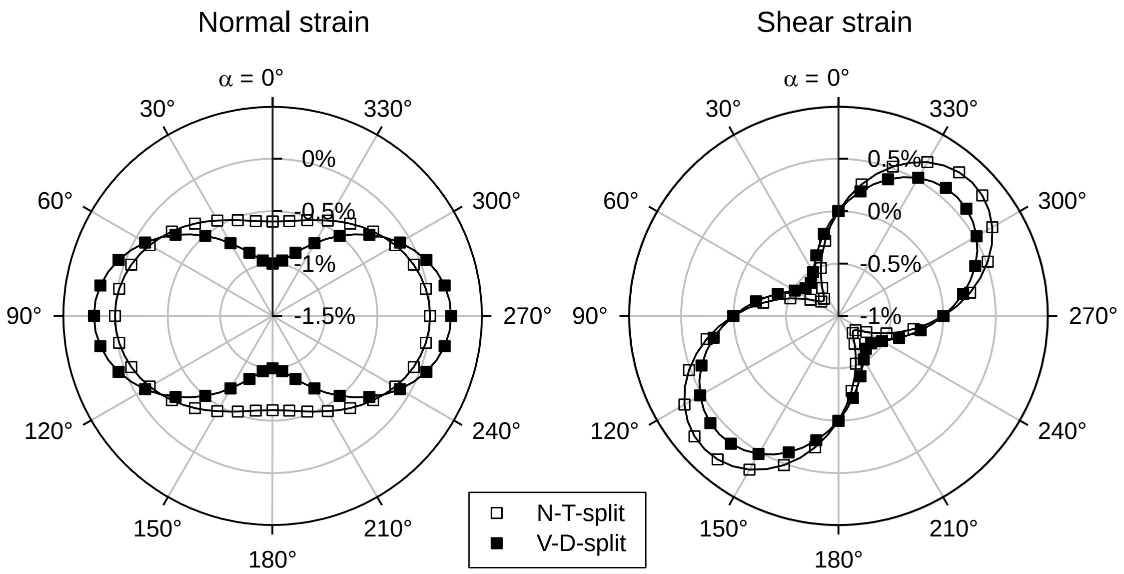

Normal strain

Shear strain

Fig. 4: Distribution of local strains in triaxial compression

3 Basic multilaminate model for soils

In this chapter the basic version of the multilaminate constitutive model for soils is presented, which is based on the model proposed by Scharinger (2007). This model has been shown to predict soil behaviour of loose to medium dense sand or normally to slightly overconsolidated clays with good accuracy (Schweiger et al. 2009). In order to apply the multilaminate model to heavily overconsolidated clay and dense sand, further developments have been necessary, which are described in detail in chapter 4 and chapter 6.

3.1 Yield criteria, hardening rules and plastic potentials

Three yield surfaces are defined on each integration plane in terms of local shear stress τ and normal stress σ'_n: A volumetric hardening surface f_{cap} for normal compression, a shear hardening surface f_{cone} for deviatoric loading and a non-hardening tension cut-off f_{tens} to limit allowable tensile stresses (Figure 5). The local shear stress τ is the resultant tangential stress on the integration plane, obtained as the geometrical sum of shear stresses in direction **s** and **t**.

The yield surfaces separate the elastic region from the plastic domain and are defined by Equations 32-34. At the end of any calculation step the local stress state must either be situated inside the elastic domain or on the yield surface. Mobilisation of the yield surfaces is formulated according to strain hardening plasticity, i.e. the change of the yield surface is driven by the change of local plastic strains.

$$f_{cap} = \frac{\sigma'^2_n}{\sigma'^2_{nc}} + \frac{\tau^2}{\left(M_{CP} \cdot \sigma'_{nc}\right)^2} - 1 = 0 \tag{32}$$

$$f_{cone} = \tau + \sigma'_n \cdot \tan\varphi'_m - c' \cdot \frac{\tan\varphi'_m}{\tan\varphi'_{max}} = 0 \tag{33}$$

$$f_{tens} = \sigma'_n - \sigma_t = 0 \tag{34}$$

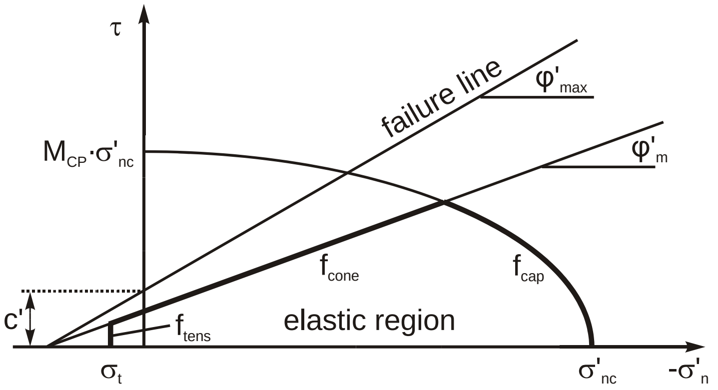

Fig. 5: Local yield surfaces

The position of the cap yield surface f_{cap} is defined by the intersection σ'_{nc} with the σ'_n –axis and the cap shape parameter M_{CP}, which controls the intersection with the τ-axis. M_{CP} is found by an iterative procedure at the beginning of the calculation, as described in chapter 3.4. Mobilisation of the cap yield surface is governed by the change of local plastic normal strains $\Delta\varepsilon^p_{n,cap}$, calculated from the cap yield surface (Equation 35). The hardening parameter K contains the volumetric stiffness in primary loading, E_{oed}, and the elastic unloading/reloading Young's modulus, E_{ur}, both at reference pressure p_{ref}. Compared with the equation proposed by Scharinger (2007), K has been multiplied by a factor of 3.0 in order to account for the multiplication with 3.0 in the summation of local plastic strain contributions (Equation 16).

Dependency of stiffness on stress level is taken into account by an exponential law using the power index m (Equation 37). Fully associated plastic flow is assumed for the cap yield surface, hence the cap plastic potential equals the yield function (Equation 38).

$$\sigma'_{nc,k+1} = -\left[\left(-\sigma'_{nc,k}\right)^{1-m} + K \cdot \frac{(m-1)}{p_{ref}^{m-1}} \cdot \Delta\varepsilon^p_{n,cap}\right]^{\frac{1}{1-m}} \tag{35}$$

$$K = \frac{3}{p_{ref} \cdot \left[\frac{1}{E_{oed,ref}} + \frac{3\cdot(1-2\nu')}{E_{ur,ref}}\right]} \tag{36}$$

$$E_{oed} = E_{oed,ref} \cdot \left(\frac{p'}{p_{ref}}\right)^m \; ; \; E_{ur} = E_{ur,ref} \cdot \left(\frac{p'}{p_{ref}}\right)^m \tag{37}$$

$$g_{cap} = f_{cap} \tag{38}$$

The strain hardening deviatoric yield surface f_{cone} is defined by the maximum friction angle, φ'_{max}, the mobilised friction angle, φ'_m, and the effective cohesion c'. At full mobilisation the cone yield surface equals the Mohr-Coulomb failure line with $\varphi'_m = \varphi'_{max}$. Mobilisation of the cone yield surface with change of local plastic shear strain $\Delta\gamma_{cone}{}^{pl}$ is controlled by the hardening parameter A_{mat}. A failure ratio $R_f = \tan\varphi'_{max}/\tan\varphi'_{mod}$ has been introduced to ensure that φ'_{max} is reached at finite shear strains. The minimum mobilised friction angle φ'_0 can be used to model an elastic range at low shear stresses.

$$\tan\varphi'_m = \tan\varphi'_0 + \left(\tan\varphi'_{mod} - \tan\varphi'_0\right) \cdot \frac{\gamma^p_{cone}}{A_{mat}/3 + \gamma^p_{cone}} \tag{39}$$

$$\tan\varphi'_{m,k+1} = \tan\varphi'_{m,k} + \cdot \frac{\Delta\gamma^p_{cone,k+1} \cdot \left(\tan\varphi'_{mod} - \tan\varphi'_{m,k}\right)}{\dfrac{A_{mat}}{3} \cdot \dfrac{\tan\varphi'_{mod} - \tan\varphi'_0}{\tan\varphi'_{mod} - \tan\varphi'_{m,k}} + \Delta\gamma^p_{cone,k+1}} \tag{40}$$

Plastic flow of the cone yield surface is controlled by the non-associated plastic potential function g_{cone}, which is defined by the mobilised angle of dilatancy, ψ_m. Mobilisation of dilatancy is governed by a cubic function dependent on the mobilised friction angle φ'_m as proposed by Scharinger (2007).

$$g_{cone} = \tau + \sigma'_n \cdot \tan\psi_m = 0 \tag{41}$$

$$\psi_m = \psi_{m,min} \cdot \left[3\left(\frac{\varphi'_m}{\varphi'^*_m}\right)^2 - 2\left(\frac{\varphi'_m}{\varphi'^*_m}\right)^3 \right] \text{ at } 0 \le \varphi'_m \le \varphi'^*_m \tag{42}$$

$$\psi_m = a_{II} \cdot \varphi'^3_m + b_{II} \cdot \varphi'^2_m + c_{II} \cdot \varphi'_m + d_{II} \text{ at } \varphi'^*_m \le \varphi'_m \le \varphi'_{cv} \tag{43}$$

$$a_{II} = \frac{k_{II}(\varphi'^*_m - \varphi'_{cv}) - 2 \cdot \psi_{m,min}}{(\varphi'^*_m - \varphi'_{cv})^3} \tag{44}$$

$$b_{II} = \frac{k_{II}(-2 \cdot \varphi'^{*2}_m + \varphi'^*_m \cdot \varphi'_{cv} + \varphi'^2_{cv}) + 3(\varphi'^*_m + \varphi'_{cv}) \cdot \psi_{m,min}}{(\varphi'^*_m - \varphi'_{cv})^3} \tag{45}$$

$$c_{II} = \frac{k_{II}\left(\varphi_m'^{*3} + \varphi_m'^{*2} \cdot \varphi'_{cv} - 2 \cdot \varphi_m'^{*} \cdot \varphi_{cv}'^{2}\right) - 6 \cdot \varphi_m'^{*} \cdot \varphi'_{cv} \cdot \psi_{m,min}}{\left(\varphi_m'^{*} - \varphi'_{cv}\right)^3} \tag{46}$$

$$d_{II} = \frac{k_{II}\left(\varphi_m'^{*2} \cdot \varphi_{cv}'^{2} - \varphi_m'^{*3} \cdot \varphi'_{cv}\right) + \psi_{m,min}\left(3 \cdot \varphi_m'^{*} \cdot \varphi_{cv}'^{2} - \varphi_{cv}'^{3}\right)}{\left(\varphi_m'^{*} - \varphi'_{cv}\right)^3} \tag{47}$$

$$k_{II} = \frac{\psi}{\varphi' - \varphi'_{cv}} \text{ for } \psi > 0 \text{ and } k_{II} = 0 \text{ for } \psi = 0 \tag{48}$$

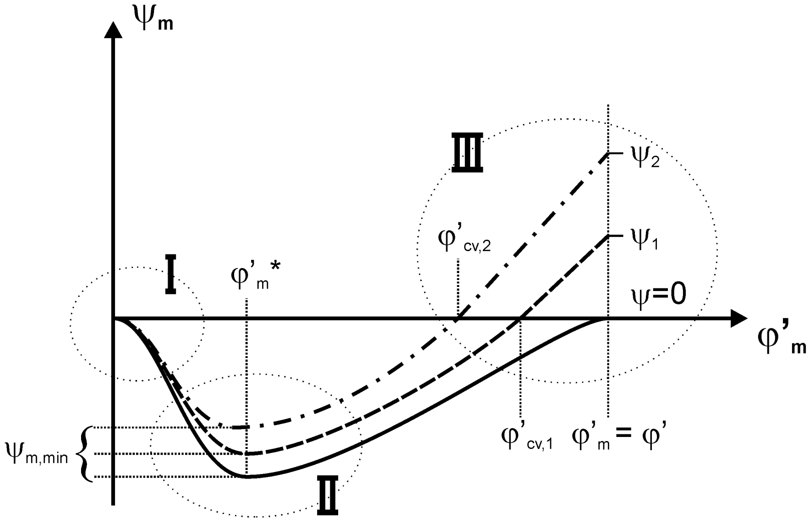

Fig. 6: Mobilisation of dilatancy (Scharinger 2007)

The tension cut-off f_{tens} is fixed by the input value of the allowable tensile normal stress, σ_t. Fully associated plastic flow is assumed for the tension cut-off.

3.2 Stress point return algorithm

The model is implemented as a user-defined soil model (UDSM) into the finite element code PLAXIS. The UDSM is called to return the stress increment according to the constitutive equations of the model for each strain increment **dε** which is provided by PLAXIS. Calculation of plastic strains is carried using an iterative procedure based on a modified Newton-Raphson scheme (Potts & Zdravković 1999) at the local level. Only a very brief overview is given here. A more detailed description of the UDSM facility and the stress point return algorithm (including the partial derivatives of the yield and plastic potential functions) can be found in Appendix B.

The change in macroscopic trial stress $\boldsymbol{\sigma}'_{trial}$ is calculated from the global elastic compliance matrix **C** and the global strain increment $\mathbf{d\varepsilon}$, which is assumed to be elastic in the first iteration.

$$\boldsymbol{\sigma}'_{trial} = \mathbf{C}^{-1} \cdot \mathbf{d\varepsilon} + \boldsymbol{\sigma}'_{previous} \tag{49}$$

$$\boldsymbol{\sigma}'_{i,trial} = (\mathbf{T}_i)^T \cdot \boldsymbol{\sigma}'_{trial} \tag{50}$$

Local plastic strains are calculated according to plasticity theory from the active yield surface, and subsequently summed up to obtain the global plastic strain increment $\mathbf{d\varepsilon^p}$.

$$\mathbf{d\varepsilon}_i^p = d\Lambda_i \cdot \frac{\partial g_i}{\partial \boldsymbol{\sigma}'_i} \tag{51}$$

$$\mathbf{d\varepsilon}^p = 3 \cdot \sum_i \mathbf{T}_i \cdot \mathbf{d\varepsilon}_i^p \cdot w_i \tag{52}$$

The new global trial stress is then calculated with the difference of the total strain increment and the plastic strain increment.

$$\boldsymbol{\sigma}'_{trial} = \mathbf{C}^{-1} \cdot \left(\mathbf{d\varepsilon} - \mathbf{d\varepsilon}^p\right) + \boldsymbol{\sigma}'_{previous} \tag{53}$$

This iterative procedure is repeated until the plastic strain contribution of the current stress point iteration is less than 0.1% of the total plastic strains increment calculated in that step. In previous multilaminate models, the condition to terminate the calculation of plastic strains was defined such that the trial stress must be sufficiently close to or inside the current yield surface on all planes. While such an approach is in principle correct, it typically results in a very high number of stress point iterations. After the first few iterations, the global trial stress $\boldsymbol{\sigma}'_{trial}$ as well as the local stresses $\boldsymbol{\sigma}'_{i,trial}$ do not change significantly anymore due to the limited impact of the remaining plastic planes on the global plastic strain increment, as illustrated in Figure 7. Furthermore, the local trial stress on the last planes remaining in plasticity is just slightly outside the yield surface, hence local plastic strain contributions from these planes are small and further hardening of the local yield surfaces is marginally. Local plastic strains are multiplied with the weight factors w_i before being summed up to obtain the global plastic strain increment of that iteration, which further reduces the impact of these local contributions, and in return leads to even smaller change of the global stress state. Eventually, the favourable quadratic convergence of the Newton-Raphson scheme is lost due to the updating of the trial stress on global level and the evaluation of the yield criteria on local level.

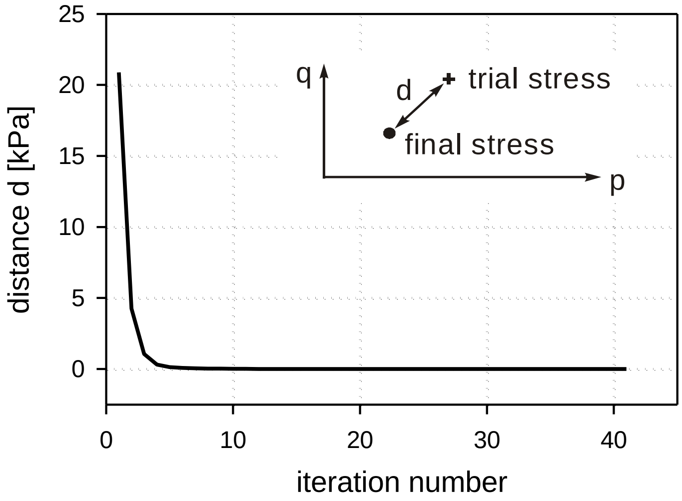

Fig. 7: Convergence of trial stress and final stress within a sample calculation step

This deficiency of the return algorithm cannot be overcome easily. At first glance it may seem appealing to finish iterations on integration plane level one after another for all planes without intermediate summation of local plastic strains and updating of the global trial stress. However, such an approach lacks physical meaning, as neither the local stresses nor the local strains would be projections of the global stresses and strains, and so neither the static nor the kinematic constraint would be fulfilled.

With the new convergence criterion the number of iterations could be considerably reduced without compromising notably on the accuracy of calculation results, as shown in Figure 8. Undrained triaxial stress point simulations of normally consolidated soil are compared, in which strains of ε_h = 7.5%, ε_v = -15% are applied in 500 steps. Both approaches deliver virtually identical stress paths, but the new convergence criterion requires only 30-50% of the iterations of the old approach.

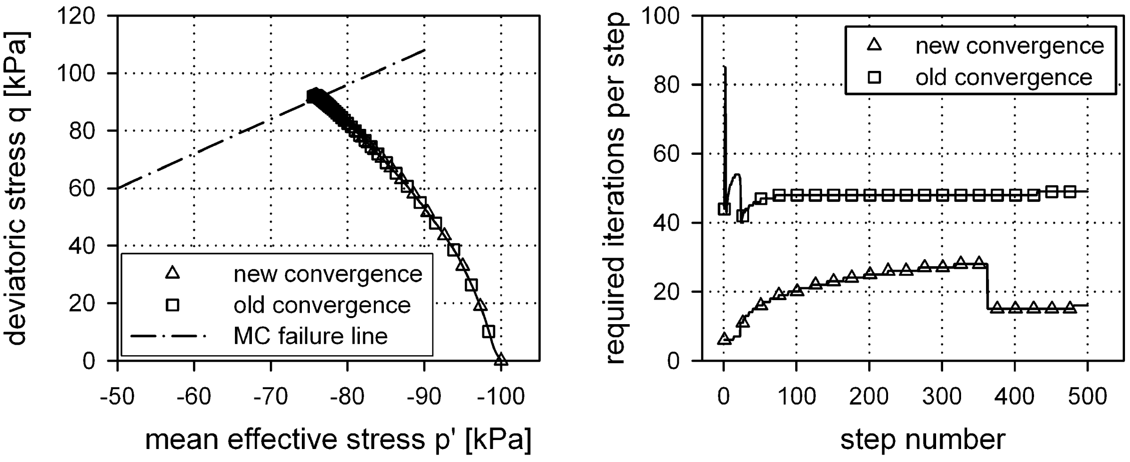

Fig. 8: Stress paths in undrained triaxial compression (left) and required number of stress point iterations (right)

3.3 Corner and apex points

Non-smooth intersections of yield surfaces or plastic potential functions require special attention, as the return stress path is influenced by the derivatives of all the adjacent yield surfaces and plastic potentials. In the basic multilaminate model that case arises at the intersection of the cone yield surface with the tension cut-off and the cap yield surface. Plastic strains at corner points can be decomposed into contributions of the neighbouring yield surfaces, which are denoted here as 1 and 2. The corresponding incremental local plastic multipliers $d\Lambda_1$ and $d\Lambda_2$ are then obtained as the solution of a linear system of equations (Potts & Zdravković 1999) as

$$\mathbf{d\varepsilon}_i^p = d\Lambda_1 \cdot \frac{\partial g_1}{\partial \boldsymbol{\sigma}'_i} + d\Lambda_2 \cdot \frac{\partial g_2}{\partial \boldsymbol{\sigma}'_i} \tag{54}$$

$$d\Lambda_1 = \frac{L_{22} \cdot f_1^{trial} - L_{12} \cdot f_2^{trial}}{L_{11} \cdot L_{22} - L_{12} \cdot L_{21}} \tag{55}$$

$$d\Lambda_2 = \frac{L_{11} \cdot f_2^{trial} - L_{21} \cdot f_1^{trial}}{L_{11} \cdot L_{22} - L_{12} \cdot L_{21}} \tag{56}$$

with

$$L_{11} = \frac{\partial f_1}{\partial \boldsymbol{\sigma}'_i} \cdot \mathbf{C}_i^{-1} \cdot \frac{\partial g_1}{\partial \boldsymbol{\sigma}'_i} - \frac{\partial f_1}{\partial \boldsymbol{\varepsilon}_i^p} \cdot \frac{\partial g_1}{\partial \boldsymbol{\sigma}'_i} \tag{57}$$

$$L_{22} = \frac{\partial f_2}{\partial \boldsymbol{\sigma}'_i} \cdot \mathbf{C}_i^{-1} \cdot \frac{\partial g_2}{\partial \boldsymbol{\sigma}'_i} - \frac{\partial f_2}{\partial \boldsymbol{\varepsilon}_i^p} \cdot \frac{\partial g_2}{\partial \boldsymbol{\sigma}'_i} \tag{58}$$

$$L_{12} = \left(\frac{\partial f_1}{\partial \boldsymbol{\sigma}'_i} \right)^T \cdot \mathbf{C}_i^{-1} \cdot \frac{\partial g_2}{\partial \boldsymbol{\sigma}'_i} \tag{59}$$

$$L_{21} = \left(\frac{\partial f_2}{\partial \boldsymbol{\sigma}'_i} \right)^T \cdot \mathbf{C}_i^{-1} \cdot \frac{\partial g_1}{\partial \boldsymbol{\sigma}'_i}. \tag{60}$$

It should be noted, that this approach requires strictly convex yield surfaces and plastic potentials, as otherwise negative or infinite values of $d\Lambda$ are obtained. Furthermore, it is necessary to work out beforehand, whether the stress path returns to yield surface 1, 2 or the corner point. For that end an iterative procedure is applied, which resembles the approach employed by Maudlin et al. (1996). First, the yield condition is evaluated at the trial stress $\boldsymbol{\sigma}'_{i,trial}$ for all local yield surfaces. Negative values of the yield criteria f indicate that the corresponding yield surface is inactive in the current loading step. If positive values of f are obtained for more than one yield surface, local plastic multipliers are calculated according to Equations 55 and 56. Positive values of $d\Lambda_1$ and $d\Lambda_2$ indicate that the stress path returns to the corner point, and that both yield surfaces are active. In case negative values are computed for either $d\Lambda_1$ or $d\Lambda_2$, the corresponding yield surface is removed from the set of potentially active surfaces and the local plastic multiplier is calculated from the remaining active yield surface according to Equation 9. As pointed out by Maudlin et al. (1996), the maximum number of active yield surfaces equals the dimension of the stress space in which the yield surfaces are defined, which is 2 in multilaminate models and 3 for models formulated in principal stress space σ'_1, σ'_2, σ'_3.

In previous multilaminate models, the return stress path was calculated without consideration of the Koiter rules. The stress path was returned to the cone yield surface if the trial stress was above the mobilised cone yield surface, and to the cap yield surface if below. Even though this approach lacks mechanical consistency, comparison of undrained triaxial and drained oedometer test simulations delivers only marginal differences between the two approaches (Figure 9, Figure 10).

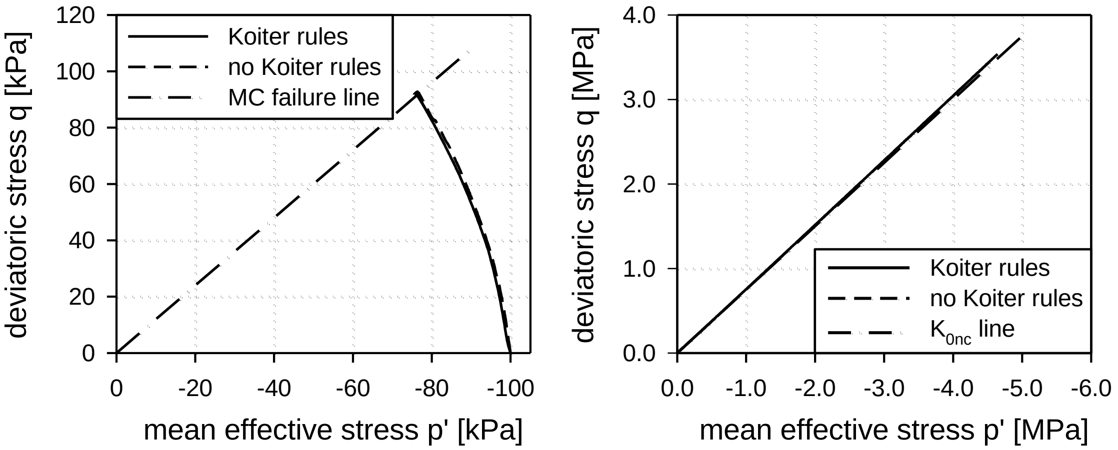

Fig. 9: Stress paths in undrained triaxial compression (left) and drained oedometric compression (right) with and without Koiter rules

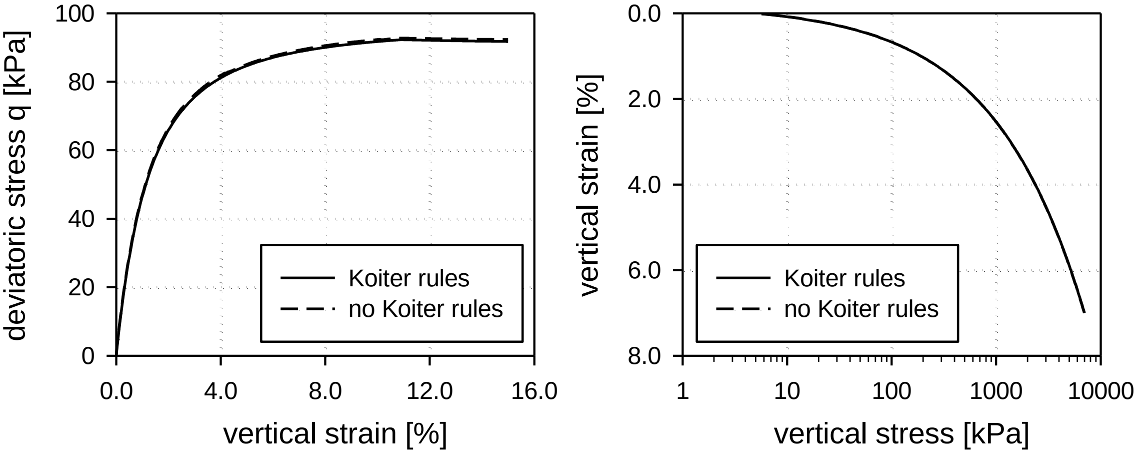

Fig. 10: Undrained triaxial compression (left) and drained oedometric compression (right) with and without Koiter rules

The limited impact of the Koiter rules results from the small number of integration planes on which the trial stress state is actually in the relevant area, and their small contribution to the global plastic strain increment. This is demonstrated for integration plane #12 for a strain increment in undrained triaxial compression in Figure 12. The initial stress state is assumed to lie at the intersection of the cap and cone yield surface (Figure 11). The elastic trial stress of plane 12 is within that section of the stress space, which activates both the cap and the cone yield surface according to the Koiter rules, while according to the old approach the stress state would return exclusively to the cone yield surface. Consequently, local plastic strains differ considerably over iterations (Figure 12 right): Without the Koiter rules, plastic strains are initially calculated solely from the cone yield surface, and zero plastic normal strains are obtained in the first two iterations (assuming $\psi = 0$ at the cone yield surface in this particular case). In later iterations also the cap yield surface gets activated, but only minor plastic normal strains are calculated. However, cap and cone yield surface are simultaneously activated with the Koiter rules already in the first iteration, and consequently larger plastic normal strains are calculated.

Comparing the local return stress paths (Figure 12 left), surprisingly little difference is found. This can be related to the calculation of the new global stress state from the macroscopic plastic strain increment, which is obtained as the sum of all local plastic strain contributions. As on most planes the trial stress is outside the area marked as “cap & cone active” in Figure 11, calculation of local plastic strains for these planes is not influenced by the difference in the return algorithm. As global plastic strains and the global trial stress state differ only marginally, also the new local trial stress of plane 12 is not significantly influenced by whether local plastic strains are calculated according to the Koiter rules or not.

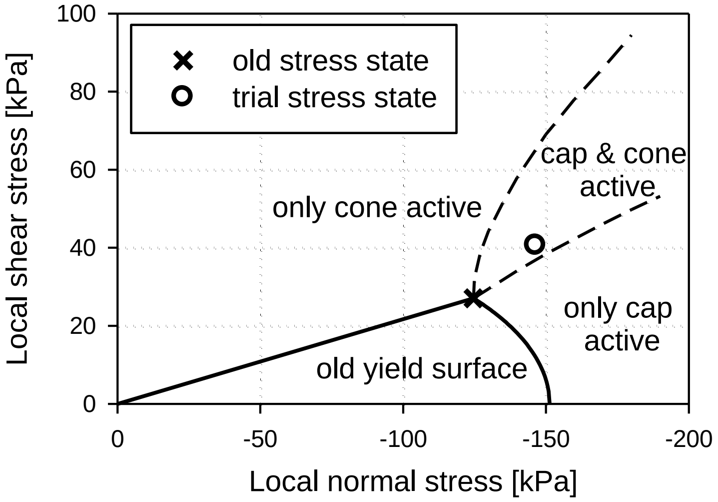

Fig. 11: Sample local stress state of integration plane #12 in undrained triaxial compression

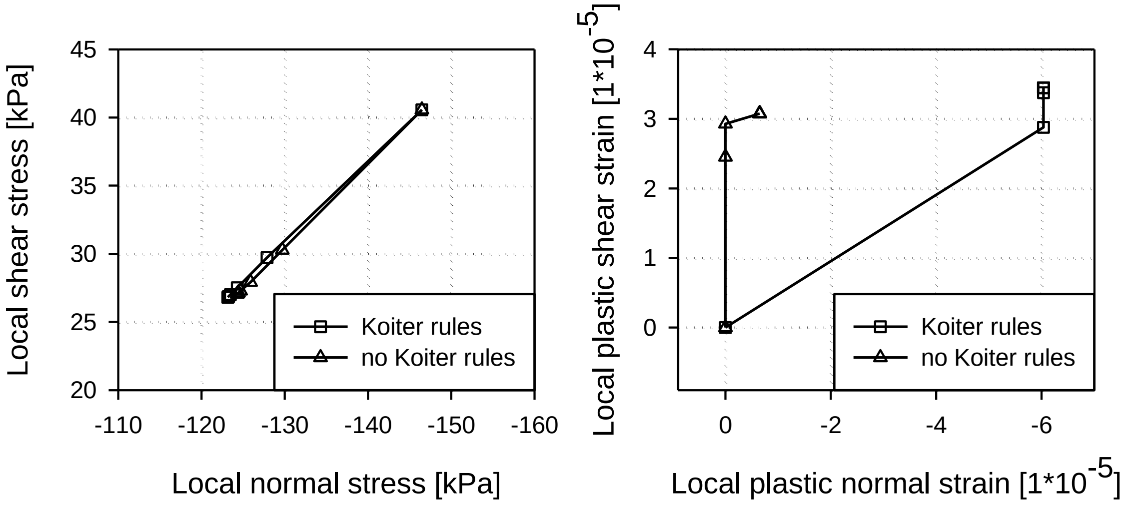

Fig. 12: Local return stress path (left) and local plastic strains (right) of integration plane #12 in subsequent iterations

3.4 Determination of cap shape parameter

The shape of the cap yield surface strongly influences the prediction of the earth pressure coefficient at rest in normal consolidation, K_{0nc}. In macroscopic models with only one yield surface of constant shape (e.g. Cam Clay model, Schofield and Wroth 1965), the value of K_{0nc} can be derived analytically (Federico et al. 2009). If multiple yield surfaces and non-associated plastic flow are involved, such analytical evaluation becomes increasingly difficult.

In multilaminate models the shape of the local cap yield surface is defined by the parameter M_{CP}, and relating local cap shape analytically to the value of macroscopic K_{0nc} is not feasible. However, if a certain value of K_{0nc} is desired, the shape of the cap yield surface can be determined by calculating an oedometric strain increment and varying the cap shape until the desired value of K_{0nc} is obtained in the simulation.

Wiltafsky (2003) reported that $M_{CP} = \alpha \cdot \tan\varphi'$ with a fixed value of $\alpha = 1 - \sin(2/3\varphi')$ provides a reasonable reproduction of $K_{0nc} = 1 - \sin\varphi'$ in oedometric compression. However, stress paths tend to deviate from the K_{0nc}-line at higher stress levels for some combinations of φ', A_{mat} and E_{oed}/E_{ur} (Figure 13 for $\varphi' = 30°$, $A_{mat} = 0.06$ and $E_{ur}/E_{oed} = 3.0$). With the iterative determination of the cap shape parameter the desired value of K_{0nc} is obtained for all combinations of input parameters.

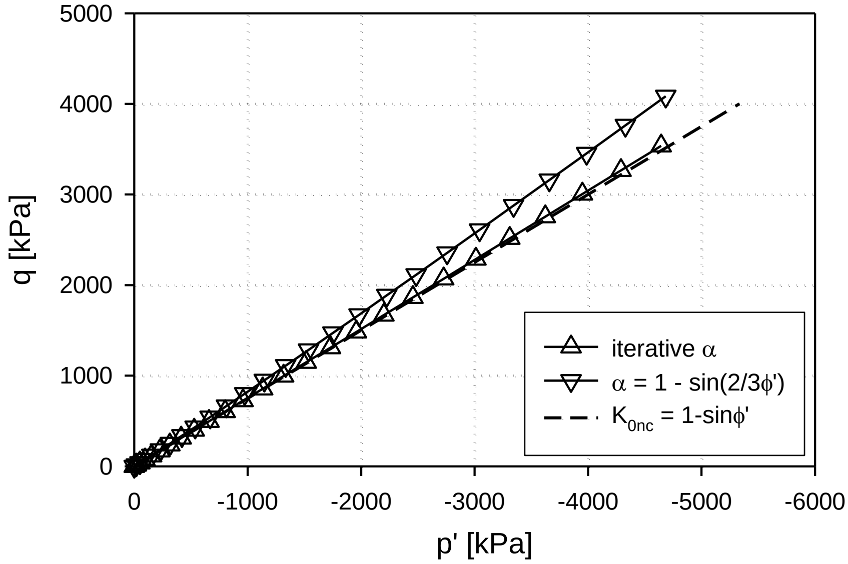

Fig. 13: Predicted stress path in oedometric normal compression – fixed cap shape parameter and iterative determination of cap shape

3.5 Macroscopic representation of local yield surfaces

One slight drawback of multilaminate soil models is the lack of a macroscopic yield surface, as yield criteria are formulated locally on integration planes. While this has little practical implications, comparison with soil models formulated in macroscopic stress invariants would be alleviated by a macroscopic representation of local yield surfaces. However, such representation is only possible for selected stress states and stress histories, as the initial stress state determines the position of local yield surfaces and hence the shape of the macroscopic yield surface.

Local stress states can be considered as points on a Mohr's circle representing the global stress state (Figure 14). In the case of isotropic overconsolidation, the initial position of all local volumetric yield surfaces is identical and defined by the normal pre-consolidation stress σ'_{nc}. Isotropic unloading and subsequent deviatoric loading results in macroscopic yielding, once the first local stress path reaches the local yield surface.

By analytically finding the Mohr's circle which first touches any of the local yield surfaces, the corresponding principal yielding stresses σ'_1 and σ'_3 can be derived. Assuming either triaxial compression (Lode's angle $\theta = -30°$) or triaxial extension ($\theta = +30°$), the corresponding macroscopic stress invariants p' and q are found. Due to the curvature of the elliptical volumetric yield surface, the orientation α of the integration plane which yields first changes with the magnitude of the local normal stress.

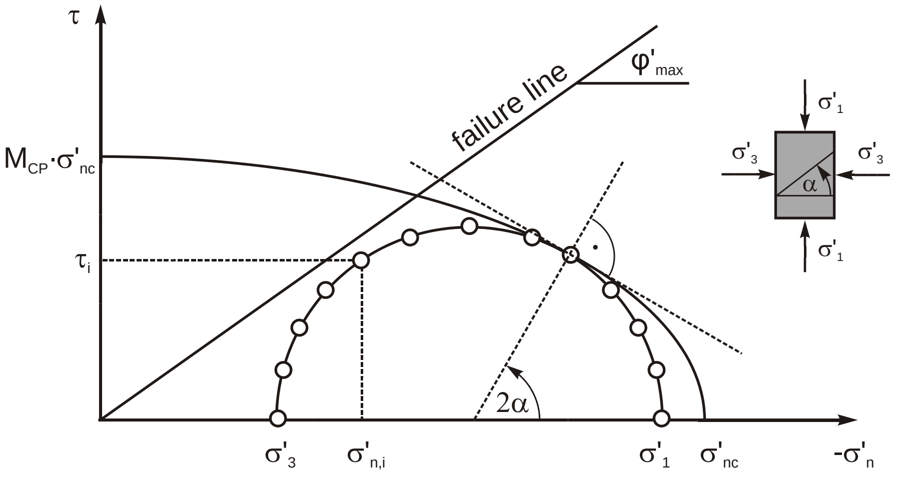

Fig. 14: Initial local yield surfaces of isotropically overconsolidated soil and Mohr's stress circle in triaxial compression

$$\tan(2\alpha) = \frac{\tau}{-\sigma'_n \cdot M_{CP}^2} \tag{61}$$

$$\sigma'_1 = \sigma'_n + \tau \cdot \frac{\cos(2\alpha)-1}{\sin(2\alpha)} \tag{62}$$

$$\sigma'_2 = \sigma'_n + \tau \cdot \frac{\cos(2\alpha)+1}{\sin(2\alpha)} \tag{63}$$

The orientation of the most critical plane for the Mohr-Coulomb failure line is constant at $\alpha = \pi/4+\varphi'/2$ with regard to the minor principal stress direction, which leads to the well-known inclination of the failure line in the p'-q-diagram of $M_{com} = 6\cdot\sin\varphi'/(3-\sin\varphi')$ in triaxial compression and $M_{ext} = 6\cdot\sin\varphi'/(3+\sin\varphi')$ in triaxial extension. The analytically derived macroscopic yield surface for isotropically consolidated soil ($\varphi' = 30°$, $c' = 0$, $M_{CP} = 0.346$, $p'_c = -100$ kPa) is shown in Figure 15, as well as undrained stress paths predicted by the basic multilaminate model. Both the macroscopic failure line and the macroscopic cap yield surface are non-symmetric with regard to the isotropic axis. The non-smooth intersection of the cap yield surfaces in extension and compression at the intersection with the isotropic axis does not pose numerical problems, as plastic strains are calculated at integration plane level.

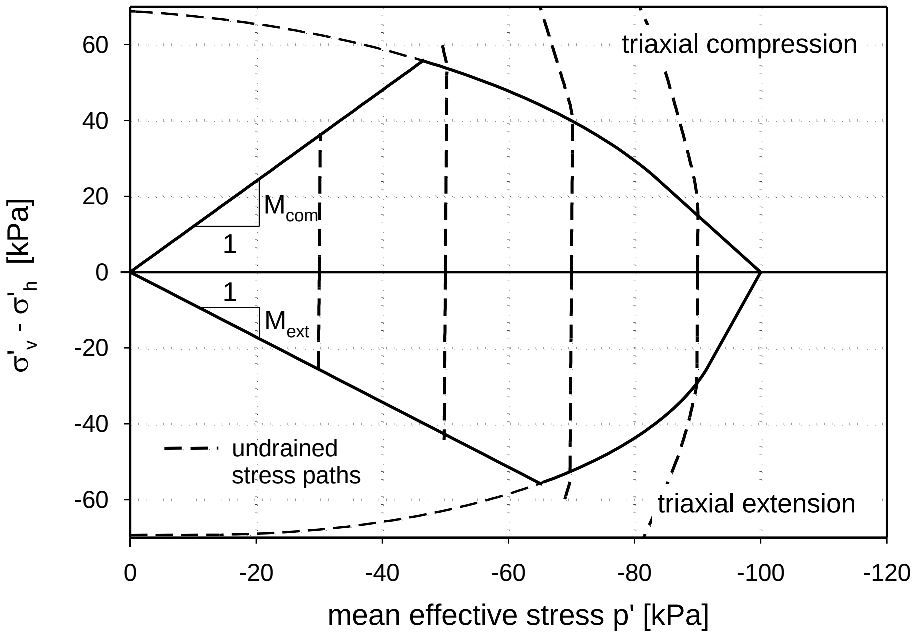

Fig. 15: Macroscopic yield surface of the basic multilaminate model for isotropically overconsolidated soil (cone yield surface fully mobilised) and predicted undrained stress paths

If the initial stress state is not isotropic, the position of initial yield surfaces varies among the planes, as shown schematically in Figure 16. The boundaries of the elastic domain in terms of macroscopic stress invariants can be found by applying virtual triaxial stress increments and monitor whether they result in local stresses violating local yield criteria. It is evident that any horizontal translation of the Mohr's circle (i.e. varying *p'* while holding *q* constant) results in activation of either local cap or cone yield surfaces, and therefore delivers plastic strains at the macroscopic level. Reducing *q* while holding *p'* constant also results in plastic strains, as in this case the minor principal stress σ'_3 is forced to increase in order to keep *p'* constant. Again, this would activate the volumetric yield surfaces on vertically orientated planes.

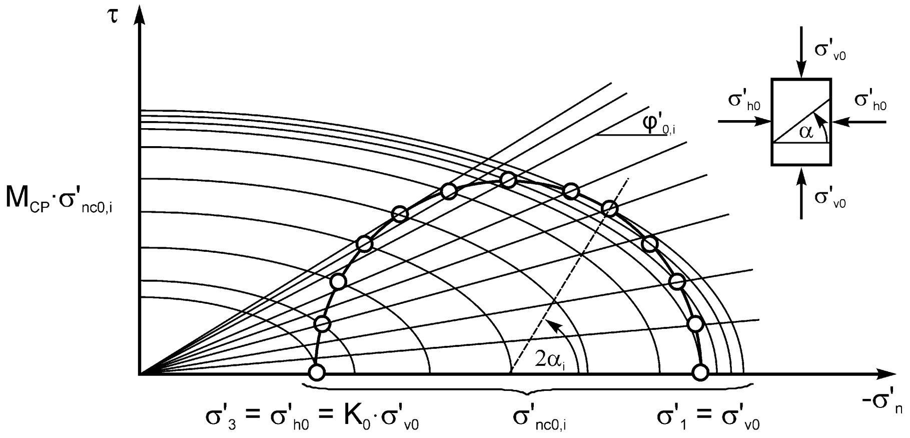

Fig. 16: Local yield surfaces for K_0-consolidated initial stress state ($K_0 < 1$)

The boundary between elastic and plastic behaviour is found by the stress path in drained triaxial unloading (reducing σ'_1 while holding σ'_3 constant), which enables the Mohr's circle to shrink without increase in local shear and normal stresses. This boundary is a straight line in the *p'*-*q* diagram and independent of the shape of the local volumetric yield surface.

Once the isotropic axis is reached in unloading, σ'_v and σ'_h exchange positions in the Mohr's circle and the critical orientation of α for a certain integration plane switches from clockwise to anticlockwise. The initial deviatoric yield surfaces get activated, once the local stress ratio τ/σ'_n exceeds the initial value $\tan\varphi'_0 = \tau/\sigma'_n$. The stress ratio $K'_1 = \sigma'_h/\sigma'_v$ which fulfils this requirement can be found analytically as

$$K'_1 = \frac{\cos(2\alpha) - K_0\cdot\cos(2\alpha) + 1}{K_0 + \cos(2\alpha) - K_0\cdot\cos(2\alpha)}, \tag{64}$$

which for $\alpha = 0°$ approaches the limiting value of

$$K'_1 = 2 - K_0\,. \tag{65}$$

The macroscopic yield surface in triaxial extension is consequently obtained as a straight line in the *p'*-*q*-diagram with the inclination $M_{yield} = (3 \cdot K_0 - 3)/(2 \cdot K_0 - 5)$. The resultant macroscopic yield surfaces for K_0-consolidated soil ($K_0 = 0.5$) are shown in Figure 17.

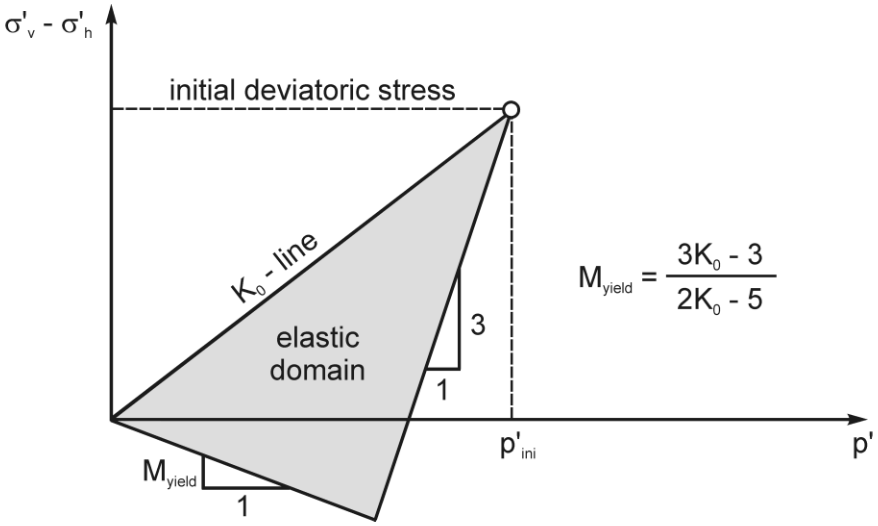

Fig. 17: Macroscopic elastic domain of K_0 - consolidated soil in the basic multilaminate model

4 Anisotropic small strain stiffness

Soils exhibit much higher stiffness at very small strains (< 10^{-5}) than in the strain range typically applied in laboratory tests. After a small initial range of constant high stiffness, which is often considered as the true elastic range of soils, shear stiffness decreases monotonically with accumulating strains (Figure 18). The stiffness of soils in the very small strain range and its degradation with accumulation of strain has been researched in laboratory and field investigations since the early 1970s. The importance of this phenomenon for the static design of engineering structures and the prediction of realistic ground deformations has been recognized not much later (Cole & Burland 1972, Simpson et al. 1979), and was highlighted by Burland (1989), Atkinson & Sallfors (1991) and Simpson (1992). With the advent of constitutive models accounting for small strain stiffness in commercial finite element packages, this aspect of soil behaviour is more and more routinely taken into account in engineering practice.

However, in most numerical simulations soil is still assumed to behave isotropically, even though the anisotropic nature of soil stiffness has already been emphasized by Atkinson (1975). Much research was devoted to investigate the anisotropic characteristics of soil stiffness in the small strain range in the last two decades (Bellotti et al. 1996, Jiang et al. 1997, Lings et al. 2000). In some cases, discrepancies between numerical simulation and field measurements are attributed to anisotropy (in both small and large strain behaviour), but only rarely the impact of anisotropy is thoroughly studied (Addenbrooke et al. 1997, Ng et al. 2004).

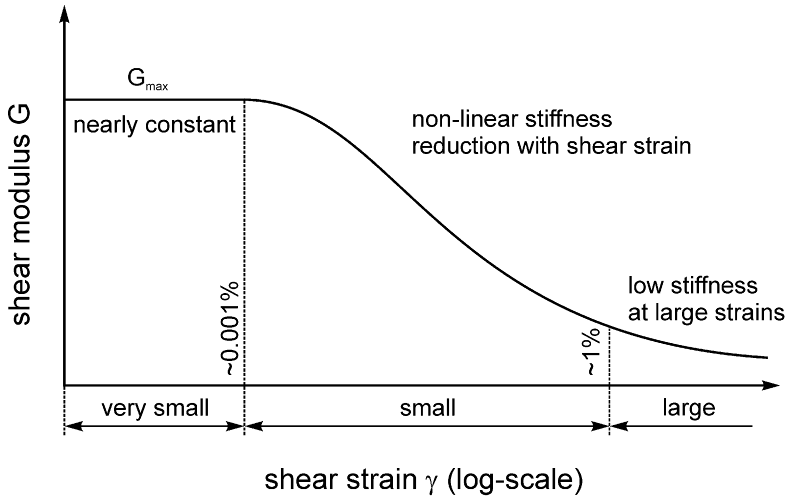

Fig. 18: Variation of stiffness at small strains (after Atkinson & Sallfors 1991)

The relatively small number of numerical studies accounting for anisotropic small strain stiffness in boundary value problems may be partly due to the difficulty in obtaining the necessary input parameters, but is also related to the lack of appropriate constitutive models.

The following chapter focusses on cross-anisotropic elasticity, which is the type of stiffness anisotropy most common in naturally deposited geomaterials. Experimental results for fine and coarse grained soils are reviewed to obtain realistic ranges of anisotropic parameters. Different approaches to model anisotropic stiffness in multilaminate constitutive models are compared, and the issue of stress dependency of elastic moduli is addressed. A constitutive model is formulated, which can account for cross-anisotropic stiffness at small strains and the dependency of stiffness on load history and the initial stress state. The model is validated in simulations of element tests, and the strengths as well as the limitations of the model are evaluated.

4.1 Cross-anisotropic elasticity

In most cases the concept of cross anisotropy or transverse isotropy is utilized to describe the anisotropic stiffness characteristics of natural soils (Kuwano and Jardine 2002, Gasparre et al. 2007, Pennington et al. 1997). Cross anisotropy exhibits one axis of symmetry, which for most naturally deposited soils and sedimentary rocks equals the vertical axis. Deformation behaviour depends on the loading direction with regard to the axis of symmetry, while it is independent of any rotation about the axis of symmetry. Assuming a horizontal bedding plane (parallel to the *x*-*z*-plane), the stress-strain behaviour can be formulated according to Equation 66.

$$\begin{pmatrix} \Delta\varepsilon_{xx} \\ \Delta\varepsilon_{yy} \\ \Delta\varepsilon_{zz} \\ \Delta\gamma_{xy} \\ \Delta\gamma_{yz} \\ \Delta\gamma_{xz} \end{pmatrix} = \begin{pmatrix} \frac{1}{E'_h} & \frac{-\nu'_{vh}}{E'_v} & \frac{-\nu_{hh}}{E_h{}'} & 0 & 0 & 0 \\ \frac{-\nu'_{hv}}{E'_h} & \frac{1}{E'_v} & \frac{-\nu'_{hv}}{E'_h} & 0 & 0 & 0 \\ \frac{-\nu'_{hh}}{E'_h} & \frac{-\nu'_{vh}}{E'_v} & \frac{1}{E'_h} & 0 & 0 & 0 \\ 0 & 0 & 0 & \frac{1}{G_{vh}} & 0 & 0 \\ 0 & 0 & 0 & 0 & \frac{1}{G_{vh}} & 0 \\ 0 & 0 & 0 & 0 & 0 & \frac{1}{G_{hh}} \end{pmatrix} \cdot \begin{pmatrix} \Delta\sigma'_{xx} \\ \Delta\sigma'_{yy} \\ \Delta\sigma'_{zz} \\ \Delta\tau_{xy} \\ \Delta\tau_{yz} \\ \Delta\tau_{xz} \end{pmatrix} \qquad (66)$$

with E'_v … Effective Young’s modulus in vertical direction
E'_h … Effective Young’s modulus in horizontal direction
G_{vh} … Shear modulus in all vertical planes
G_{hh} … Shear modulus in horizontal plane
ν'_{hh} … Poisson’s ratio linking horizontal loading and horizontal strain perpendicular to loading direction
ν'_{vh} … Poisson’s ratio linking vertical loading and horizontal strain
ν'_{hv} … Poisson’s ratio linking horizontal loading and vertical strain

Enforcing symmetry of the elastic compliance matrix requires

$$\frac{-\nu'_{hv}}{E'_h} = \frac{-\nu'_{vh}}{E'_v}. \tag{67}$$

Material behaviour within all planes parallel to the bedding plane is isotropic, which leads to

$$G_{hh} = \frac{E'_h}{2(1+\nu'_{hh})}. \tag{68}$$

Stress strain behaviour of a cross anisotropic elastic material is therefore fully defined by five independent material parameters.

From the thermodynamic requirement that for any type of loading a strictly positive strain energy must be ensured, the following bounds of the anisotropic material parameters can be derived (Theocaris & Philippidis 1991):

$$\{E'_v, E'_h, G_{hh}, G_{vh}\} > 0, \tag{69}$$

$$-1 < \nu'_{hh} < 1, \tag{70}$$

$$|\nu'_{vh}| < \left[(1-\nu'_{hh})\frac{E'_v}{2E'_h}\right]^{1/2}. \tag{71}$$

It should be noted, that the limits of Poisson’s ratios ν'_{vh} and ν'_{hh} of cross anisotropic materials are wider than for isotropic materials, which in the case of isotropic elasticity are restricted to $-1 \leq \nu' \leq 0.5$. For a ratio of axial moduli $E'_v/E'_h = 4.0$ and $\nu'_{hh} = 0.2$, the Poisson’s ratio ν'_{vh} can take values in the range $-1.79 \leq \nu'_{vh} \leq 1.79$.

4.2 Review of anisotropic small strain stiffness of soils

Due to sedimentation processes, non-spherical particle shapes and load history, most soils exhibit a certain degree of anisotropy in both shear strength and stiffness characteristics. Consideration of anisotropy is focussed on small strain stiffness here, i.e. soil stiffness at very small strains ($< 1\cdot10^{-5}$), which can be regarded as the true elastic region of soil behaviour.

Stiffness anisotropy of soils can be split into two parts:

1. An inherent component due to loading history and soil structure, which is independent of the current stress state.
2. Stress induced anisotropy, which is solely a result of anisotropic stress states and supplements the inherent anisotropy of the material.

The magnitude of these two components is addressed in separate sections of this chapter. Further distinction is made between fine and coarse grained soils.

4.2.1 Inherent anisotropy

In order to separate inherent from stress induced anisotropy, only experimental small strain stiffness data at isotropic stress states are summarized in Table 2. The degree of anisotropy displayed in the ratios E'_h/E'_v and G_{vh}/G_{hh} as well as in the difference between ν'_{vh} and ν'_{hh} can therefore be attributed solely to inherent stiffness characteristics.

It should be noted that the experimental data were obtained by a variety of static and dynamic measurement techniques. Small vertical triaxial load amplitudes are the most common strategy to determine E'_v and ν'_{vh} directly. In order to find E'_h and ν'_{hh} (which cannot be measured directly in triaxial stress conditions), either assumptions are made with regard to ν'_{hh} (Jiang et al. 1997, Hoque & Tatsuoka 2004), or the shear modulus G_{hh} is measured by shear wave velocity measurements and is than related to E'_h and ν'_{hh} by Equation 68 (Kuwano 1999, Pirijakul 2007, Yimsiri & Soga 2011). Bellotti et al. (1996) obtained the full set of cross anisotropic parameters by seismic wave measurements in a large calibration chamber. AnhDan et al. (2006) used a large scale true triaxial apparatus for their studies, in which it is possible to vary the horizontal stresses independently and thus determine the horizontal modulus E'_h directly.

Tab. 2: Stiffness anisotropy at isotropic stress states

Soil name	E'_h/E'_v	G_{vh}/G_{hh}	ν'_{vh}	ν'_{hh}	**Reference**
Chiba gravel, medium dense	0.72^1 / 1.45^2	--	--	--	AnhDan et al. 2006
Chiba gravel, very dense	1.0^1 / 2.07^2	--	0.12-0.30	--	AnhDan et al. 2006
Chiba gravel	0.46	--	0.22-0.30	$(= \nu_{vh})^{3}$	Jiang et al. 1997
Colorado shale	1.99	0.53-0.66	0.0-0.3	0.00	Gautam et al. 2006
Dunkerque sand	0.91-1.08	0.72-0.80	0.25-0.40	0.10-0.15	Kuwano 1999
Ham River sand	0.69-0.89	0.86-0.95	0.20-0.40	0.05-0.20	Kuwano 1999
Hime gravel	0.56-0.62	--	0.14-0.16	$(= \nu_{vh})^{3}$	Hoque & Tatsuoka 2004
Hostun Sand, dense	1.35	0.85	0.17	0.32	Sadek et al. 2007
Ticino sand	1.21-1.22	0.82-0.85	0.17-0.19	0.16-0.18	Bellotti et al. 1996
Ticino sand	~0.95	--	~0.16	$(= \nu_{vh})^{3}$	Hoque & Tatsuoka 2004
Toyoura sand	1.10-1.30	--	0.12-0.22	--	AnhDan & Koseki 2005
Toyoura sand	0.88-0.94	--	0.16-0.18	$(= \nu_{vh})^{3}$	Hoque & Tatsuoka 2004
London clay, undisturbed	2.18	0.83	0.07	0.18	Yimsiri & Soga 2011
Gault clay, undisturbed	2.32	0.60	0.13	0.21	Yimsiri & Soga 2011

[1] during isotropic primary loading at p' = -100 kPa

[2] during isotropic unloading from p' = -500 kPa to p' = -100 kPa

[3] assumption at isotropic stresses to determine E'_h

There is some discrepancy regarding the inherent ratio E'_v/E'_h reported for sandy and gravelly soils by various authors. While Bellotti et al. (1996), AnhDan & Koseki (2005) and AnhDan et al. (2006) reported $E'_h > E'_v$, Kuwano (1999), Hoque & Tatsuoka (2004) and Jiang et al. (1997) found $E'_h < E'_v$. The source for these differences – in some cases obtained for the same soil type – is not entirely clear. Within the experimental setup of Hoque & Tatsuoka (triaxial tests with local strain transducers), ν'_{hh} and E'_h could not be obtained directly. The evaluation of E'_h was therefore based on the assumption that ν'_{hh} equals ν'_{vh} at isotropic stresses. Taking into account the results of Bellotti (1996), who obtained $\nu'_{hh} \approx \nu'_{vh}$ for Ticino sand by wave measurements, such an assumption appears to be valid for Ticino sand and can hardly be regarded as the source of these differences. AnhDan et al. 2006 attributed the discrepancies in E'_v/E'_h to different soil fabric evolving in loading and unloading and thus to overconsolidation, as their tests on Chiba gravel (true triaxial small load cycles) delivered $E'_h < E'_v$ in isotropic primary loading and $E'_h > E'_v$ after the sample is isotropically unloaded from a previously higher stress level. However, they could not establish a similar trend for Toyoura sand, and the large scatter within their experimental results on Chiba gravel also casts this explanation into doubt.

Furthermore, Bellotti (1996) and Kuwano & Jardine (2002) noted that load history and overconsolidation had no significant impact on the degree of inherent anisotropy in their studies on sands. Kuwano (1999) mentioned that elastic moduli derived by dynamic measurements are 5-10% higher than those obtained in static tests at the same strain energy level, and that also the resultant ratio E'_h/E'_v is affected by the type of measurement. Whether the static or the dynamic tests provide a more accurate description of soil stiffness and anisotropy is hard to judge und requires further investigation. From a practical point of view, assuming $E'_h/E'_v \approx 0.8\ldots1.0$ for sands and $E'_h/E'_v \approx 0.4\ldots0.7$ for gravel seems to be a reasonable estimate.

Due to the difficulty of measuring Poisson's ratios within the small strain region, the scatter of experimental values of ν'_{vh} and ν'_{hh} is in general much larger than for the elastic moduli E'_v, E'_h and G_{vh}. In the few studies investigating inherent Poisson's ratios ν'_{vh} and ν'_{hh}, values were ranging from 0.0 to 0.4.

Significantly less experimental data have been published on the inherent anisotropy of fine grained soils. A recent study on undisturbed samples of overconsolidated Gault clay and London clay (Yimsiri and Soga 2011) showed significant inherent anisotropy at isotropic stress states. Jovičivić & Coop (1998) found that most of the inherent anisotropy of overconsolidated clays is the result of anisotropic plastic straining during previous loading and thus related to load history. They introduced the term "strain induced anisotropy" in contrast to inherent anisotropy due to depositional soil fabric, which is reportedly more pronounced in sands (Arthur & Menzies 1972).

The influence of structure and bonding is highlighted in the experiments conducted by Pirijakul (2007), who tested undisturbed and reconstituted samples of overconsolidated Boom clay at the same stress ratio of $K' = 2.0$. Both undisturbed and reconstituted samples were tested at the same water content and had been subjected to the same load history (one-dimensional compression, followed by unloading) before testing. The cross-anisotropic axial and shear moduli of the undisturbed samples were about 1.5-2.4 times higher than those obtained from the reconstituted samples, with the differences reducing as the stress level increased. However, the anisotropy ratios E'_v/E'_h and G_{vh}/G_{hh} as well as the Poisson's ratios ν'_{hh} and ν'_{vh} were fairly similar for undisturbed and reconstituted samples. The development of inter-particle bonding after deposition obviously increased the stiffness of the natural soil as a whole, but did not change the degree of anisotropy induced by straining during deposition und subsequent unloading.

4.2.2 Stress dependency of coarse grained soils

Some selected experimental results for small strain stiffness of coarse and fine grained soils at anisotropic stress states are summarized in Table 3. Equations 72 to 75 have been adopted by various authors to describe the stress dependency of cross anisotropic stiffness parameters (Roesler 1979, Bellotti et al. 1996, Kuwano & Jardine 2002, Hoque & Tatsuoka 2004). The function $f(e) = (2.17 - e)^2 / (1+e)$ accounts for variations of void ratio e, as proposed by Hardin & Richart (1963). S_v, S_h, S_{vh} and S_{hh} are material constants describing the inherent anisotropy of the material, p'_{ref} is a reference pressure, and the material constants a_v, b_v, a_{vh}, b_{vh}, a_{hh} and b_{hh} govern the stress dependency of the cross anisotropic stiffness moduli.

$$E'_v = S_v \cdot f(e) \cdot \left(\frac{\sigma'_v}{p_{ref}} \right)^{a_V} \tag{72}$$

$$E'_h = S_h \cdot f(e) \cdot \left(\frac{\sigma'_h}{p_{ref}} \right)^{b_h} \tag{73}$$

$$G_{vh} = S_{vh} \cdot f(e) \cdot \left(\frac{\sigma'_v}{p_{ref}} \right)^{a_{vh}} \cdot \left(\frac{\sigma'_h}{p_{ref}} \right)^{b_{vh}} \tag{74}$$

$$G_{hh} = S_{hh} \cdot f(e) \cdot \left(\frac{\sigma'_v}{p_{ref}} \right)^{a_{hh}} \cdot \left(\frac{\sigma'_h}{p_{ref}} \right)^{b_{hh}} \tag{75}$$

The axial moduli E'_v and E'_h depend on the corresponding axial stresses σ'_v and σ'_h, while the shear moduli G_{vh} and G_{hh} depend on a combination of the axial stresses. The power indices a_v, b_h and the sums $a_{vh} + b_{vh}$ and $a_{hh} + b_{hh}$ typically vary from 0.5 to 0.6 for sands. The ratio E'_h/E'_v therefore approximately follows the stress ratio $(\sigma'_v/\sigma'_h)^{\sim 0.5}$, such that even an inherently isotropic sand will become anisotropic at non-isotropic stress states (Figure 19).

Tab. 3: Stiffness anisotropy at anisotropic stress states

Soil name	$K' = \sigma'_h/\sigma'_v$	E'_h/E'_v	G_{vh}/G_{hh}	ν'_{vh}	ν'_{hh}	**Reference**
Ham River sand	0.45	0.50-0.54	1.15-1.28	0.30-0.40	0.08-0.15	Kuwano & Jardine 2002
Dunkerque sand	0.35	0.57-0.53	0.80-0.90	0.2-0.25	0.05-0.2	Kuwano 1999
Ticino Sand	0.5	0.79-0.83	1.01-1.06	0.14-0.15	0.19-0.20	Bellotti et al. 1996
Ticino Sand	2.0	1.83-1.90	0.68-0.70	0.14-0.17	0.16-0.19	Bellotti et al. 1996
London clay	1.7	1.95	0.53	0.10	-0.02	Gasparre 2007
Gault clay	2.0	3.97	0.44	0.00	-0.04	Lings et al. 2000
Boom clay, undisturbed	2.0	1.74-2.30	0.49-0.67	~0	-0.03-0.04	Pirijakul 2007
Boom clay, reconstituted	2.0	2.01-2.51	0.59-0.64	~0	0.04-0.06	Pirijakul 2007

As a consequence of Equation 75, the Poisson's ratio ν'_{hh} is also a function of the stress state, as $G_{hh} = E'_h \,/\, 2\cdot(1+\nu'_{hh})$ must be fulfilled for any cross anisotropic material. However, as a_{hh} is typically close to 0 and $b_{hh} \sim b_h$, G_{hh} follows the same stress dependency as E'_h and ν'_{hh} can be considered as a constant. In his experiments on Ticino sand, Bellotti et al. (1996) found some variation of ν'_{vh} with changing $K' = \sigma'_h \,/\, \sigma'_v$, but no clear relationship could be established (Figure 20). Hoque & Tatsuoka (2004) reported a clear trend of decreasing ν'_{vh} with increasing K' for both Toyoura and Silver Leighton Buzzard sand and proposed Equation 76 to fit the experimental data. However, in both cases the variation of ν'_{vh} with stress ratio was rather small.

$$\nu'_{vh} = \nu'_{vh,iso} \cdot \left(\frac{\sigma'_v}{\sigma'_h} \right)^{a_v/2} \tag{76}$$

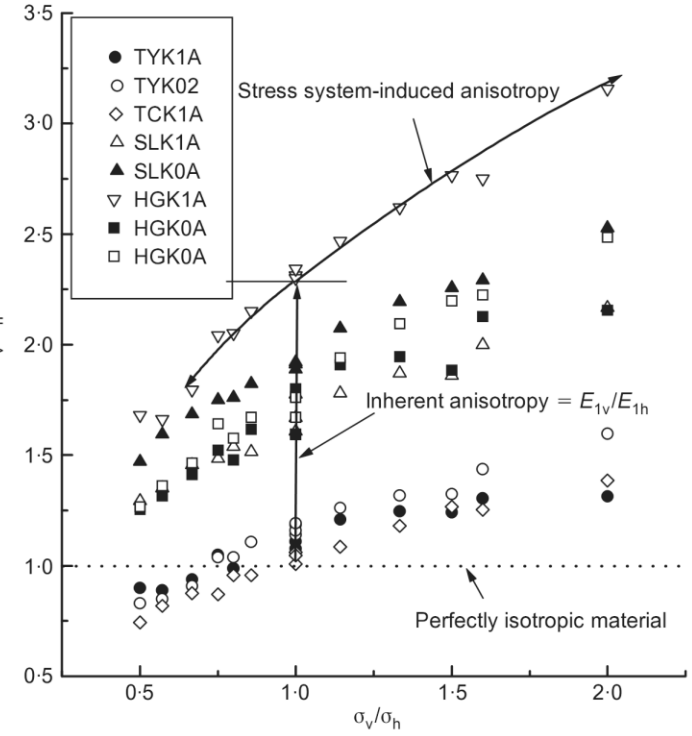

Fig. 19: Influence of stress ratio on anisotropy ratio for Toyoura sand (TYK) Ticino sand (TCK), Silver Leighton Buzzard sand (SLK) and Hime gravel (HGK), (Hoque & Tatsuoka 2004)

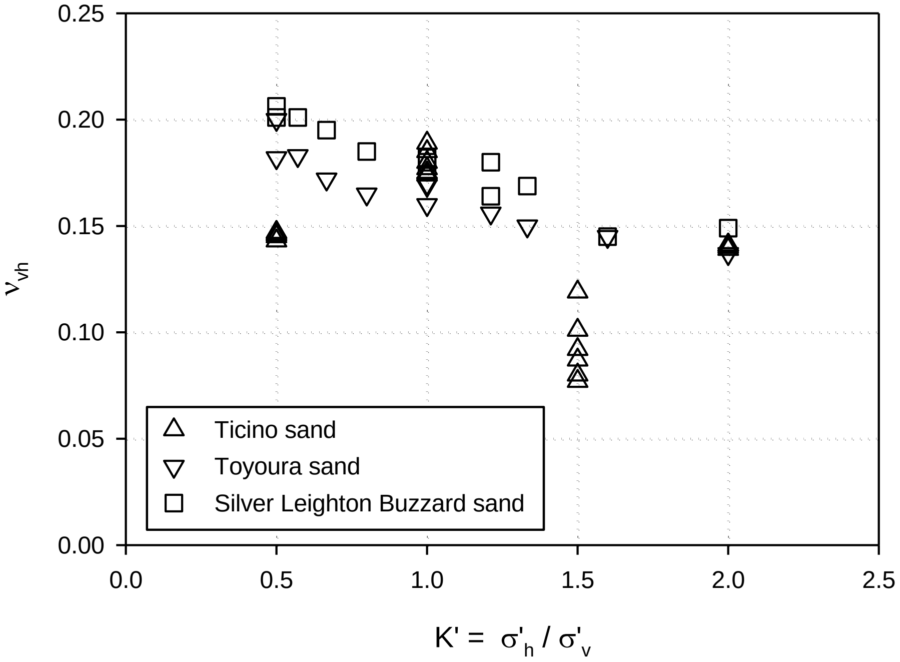

Fig. 20: Influence of stress ratio on Poisson's ratio ν'_{vh}

It should be noted that all the experimental data discussed so far were obtained at triaxial stress states, in which the axis of symmetry of the material coincided with that of the stress state. Such a situation is rarely the case in real boundary value problems. Extending Equations 72 and 73 to general stress states with $\sigma'_{xx} \neq \sigma'_{yy} \neq \sigma'_{zz}$ results in an orthotropic material with $E'_x \neq E'_y \neq E'_z$. To define such a material one additional shear modulus and one additional Poisson's ratio are required, which cannot be derived from the experimental data obtained in triaxial tests.

4.2.3 Stress dependency of fine grained soils

Establishing relationships to describe the stress dependency of fine grained soils is complicated by the concurrent evolution of stress and strain induced anisotropy, which is less significant for coarse grained soils. Regarding the shear moduli G_{hh} and G_{vh}, stress dependency is often expressed in a similar manner as for coarse grained soils. Nash et al. (1999) proposed Equations 77 and 78, which differ from the corresponding relationships for coarse grained soils only by assuming the same power index n for both axial stresses.

$$G_{vh} = S_{vh} \cdot f(e) \cdot \left(\frac{\sqrt{\sigma'_v \cdot \sigma'_h}}{p'_{ref}} \right)^{n_{vh}} \tag{77}$$

$$G_{hh} = S_{hh} \cdot f(e) \cdot \left(\frac{\sqrt{\sigma'_v \cdot \sigma'_h}}{p'_{ref}} \right)^{n_{hh}} \tag{78}$$

Tab. 4: Power indices for stress induced anisotropy of clays (data from Pirijakul 2007)

clay	n_{vh}	n_{hh}
Recon. Gault	0.56	0.49
Undist. Boom (primary loading)	0.51	0.37
Undist. Boom (unloading – reloading)	0.51	0.37
Recon. Boom (primary loading)	0.44	0.37
Recon. Boom (unloading – reloading)	0.33	0.34

Typical values of n_{vh} and n_{hh} for some overconsolidated clays are listed in Table 4. These data show that the magnitude of stress dependency is similar to that of coarse grained soils, with power indices n_{vh} and n_{hh} usually smaller than or close to 0.5. From a practical point of view, the influence of stress ratio on the shear moduli is rather limited. E.g. for $n = 0.5$, an anisotropic stress state with $K' = \sigma'_h/\sigma'_v = 0.5$ results in a factor of ~1.03 compared with the corresponding isotropic case at the same mean effective stress, while $K' = 2.0$ delivers a factor of 0.92.

Comparable studies concerning the variation of the axial moduli E'_v and E'_h with effective stress ratio K' are still rare, and in some cases provide contradictory results. While the anisotropy ratio E'_v/E'_h seems to be virtually independent of the current stress ratio for London clay (Yimsiri and Soga 2011: $E'_h/E'_v = 2.18$ at $K' = 1.0$; Gasparre 2007: $E'_h/E'_v = 1.95$ at $K' = 1.7$), anisotropy is reportedly magnified by anisotropic stresses for Gault clay (Yimsiri and Soga 2011: $E'_h/E'_v = 2.32$ at $K' = 1.0$; Lings et al. 2000: $E'_h/E'_v = 3.97$ at $K' = 2.0$).

In a rather pragmatic manner, axial moduli for clays are often related to mean effective stress p' according to Equations 79 and 80. If a_v and b_h are assumed to be equal, the inherent anisotropy ratio E'_h/E'_v of the soil remains constant with changes of the stress ratio.

$$E'_v = S_v \cdot f(e) \cdot \left(\frac{p'}{p'_{ref}} \right)^{a_v} \tag{79}$$

$$E'_h = S_h \cdot f(e) \cdot \left(\frac{p'}{p'_{ref}} \right)^{b_h} \tag{80}$$

Figure 21 represents experimental data of London clay and Gault clay, with Equations 79 and 80 superimposed on the experimental results (Yimsiri & Soga 2011). Given the very limited database, the validity of the proposed stress dependency of axial small strain moduli is hard to assess. It may seem justified to relate shear moduli G_{hh} and G_{vh} and axial moduli E'_v and E'_h to mean effective stress p' with the same power index.

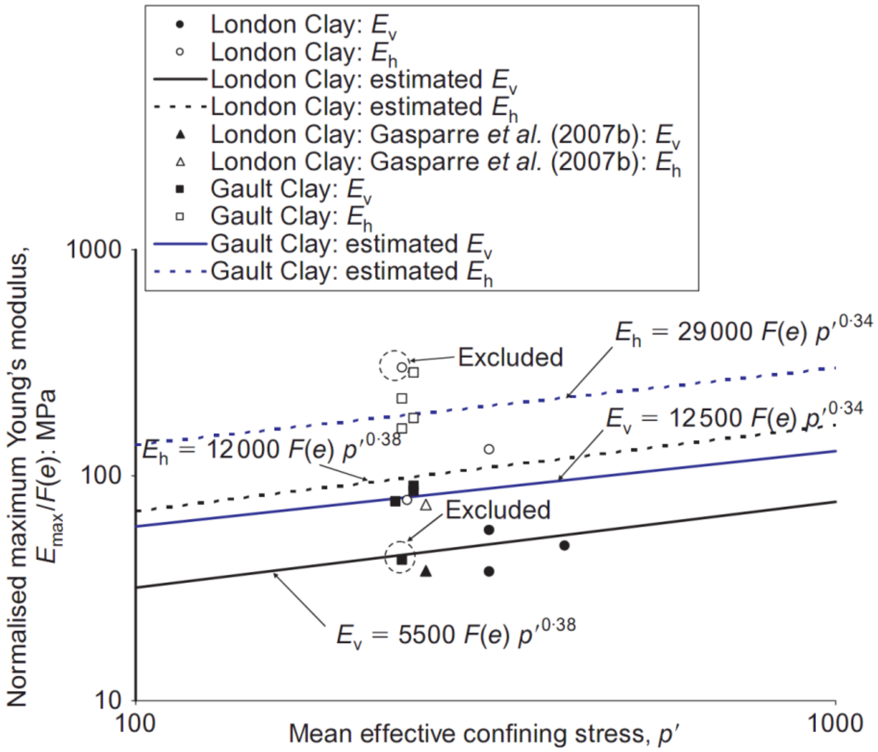

Fig. 21: Relationship between small-strain elastic moduli and mean effective stress (Yimsiri & Soga 2011)

4.3 Micro-macro relations for anisotropic elastic stiffness

As multilaminate soil models are based on formulating constitutive equations on integration plane level, local elastic stiffness parameters are required to obtain the stress-strain response for a macroscopic load step. However, in the case of a cross-anisotropic elastic material these parameters are not known beforehand and need to be correlated to macroscopic parameters. The following section of this chapter presents two approaches to obtain such micro-macro-relations for cross-anisotropic elasticity.

4.3.1 Microstructure tensor

Anisotropic shear strength in multilaminate or conceptually similar micromechanical models has been described previously by introducing a so-called microstructure tensor (Pietruszczak & Mroz 2001, Cudny & Vermeer 2004, Galavi 2007). With this approach anisotropy is taken into account by evaluating the microstructure tensor for each plane orientation, which results in local material parameters varying with plane orientation. The type of anisotropy is defined by the structure of the microstructure tensor, while the magnitude of anisotropy is described by a scalar valued anisotropy parameter. For cross anisotropy with a vertical axis of symmetry the variation of the local parameter α_u can be derived as

$$\alpha_u = \alpha_0 \cdot \left(1 - \frac{A_r - 1}{A_r + 2} \cdot \left(1 - 3 \cdot (u_v)^2\right)\right) \tag{81}$$

with	α_u	directional dependent local parameter
	α_0	mean value of the local parameter
	$A_r = \alpha_v / \alpha_h$	ratio of local anisotropy
	u_v	vertical component of the unit vector in which α_u is calculated.

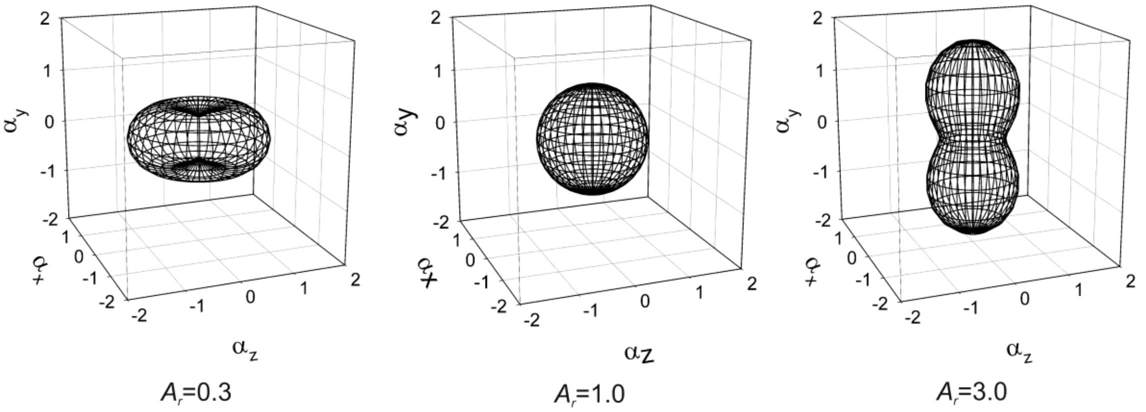

A_r=0.3 A_r=1.0 A_r=3.0

Fig. 22: Spatial distribution of the cross-anisotropic parameter resulting from Equation 81 for different values of parameter A_r (Galavi 2007)

For macroscopic cross-anisotropic stiffness it is a reasonable starting point to expect that also the local stiffness parameters vary in a cross-anisotropic manner, and that the macroscopic and local axis of symmetry coincide. Following that approach in the context of the N-T-split of local stresses, the local normal and tangential compliance parameters can be written as

$$C_n = C_{n0} \cdot \left(1 - \frac{A_{r,Cn} - 1}{A_{r,Cn} + 2} \cdot \left(1 - 3 \cdot (n_v)^2\right)\right), \tag{82}$$

$$C_{ts} = C_{t0} \cdot \left(1 - \frac{A_{r,Ct} - 1}{A_{r,Ct} + 2} \cdot \left(1 - 3 \cdot (s_v)^2\right)\right), \tag{83}$$

$$C_{tt} = C_{t0} \cdot \left(1 - \frac{A_{r,Ct} - 1}{A_{r,Ct} + 2} \cdot \left(1 - 3 \cdot (t_v)^2\right)\right). \tag{84}$$

C_n is the normal compliance, C_{ts} and C_{tt} are the tangential compliances in **s**- and **t**-direction, n_v, s_v and t_v are the vertical components of the normal and tangential vectors as defined in Equations 1 and 2. As n_v, s_v and t_v are related to the plane orientation angle α, the local compliances also depend on plane orientation. The tangential stiffness in general differs in **s**- and **t**-direction on one plane, as the microstructure tensor is evaluated for different directions. It is implicitly assumed, that the local compliance maintains its diagonal shape, such that local stresses and strains are decoupled.

$$\mathbf{C}_i(\alpha,\beta)=\begin{pmatrix} C_n(\alpha,\beta) & 0 & 0 \\ 0 & C_{ts}(\alpha,\beta) & 0 \\ 0 & 0 & C_{tt}(\alpha,\beta) \end{pmatrix} \tag{85}$$

The global compliance matrix **C** is obtained in the same manner as for isotropic elasticity by analytical integration over the surface of the unit sphere (Equation 86). The structure of **C** is symmetric and cross-anisotropic with an x-z bedding plane (y has been taken as the vertical axis), which validates the assumption concerning congruence of local and global anisotropy.

$$\mathbf{C}=\frac{3}{4\Pi}\cdot\int_{\alpha}\int_{\beta}\left[\mathbf{T}_i(\alpha,\beta)\cdot\mathbf{C}_i(\alpha,\beta)\cdot\mathbf{T}_i(\alpha,\beta)^T\right]\cdot\sin\alpha\cdot d\beta\cdot d\alpha \tag{86}$$

The elements of **C** can be related to the cross-anisotropic elastic constants of Equation 66, which gives global parameters in terms of local compliances and anisotropy ratios:

$$E'_v=\frac{35}{9\cdot C_{n0}\cdot\dfrac{5\cdot A_{r,Cn}+2}{A_{r,Cn}+2}+6\cdot C_{t0}\cdot\dfrac{3+4\cdot A_{r,Ct}}{A_{r,Ct}+2}} \tag{87}$$

$$E'_h=\frac{35}{9\cdot C_{n0}\cdot\dfrac{A_{r,Cn}+6}{A_{r,Cn}+2}+3\cdot C_{t0}\cdot\dfrac{11+3\cdot A_{r,Ct}}{A_{r,Ct}+2}} \tag{88}$$

$$G_{vh}=\frac{35}{12\cdot C_{n0}\cdot\dfrac{3\cdot A_{r,Cn}+4}{A_{r,Cn}+2}+3\cdot C_{t0}\cdot\dfrac{23+19\cdot A_{r,Ct}}{A_{r,Ct}+2}} \tag{89}$$

$$\nu'_{vh} = \frac{C_{t0} \cdot \left(4 \cdot A_{r,Ct} + 3\right) \cdot \left(A_{r,Cn} + 2\right) - C_{n0} \cdot \left(3 \cdot A_{r,Cn} + 4\right) \cdot \left(A_{r,Ct} + 2\right)}{2 \cdot C_{t0} \cdot \left(4 \cdot A_{r,Ct} + 3\right) \cdot \left(A_{r,Cn} + 2\right) + 3 \cdot C_{n0} \cdot \left(5 \cdot A_{r,Cn} + 2\right) \cdot \left(A_{r,Ct} + 2\right)} \tag{90}$$

$$\nu'_{hh} = -\frac{C_{t0} \cdot \left(A_{r,Ct} - 8\right) \cdot \left(A_{r,Cn} + 2\right) + C_{n0} \cdot \left(A_{r,Cn} + 6\right) \cdot \left(A_{r,Ct} + 2\right)}{C_{t0} \cdot \left(3 \cdot A_{r,Ct} + 11\right) \cdot \left(A_{r,Cn} + 2\right) + 3 \cdot C_{n0} \cdot \left(A_{r,Cn} + 6\right) \cdot \left(A_{r,Ct} + 2\right)} \tag{91}$$

Equations 87 to 91 return isotropic macroscopic parameters, if the local anisotropy ratios $A_{r,Cn}$ and $A_{r,ct}$ are set to unity. It should be noted, that these micro-macro relations are non-unique. While it is possible to derive global parameters for a chosen set of local compliances and anisotropy ratios, this is not possible in reverse. Evidently, four local variables cannot be uniquely determined such that a chosen set of five global parameters is matched without introducing some artificial coupling between the global parameters.

The relationship between local anisotropy ratio and global cross-anisotropic parameters is plotted in Figure 23 and Figure 24. For simplicity $A_{r,Cn} = A_{r,Ct}$ and $C_{n0} = 3/8 \cdot C_{t0}$ (equivalent to $\nu' = 0.2$ at isotropy) was assumed. For $A_{r,Cn} < 1$ a horizontal plane is stiffer in normal compression than a vertical one, which results in an increase in E'_v and decrease of E'_h compared to the isotropic case ($A_{r,Cn} = 1$). G_{vh} follows the same trend as E'_v, albeit to a lesser degree. Poisson’s ratio ν'_{vh} is virtually independent of the local anisotropy ratio for a given ratio of C_{n0}/C_{t0}. The global anisotropy ratio is limited to E'_h/E'_v ~0.5 at $A_{r,Cn} = 0$ and E'_h/E'_v ~3 at high values of $A_{r,Cn}$.

These boundaries do not change significantly when C_{n0}/C_{t0} and $A_{r,Cn}/A_{r,Ct}$ are varied, and cover the range of experimental ratios fairly well (Table 2). However, the microstructural approach also predicts a strong correlation between E'_h/E'_v and G_{vh}/G_{hh}. (Figure 24, right), as it is not possible to obtain $E'_h/E'_v < 1$ and $G_{vh}/G_{hh} < 1$ with the same set of local parameters. Experimental data on Ham River sand and Dunkerque sand (Table 2) suggest that such a correlation does not exist and soils can exhibit low ratios of E'_h/E'_v and G_{vh}/G_{hh} at the same time.

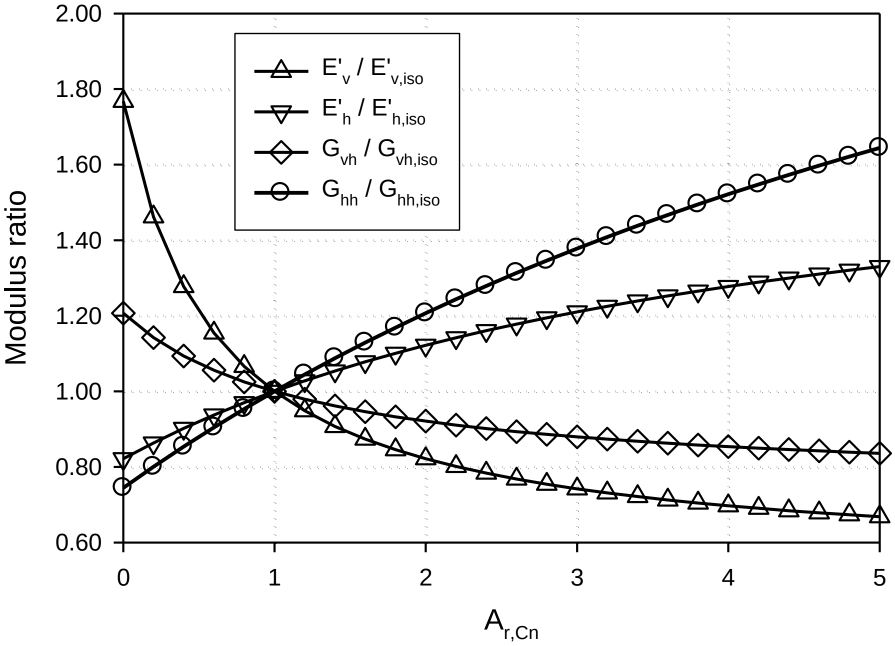

Fig. 23: Relationship between global elastic moduli and local ratio of anisotropy as predicted with the microstructural approach ($A_{r,Cn} = A_{r,Ct}$, $C_{n0}/C_{t0} = 3/8$)

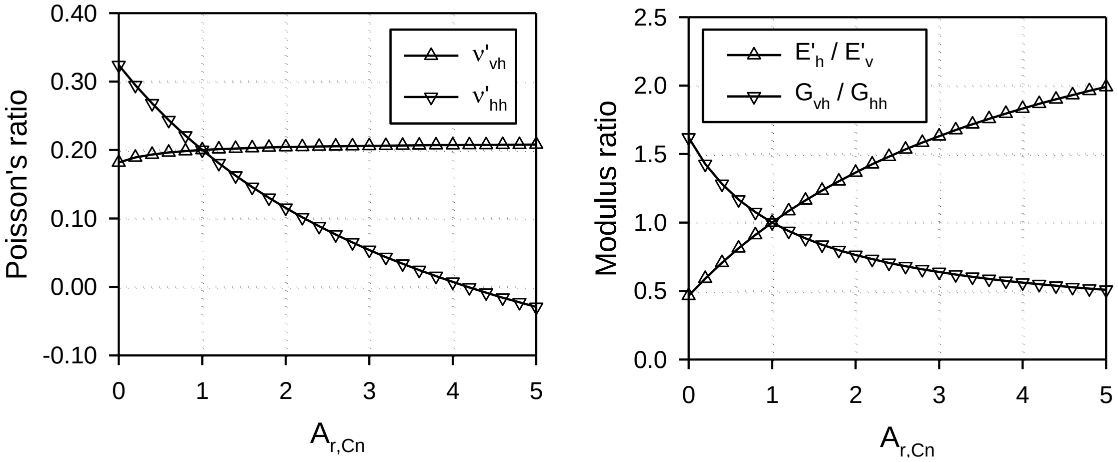

Fig. 24: Relationship between global Poisson's ratios (left) / global anisotropy ratio (right) and local ratio of anisotropy ($A_{r,Cn} = A_{r,Ct}$, $C_{n0}/C_{t0} = 3/8$)

A similar approach has been employed by Yimsiri & Soga (2000) and Hicher & Chang (2006) to derive cross anisotropic small strain stiffness moduli based on micromechanical considerations. They described a directional variation of the density of particle contacts by a cross-anisotropic fabric tensor. Yimsiri & Soga varied tangential and normal stiffness in the same manner (i.e., $A_{r,Cn} = A_{r,ct}$ in Equations 82 to 84), thereby reducing the number of local variables to three. Despite using a slightly different definition of the microstructure tensor, their range of global anisotropy ratios E'_h/E'_v and G_{vh}/G_{hh} resembles the ranges presented here.

The following conclusions can be drawn from the studies on the microstructure tensor:

1. Defining cross-anisotropic spatial distribution of local compliance parameters by means of a microstructure tensor yields cross-anisotropic elasticity on global level. The axes of symmetry of local and global anisotropy coincide.
2. The resulting micro-macro-relations are non-unique. It is not possible to derive local elastic parameters for any given, mechanically possible set of macroscopic cross-anisotropic parameters.
3. The microstructural approach imposes restrictions on the combinations of global elastic parameters, which are not reinforced by the experimental data.

While it may be appropriate to model cross-anisotropic elasticity of some specific soils by means of a microstructure tensor, this approach is not sufficient as a general approach for fine and coarse grained soils.

4.3.2 Spectral decomposition

The analytical integration procedure followed for isotropic material in the previous section started at the micro-level and then proceeded up to the macroscopic level. Basic assumptions were made on local level regarding the decoupling of shear and normal strains, and local parameters were later related to macroscopic elastic parameters. With such a decoupled local compliance, no local shear strains are obtained in isotropic compression (as σ'_n is equal and $\tau = 0$ on all planes), even if the local compliance parameters are allowed to vary with plane orientation.

However, isotropic compression of a cross anisotropic material results in different macroscopic strains in and perpendicular to the axis of symmetry, which indicates the presence of shear strains within the material. In order to capture that effect, coupling of normal stresses and shear strains on local level seems inevitable, which means that the structure of the local compliance is an unknown as well as the local stiffness parameters. In order to avoid arbitrary assumptions regarding the coupling, a different approach is followed further on.

The new approach is based on the spectral decomposition of the global compliance matrix and the subsequent projection of its components into the local coordinate system, which has first been employed for microplane models by Cusatis et al. (2008). The spectral decomposition offers the possibility to obtain local compliance matrices directly. A cross-anisotropic material with a vertical axis of symmetry is considered here, although the method is also applicable to a fully anisotropic material. Only the step-by-step procedure will be demonstrated here. For details on the theoretical background see Theocaris et al. (1991) and Cusatis et al. (2008)

If written in Kelvin notation, the global cross-anisotropic compliance matrix **C** possesses $m = 4$ eigenvalues λ_m, which are given in Appendix A. The Kelvin notation used in Equations 92-94 preserves the sum of the elements of the second order tensors $\boldsymbol{\sigma}$ and $\boldsymbol{\varepsilon}$.

$$\boldsymbol{\sigma}' = \left(\sigma'_{xx} \quad \sigma'_{yy} \quad \sigma'_{yy} \quad \sqrt{2}\tau_{xy} \quad \sqrt{2}\tau_{yz} \quad \sqrt{2}\tau_{xz}\right)^T \tag{92}$$

$$\boldsymbol{\varepsilon} = \left(\varepsilon_{xx} \quad \varepsilon_{yy} \quad \varepsilon_{yy} \quad \sqrt{2}\gamma_{xy} \quad \sqrt{2}\gamma_{yz} \quad \sqrt{2}\gamma_{xz}\right)^T \tag{93}$$

$$\mathbf{C} = \begin{pmatrix} \frac{1}{E'_h} & \frac{-\nu'_{hv}}{E'_h} & \frac{-\nu'_{hh}}{E'_h} & 0 & 0 & 0 \\ \frac{-\nu'_{hv}}{E'_h} & \frac{1}{E'_v} & \frac{-\nu'_{hv}}{E'_h} & 0 & 0 & 0 \\ \frac{-\nu'_{hh}}{E'_h} & \frac{-\nu'_{hv}}{E'_h} & \frac{1}{E'_h} & 0 & 0 & 0 \\ 0 & 0 & 0 & \frac{1}{2G_{vh}} & 0 & 0 \\ 0 & 0 & 0 & 0 & \frac{1}{2G_{vh}} & 0 \\ 0 & 0 & 0 & 0 & 0 & \frac{1+\nu'_{hh}}{E'_h} \end{pmatrix} \tag{94}$$

Using the idempotent matrices $\mathbf{E}_m$ (Appendix A), which are defined by the eigenvectors of **C**, the global stress vector can be split up into its spectral components or stress modes $\boldsymbol{\sigma}'_m$.

$$\boldsymbol{\sigma}' = \sum_m \boldsymbol{\sigma}'_m = \sum_m \left(\mathbf{E}_m \cdot \boldsymbol{\sigma}'\right) \tag{95}$$

Local stress modes $\boldsymbol{\sigma}'_{i,m}$ on plane i are obtained by projecting each global stress mode separately.

$$\boldsymbol{\sigma}'_{i,m} = \mathbf{T}_i^T \cdot \boldsymbol{\sigma}'_m \tag{96}$$

Local strain modes $\boldsymbol{\varepsilon}_{i,m}$ are calculated by multiplying each local stress mode $\boldsymbol{\sigma}'_{i,m}$ separately with the corresponding eigenvalue λ_m. The sum of all local strain modes yields the local strain vector $\boldsymbol{\varepsilon}_i$, and the sum of all local stress modes equals the local stress vector $\boldsymbol{\sigma}'_i$.

$$\boldsymbol{\varepsilon}_{i,m} = \lambda_m \cdot \boldsymbol{\sigma}'_{i,m} \tag{97}$$

$$\boldsymbol{\sigma}'_i = \sum_m \boldsymbol{\sigma}'_{i,m} \; ; \qquad \boldsymbol{\varepsilon}_i = \sum_m \boldsymbol{\varepsilon}_{i,m} \tag{98}$$

Combining Equations 96-98 yields local strains $\boldsymbol{\varepsilon}_i$ expressed in terms of global stresses $\boldsymbol{\sigma}'$ and global stiffness parameters λ_m:

$$\boldsymbol{\varepsilon}_i = \mathbf{T}_i^T \cdot \sum_m \left(\lambda_m \cdot \mathbf{E}_m\right) \cdot \boldsymbol{\sigma}' = \mathbf{C}_i \cdot \mathbf{T}_i^T \cdot \boldsymbol{\sigma}' \tag{99}$$

The only unknown in Equation 99 is the local compliance matrix $\mathbf{C}_i$, as $\mathbf{E}_m$ and λ_m are material constants describing the global anisotropy and $\mathbf{T}_i$ only depends on the plane orientation. The global stress vector $\boldsymbol{\sigma}'$ can be omitted as it appears on both sides of the equation. As the matrices $\mathbf{E}_m$ are of the order 6 x 6, Equation 99 only has a unique solution for $\mathbf{C}_i$ if both $\mathbf{T}_i$ and $\mathbf{C}_i$ are also 6 x 6 square matrices. In that case Equation 99 can be transformed such that the local compliance matrix $\mathbf{C}_i$ is obtained directly.

$$\mathbf{C}_i = \mathbf{T}_i^T \cdot \sum_m \left(\lambda_m \cdot \mathbf{E}_m\right) \cdot \left(\mathbf{T}_i^T\right)^{-1} \tag{100}$$

$$\sum_m \left(\lambda_m \cdot \mathbf{E}_m\right) = \mathbf{C} \tag{101}$$

$$\mathbf{C}_i = \mathbf{T}_i^T \cdot \mathbf{C} \cdot \left(\mathbf{T}_i^T\right)^{-1} \tag{102}$$

Consequently, the local stress vector needs to be split up into six components. As the volumetric-deviatoric split was necessary to derive consistent micro-macro-relation for isotropic material, it is also utilized for cross-anisotropic material. Furthermore, local shear stresses are split into components resulting from global axial stresses and global shear stresses.

$$\boldsymbol{\sigma}'_i = \begin{pmatrix} \sigma'_{nv} \\ \sigma_{nd} \\ \tau_{s1} \\ \tau_{s2} \\ \tau_{t1} \\ \tau_{t2} \end{pmatrix}; \ \boldsymbol{\varepsilon}_i = \begin{pmatrix} \varepsilon_{nv} \\ \varepsilon_{nd} \\ \gamma_{s1} \\ \gamma_{s2} \\ \gamma_{t1} \\ \gamma_{t2} \end{pmatrix} \tag{103}$$

With	σ'_{nv}	volumetric normal stress
	σ_{nd}	deviatoric normal stress
	τ_{s1} and τ_{t1}	tangential stresses in direction of $\mathbf{s}_i$ and $\mathbf{t}_i$ due to global axial stresses
	τ_{s2} and τ_{t2}	tangential stresses in direction of $\mathbf{s}_i$ and $\mathbf{t}_i$ due to global shear stresses

For this split, the transformation matrix of plane *i* is modified to

$$\mathbf{T}_i = \left[\begin{matrix} 1/3 & n_{i,1}^2 - 1/3 & n_{i,1} \cdot s_{i,1} & 0 \\ 1/3 & n_{i,2}^2 - 1/3 & n_{i,2} \cdot s_{i,2} & 0 \\ 1/3 & n_{i,3}^2 - 1/3 & n_{i,3} \cdot s_{i,3} & 0 \\ 0 & 2n_{i,1} \cdot n_{i,2} & 0 & n_{i,1} \cdot s_{i,2} + n_{i,2} \cdot s_{i,1} \\ 0 & 2n_{i,2} \cdot n_{i,3} & 0 & n_{i,3} \cdot s_{i,2} + n_{i,2} \cdot s_{i,3} \\ 0 & n_{i,1} \cdot n_{i,3} & 0 & n_{i,3} \cdot s_{i,1} + n_{i,1} \cdot s_{i,3} \end{matrix}\right. \cdots$$

$$\cdots \left.\begin{matrix} n_{i,1} \cdot t_{i,1} & 0 \\ n_{i,2} \cdot t_{i,2} & 0 \\ n_{i,3} \cdot t_{i,3} & 0 \\ 0 & n_{i,1} \cdot t_{i,2} + n_{i,2} \cdot t_{i,1} \\ 0 & n_{i,3} \cdot t_{i,2} + n_{i,2} \cdot t_{i,3} \\ 0 & n_{i,3} \cdot t_{i,1} + n_{i,1} \cdot t_{i,3} \end{matrix}\right] \tag{104}$$

$\mathbf{C}_i$ varies with plane orientation and contains non-zero off-diagonal elements, which introduces the necessary coupling of normal stresses and shear deformation. Equation 100 is also obtained if the kinematic constraint is used for the spectral decomposition, which indicates that the double constraint is satisfied.

It should be noted that the transformation matrix $\mathbf{T}_i$ needs to be inverted in order to apply Equation 100. This is not fulfilled for the planes perpendicular to the axes of the global coordinate system. Consequently, either an integration rule without integration points directly at the *x*, *y* and *z*-axis must be used (e.g. the 28-

plane integration rule of Bažant & Oh 1986), or a slight rotation of all integration points needs to be carried out.

In the case of isotropic elastic material, **C** possesses only two unique eigenvalues as given in Equation 105, yielding a diagonal local compliance matrix $\mathbf{C}_i$ (Equation 106). The eigenvalues λ_1 and λ_2 equal C_d and C_v, as derived analytically in the previous chapter for the V-D split.

$$\lambda_1 = C_d = \frac{\nu'+1}{E};\ \lambda_2 = C_v = \frac{1-2\cdot\nu'}{E} \tag{105}$$

$$\mathbf{C}_i = \begin{bmatrix} \lambda_2 & 0 & 0 & 0 & 0 & 0 \\ 0 & \lambda_1 & 0 & 0 & 0 & 0 \\ 0 & 0 & \lambda_1 & 0 & 0 & 0 \\ 0 & 0 & 0 & \lambda_1 & 0 & 0 \\ 0 & 0 & 0 & 0 & \lambda_1 & 0 \\ 0 & 0 & 0 & 0 & 0 & \lambda_1 \end{bmatrix} \tag{106}$$

4.3.3 Local strain distributions

The differences in local strain distributions obtained by applying the microstructural approach and the spectral decomposition method are highlighted by the following simple stress point test. A cross-anisotropic elastic material with a vertical axis of symmetry is subjected to isotropic and triaxial stress increments. Local compliance parameters for the microstructural approach are assumed as $A_{r,Cn} = 5$, $A_{r,Ct} = 2.5$, $C_{t0} = 0.0001$ and $C_{n0} = 3/8 \cdot C_{t0}$. The resulting global cross-anisotropic parameters are obtained from Equations 87-91 and summarized in Table 5.

Tab. 5: Cross-anisotropic elastic material parameters

E'_v **[kPa]**	E'_h **[kPa]**	G_{vh} **[kPa]**	ν'_{vh}	ν'_{hh}
11 531	19 840	5 911	0.185	0.108

These parameters were then used as the input for the spectral decomposition method. Hence, both the microstructural and the spectral decomposition approach represent the same macroscopic stiffness. Distribution of local strains is studied for stress increments of $\Delta\sigma'_h = \Delta\sigma'_v = -100$ kPa (isotropic compression) and $\Delta\sigma'_h = +100$ kPa, $\Delta\sigma'_v = -200$ kPa (triaxial compression). For these simple stress conditions the local normal and shear strain distributions can be obtained analytically for both methods. As reference the global strain increment has also been projected directly into the different orientations using Equation 107 (kinematic constraint).

$$\mathbf{d\varepsilon}_i = \left(\mathbf{T}_i(\alpha,\beta)\right)^T \cdot \mathbf{d\varepsilon} = \left(d\varepsilon_n \quad d\gamma_s \quad d\gamma_t\right)^T \tag{107}$$

Plotting all three in the same polar diagram over orientation angle α (with $\alpha = 0$ denoting a horizontal plane) reveals significant differences for both isotropic and anisotropic loading (Figure 25, Figure 26). In isotropic loading, the microstructural approach predicts a more extreme normal strain distribution than the spectral decomposition, but no local shear strains at all. This is due to the decoupling of local normal stresses and local shear strains, with the latter originating only from local shear stresses (which are zero in isotropic loading). On the other hand, the spectral decomposition method predicts maximum shear strains at $\alpha = \pm 45°$ to the vertical axis, which coincides with the reference solution and demonstrates that the double constraint is fulfilled. In triaxial loading, the spectral decomposition predicts the more extreme distribution of local normal strains and less shear strain than the microstructural approach.

As the macroscopic response is the primary objective of the model, getting the correct local strain distribution may seem of secondary importance. However, it should be noted that in small strain stiffness models the local stiffness parameters vary with strains. Incorrect local strain distributions would therefore result in different macroscopic stiffness degradation behaviour, and would also change the strain induced anisotropy, which is a key feature of the multilaminate framework. The spectral decomposition delivers not only the analytical solution for the distribution of local strain, but is also applicable to a wider range of cross-anisotropic parameter sets. The cross-anisotropic constitutive model presented in the following chapter is therefore based on the spectral decomposition of the global compliance matrix.

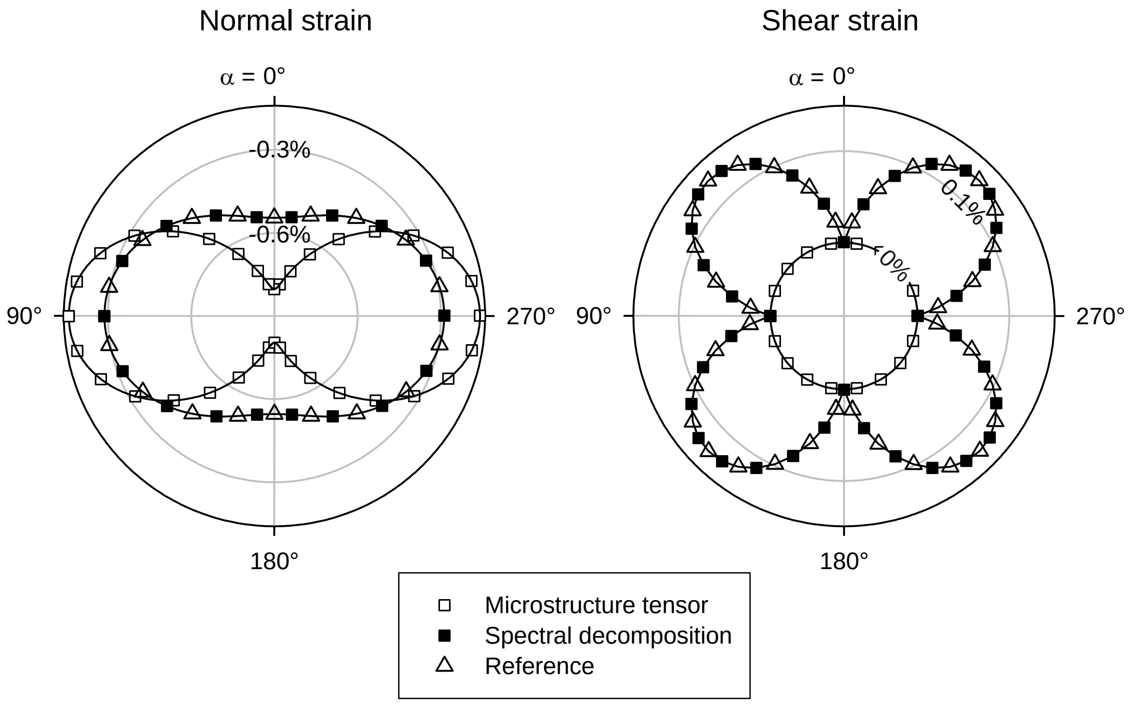

Fig. 25: Distribution of local strains in isotropic compression

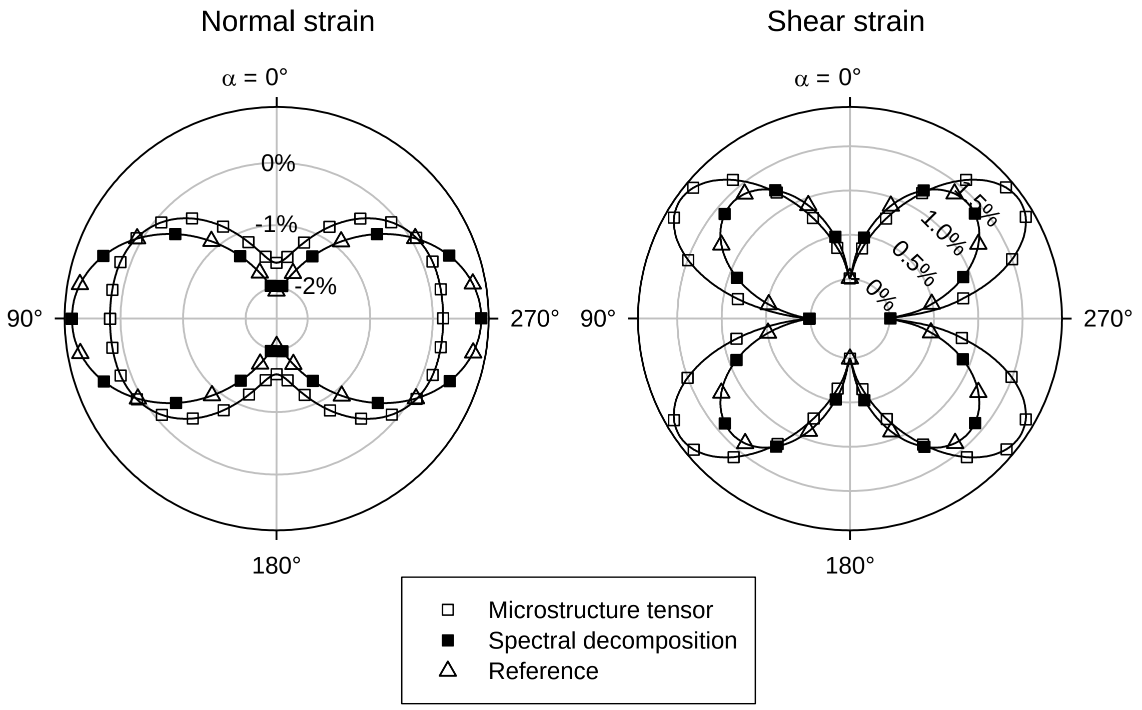

Fig. 26: Distribution of local strains in triaxial compression

4.4 Cross-anisotropic small strain stiffness model

4.4.1 Stress dependency of stiffness

Three different approaches for modelling the dependency of elastic small strain stiffness on the stress state are available in the model, as given in Equations 108 to 110.

In approach 1 the cross anisotropic axial and shear moduli depend on the mean effective stress p' (equal to the volumetric normal stress σ'_{nv} on the plane). As elastic moduli in approach 1 depend on the macroscopic stress p' for all planes, macroscopic and local ratios of anisotropy remain constant for all isotropic and non-isotropic stress states. This approach is applicable to overconsolidated fine grained soils, as these soils reportedly exhibit less dependency of anisotropy on the current axial stress ratio than coarse grained soils (see chapter 4.2.3 for experimental results).

In approach 2 elastic moduli are related to the local normal stress $\sigma'_n = \sigma'_{nv} + \sigma_{nd}$. If approach 2 is applied to non-isotropic stress states, macroscopic anisotropy varies with the ratio of σ'_h/σ'_v, and slightly higher stiffness in the direction of the higher axial stress is obtained.

In approach 3 the input elastic parameters are modified according to the initial stress state $\boldsymbol{\sigma}_0$, with the axial moduli E'_{v0}, E'_{h0} being adjusted for the corresponding axial stresses and G_{vh0} for the product of the axial stresses. The input values $E'_{h0,ref}$ $E'_{v0,ref}$ and $G_{vh0,ref}$ therefore relate to isotropic stress states. After the initial stress state, elastic stiffness parameters depend on mean effective stress p' as in approach 1. Approach 3 can be used to model the initial stiffness of coarse grained soils, which typically show notable dependency of elastic moduli on stress ratio, as described in chapter 4.2.2.

In all three approaches the Poisson's ratios are independent of stress level and stress ratio. The same power index m applies to the elastic moduli in the small and large strain range.

Approach 1:

$$E'_{h0} = E'_{h0,ref} \cdot \left(\frac{p'}{p_{ref}} \right)^m ,\ E'_{v0} = E'_{v0,ref} \cdot \left(\frac{p'}{p_{ref}} \right)^m ;$$

$$G_{vh0} = G_{vh0,ref} \cdot \left(\frac{p'}{p_{ref}} \right)^m \tag{108}$$

Approach 2:

$$E'_{h0} = E'_{h0,ref} \cdot \left(\frac{\sigma'_n}{p_{ref}} \right)^m \; ; \; E'_{v0} = E'_{v0,ref} \cdot \left(\frac{\sigma'_n}{p_{ref}} \right)^m \; ;$$

$$G_{vh0} = G_{vh0,ref} \cdot \left(\frac{\sigma'_n}{p_{ref}} \right)^m \tag{109}$$

Approach 3:

$$E'_{h0} = E'_{h0,ref} \cdot \left(\frac{\sigma'_{h,0}}{p'_0} \right)^m \cdot \left(\frac{p'}{p_{ref}} \right)^m \; ; \; E'_{v0} = E'_{v0,ref} \cdot \left(\frac{\sigma'_{v,0}}{p'_0} \right)^m \cdot \left(\frac{p'}{p_{ref}} \right)^m \; ;$$

$$G_{vh0} = G_{vh0,ref} \cdot \left(\frac{\sqrt{\sigma'_{v,0} \cdot \sigma'_{h,0}}}{p'_0} \right)^m \cdot \left(\frac{p'}{p_{ref}} \right)^m \tag{110}$$

Figure 27 and Figure 28 show predictions by approach 1-3 and experimental data of Ham River sand reported by Kuwano & Jardine (2002) for a cross anisotropic stress state ($K' = 0.45$). The reference elastic moduli reported by Kuwano & Jardine for $K' = 1.0$ are listed in Table 6. As the model does not account for changes in void ratio, the influence of void ratio e has been incorporated into the reference values with $f(e) = 1.37$ for $e = 0.66$.

Tab. 6: Reference cross-anisotropic material parameters of Ham River sand at isotropic stresses (Kuwano & Jardine 2002)

	$E'_{v0,ref}$ **[kPa]**	$E'_{h0,ref}$ **[kPa]**	$G_{vh0,ref}$ **[kPa]**	m
Ham River sand	204 000	174 000	72 000	0.52

G_{vh} matches the experimental data reasonably well for approaches 1 and 2, but distinct differences can be observed for the axial moduli E'_h and E'_v. The strong influence of stress induced anisotropy observed in the experiments cannot be reproduced by neither the dependency on p' nor on σ'_n, and the difference between approach 1 (p') and approach 2 (σ'_n) is remarkably small. The magnitude of anisotropy induced numerically by anisotropic stresses is rather small, as macroscopic anisotropy is the averaged sum of all local contributions. This observation is in agreement with the findings of Hicher & Chang (2006), who related contact stiffness to contact normal stress in their micromechanical model in a similar manner as in approach 2. While they were able to simulate cross-anisotropic elastic behaviour well at isotropic stresses, the degree of anisotropy was also underestimated at anisotropic stress states.

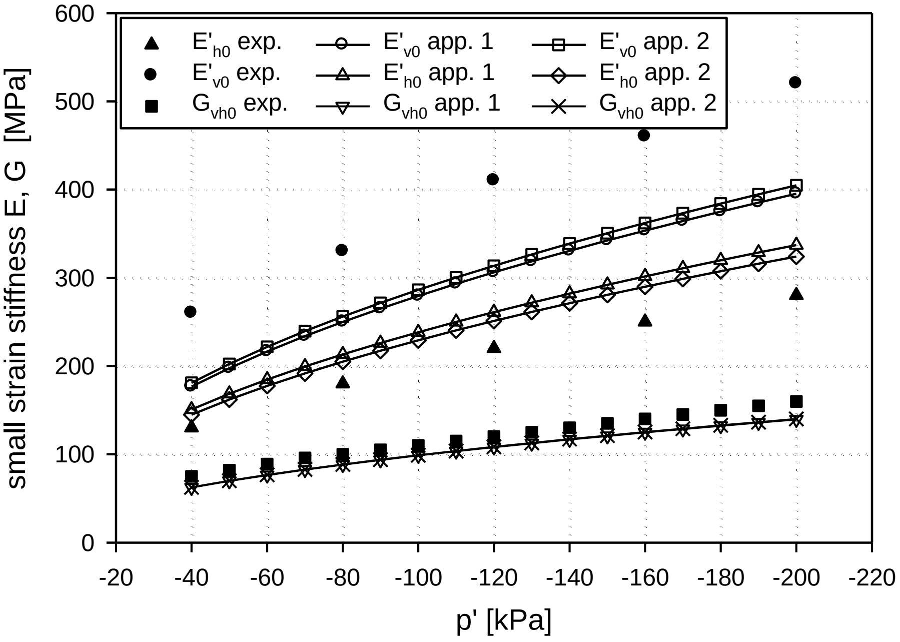

Fig. 27: Predicted and measured stress dependency of stiffness, approach 1 and 2

Approach 3 delivers an almost perfect match with the experimental data for both the axial and the shear moduli. However, it should be noted that approach 3 only accounts for stress induced anisotropy at the initial stress state, and further stress dependency is governed by mean stress *p'*. If large deviations from the initial ratio of σ'_h/σ'_v occur, also the elastic moduli obtained by approach 3 may deviate from the experimental results.

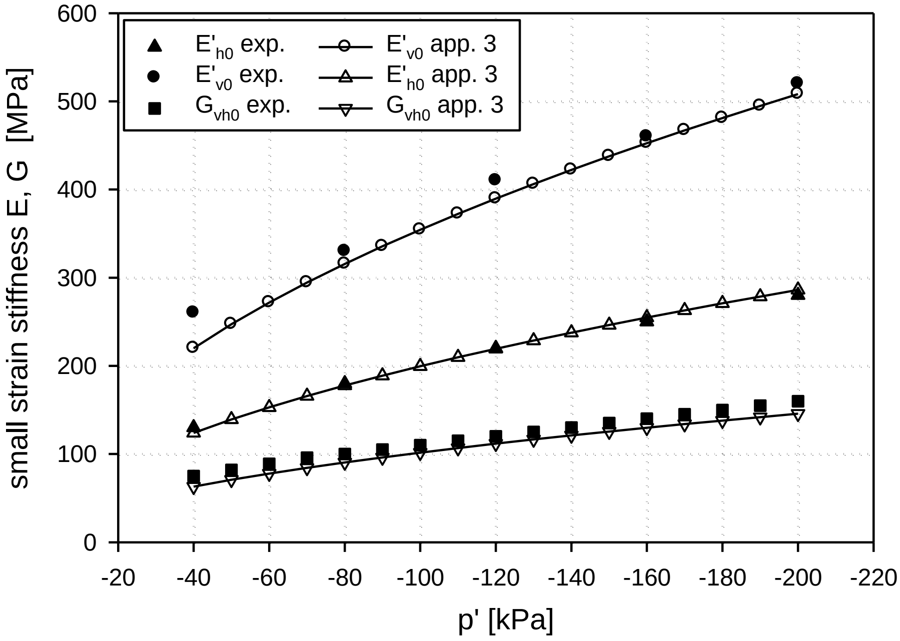

Fig. 28: Predicted and measured stress dependency of stiffness, approach 3

4.4.2 Stiffness degradation

The degradation of local small strain stiffness depends on the magnitude of the local deviatoric strain ε_{deg} (Equation 111) and is described by a tri-linear function with regard to log(ε_{deg}), Figure 29. Initially all planes start with the same cross anisotropic stiffness, which is projected separately into the plane coordinate system.

With accumulation of local deviatoric strains, the initial anisotropy diminishes and the material approaches isotropic elasticity at the large strain range, which is backed by (albeit limited) experimental data (Gasparre et al. 2007, Lings et al. 2000). The parameters $\varepsilon_{deg,1}$ and $\varepsilon_{deg,2}$ are input parameters and define the local deviatoric strain at the onset of degradation and the transition to large strain behaviour.

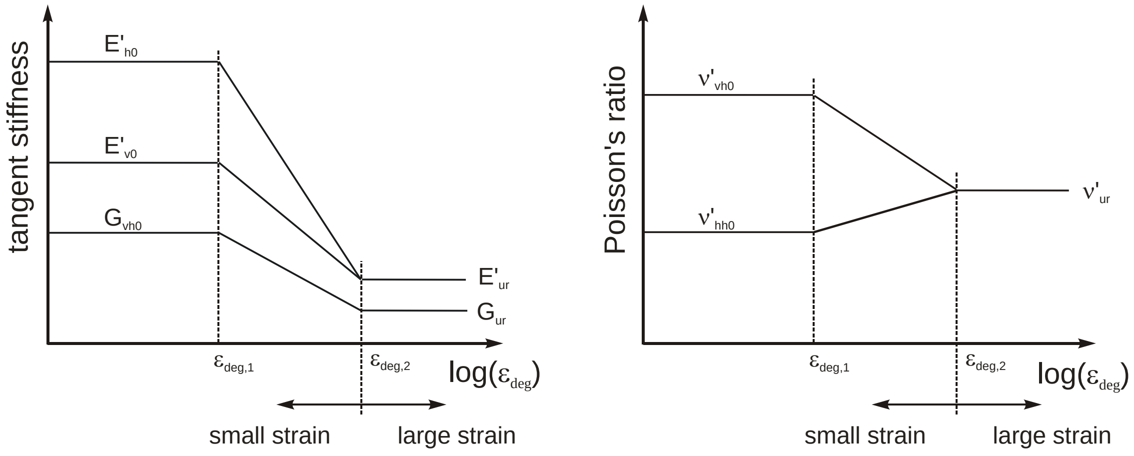

Fig. 29: Degradation of anisotropic small strain stiffness and transition to large strain behaviour

Figure 30 shows the macroscopic stiffness degradation curve (Figure 30a) in triaxial compression in comparison to the degradation of local shear stiffness (Figure 30b). As the deviatoric strains vary from plane to plane, degradation of initial stiffness starts at different stages of macroscopic loading on different planes, which results in a relatively smooth transition from small strain to large strain behaviour on macroscopic level.

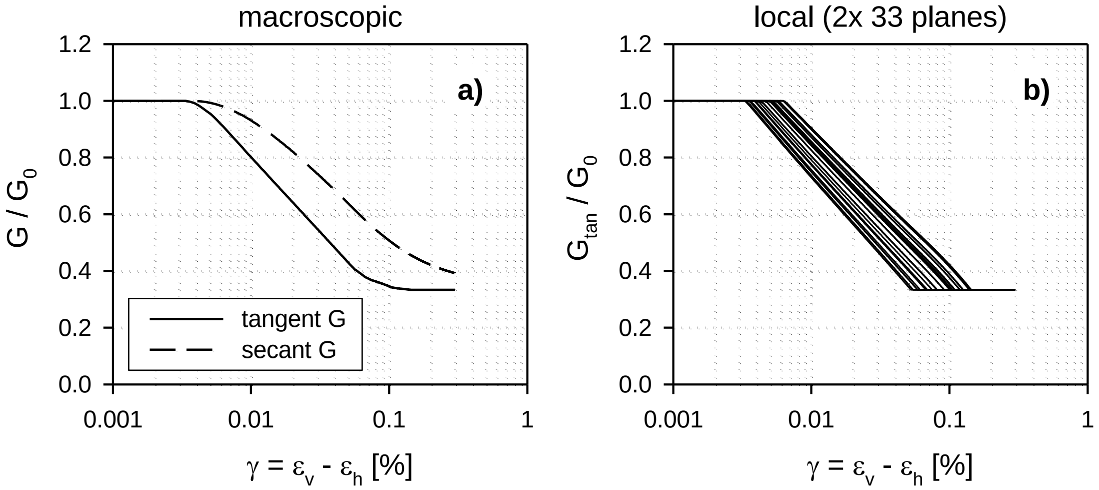

Fig. 30: Macroscopic (a) and local (b) degradation of small strain stiffness in triaxial compression

4.4.3 Dependency on load history

It has been demonstrated experimentally that soil stiffness does not only depend on the magnitude of accumulated deviatoric strain but also on the stress path and hence on load history (Richardson 1988). Different approaches have been followed in constitutive modelling in order to capture this effect. Whereas kinematic hardening models monitor load history in stress space (Al-Tabaa & Wood 1989, Puzrin & Burland 1998), defining load history in strain space has been preferred in small strain stiffness models (Simpson 1992, Benz et al. 2009). While each approach has its merits, monitoring load history in terms of strains is more consistent with stiffness degradation, which is also driven by strains rather than stresses.

In this study strain history is memorized on each plane separately in spherical contours which represent levels of equal degradation strain ε_{deg}. Each sphere is defined by its centre coordinates and its radius in the local deviatoric strain space $\{\varepsilon_{nd}, \gamma_s , \gamma_t\}$. The degradation strain ε_{deg} is defined as the distance of the current deviatoric strain state $\{\varepsilon_{nd}, \gamma_s, \gamma_t\}$ to the centre of the currently active strain sphere $\{\varepsilon_{nd,centre}, \gamma_{s,centre}, \gamma_{t,centre}\}$:

$$\varepsilon_{deg} = \sqrt{(\varepsilon_{nd} - \varepsilon_{nd,centre})^2 + (\gamma_s - \gamma_{s,centre})^2 + (\gamma_t - \gamma_{t,centre})^2} \qquad (111)$$

The different cases considered in the model are shown schematically in Figure 31. As a full three-dimensional illustration of strain development is hardly feasible, the local strain spheres are depicted as circular, two-dimensional contours ($\varepsilon_{nd} = 0$).

Initially, only one strain sphere (SC1) exists, which is subsequently enlarged in monotonic loading (case 1). If the current load step reduces ε_{deg}, this indicates that the strain path turns inside the active sphere (case 2). Consequently, a reversal of the load path is detected and a new sphere (SC2) is created, which is employed as the active sphere further on. The new sphere is fixed to the previous one at the reversal point, and the centre and the size of the new sphere is updated in further loading. Reduction of ε_{deg}, now calculated from SC2, again results in the creation of a new strain sphere, SC3, and SC2 becomes inactive (case 3). If a later load step again enlarges one of the outer spheres SC1 or SC2, an intersection with a previous strain path is detected (case 4). In that case the inner spheres are erased from the strain history of the stress point, and the outer sphere gets reactivated. Consequently, the model resembles the Simpson brick model (Simpson 1992), with the number of bricks equating the number of integration planes.

With that approach the two original and the two extended Masing rules as reported by Pyke (1979) can be fulfilled for the elastic part of the model:

1. For primary loading the stress-strain curve follows the back-bone curve.
2. After load reversal the size of the hysteretic loop is increased by a factor of 2.
3. If the past maximum shear strain is exceeded the stress-strain curve follows the backbone curve.
4. If the unloading-reloading curve intersects a previous unloading-reloading curve, it follows the previous curve.

The third Masing rule is treated as a special case of the fourth rule, as the primary strain sphere differs from the others only by its fixed centre at the origin of axis. The second rule is fulfilled without modifying degradation parameters in unloading / reloading, as the shear strain controlling stiffness degradation refers to the centre of the strain contour rather than the reversal point.

In principle, an infinite number of spheres could be taken into account. As the information on local strain history has to be stored as state variables, a limited number of four strain spheres is implemented in the model. It should be noted that still an infinite number of load cycles can be modelled, as only the number of load reversals going inside the outer strain contour is limited.

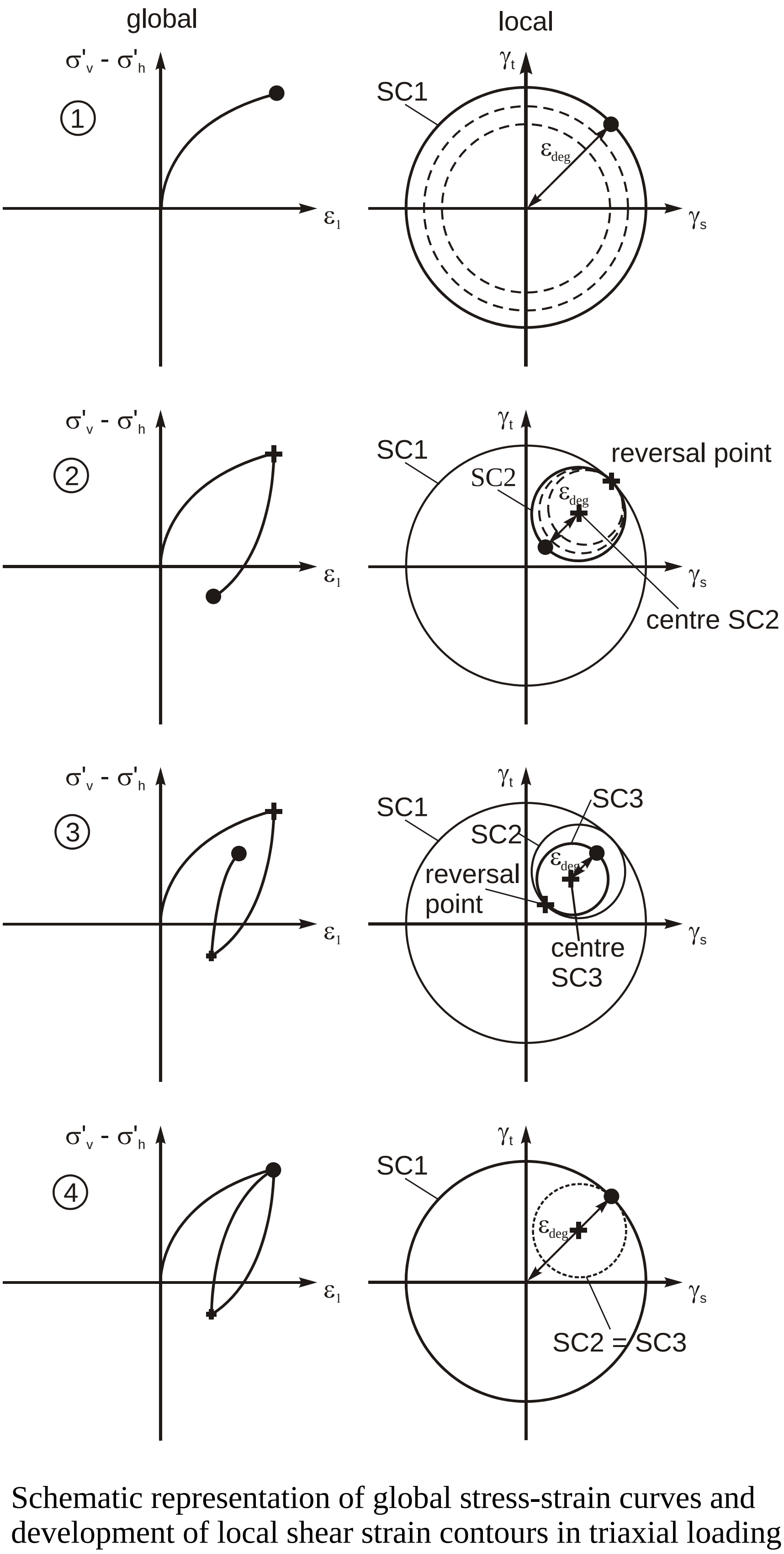

Fig. 31: Schematic representation of global stress-strain curves and development of local shear strain contours in triaxial loading - unloading – reloading

4.4.4 Modification of strain hardening

The stiffness degradation curve shown in Figure 29 only applies to the elastic part of the model. As the strain increment in elastoplastic constitutive models comprises elastic and plastic portions, the resultant shear modulus is significantly lower than the elastic one if plastic strains are allowed in the small strain range, and the desired effect of high initial stiffness gets lost. To avoid this effect, the cap and cone yield surfaces are expanded according to the current position on the stiffness degradation curve, before the calculation of plastic strain is initiated. The yield surfaces are set to the full value of the elastic trial stress in the very small strain range ($\varepsilon_{deg} < \varepsilon_{deg,1}$) and hence no plastic strains are calculated. In the transition range $\varepsilon_{deg,1} < \varepsilon_{deg} < \varepsilon_{deg,2}$, the position of f_{cone} and f_{cap} is adjusted for the degradation parameter x_{stiff}, such that yield surfaces are shifted to the full elastic trial stress at $\varepsilon_{deg} = \varepsilon_{deg,1}$, and no modification is carried out at $\varepsilon_{deg} = \varepsilon_{deg,2}$.

$$x_{stiff} = \frac{\log(\varepsilon_{deg,2}) - \log(\varepsilon_{deg})}{\log(\varepsilon_{deg,2}) - \log(\varepsilon_{deg,1})} \tag{112}$$

$$\tan\varphi'_{m,mod} = \tan\varphi'_m + x_{stiff} \cdot (\tan\varphi'_{m,trial} - \tan\varphi'_m) \tag{113}$$

$$\sigma'_{nc,mod} = \sigma'_{nc} + x_{stiff} \cdot (\sigma'_{nc,trial} - \sigma'_{nc}) \tag{114}$$

$\varphi'_{m,trial}$ and $\sigma'_{nc,trial}$ are the values of φ'_m and σ'_{nc} at the elastic trial stress, $\boldsymbol{\sigma}'_{trial}$. The modified values $\varphi'_{m,mod}$ and $\sigma'_{nc,mod}$ define the position of the shifted yield surfaces, which are used in the subsequent calculation of plastic strains.

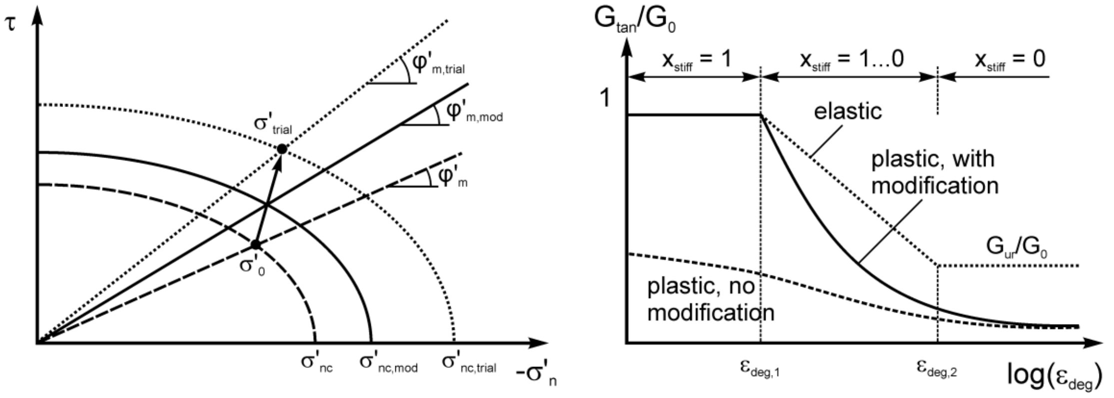

Fig. 32: Modification of yield surfaces in small strain range

4.5 Simulation of element tests

It has been shown previously by Wiltafsky (2003), Scharinger (2007) and Galavi (2007), that the basic version of the multilaminate model is capable of reproducing experimental results in oedometric and triaxial conditions for various coarse and fine grained soils with good accuracy. Simulation of element tests in this chapter is therefore focussed on cross-anisotropic stiffness characteristics and the predicted behaviour at load reversals. Some selected drained triaxial test simulations on Hostun sand using the basic isotropic model are presented to validate the parameters used in subsequent chapters for the simulation of boundary value problems.

4.5.1 Triaxial compression of Hostun sand

Hostun sand is a quartzitic, angular to sub-angular sand from south eastern France, which has been extensively studied in laboratory testing (Schanz & Vermeer 1996, Desrues et al. 2000). Drained triaxial test simulations are performed with the basic multilaminate model with isotropic small strain stiffness at -100 kPa, -300 kPa and -600 kPa of confining pressure and compared with the experimental data for dense Hostun sand reported by Benz (2007).

Additional simulations using the Hardening Soil Small (HSS) model were carried out in order to compare shear strength mobilisation and small strain stiffness degradation in both models. Material parameters are listed in Table 7 for the multilaminate model and in Table 8 for the HSS model. Even though formulated within different frameworks, both models employ the stiffness parameters $E_{oed,ref}$ and $E_{ur,ref}$ as well as the shear strength parameters φ' and c', which facilitates comparison of these models. The main difference between both models is the shear hardening parameter A_{mat} of the multilaminate model, which needs to be calibrated against the experimental stress-strain behaviour.

Stress-strain curves predicted by both models match the experimental data reasonably well for lower stress levels (Figure 33, Figure 34). The experimental data at -300 kPa and -600 kPa show some offset at the beginning of deviatoric loading, which is possibly due to apparatus slip and not a result of material behaviour. At -600 kPa confining pressure both models predict too high shear strength and too stiff material behaviour. While the stiffness at higher stress levels could be reduced by lower values of m, reducing shear strength with increasing confining pressure would require a curved strength envelope, which is not compatible with the Mohr-Coulomb failure line of the basic model. The volumetric behaviour reflects the differences in the stress-strain curves. The contractant behaviour up to ε_1 = -2% and dilatancy at larger strains is in principal reproduced by both models. But due to faster mobilisation of shear strength in the multilaminate model at higher confining stresses, dilatancy is overestimated at σ'_h = -300 kPa and σ'_h = -600 kPa.

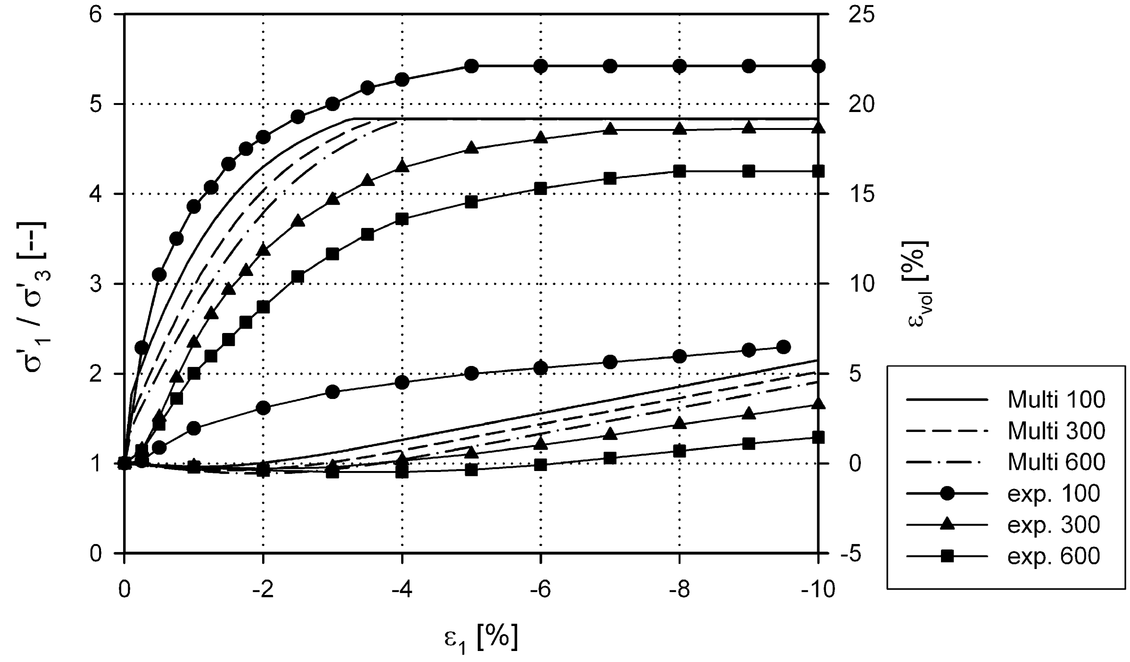

Fig. 33: Stress-strain behaviour of dense Hostun Sand in drained triaxial compression at confining pressures of -100, -300 and -600 kPa and simulation with the multilaminate model

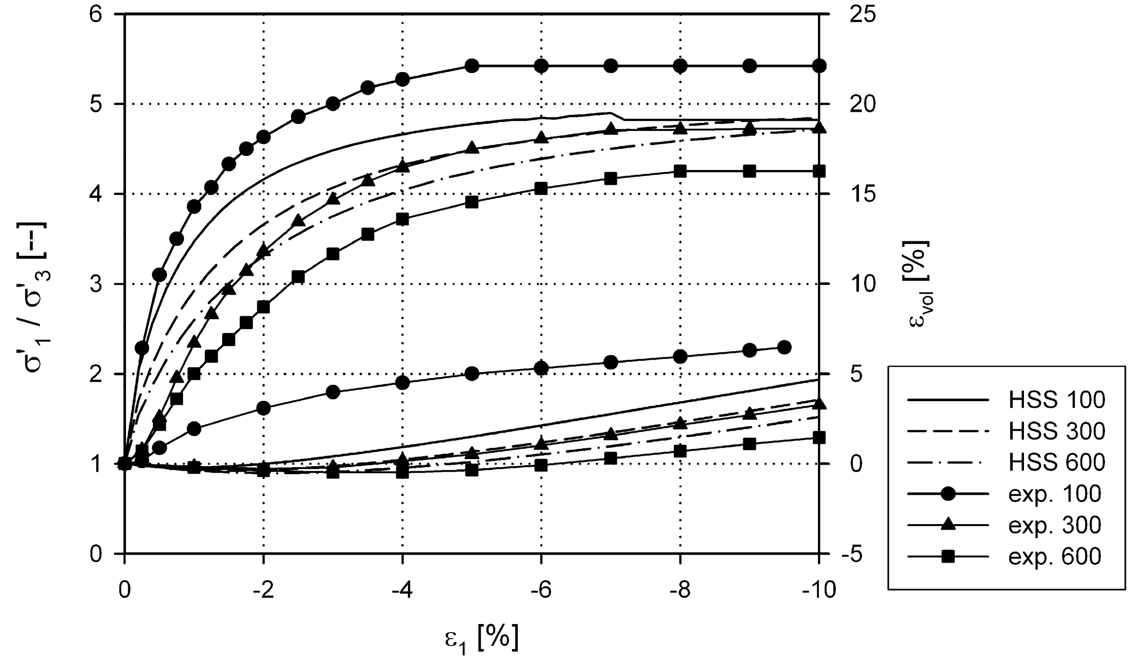

Fig. 34: Stress-strain behaviour of dense Hostun Sand in drained triaxial compression at confining pressures of -100, -300 and -600 kPa and simulation with the Hardening Soil Small model

Figure 35 shows the degradation of small strain stiffness moduli, back calculated from the stress-strain response in triaxial test simulations. Tangent moduli are derived from the incremental changes of shear strain, $\Delta\gamma$, and shear stress, $\Delta\tau$. Secant moduli are calculated from the total shear strain γ and shear stress τ. Shear moduli in Figure 35 have been normalized for the change in stress level.

Degradation curves differ notably due to the different formulation of stiffness degradation. In the multilaminate model an initial range of constant stiffness is assumed on local level, which results in a distinct kink of the macroscopic degradation curve once degradation starts locally on the first integration plane. As degradation progresses at integration plane level, plastic strains are gradually allowed for, accelerating local and macroscopic stiffness degradation. This reflects in the concave curvature of tangent stiffness degradation. The HSS model employs a smooth, convex degradation curve without initial plateau. Remarkably, the HSS model starts about 10% below the input value of $G_{0,ref}$ at very small strains.

Tab. 7: Large and small strain parameters of the multilaminate soil model for dense Hostun sand

parameter		**value**	**unit**
Unit weight above groundwater table	γ_{unsat}	18.0	kN/m^3
Unit weight below groundwater table	γ_{sat}	20.0	kN/m^3
Oedometric stiffness	$E_{oed,ref}$	30 000	kPa
Isotropic large strain Young’s modulus	$E_{ur,ref}$	90 000	kPa
Isotropic large strain Poisson’s ratio	ν'_{ur}	0.2	--
Reference pressure	p_{ref}	100	kPa
Power index for stress dependency of stiffness	m	0.55	--
Shear hardening parameter	A_{mat}	0.020	--
Effective friction angle	φ'_{max}	41	°
Effective cohesion	c'	0	kPa
Dilatancy angle	ψ	14	°
Isotropic shear stiffness at very small strains	$G_{0,ref}$	112 500	kPa
threshold strain level for stiffness degradation	$\varepsilon_{deg,1}$	2e-5	--
transition to large strains	$\varepsilon_{deg,2}$	6e-4	--

Tab. 8: Large and small strain parameters of the Hardening Soil Small model for dense Hostun sand

parameter		**value**	**unit**
Oedometric stiffness	$E_{oed,ref}$	30 000	kPa
Oedometric stiffness	$E_{50,ref}$	30 000	kPa
Isotropic large strain Young's modulus	$E_{ur,ref}$	90 000	kPa
Isotropic large strain Poisson's ratio	ν'_{ur}	0.2	--
Reference pressure	p_{ref}	100	kPa
Power index for stress dependency of stiffness	m	0.55	--
Failure ratio	R_f	0.9	--
Effective friction angle	φ'_{max}	41	°
Effective cohesion	c'	0	kPa
Dilatancy angle	ψ	14	°
Isotropic shear stiffness at very small strains	$G_{0,ref}$	112 500	kPa
Reference shear strain	$\gamma_{0.7}$	2e-4	--

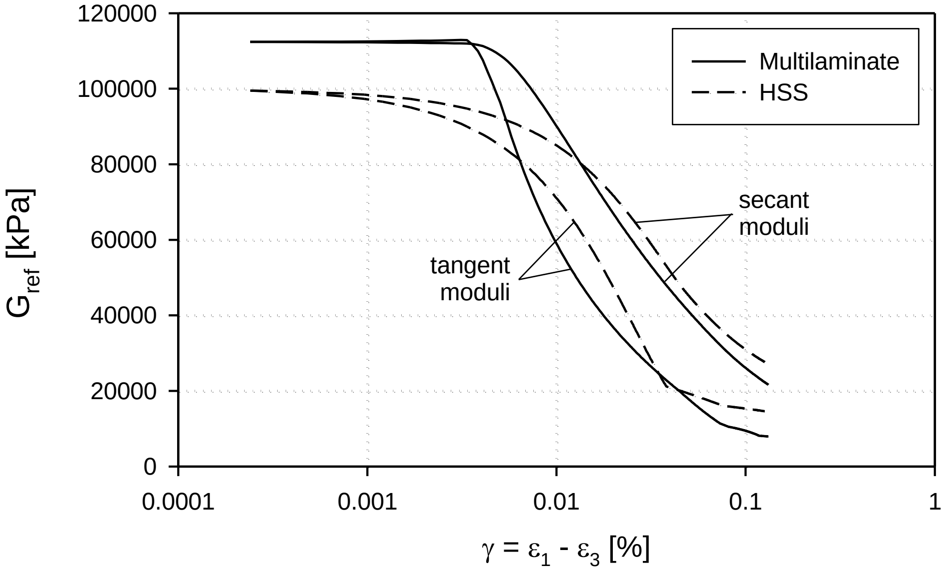

Fig. 35: Degradation of small strain stiffness in multilaminate model and Hardening Soil Small model

4.5.2 Calibration of small strain stiffness parameters

The cross-anisotropic initial stiffness is defined by the axial stiffness moduli E'_{h0} and E'_{v0}, the independent shear modulus G_{vh0}, and the Poisson's ratios ν'_{hh0} and ν'_{vh0}. The full set of parameters can be obtained experimentally by a combination of static and dynamic measurements from bender element aided triaxial tests (e.g. Kuwano 1999, Lings et al. 2000, Gasparre 2005), or with the hollow cylinder apparatus (Nishimura 2005). In true triaxial tests, axial moduli and Poissons's ratios can be assessed by independent variation of the axial stresses, but direct determination of shear moduli requires additional dynamic measurements (Callisto & Rampello 2002, AnhDan & Koseki 2005).

Degradation of small strain stiffness is governed by the parameters $\varepsilon_{deg,1}$ and $\varepsilon_{deg,2}$, which define the onset of degradation and the transition to large strains on integration plane level. These parameters can be obtained by calibration against experimental degradation curves of the macroscopic shear modulus. Figure 36 shows the influence of $\varepsilon_{deg,1}$ and $\varepsilon_{deg,2}$ on the macroscopic stiffness degradation curve in triaxial compression and compares the resultant degradation curves with test data for sands (Seed & Idriss 1970). Simulations have been performed with large strain parameters of dense Hostun sand (Table 7), and isotropic small strain stiffness was assumed.

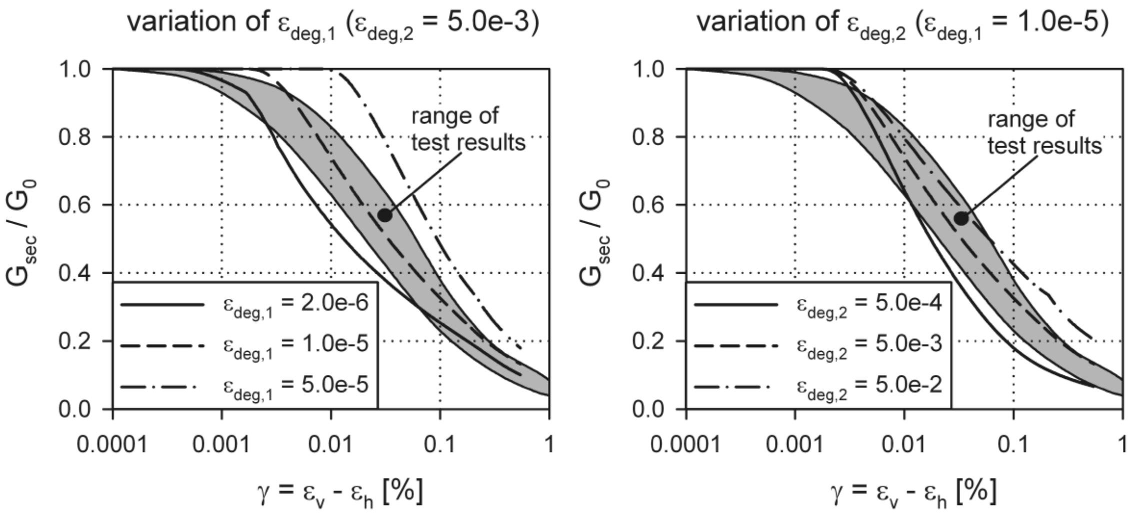

Fig. 36: Normalized experimental stiffness degradation curves for different sands according to Seed & Idriss (1970) (as reported by Benz 2007) and model predictions for different values of $\varepsilon_{deg,1}$ and $\varepsilon_{deg,2}$

As expected, increasing $\varepsilon_{deg,1}$ or $\varepsilon_{deg,2}$ shifts the degradation curve to the large strain range. Predicted degradation curves cover the range of the test data reasonably well. Model predictions show, however, a concave curvature not seen in the experiments, which can be explained by the allowance of plastic strains in the model once local strains exceed $\varepsilon_{deg,1}$. While the different curvature is of limited relevance in static geotechnical problems, the model may not predict realistic damping for sands in dynamic simulations.

Slightly differently shaped degradation curves than for sands are reported for stiff clays. Out of an extensive experimental study on the stiffness characteristics of heavily overconsolidated London clay (Gasparre et al. 2007), an exemplary degradation curve for a sample from 6.5 m depth (test 12.5gUC, geological unit B2(c)) is shown in Figure 37. The undisturbed sample has been tested in undrained triaxial compression, starting from an anisotropic stress state of σ'_v = -202 kPa and σ'_h = -288 kPa. After passing a distinct yielding point at about 0.0006% of shear strain, stiffness degradation is almost linear in log-scale. Like most natural stiff clays, London clay exhibits cross-anisotropic behaviour in the small strain range. In particular anisotropic Poissons's ratios are difficult to determine, which reflects in a wide range of experimental results.

Back-analysis of the test data has been conducted with three different sets of anisotropic small strain parameters, which are listed in Table 9. Set 1 was derived from the values given by Gasparre et al. (2007) as averaged parameters for sub-unit B2(c), set 2 has been taken from the original data of test 12.5gUC (Gasparre 2005), and set 3 equals set 2 except for a change in Poisson's ratios. Elastic moduli are related to mean stress p' (approach 1). Large strain parameters are listed in Table 10. $E_{ur,ref}$ and $E_{oed,ref}$ were derived from isotropic compression data given by Gasparre (2005) for natural London clay. Apart from the power index m, these parameters have minor influence on the stiffness degradation curve at small strains.

Experimental and simulated stiffness degradation is compared in terms of secant equivalent shear modulus G_{eq}, which in undrained conditions is governed by four of the five cross-anisotropic elastic constants (Equation 115, as reported by Lings et al. 2000).

$$G_{eq} = \frac{\Delta\sigma'_v - \Delta\sigma'_h}{2 \cdot \left(\Delta\varepsilon_v - \Delta\varepsilon_h\right)} = \frac{E'_v}{6}\left(\frac{2(1-\nu'_{hh})E'_v + (1-4\nu'_{vh})E'_h}{(1-\nu'_{hh})E'_v - \nu'^{\,2}_{vh}\,E'_h}\right) \tag{115}$$

The shape of the predicted stiffness degradation curves matches well with the test data. Not surprisingly, the best match is obtained with set 2, i.e. with the parameters obtained directly from the sample. With the averaged values of set 1, about 20% less initial shear stiffness is predicted, which however still fits within the range of experimental results obtained from other samples of unit B2(c). Set 3 plots close to set 1, even though the elastic moduli of set 2 have been employed, and only anisotropic Poisson's ratios have been changed to $\nu'_{hh0} = \nu'_{vh0} = 0.2$. Obviously, the initial stiffness in undrained conditions is relatively sensitive to the choice of anisotropic Poisson's ratios. This is however not a deficiency of the multilaminate model, but a result of cross-anisotropic elastic material behaviour.

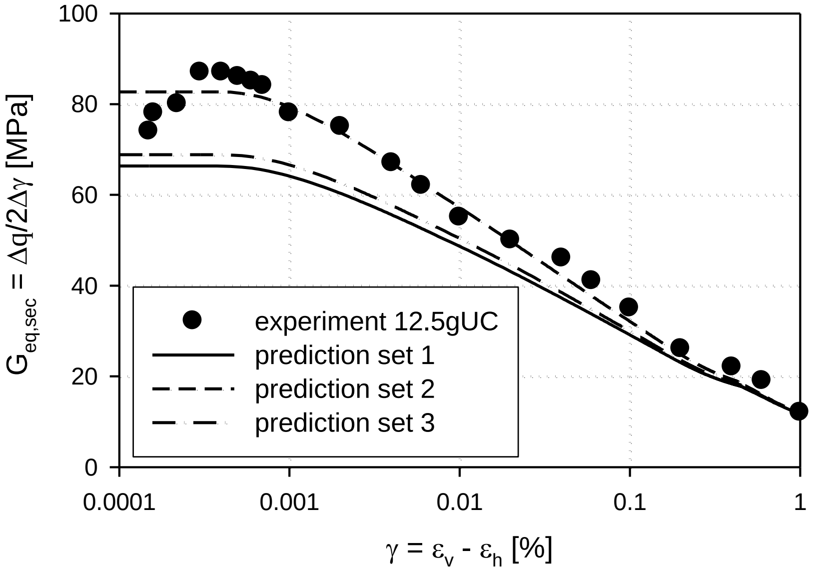

Fig. 37: Experimental and simulated stiffness degradation curves for London clay

Tab. 9: Small strain parameters for London clay (reference stiffness parameters at p' = -100 kPa)

parameter		**set 1**	**set 2**	**set 3**	**unit**
initial vertical stiffness	$E'_{v0,ref}$	46 900	55 800	55 800	kPa
initial horizontal stiffness	$E'_{h0,ref}$	91 500	89 200	89 200	kPa
initial cross-anisotropic shear modulus	$G_{vh0,ref}$	65 000	60 000	60 000	kPa
initial anisotropic Poisson's ratio	ν'_{vh0}	0.10	0.03	0.20	kPa
initial anisotropic Poisson's ratio	ν'_{hh0}	-0.02	0.01	0.20	--
threshold strain level for stiffness degradation	$\varepsilon_{deg,1}$	2×10^{-6}	2×10^{-6}	2×10^{-6}	--
transition to large strains	$\varepsilon_{deg,2}$	1×10^{-3}	1×10^{-3}	1×10^{-3}	--

Tab. 10: Large strain parameters for London clay

parameter		**value**	**unit**
isotropic large strain Young's modulus	$E_{ur,ref}$	13 000	kPa
oedometric stiffness	$E_{oed,ref}$	1020	kPa
reference pressure	p_{ref}	100	kPa
isotropic large strain Poisson's ratio	ν'_{ur}	0.20	--
power index for stress dependency	m	1.0	--
shear hardening parameter	A_{mat}	0.02	--
effective friction angle (peak)	φ'_{max}	32.0	°
effective cohesion	c'	0	kPa
dilatancy angle	ψ	8.0	°

4.5.3 Validation of stress dependency

Bellotti et al. (1996) measured the elastic moduli and Poisson's ratios of inherently cross anisotropic Ticino Sand by seismic wave measurements in laboratory tests. The tests were performed in triaxial stress conditions at varying anisotropic and isotropic stress levels.

Input values $E'_{h0,ref}$, $E'_{v0,ref}$ and $G_{vh0,ref}$ as summarised in Table 11 were taken directly from the test data at isotropic stresses, $p' = -100$ kPa. A power index of $m = 0.5$ was employed for the stress dependency of small strain stiffness. This value was calibrated to fit the test data at $K' = 1.0$ for different levels of mean stress p'.

While only modest anisotropy was found at isotropic stresses, significant anisotropy was induced by anisotropic stress states. Figure 38 shows the experimental results for the various stress states and the elastic moduli predicted by the model with approach 3 (Equation 110). The model slightly underestimates E'_v at $K' = 0.5$, but delivers good agreement with the experimental data for the other elastic moduli and for stress states $K' > 1$.

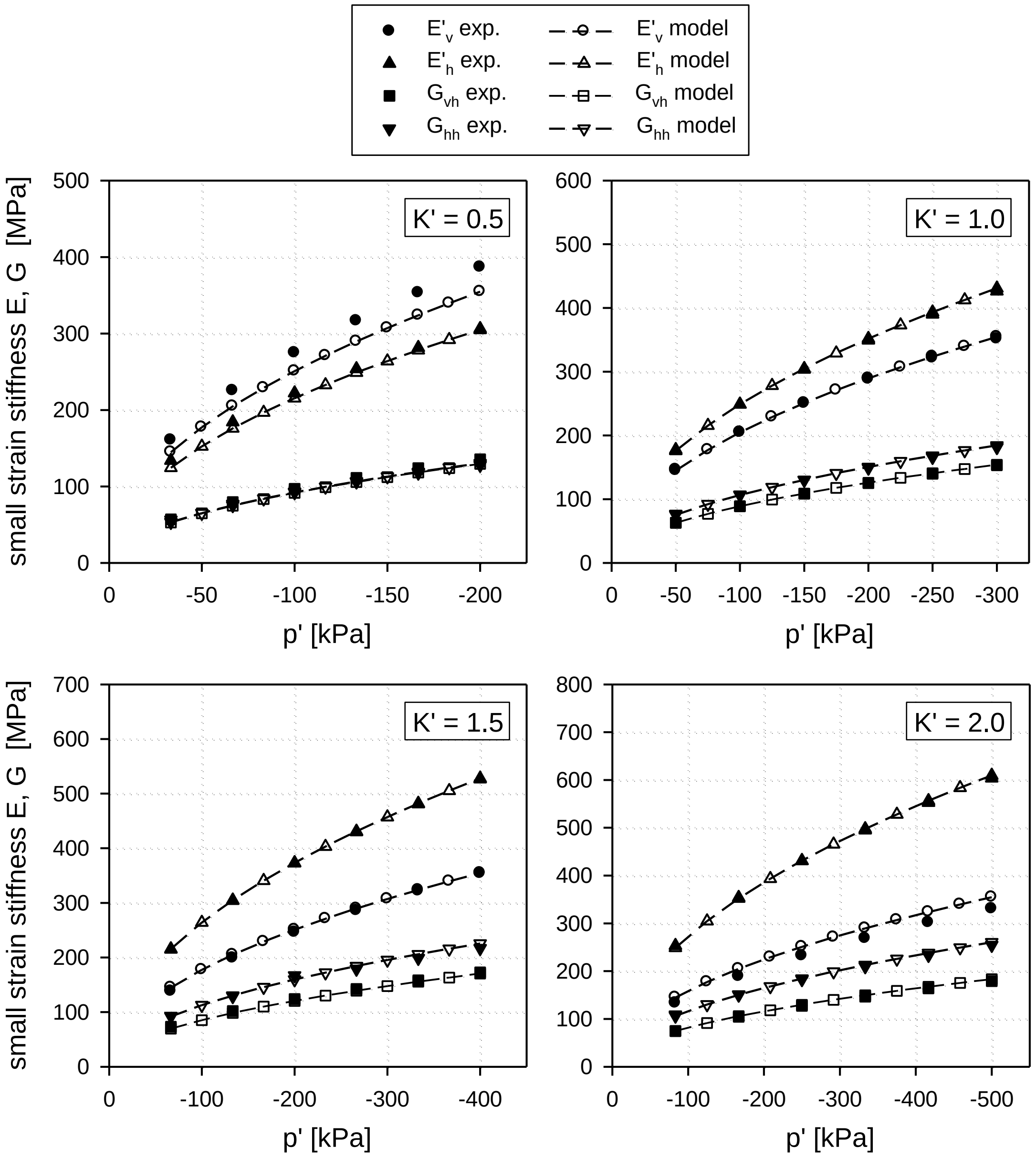

Fig. 38: Cross anisotropic elastic moduli of Ticino Sand at different anisotropic stress states (experimental data from Bellotti et al. 1996)

Tab. 11: Elastic stiffness parameters for Ticino Sand at *p'* = -100 kPa

parameter		**value**	**unit**
initial vertical elastic stiffness	$E'_{v0,ref}$	204 800	kPa
initial horizontal elastic stiffness	$E'_{h0,ref}$	248 800	kPa
initial cross-anisotropic elastic shear modulus	$G_{vh0,ref}$	88 900	kPa
initial anisotropic Poisson's ratio	ν'_{vh0}	0.185	--
initial anisotropic Poisson's ratio	ν'_{hh0}	0.17	--

4.5.4 Small amplitude load cycles

Kuwano & Jardine (2002) performed triaxial tests on inherently cross anisotropic Ham River Sand involving small stress probes at different stress states. The sample was anisotropically consolidated to p' = -200 kPa (compression negative), following a near K_0 stress path up to σ'_h = -142 kPa and σ'_v = -316 kPa (K_0 = 0.45). The specimen was then subjected to drained vertical unloading and reloading by 10 kPa, followed by vertical loading past the previous maximum stress by -10 kPa and unloading to the initial stress state of σ'_h = -142 kPa and σ'_v = -316 kPa. The horizontal stress was held constant in this load cycle. Subsequently, an inverse pattern of horizontal unloading and loading was applied ($\Delta\sigma'_h$ = +6.5 kPa/-6.0 kPa), while the vertical stress remained constant. It is reported that the sample was allowed to age at the K_0 stress state before the small stress cycles were conducted.

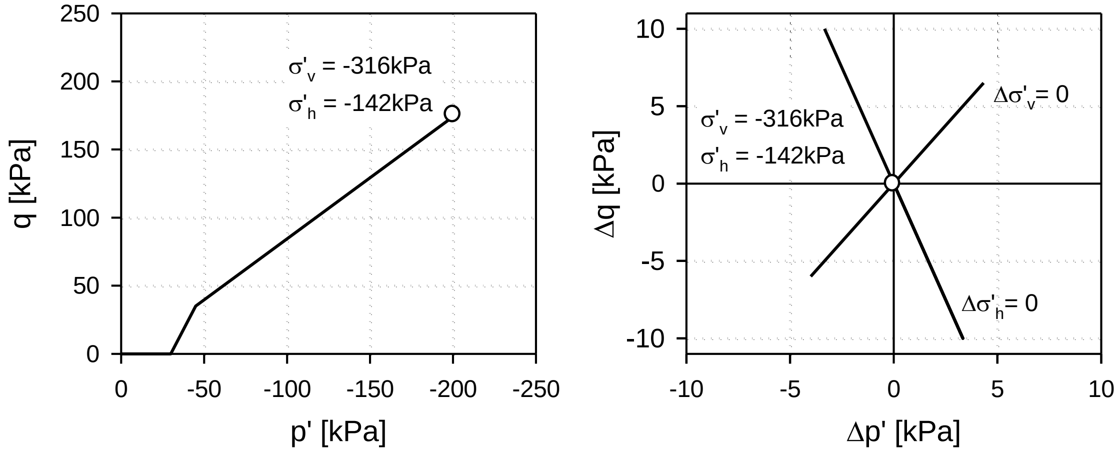

Fig. 39: Stress path and small stress probes in triaxial test on Ham River Sand (after Kuwano & Jardine 2002)

The cross-anisotropic small strain parameters for the back-analysis of the tests are taken from the data published by Kuwano & Jardine (2002) and are summarized in Table 12. In the simulation, stress-dependency of stiffness moduli is related to the corresponding initial axial stresses (approach 3). As the small stress cycles take place almost entirely within the linear elastic range, shear strength and parameters governing plastic deformations are of minor relevance for the calculation results.

The experimental and calculated response for the vertical loading / unloading is shown in Figure 40. The experimental stress-strain curve shows a much shorter linear elastic range and more significant hysteresis in vertical loading than in unloading, as vertical loading involves plastic straining. Such behaviour is in principle well captured, even though the model cannot account for the creep effects which considerably enlarged the hysteresis loop in the experiments. The initial inclination of the stress-strain curves matches very well, indicating that the initial cross-anisotropic stiffness of the material is well captured.

In the horizontal unloading / reloading test very little hysteresis was noticed in neither the horizontal unloading (deviatoric loading) nor the horizontal loading (deviatoric unloading) cycle (Figure 41). The model predicts some slight hysteresis, caused by plastic strains in horizontal unloading, but overall predicted and experimental stress-strain curves match very well.

It should be noted, that the experimental results showed evidence of kinematic yielding in unloading (Kuwano & Jardine 2002). Small stress probes performed at σ'_h = -127 kPa, σ'_v = -243 kPa (after unloading from σ'_h = -142 kPa, σ'_v = -316 kPa and subsequent aging) delivered plastic strains in further vertical unloading by 6 kPa, whereas strains in vertical reloading by 7 kPa were fully recoverable. Hence, plastic straining was observed even though both axial stresses and p' and q' were below those previously experienced. Such effects cannot be reproduced by the current strain hardening multilaminate model, which does not account for plastic strains below the current yield surface.

Tab. 12: Elastic input parameters for Ham River Sand

parameter		**value**	**unit**
initial vertical elastic stiffness	$E'_{v0,ref}$	279 500	kPa
initial horizontal elastic stiffness	$E'_{h0,ref}$	238 400	kPa
initial cross-anisotropic elastic shear modulus	$G_{vh0,ref}$	98 640	kPa
initial anisotropic Poisson's ratio	ν'_{vh0}	0.35	--
initial anisotropic Poisson's ratio within horizontal plane	ν'_{hh0}	0.07	--
threshold strain level for stiffness degradation	$\varepsilon_{deg,1}$	8e-6	--
transition to large strains	$\varepsilon_{deg,2}$	2e-4	--
reference pressure	p_{ref}	100	kPa
power index for stress dependency	m	0.50	--

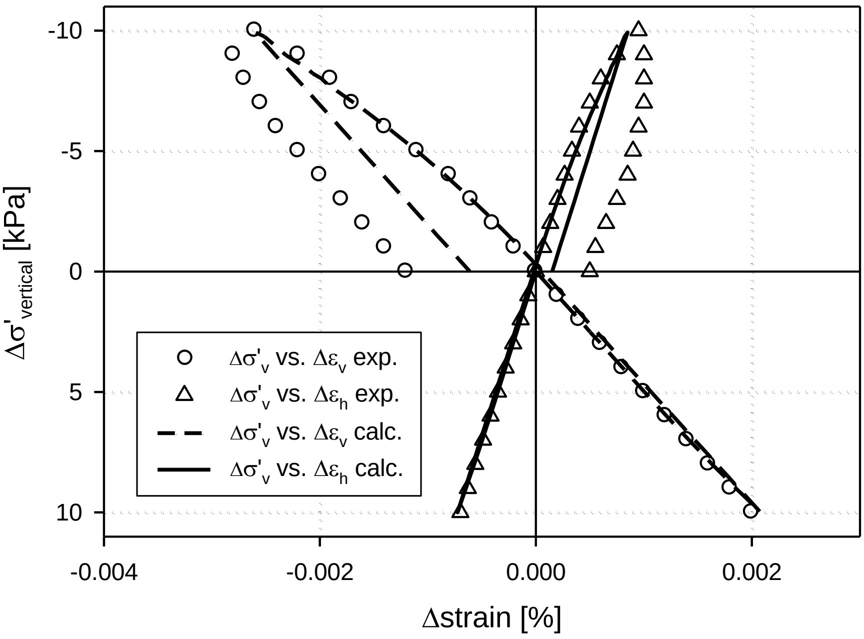

Fig. 40: Stress-strain curves in small vertical loading cycle ($\Delta\sigma'_h = 0$) on Ham River Sand (after Kuwano & Jardine 2002) and simulation with the multilaminate model

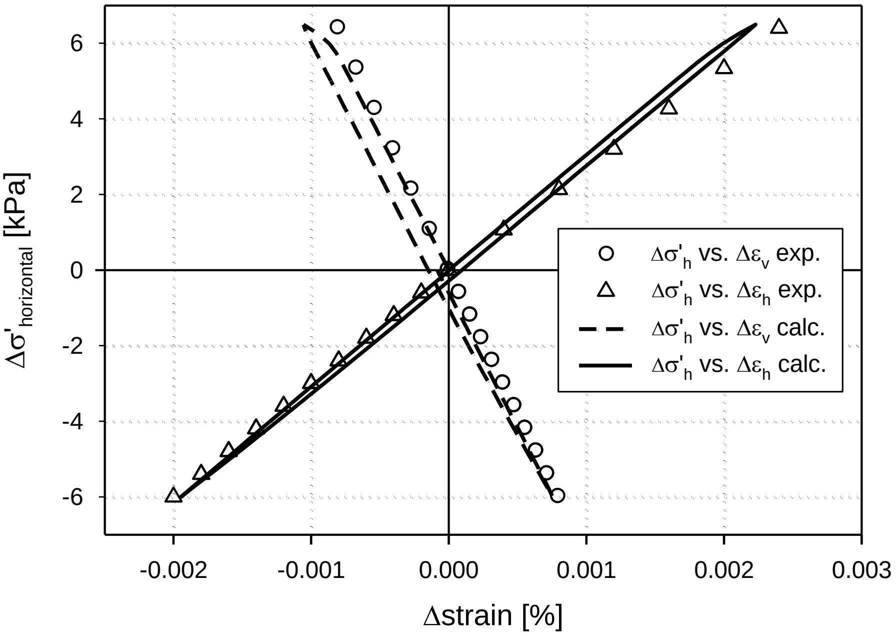

Fig. 41: Stress-strain curves in small horizontal loading cycle ($\Delta\sigma'_v = 0$) on Ham River Sand (after Kuwano & Jardine 2002) and simulation with the multilaminate model

4.5.5 Large stress reversals

Jiang et al. (1997) conducted triaxial tests on crushed sandstone gravel (Chiba Gravel) involving large stress path reversals. The elastic small strain properties of the material are reported as cross anisotropic with $E'_v/E'_h \sim 2$ at isotropic stresses with a power index of $m = 0.5$ for the stress dependency. Starting at different levels of isotropic stress, large triaxial loading / unloading / reloading loops were performed, with smaller sub-loops at intermediate load levels. Part of such a cycle (comprising primary loading, unloading and reloading) is shown in Figure 42.

The experimental results validate the 4th Masing rule as all the sub-loops converge with the stress-strain curve previously followed as soon as the previous load level is reached. It is reported that the stiffness within these sub-loops decreased as the stress state approached failure.

The model parameters used in the simulation are summarized in Table 13. Elastic small strain stiffness parameters have been taken from the data published by Jiang et al. (1997). Model specific parameters (A_{mat}, $\varepsilon_{deg,1}$, $\varepsilon_{deg,2}$) have been calibrated against the first part of the experimental stress strain curve (O-A). Stress dependency of small strain stiffness is modelled with approach 3 (dependency on initial axial stresses), which is however of limited relevance for the simulation of large stress reversals.

Figure 42 shows the stress-strain curves predicted by the multilaminate model in comparison to the experimental results. Experiment and model prediction match very well in the primary loading path O-A, as this part of the curve has been used to calibrate the deviatoric hardening parameter, A_{mat}, and the degradation parameters $\varepsilon_{deg,1}$ and $\varepsilon_{deg,2}$. Along the unloading path A-B the model initially predicts a slightly stiffer response, indicating the occurrence of plastic strains in the experiment also in the perceived elastic region below the yield surface. As extension failure is approached, model prediction and experiment again match very well.

However, stress strain curves diverge significantly for the reloading path B-C, as the constitutive model does not account for plastic strains in reloading. Since the 4th Masing rule is enforced for the elastic part of the model, the higher initial stiffness gets reactivated within the small sub-loops along the reloading path, and the corresponding stress-strain loops converge with the large strain reloading curve. Model predictions in reloading could be improved by taking account of kinematic hardening, yet this is beyond the scope of the present study.

Tab. 13: Input parameters for Chiba Gravel

parameter		**value**	**unit**
initial vertical elastic stiffness	$E'_{v0,ref}$	383 000	kPa
initial horizontal elastic stiffness	$E'_{h0,ref}$	191 000	kPa
initial cross-anisotropic elastic shear modulus	$G_{vh0,ref}$	100 000	kPa
initial anisotropic Poisson's ratio	ν'_{vh0}	0.24	--
initial anisotropic Poisson's ratio	ν'_{hh0}	0.24	--
threshold strain level for stiffness degradation	$\varepsilon_{deg,1}$	5×10^{-6}	--
transition to large strains	$\varepsilon_{deg,2}$	8×10^{-4}	--
reference pressure	p_{ref}	100	kPa
power index for stress dependency	m	0.50	--
isotropic large strain Young's modulus	$E_{ur,ref}$	90 000	kPa
isotropic large strain Poisson's ratio	ν'_{ur}	0.2	--
Oedometric stiffness	$E_{oed,ref}$	30 000	kPa
shear hardening parameter	A_{mat}	0.041	--
effective friction angle	φ'_{max}	43	°
effective cohesion	c'	0	kPa
dilatancy angle	ψ	10	°

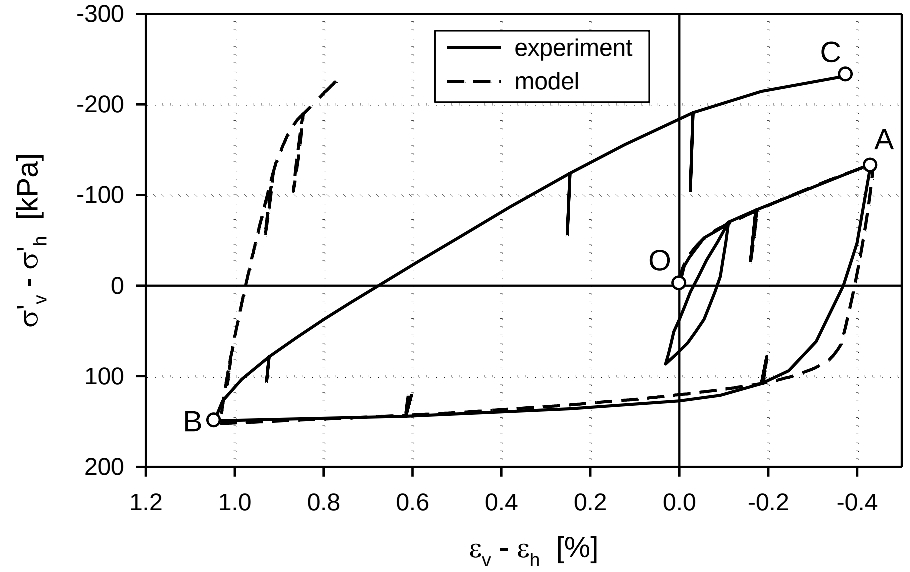

Fig. 42: Stress-strain behaviour of Chiba Gravel (after Jiang et al. 1997)

4.5.6 Stiffness recovery at load reversals

The dependency of stiffness on change of the macroscopic loading direction is an outcome of the model rather than an input. This can be considered as a major advantage compared to models where a function has to be defined relating the change of the strain or stress path to the magnitude of recovered small strain stiffness. At local level the full initial stiffness is recovered, as soon as the local strain path turns inside the active strain contour, but apart from full load reversal this does not occur at all planes simultaneously. Consequently, the macroscopic elastic stiffness takes intermediate values between small strain and large strain stiffness, as it is obtained by the sum of the weighted contributions from all planes.

The model response is demonstrated in biaxial test simulations with varying strain path direction (Figure 43). The material is taken as isotropic elastic with G_0 = 100 Mpa, G_{ur} = 20 MPa and $\nu_0 = \nu'_{ur} = 0.2$. Starting from an initial stress state of $\sigma'_{xx} = \sigma'_{yy} = -100$ kPa and $\sigma'_{zz} = -40$ kPa, compressive strains ε_{xx} and ε_{yy} are increased simultaneously. The resulting deviatoric strain causes gradual degradation of initial small strain stiffness, until at about $\varepsilon_{xx} = \varepsilon_{yy} = -0.15\%$ the large strain range is reached. At varying intermediate strain levels the response of the material to changes in loading direction is tested by applying small strain increments of prescribed orientation α with regard to the monotonic loading path (Figure 43).

As deviatoric strains evolve at different pace on different planes, the initially isotropic material becomes anisotropic during biaxial loading. In order to quantify the increase of shear stiffness with deviation from the monotonic strain path, the equivalent tangent shear modulus G_{tan} has been derived from the increments of the second deviatoric stress and strain invariants J and E_d.

$$G_{tan} = \Delta J \,/\, \Delta E_d \tag{116}$$

$$J = \frac{1}{\sqrt{6}}\sqrt{(\sigma'_1 - \sigma'_2)^2 + (\sigma'_1 - \sigma'_3)^2 + (\sigma'_2 - \sigma'_3)^2} \tag{117}$$

$$E_d = \frac{2}{\sqrt{6}}\sqrt{(\varepsilon_1 - \varepsilon_2)^2 + (\varepsilon_1 - \varepsilon_3)^2 + (\varepsilon_2 - \varepsilon_3)^2} \tag{118}$$

The ratio of G_{tan}/G_{ur} against orientation is plotted for varying strain levels in Figure 44. Continuing on the monotonic strain path does not result in any recovery of stiffness, consequently $G_{tan}/G_{ur} = 1$ for large strain levels. Strain path deviation of 90° delivers an increase of stiffness to G_{tan}/G_{ur} ~ 2.2, and for deviation beyond $\alpha = 135°$ virtually the full initial stiffness is recovered.

Also shown in Figure 44 is the variation of interpolated stiffness $M = G_{tan}/G_{ur}$ of a hypoplastic constitutive model incorporating intergranular strain (Niemunis & Herle 1997, as reported by Benz et al. 2009). The shape of the envelope is defined by the parameters m_t (M at $\alpha = 90°$) and m_r (M at $\alpha = 180°$), which have been taken as $m_t = 2$ and $m_r = 5$. For angular change up to 90° the multilaminate and the hypoplastic model differ only marginally, as $m_t = 2$ enforces $G_{tan}/G_{ur} = 2$ at $\alpha = 90°$. Beyond $\alpha = 90°$ the hypoplastic model predicts a slower convergence towards the full initial stiffness, and only close to $\alpha = 180°$ the full initial stiffness is recovered with the hypoplastic model.

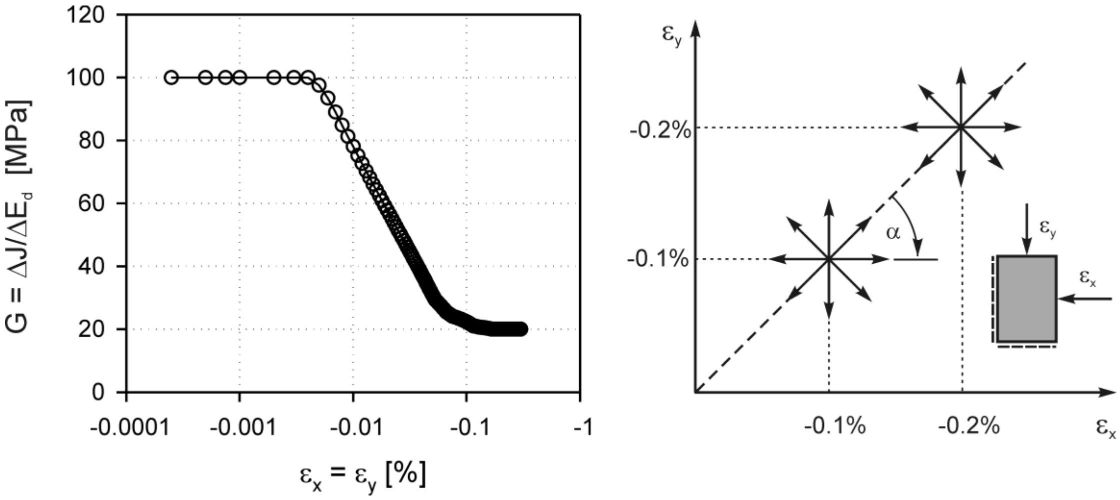

Fig. 43: Macroscopic stiffness degradation as obtained by the multilaminate model and strain paths applied in the biaxial test simulation

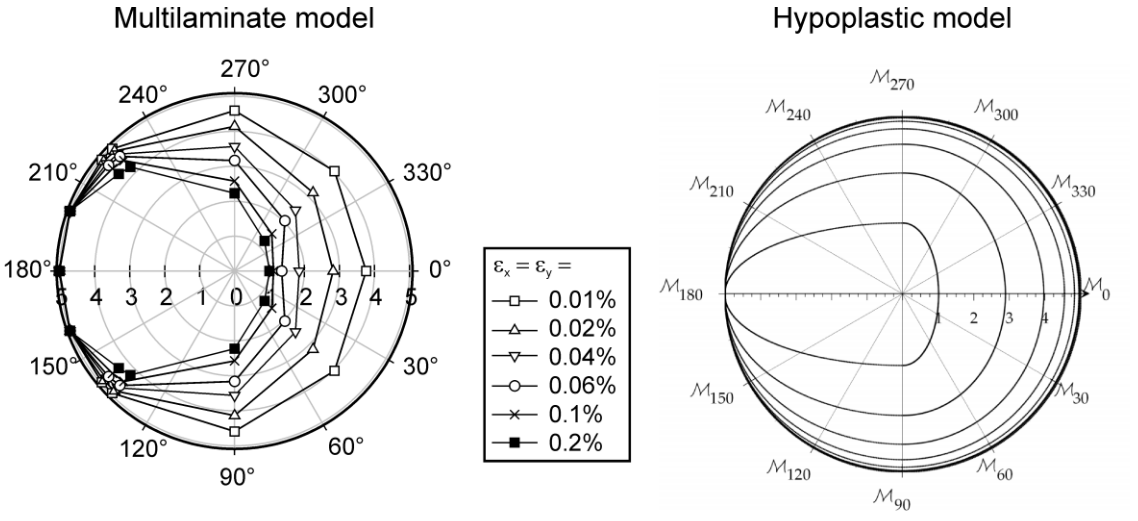

Fig. 44: G_{tan}/G_{ur} over angular change of the macroscopic strain path: Multilaminate model (left) and hypoplastic model with intergranular strain (Niemunis & Herle 1997, as reported by Benz et al. 2009)

5 Influence of small strain stiffness anisotropy in geotechnical problems

The impact of cross anisotropic elasticity in the small strain range on ground deformations is difficult to evaluate in practice. Measured deformations in general comprise elastic and plastic strains of varying mutual proportion, and distinction between the two is usually not possible. In the following chapter the impact of different isotropic and cross-anisotropic small strain stiffness parameters in numerical simulations is assessed for an excavation problem and the settlements of a shallow strip footing. The calculations have been performed with the finite element package PLAXIS 2D 2010 and the multilaminate soil model presented in previous chapters.

5.1 Excavation problem

5.1.1 Numerical model and input parameters

The geometric layout of the example follows from Figure 45. Homogeneous, drained ground conditions are assumed and a hydraulic barrier is placed at the base of the wall. The excavation process is modelled by three steps with 2 m of excavation each. After the first excavation step the groundwater table within the excavation is lowered to -6.0 m with linear interpolation of water pressures over the hydraulic barrier.

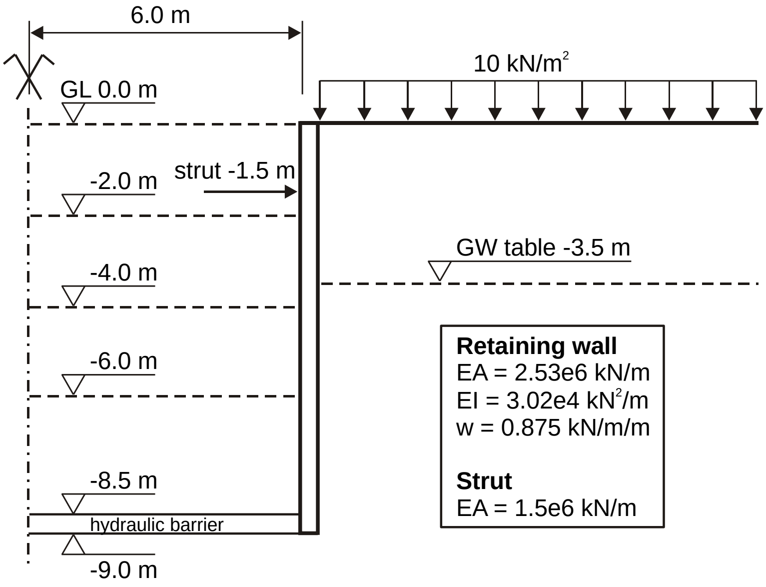

Fig. 45: Geometry overview

Interface elements are placed at both sides of the retaining wall to account for the reduced friction between wall and soil, which has been taken as 2/3 of the friction angle of the soil. The model has been discretized with 15-noded, triangular elements. Large strain soil parameters and isotropic small strain parameters have been calibrated to fit experimental data of dense Hostun sand (Table 7).

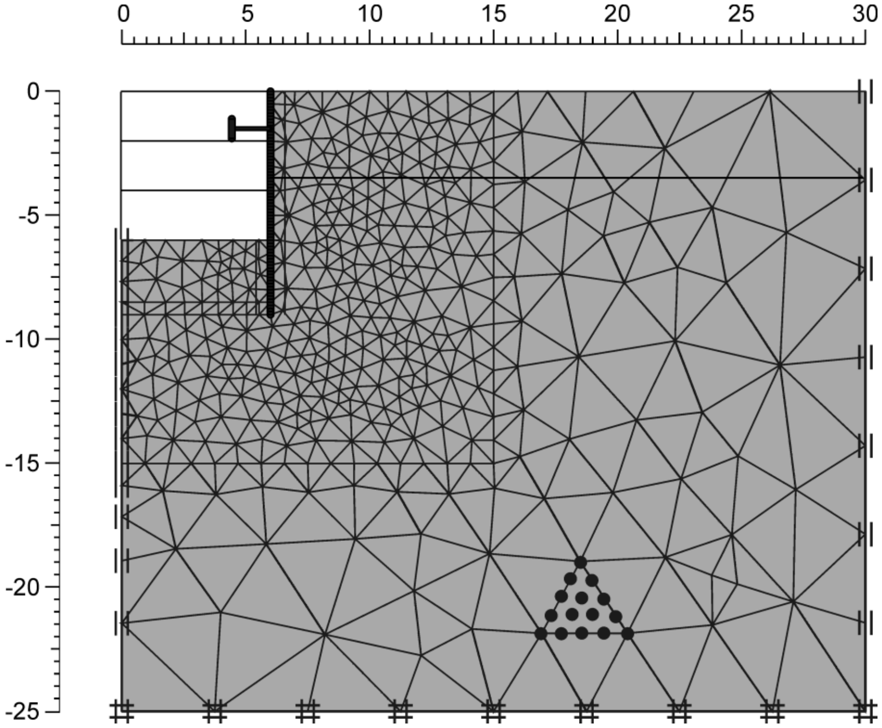

Fig. 46: Finite element model (dimensions in m)

For demonstration purposes a much wider range of cross-anisotropy in small strain stiffness has been assumed in this study (Table 14) than observed in experiments on Hostun sand (Sadek et al. 2007). The same value of E'_{v0} is utilized for all the anisotropic calculations, but the ratio E'_{v0}/E'_{h0} changes from 2.0 (case 1) to 0.5 (case 2). In an additional calculation the independent shear modulus was lowered to 2/3 of the isotropic value (case 3). Stiffness degradation parameters $\varepsilon_{deg,1} = 2 \cdot 10^{-5}$ and $\varepsilon_{deg,2} = 6 \cdot 10^{-4}$ are utilized in all calculations.

Even though material behaviour is strongly cross anisotropic, in none of the cases the stiffness anisotropy would be detected in a conventional triaxial compression test ($\Delta\sigma'_h = 0$). If the horizontal stress is constant, initial shear stiffness $G_{eq,0}$ exclusively depends on the axial elastic modulus in vertical direction E'_{v0} and the Poisson's ratio ν'_{vh0} (Equation 119, Figure 47 left). However, if the vertical stress σ'_v is held constant and the horizontal stress σ'_h is increased, $G_{eq,0}$ depends on the axial moduli E'_{v0}, E'_{h0} and the Poisson's ratio ν'_{vh0} and ν'_{hh0} (Equation 120). Hence, significantly different values of $G_{eq,0}$ are obtained for the different parameter sets in horizontal loading (Figure 47 right).

$$G_{eq,0} = \frac{\Delta\sigma'_v}{\Delta\varepsilon_v - \Delta\varepsilon_h} = \frac{E'_{v0}}{2\cdot\left(1+\nu'_{vh0}\right)} \quad \text{for } \Delta\sigma'_h = 0 \tag{119}$$

$$G_{eq,0} = \frac{-\Delta\sigma'_h}{\Delta\varepsilon_v - \Delta\varepsilon_h} = \frac{E'_{v0}\cdot E'_{h0}}{\nu'_{vh0}\cdot E'_{h0} + \left(1-\nu'_{hh0}\right)\cdot E'_{v0}} \quad \text{for } \Delta\sigma'_v = 0 \tag{120}$$

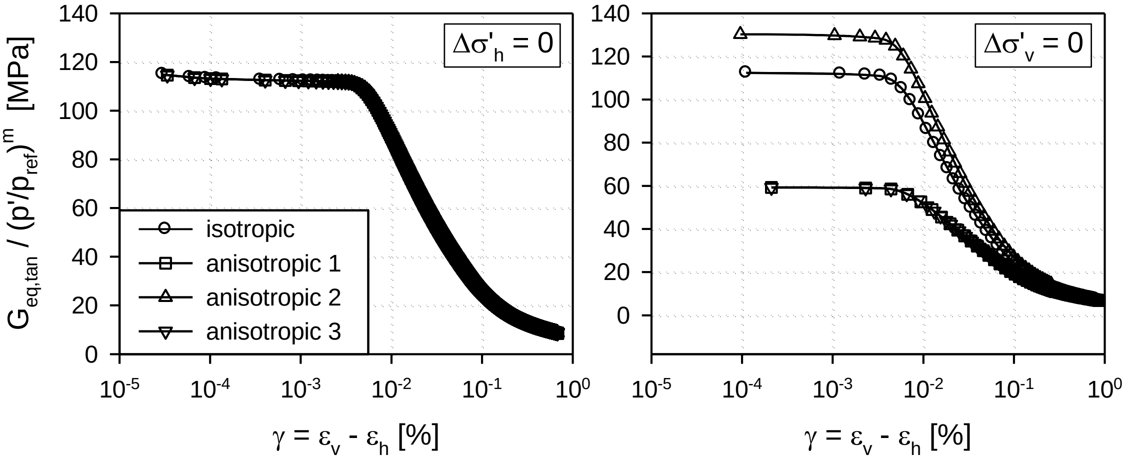

Fig. 47: Equivalent shear stiffness G_{eq} in triaxial vertical and horizontal loading

It should be noted that the small strain stiffness parameters listed in Table 14 represent initial soil stiffness at isotropic stresses, while the stiffness utilized in the anisotropic simulations is influenced by the initial axial stress ratio (approach 3). The resultant values activated at the initial stress state with $K_{0nc} = 1 - \sin\varphi' = 0.34$ are listed in Table 15. The anisotropy ratios at the start of the calculations are $E'_{v0}/E'_{h0} = 3.6$ for cases 1 and 3 and $E'_{v0}/E'_{h0} = 0.9$ for case 2, thus resulting in almost isotropic stiffness for case 2. The independent shear modulus G_{vh0} is considerably less influenced by the cross anisotropic stress state than the axial elastic moduli.

Tab. 14: Small strain parameters – input values at p'= -100 kPa

parameter	**unit**	**isotropic**	**anisotropic 1**	**anisotropic 2**	**anisotropic 3**
$E'_{v0,ref}$	kPa	270 000	303 800	303 800	303 800
$E'_{h0,ref}$	kPa	270 000	151 900	607 600	151 900
$G_{vh0,ref}$	kPa	112 500	112 500	112 500	75 000
ν'_{vh0}	--	0.20	0.35	0.35	0.35
ν'_{hh0}	--	0.20	0.07	0.07	0.07

Tab. 15: Initial small strain stiffness moduli at $K_0 = 0.34$ and $p' = -100$ kPa

parameter	**unit**	**isotropic**	**anisotropic 1**	**anisotropic 2**	**anisotropic 3**
E'_{v0}	kPa	270 000	416 837	416 837	416 837
E'_{h0}	kPa	270 000	115 878	463 514	115 878
G_{vh0}	kPa	112 500	115 097	115 097	76 731

5.1.2 Calculation phases

After the definition of the normally consolidated initial stress state with $\sigma'_v = \gamma \cdot h$ and $\sigma'_h = K_0 \cdot \sigma'_v$ ($K_0 = 1 - \sin\varphi'$), the following calculation phases are performed:

Phase 1:	Apply surcharge load (permanent load of 10 kPa)
Phase 2:	Activate wall (wished-in-place), set displacements to zero
Phase 3:	Excavation to level -2.0 m
Phase 4:	Activate strut at level -1.5 m
Phase 5:	Lowering of GW-table to -6.0 m inside excavation
Phase 6:	Excavation to level -4.0 m
Phase 7:	Excavation to level -6.0 m

5.1.3 Results

Wall deflection at the end of excavation (phase 7) for the various parameter sets is shown in Figure 48. Taking account of isotropic small strain stiffness reduces wall deformation by ~30%, whereas with anisotropic parameter sets 1 and 3 wall deflection increased by ~19% with regard to the isotropic small strain stiffness case. A similar trend can be observed for the wall bending moments.

This matches well with the lower initial shear stiffness $G_{eq,0}$ obtained for the anisotropic sets 1 and 3 in horizontal triaxial loading (Figure 47), which is comparable to the horizontal unloading situation behind the sheet pile wall and the horizontal loading at the wall base. However, the difference in wall deformation is much smaller than what would be expected by the difference of ~50% in elastic initial shear stiffness $G_{eq,0}$. This indicates the presence of plastic strains, which dominate soil deformation at larger strains and diminish the influence of small strain stiffness on final wall deformation. Hence, the impact of cross anisotropy in small strain stiffness depends on the strain level, and increases as the strain level reduces.

A similar trend can be observed for the vertical deformations at ground surface (Figure 49). The settlement at the model boundary at x = 24 m for the case without small strain stiffness indicates, that the model needs to be much wider in this case, but not for the calculations with small strain stiffness. Taking isotropic small strain stiffness into account reduces surface settlements by ~45%, and the isotropic case and the anisotropic set 2 with high stiffness in horizontal direction again deliver very similar results. Settlements increase by ~20% with the anisotropic sets 1 and 3 compared to the isotropic small strain case.

The heave at the bottom of the excavation at -6 m can be related to the axial stiffness in vertical direction employed in the various calculations (Figure 50). Taking account of isotropic small strain stiffness reduces ground deformations from 25 mm to 13 mm, with a further reduction to 9-10 mm for the anisotropic cases. This trend can be explained by the comparatively small value of E'_{v0} = 270 MPa used in the isotropic small strain case, while all the anisotropic cases utilize the same value of E'_{v0} = 417 MPa and therefore deliver fairly similar displacements. The small differences among the anisotropic calculations can be explained by the different values of E'_{h0} and G_{vh0}, but are not significant from a practical point of view. Again, the difference in displacements is notably smaller than the difference in stiffness.

In summary, ground deformations correlate to the stiffness activated in the corresponding loading direction. While there is no significant difference between the isotropic case and the anisotropic case 2 in terms of wall displacements and surface settlements, base heave in the excavation differs by ~20% due to the difference in vertical initial stiffness. On the other hand, all the anisotropic cases deliver similar displacements at the base of the excavation, but wall deflection and surface settlements differ by up to 19% as a result of the varying stiffness in horizontal loading. However, the range of numerical results is much smaller than the variation of small strain stiffness parameters, and the influence of anisotropy in the small strain range reduces with increasing strain level.

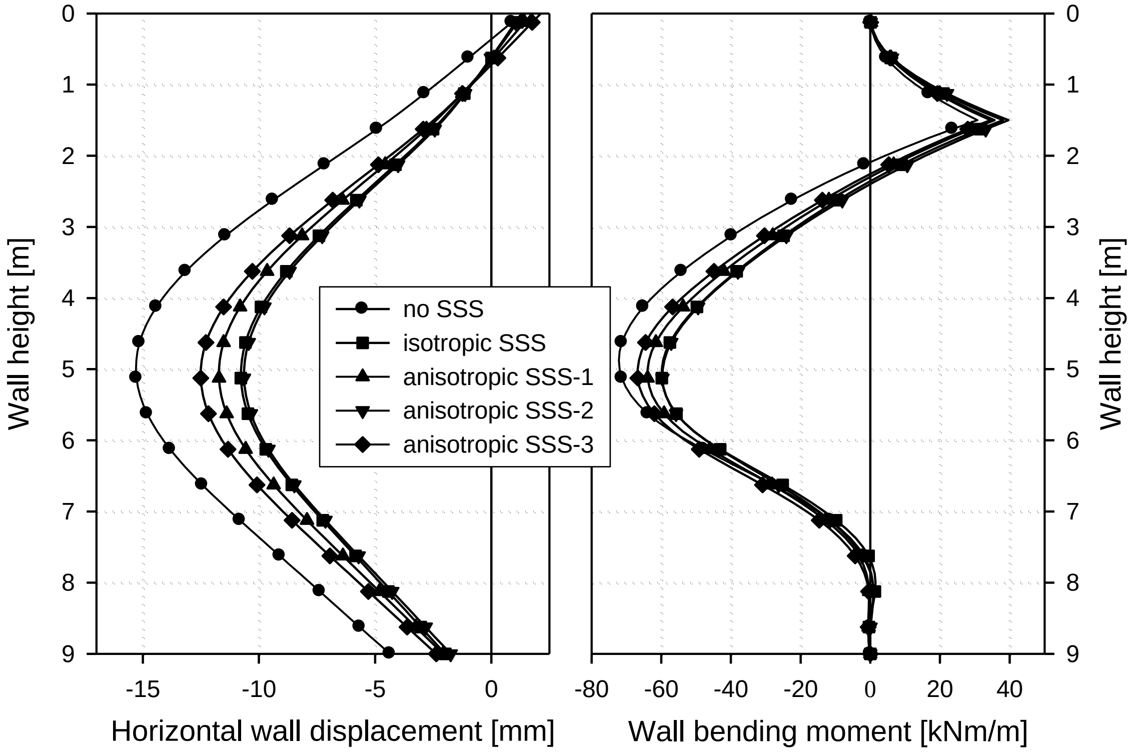

Fig. 48: Horizontal wall displacements and distribution of bending moments

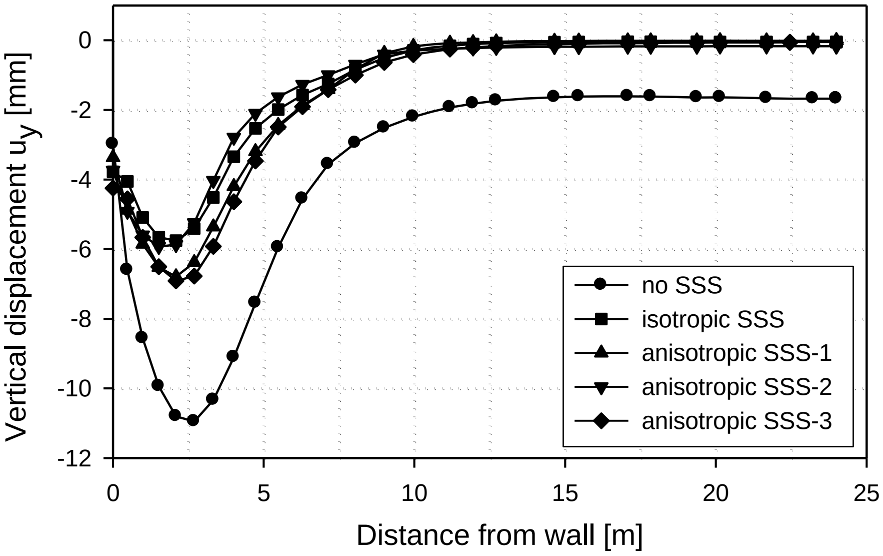

Fig. 49: Vertical displacements of the surface next to the retaining wall

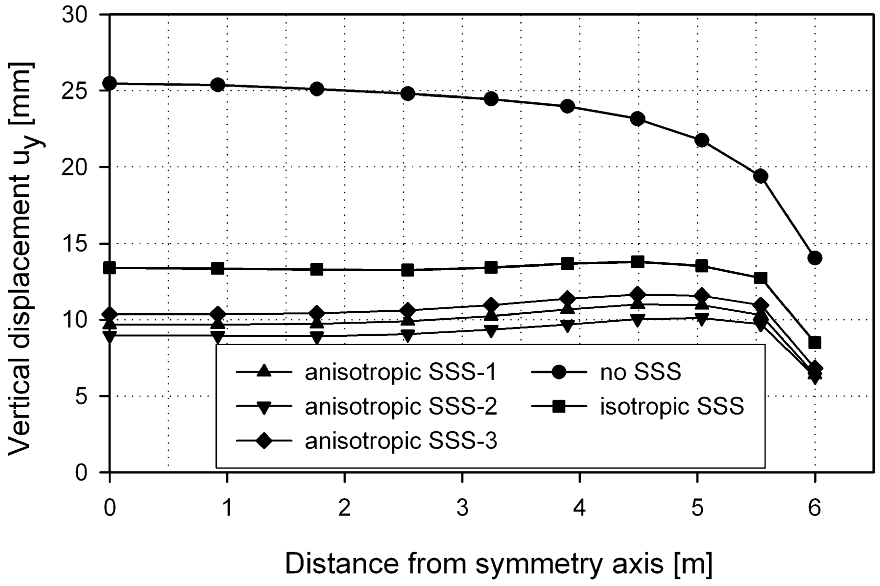

Fig. 50: Vertical displacements at excavation base

5.2 Strip footing

5.2.1 Numerical model and input parameters

A 4 m wide shallow strip footing on dense Hostun sand is subjected to incremental increase of vertical loading up to 300 kPa, and development of vertical displacement is compared for different isotropic and cross-anisotropic sets of soil parameters. The concrete slab of 1 m thickness can be considered as rigid (E = 30 GPa, $\nu = 0.2$). The finite element model used for all calculations in this chapter is shown in Figure 51. A surface load of 10 kPa is applied at ground surface before increasing the load on the footing. Due to symmetry only half of the full system is modelled.

Large strain soil parameters have been calibrated to fit experimental data of dense Hostun sand (chapter 4.5.1, Table 7). Additional to the cross-anisotropic parameter combinations employed in the previous excavation example, further combinations have been chosen such that either one of the axial moduli equals the isotropic small strain stiffness at the in situ stress state, or that the mean of E'_{h0} and E'_{v0} equals the isotropic value (Table 16). Stiffness degradation parameters $\varepsilon_{deg,1} = 2 \cdot 10^{-5}$ and $\varepsilon_{deg,2} = 6 \cdot 10^{-4}$ are utilized in all calculations, and anisotropy ratios E'_{h0}/E'_{v0} of 0.5 and 2.0 are assumed.

Stiffness recovery at load reversals has been deactivated in this example, as the footing load is monotonically increased. In all cross-anisotropic calculations Poisson’s ratios have been taken as $\nu'_{vh0} = 0.35$ and $\nu'_{hh0} = 0.07$. Set ‘anisotropic 10’ equals the isotropic case except for the cross-anisotropic Poisson’s ratios.

Calculations have also been performed with the (isotropic) Hardening Soil and Hardening Soil Small model, employing the same set of material parameters as in the element test simulations (Table 8).

Tab. 16: Cross-anisotropic small strain stiffness parameters at isotropic stresses and at $K_0 = 0.34$

parameter set	$K' = \sigma'_h/\sigma'_v$	$E'_{h0,ref}$ **[MPa]**	$E'_{v0,ref}$ **[MPa]**	**In situ** E'_{h0}/E'_{v0}	$G_{vh0,ref}$ **[MPa]**
anisotropic 1	1.0	151.9	303.8		112.5
	0.34	115.9	416.8	0.28	115.1
anisotropic 2	1.0	607.6	303.8		112.5
	0.34	463.5	416.8	1.11	115.1
anisotropic 3	1.0	151.9	303.8		75
	0.34	115.9	416.8	0.28	76.7
anisotropic 4	1.0	353.9	98.4		112.5
	0.34	270	135	2.0	115.1
anisotropic 5	1.0	177	196.8		112.5
	0.34	135	270	0.5	115.1
anisotropic 6	1.0	353.9	393.6		112.5
	0.34	270	540	0.5	115.1
anisotropic 7	1.0	707.9	196.8		112.5
	0.34	540	270	2.0	115.1
anisotropic 8	1.0	265.45	295.2		112.5
	0.34	202.5	405	0.5	115.1
anisotropic 9	1.0	424.7	118.1		112.5
	0.34	324	162	2.0	115.1
anisotropic 10	1.0	353.9	196.8		112.5
	0.34	270	270	1.0	115.1

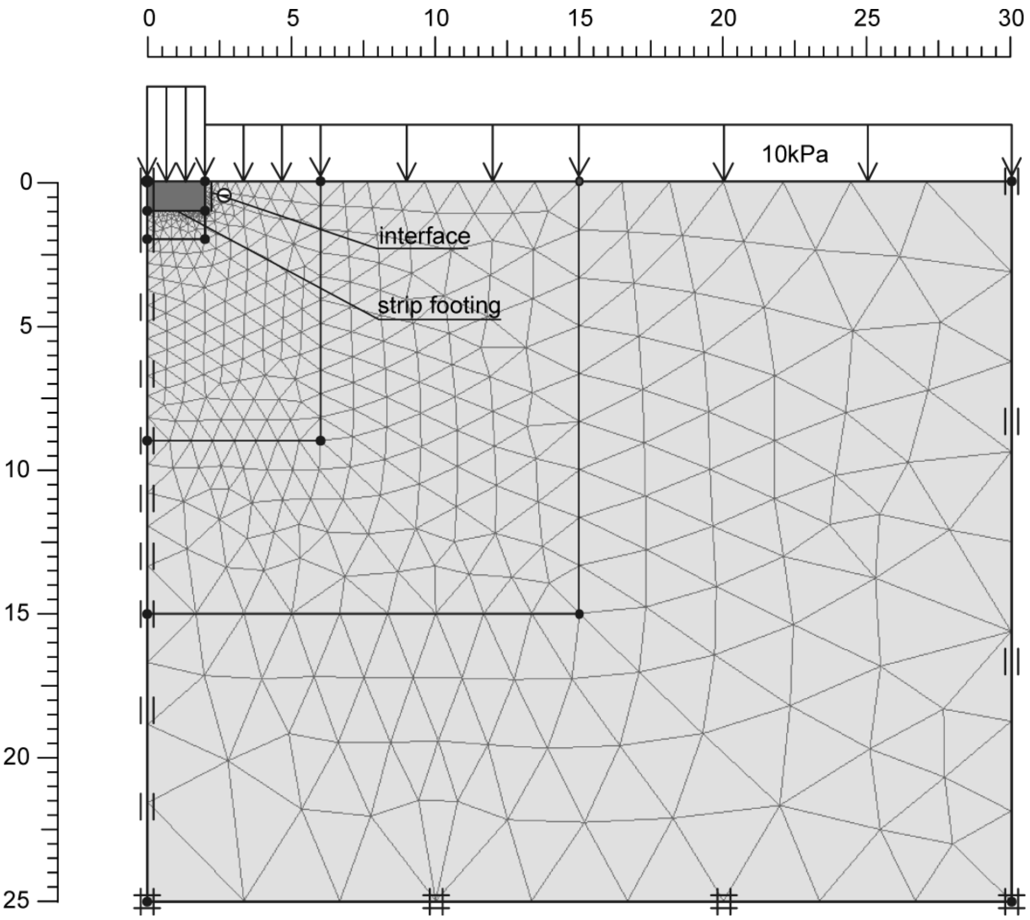

Fig. 51: Numerical model of strip footing (dimensions in m)

5.2.2 Calculation phases

After the definition of the normally consolidated initial stress state with $\sigma'_v = \gamma \cdot h$ and $\sigma'_h = K_0 \cdot \sigma'_v$ ($K_0 = 1 - \sin\varphi'$), the following calculation phases are performed:

Phase 1:	Application of surcharge load of 10 kPa
Phase 2:	Activation of foundation slab, reset displacements to zero
Phase 3:	Increase of additional load at top of footing

5.2.3 Results

Calculated load-displacement curves delivered by the multilaminate model with and without isotropic small strain stiffness are compared with the Hardening Soil (HS) and Hardening Soil Small model (HSS) in Figure 52. HSS_{ref} denotes the calculation using the input parameters of Table 8 ($G_{0,ref}$ = 112.5 MPa). It should be noted that while G_0 depends on p' in the multilaminate model, dependency of

G_0 on σ'_3 is assumed in the HSS model. In order to start with the same small strain stiffness at the initial stress state in both models, in calculation HSS* $G_{0,ref}$ has been increased by the factor $((1+2K'_{0nc})/(3K'_{0nc}))^{0.55}$.

Both models deliver similar load-displacement curves and final settlements at 300 kPa footing load. The slightly softer response of the HSS* calculation can be related to the ~10% lower initial shear modulus in primary loading (Figure 35). Neglecting small strain stiffness results in an almost linear load-displacement curve, with a slightly stiffer behaviour at higher load levels due to stress dependent stiffness. Taking account of isotropic small strain stiffness reduces final settlements to ~53% of the value without small strain stiffness, which demonstrates the importance of small strain stiffness for settlement calculations in working load conditions.

The curvature of the load-displacement curves shows clear evidence of stiffness degradation, as the initial inclination of the curve changes with increasing load level. However, not all the soil body contributing to raft settlements has reached the large strain range yet, as the load displacement curves ‘ML iso G0’ and ‘HSS’ continue to diverge from the curve without small strain stiffness at the final load level.

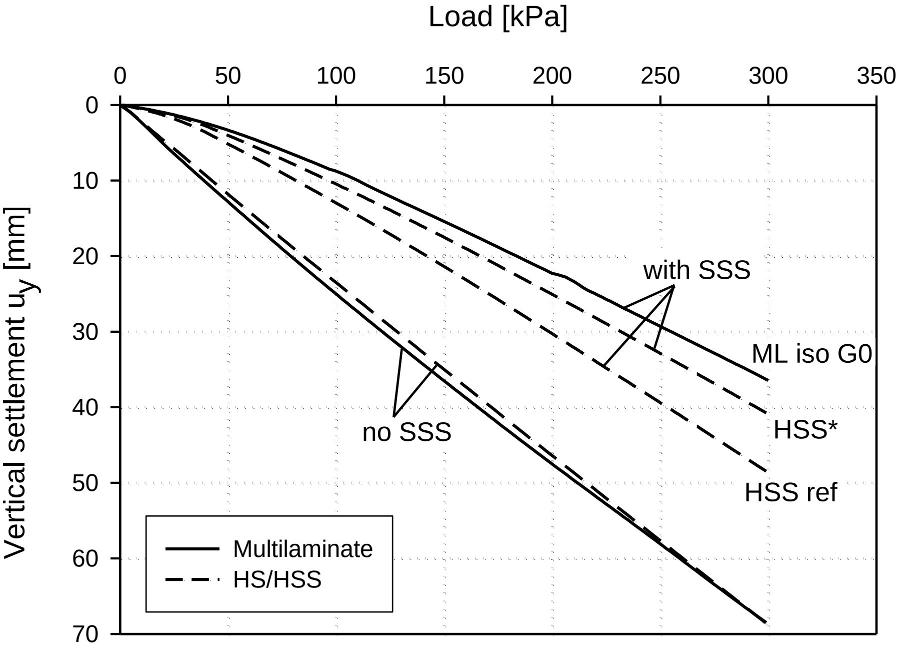

Fig. 52: Comparison of load – displacement curves predicted by multilaminate and HS / HSS model for isotropic material

Deformations below the footing reduce significantly faster with depth, if small strain stiffness is taken into account (Figure 53). Vertical displacements at 10 m depth (9 m below footing) are ~25% of the maximum footing settlements if calculated without small strain stiffness, but reduce to less than 10% if small strain stiffness is accounted for. Considering anisotropic small strain stiffness does not change that ratio any further.

The calculations with cross-anisotropic small strain stiffness deliver a rather wide range of load displacement curves (Figure 54) and final settlements (Figure 55). Variation of the Poisson's ratios while keeping the isotropic axial moduli constant (anisotropic 10) does not influence predicted settlements significantly. Final settlements decrease by ~17% if one of the axial moduli are kept at the isotropic value and the elastic modulus in the other direction is doubled (anisotropic 6 and 7). The reverse pattern (reducing the axial modulus in one direction by 50%, anisotropic 4 and 5) delivers ~15% larger settlements than the isotropic case. Both calculations 'anisotropic 8' and 'anisotropic 9', which employ the same mean axial stiffness of $E_{mean} = (2E'_{h0} + E'_{v0})/3 = 270$ MPa but opposing ratios of anisotropy, give final settlements close to the isotropic case.

Consequently, the magnitude of final settlements seems to be governed by the average axial stiffness of the material rather than the ratio of anisotropy. This is demonstrated in Figure 56, which plots final settlements against mean axial stiffness E_{mean}. Results of the various cross-anisotropic and isotropic calculations plot within a narrow band, with settlements decreasing as the mean stiffness of the material increases. At higher mean stiffness the cross-anisotropic calculations predict slightly softer behaviour, as the anisotropic shear modulus G_{vh0} was held constant whereas G_0 steadily increases in the isotropic calculations.

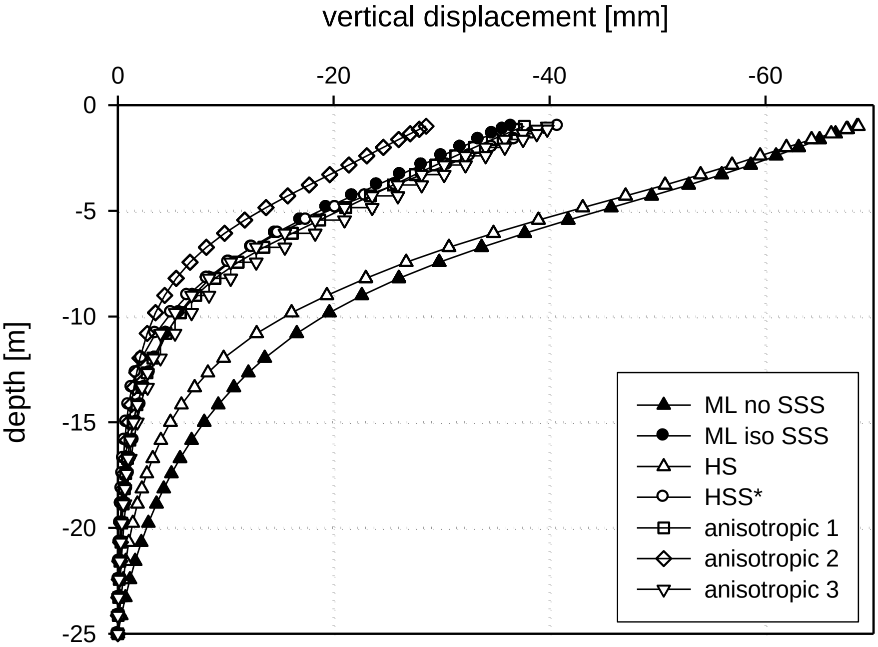

Fig. 53: Profile of vertical displacements below footing over depth

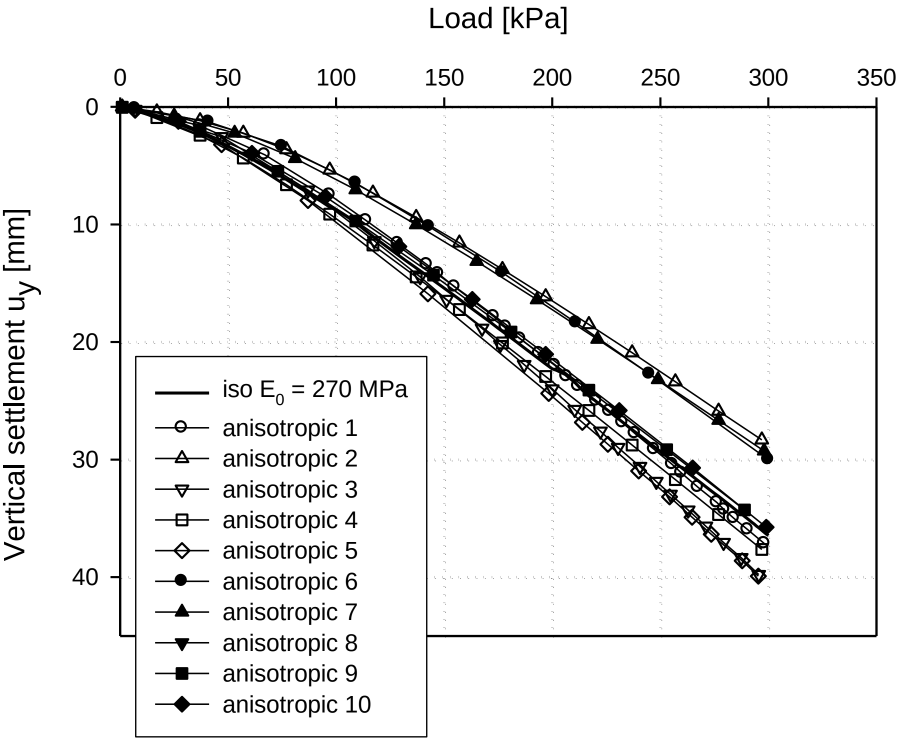

Fig. 54: Load – displacement curves with isotropic and cross-anisotropic small strain stiffness

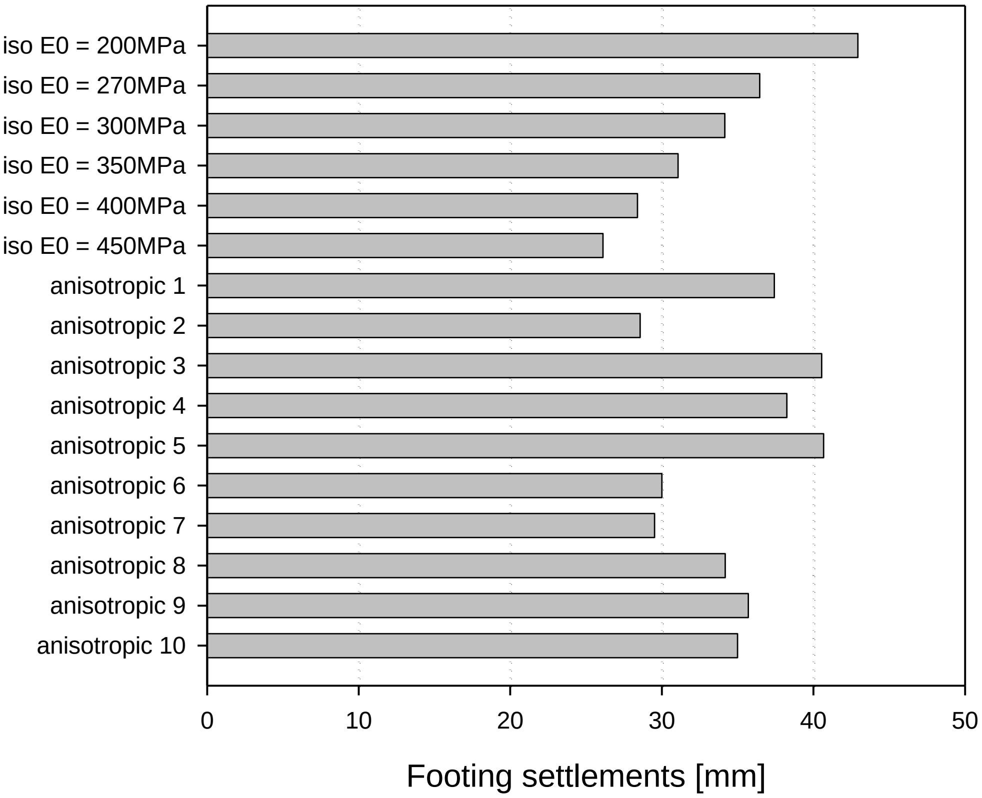

Fig. 55: Footing settlements at a foundation load of 300 kPa

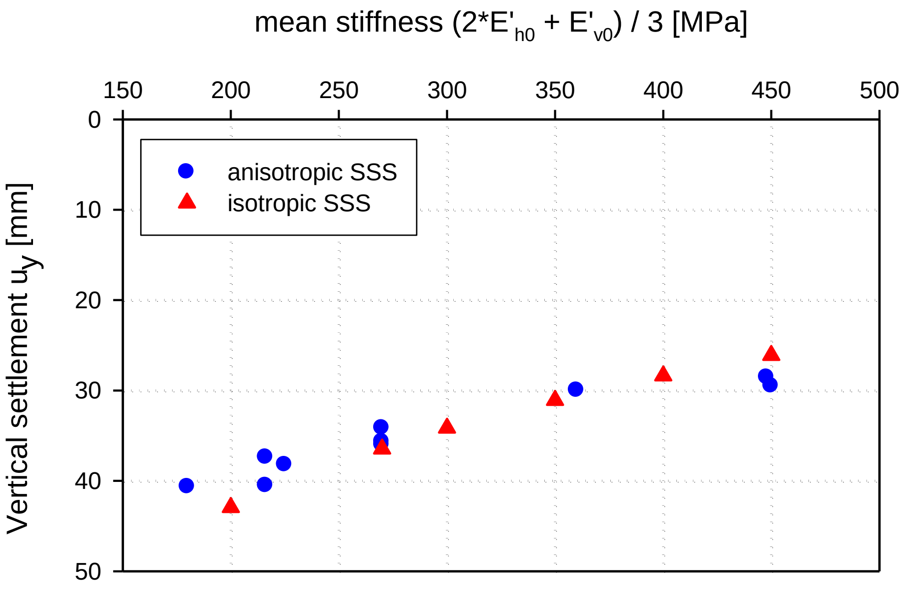

Fig. 56: Dependency of footing settlements obtained in isotropic and anisotropic calculations on mean axial stiffness

As stiffness degradation occurs independently on the various multilaminate planes, a global degradation parameter SSS_{gl} was defined to evaluate macroscopic stiffness degradation. SSS_{gl} is obtained as the weighted sum of local stiffness degradation:

$$SSS_{gl} = 1 - \sum_i \left[w_i \cdot \frac{G_0 - G_i}{G_0 - G_{ur}} \right] \tag{121}$$

SSS_{gl} equals 1 if no degradation has occurred and approaches 0 if the large strain range is reached on all integration planes. For the HSS model, global stiffness degradation has been worked out in an equivalent way by using the state variable G_s, which is the current shear modulus at reference pressure. Degradation of small strain stiffness within the finite element model is compared for selected parameter sets in Figure 57. Due to the higher initial stiffness, deviatoric strains were smallest for set ‘anisotropic 2’, and consequently a larger part of the soil body remained at the high initial stiffness. Compared with the isotropic calculation, set ‘anisotropic 1’ with its low horizontal stiffness delivered similar horizontal spread of stiffness degradation, while less stiffness degradation occurred in vertical direction.

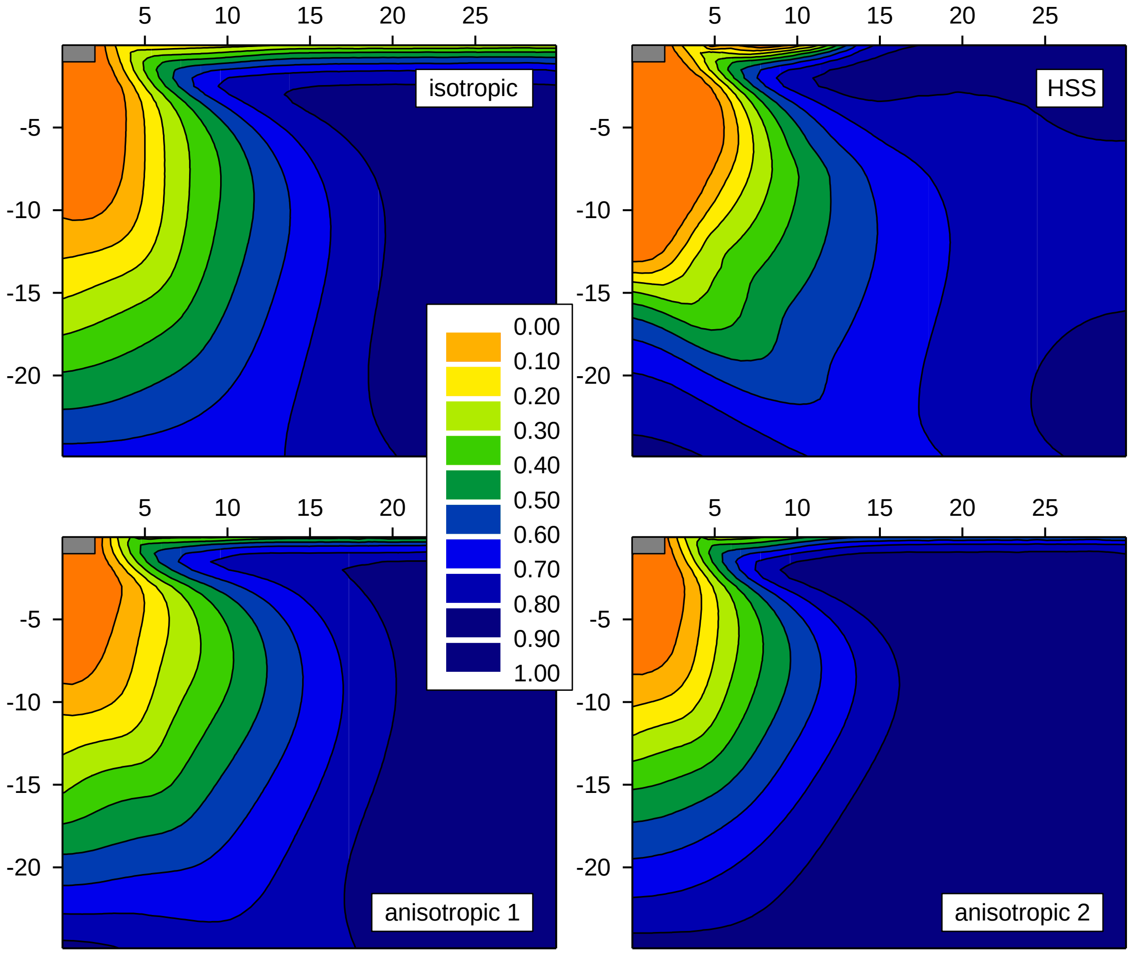

Fig. 57: Degradation of small strain stiffness in the numerical model: Macroscopic small strain stiffness parameter SSS_{gl} at 300 kPa footing load (dimensions in m)

6 Shear strength of stiff soils

The behaviour of stiff clays and dense sands differs substantially from their soft respectively loose counterparts: They are characterized by lower initial void ratio, higher shear strength and often exhibit anisotropic stiffness and shear strength. Shear strength of natural soils may be further increased by inter-particle bonding and cementation (Burland et al. 1996), resulting in gradual transition to soft rock materials. For clarity both heavily overconsolidated, stiff clays and dense sands are termed stiff soils in this chapter, in contrast to normally consolidated soft clays and loose sands.

In most practical cases the higher shear strength of such materials is accounted for by increasing the friction angle φ' (dense sands) or by introducing a cohesion intercept c' (stiff clays) while using a classical Mohr-Coulomb failure criterion. Doing so, however, fails to capture important features of soil behaviour, namely the transition to normally consolidated behaviour at high stress levels, the localization of strains in shear bands and the subsequent reduction of shear strength in strain softening.

While in general these phenomena may not be relevant under working load conditions, where shear strength is not fully mobilised, realistic prediction of bearing capacity and deformations close to and beyond failure requires consideration of the post-peak strain softening behaviour. This is in particular evident if the strain distribution along slips surfaces is highly non-uniform, which causes parts of the slip surface to soften before the peak shear strength has been mobilised along the whole slip surface.

This chapter starts with an overview on the mechanical behaviour of heavily overconsolidated clays and dense sands. Subsequently, the mathematical formulations for a Hvorslev surface multilaminate model, accounting for the shear strength of heavily overconsolidated clay, are presented. Implementation of strain regularization is explained only briefly in the context of the current model, as to a large extent the approach proposed by Galavi (2007) is employed. Pre-peak stress-strain behaviour and undrained shear strength predicted by the model is compared with experimental results of undrained triaxial tests. The efficiency of the employed regularization technique to obtain mesh independent results is demonstrated in biaxial test simulations. The influence of different assumptions in strain regularization is discussed in the context of shear band evolution in plane strain conditions.

6.1 Mechanical behaviour and experimental background

Figure 58 schematically shows the differences in stress-strain and volumetric-deviatoric behaviour between heavily overconsolidated and normally consolidated soils in drained triaxial compression. Overconsolidated soils reach the maximum shear strength at peak dilation (maximum inclination of ε_{vol}-ε_1 curve), followed by subsequent reduction of stress ratio q/p'. The final stress ratio M_{CS} is reached when additional shearing does not result in further volumetric strains. While normally consolidated soils show contractant behaviour in shearing, heavily overconsolidated samples expand in volume after some small initial range of compression.

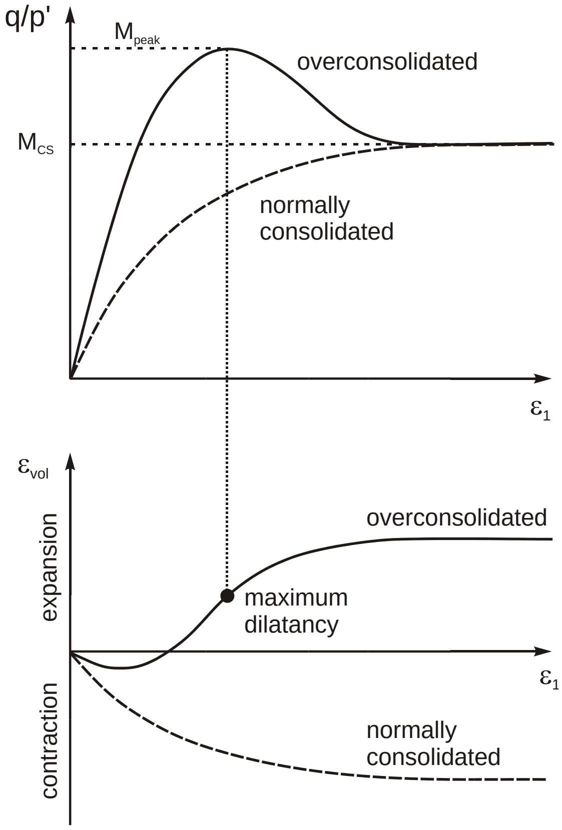

Fig. 58: Stress-strain behaviour and dilatancy

The different behaviour of normally and overconsolidated samples can be qualitatively explained by considering soils as an assembly of spherical particles. Arranging particles in the loosest way possible means that any distortion of the initial state by deviatoric loading results in a denser packing, while distortion of the dense packing is only possible if the soil sample is allowed to expand.

Figure 59 shows the schematic drained and undrained stress paths in triaxial compression which follow from the behaviour explained above. Undrained stress paths of normally consolidated samples continuously turn left in the *p'*-*q* diagram and reach failure at the critical state stress ratio M_{CS}. Both the drained and undrained stress paths of the overconsolidated soil travel beyond the line inclined at M_{CS}, with the undrained stress path turning to the right due to tensile excess pore pressures as a result of dilatant behaviour. The stress ratio M_{CS} is approached only after substantial loosening of the material (drained conditions) or development of excess pore pressures (undrained conditions).

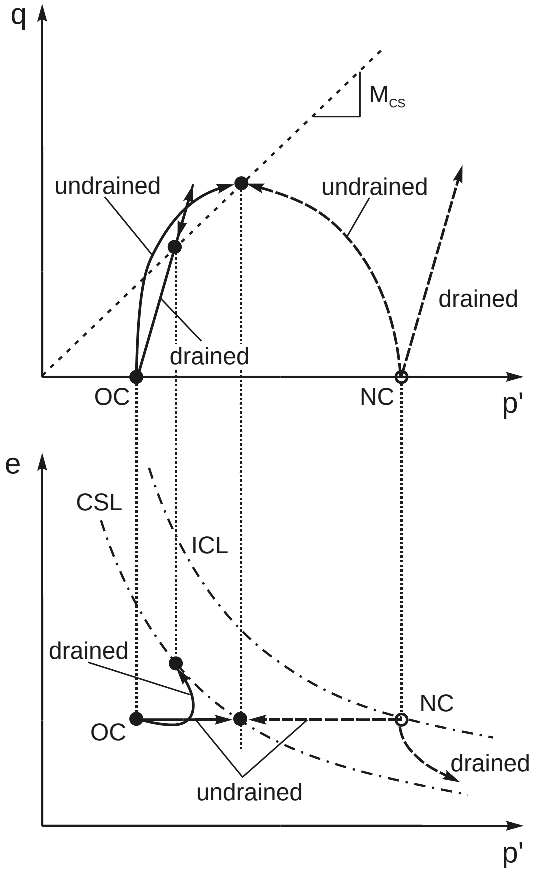

Fig. 59: Schematic stress paths and volumetric behaviour

The experimentally observed behaviour of soils at different densities and stress levels was first merged by Schofield & Wroth (1968) in the framework of Critical State Soil Mechanics. Combining the two diagrams of Figure 59, they proposed a three-dimensional state boundary surface in *e*-*p'*-*q* space to separate admissible and non-admissible states (Figure 60).

The overconsolidation ratio $OCR = p'/p'_c$ (with p'_c the maximum previous value of *p'*) defines the position within the state boundary surface at a certain void ratio *e*. If a soil sample is subjected to sufficient deviatoric loading, the stress path will finally end up at the critical state line (CSL), irrespective of *OCR* and whether loading is drained or undrained. On the right (or “wet”) side of the CSL the state boundary surface is defined by the Roscoe-Rendulic surface, while on the left (or “dry”) side of the CSL shear strength is limited by the Hvorslev surface.

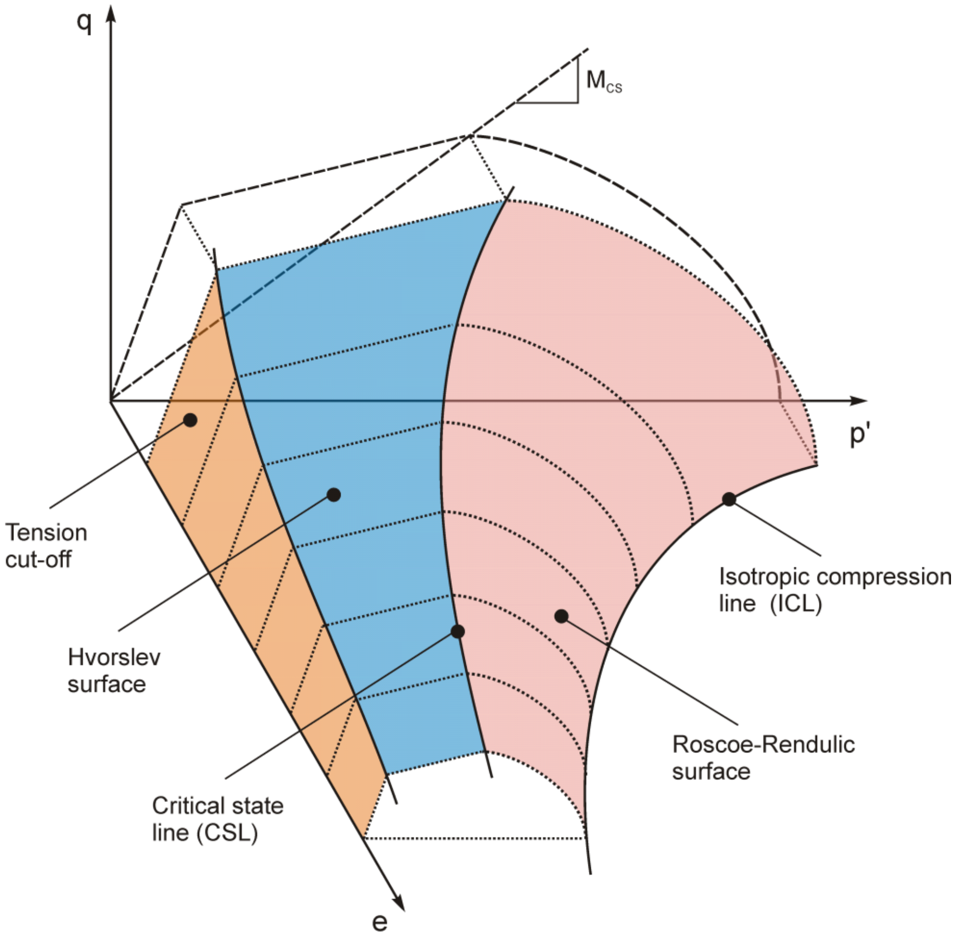

Fig. 60: State boundary surface in critical state soil mechanics

Hvorslev (1937) first proposed a linear relationship to describe peak shear strength of heavily overconsolidated clays at various initial volumes, if stresses are normalized to the pressure at the normal consolidation line at the current void ratio (Figure 61). As he conducted undrained shear box tests, both the horizontal shear stress τ and the vertical effective stress σ'_v at failure were normalized by the equivalent vertical stress σ'_{ve} on the 1D-normal compression line:

$$\frac{\tau}{\sigma'_{ve}} = \frac{\sigma'_v}{\sigma'_{ve}} \cdot \tan\varphi'_e + c'_{ve} \tag{122}$$

The parameters φ'_e and c'_{ve} give the inclination and intercept of the failure line in the normalized τ/σ'_{ve} vs. σ'_v/σ'_{ve} diagram. If rewritten in the form of the classical Mohr-Coulomb failure line it becomes evident, that the cohesion intercept $c' = c'_{ve} \cdot \sigma'_{ve}$ is no true material constant but depends on the equivalent stress σ'_{ve} and hence on the position of the 1-D normal compression line at the current void ratio.

$$\tau = \sigma'_v \cdot \tan\varphi'_e + c'_{ve} \cdot \sigma'_{ve} \tag{123}$$

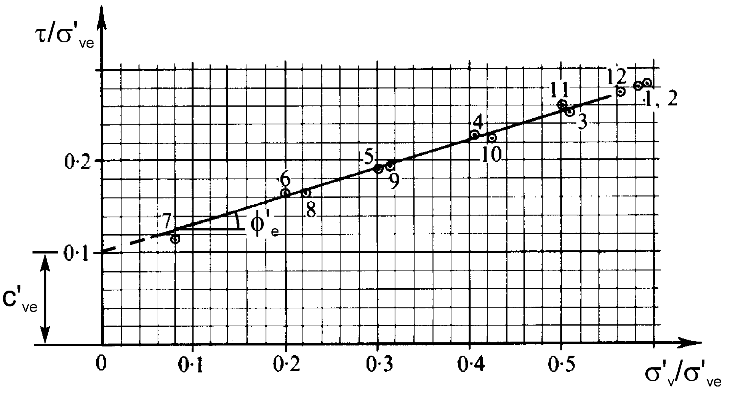

Fig. 61: Failure line of Wiener Tegel (after Hvorslev 1937)

For the interpretation of triaxial test data it is more convenient to normalize with respect to the equivalent stress p'_e on the isotropic compression line. In that case Equations 122 and 123 can be translated to p'-q stress space as

$$\frac{q}{p'_e} = m_H \cdot \frac{p'}{p'_e} + m_H \cdot g_H \tag{124}$$

with

$$m_H = \frac{6 \cdot \sin\varphi'_e}{3 - \sin\varphi'_e} \text{ in triaxial compression,} \tag{125}$$

$$m_H = \frac{6 \cdot \sin\varphi'_e}{3 + \sin\varphi'_e} \text{ in triaxial extension and} \tag{126}$$

$$g_H = \frac{c'_{pe}}{\tan\varphi'_e}\,. \tag{127}$$

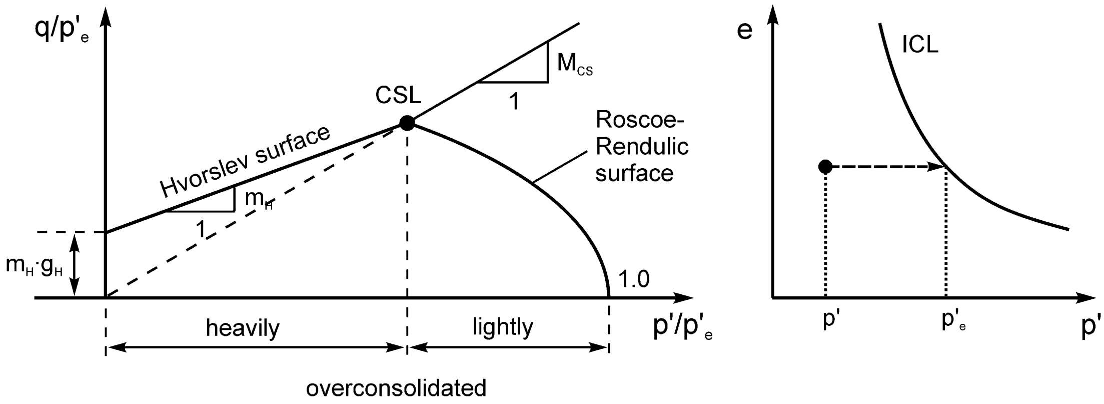

Fig. 62: Definition of Hvorslev surface parameters in p'-q notation

The validity of the linear relationship proposed by Hvorslev has been confirmed experimentally for numerous clays. Figure 63 shows peak shear strength data of drained and undrained triaxial tests on Weald clay, which when normalized according to Equation 124 plot on a single straight line. For most natural and reconstituted clays the difference between φ'_{cs} and φ'_e is about 3°-6° (Table 17).

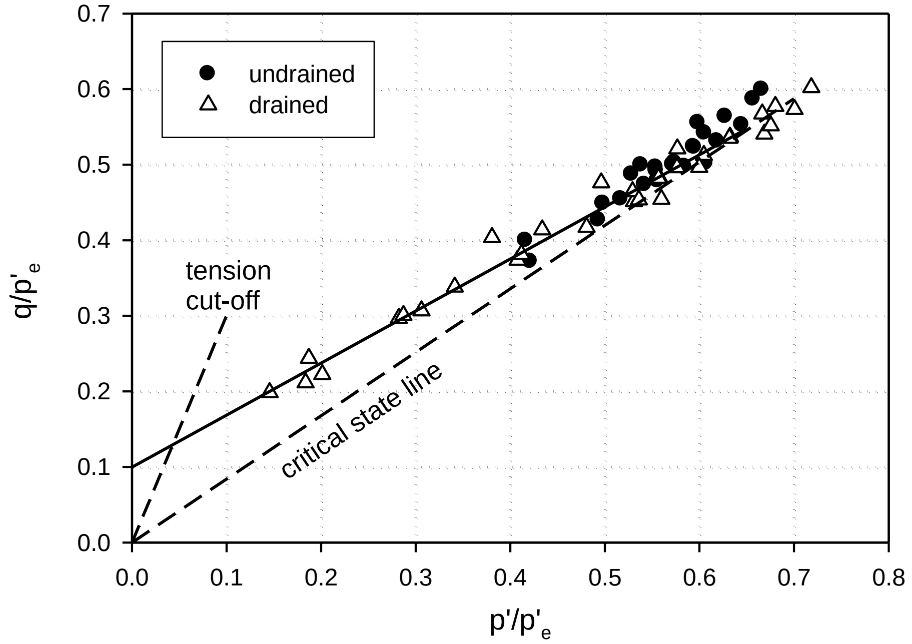

Fig. 63: Peak shear strength of Weald clay in drained and undrained triaxial compression (data from Parry, 1960 and Henkel, 1956)

Tab. 17: Hvorslev surface parameters of reconstituted clays

Soil	c'_{pe}	φ'_e **[°]**	φ'_{cs} **[°]**	**Reference**
Vienna clay	0.141[3]	17.5	26.0	Hvorslev (1937)[1]
Little Belt clay	0.187[3]	9.9	19.6	Hvorslev (1937)[1]
Weald clay	0.047	18.0	21.6	Parry (1960)
London clay	0.065	14.0	18.2	Parry (1960)
Pietrafitta clay	0.117[3]	23.8	28.4	Burland et al. (1996)
Todi clay	0.113[3]	19.4	25.8	Burland et al. (1996)
Vallericca clay	0.058[2]	22.6	26.7	Burland et al. (1996)
Corinth marl	0.100[3]	33.9	36.9	Burland et al. (1996)

[1] as reported by Muir Wood (1990)

[2] data normalized with isotropic compression parameters reported by Callisto & Rampello (2004)

[3] calculated assuming $\sigma'_{ve}/p'_e = 3/(1+2K_{0nc}) = 3/(3-2\sin\varphi'_{cs})$

After reaching peak strength, strains localize in narrow shear bands, followed by loosening and subsequent loss of shear strength within the shear band and unloading in the material adjacent to it. Burland et al. (1996) emphasized that undrained effective stress paths of overconsolidated clay samples approach the critical state line after sufficient shearing, and that the post-rupture friction angle equals the critical state friction angle φ'_{cs} (Figure 64). In his experiments the undrained stress paths of the overconsolidated samples started to turn right before reaching the maximum stress ratio, indicating that dilatancy occurred considerably before peak shear strength has been mobilised.

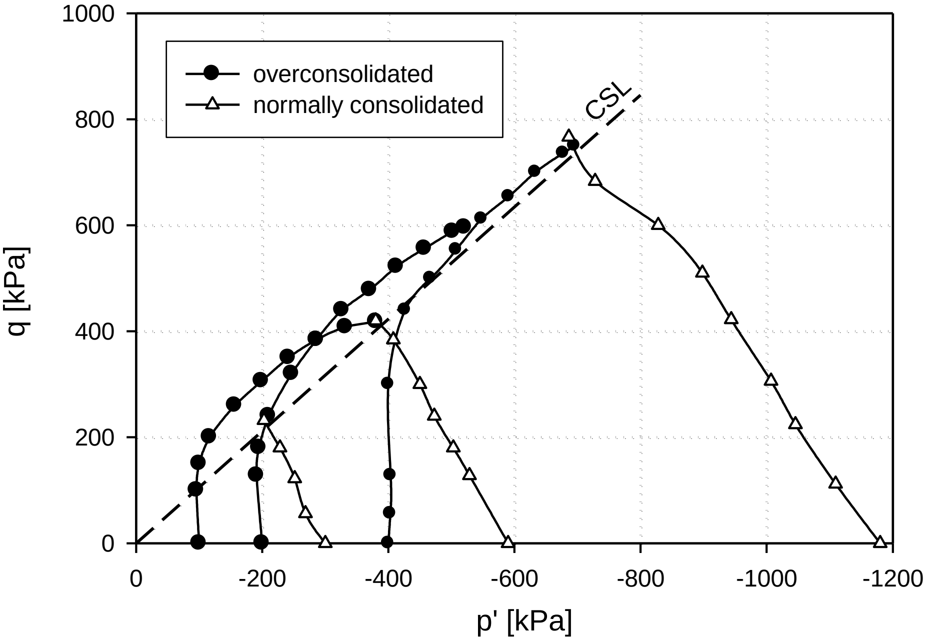

Fig. 64: Effective stress paths from undrained triaxial tests on reconstituted Vallericca clay (data from Burland et al. 1996)

Due to the dependency of soil behaviour on the degree of overconsolidation, soil samples with the same pre-consolidation pressure will behave very differently at different stress levels. While at low confining pressure pronounced dilatancy and shear strength higher than critical may be observed, the same soil will contract and steadily approach critical state shear strength at high stress levels (Figure 65).

It should be noted that shear strength of overconsolidated clays can drop below the critical state friction angle at very large deformations. Platy clay particles tend to align parallel to the slip surface at very large deformations and therefore provide lower shearing resistance than at critical state, which is characterized by rather random particle orientation (Muir Wood 1990).

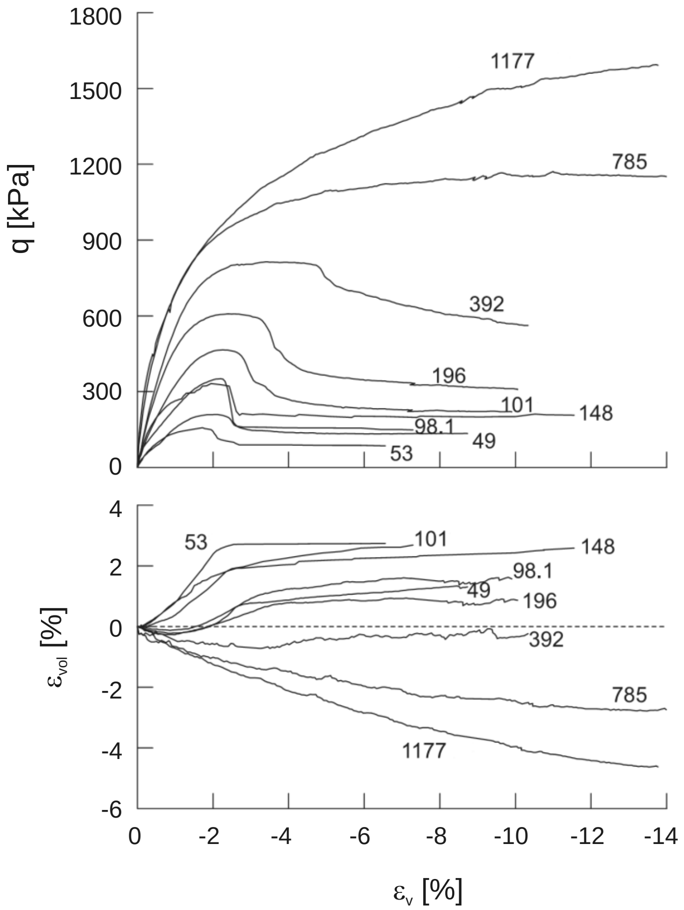

Fig. 65: Stress-strain behaviour of natural Vallericca clay at varying consolidation pressure (Callisto & Rampello 2004)

The behaviour of coarse grained soils is qualitatively similar to that of stiff, heavily overconsolidated clay. Dense sands also show distinct peak shear strength accompanied by dilatancy and shear banding, while loose sands behave similar to normally consolidated clays (Figure 66).

However, the existence of a Hvorslev surface is hard to establish for sand. Normalisation of stresses with respect to the isotropic normal compression line at the current volume is difficult as sands of different initial density converge towards a unique line only at very high stress levels, which are difficult to achieve in laboratory testing and may involve particle crushing. The concept of a Hvorslev strength surface is therefore in general not applicable to coarse grained soils.

Experimental data from undrained triaxial tests (conducted at the same initial volume) indicate that the strength envelope of dense sands is non-linear (Figure 67), as opposed to the linear Hvorslev surface for clays. Bolton (1986) proposed an empirical relationship linking peak friction angle φ'_{max} to initial relative density, I_D, and effective mean stress at failure, p'_f.

$$\varphi'_{max} = \varphi'_{cs} + 3I_D\left(10 - \ln p'_f\right) - 3°\,,\ I_D = \frac{e_{max} - e}{e_{max} - e_{min}} \tag{128}$$

Figure 67 shows undrained stress paths of dense Toyoura sand at the same initial volume and the corresponding peak strength envelope predicted by Equation 128 (e_{max} = 0.98, e_{min} = 0.6, e = 0.735, φ'_{cs} = 31°). In particular at stress levels up to p' = -1000 kPa peak shear strength lies significantly above the critical state line and matches well with the prediction obtained from Equation 128. Compared to overconsolidated clays, the undrained stress paths travel much longer along the failure envelope before approaching the critical state line.

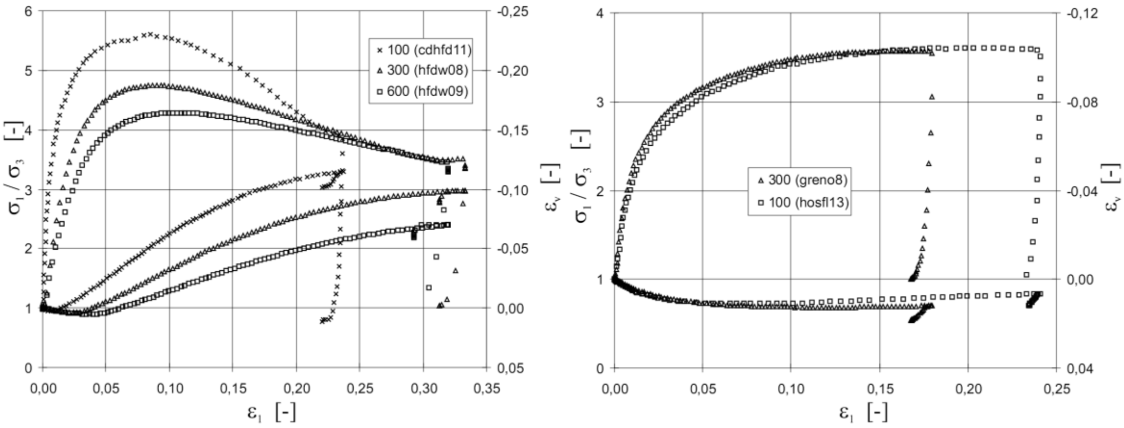

Fig. 66: Mobilisation of stress ratio in dense (left) and loose (right) Hostun sand (Marcher 2003)

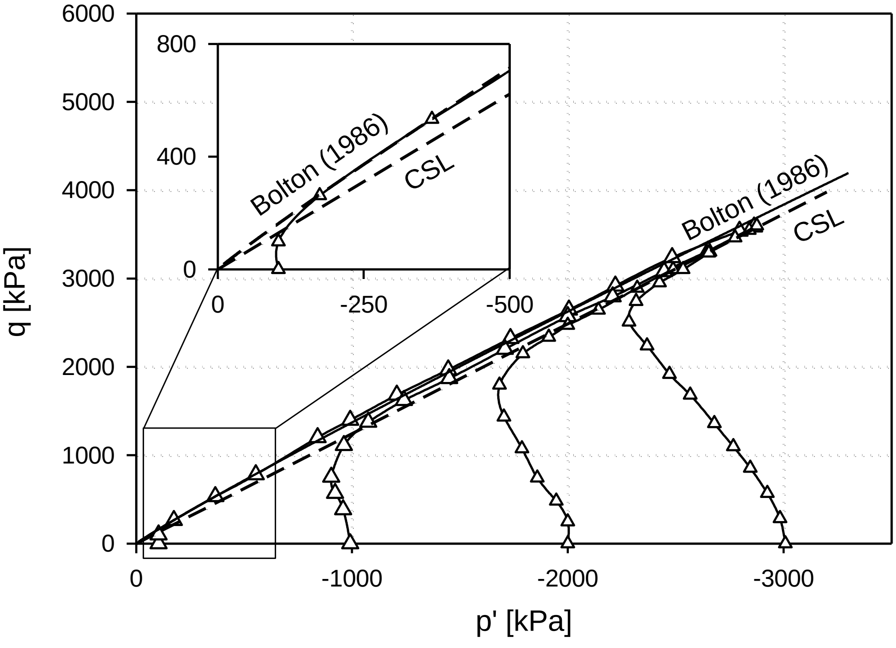

Fig. 67: Effective stress paths from undrained triaxial tests on dense Toyoura sand (data from Verduro & Ishihara 1996)

6.2 Hvorslev surface in multilaminate soil models

6.2.1 Yield function and softening rule

Additional to the volumetric and deviatoric yield surfaces of the basic model a Hvorslev failure envelope is introduced on integration plane level. The macroscopic Hvorslev surface definition (Equation 122) is adapted to the multilaminate definition of local stresses by using the equivalent normal stress σ'_{ne} at the local normal compression line (Equation 129). Stresses τ and σ'_n are local shear and normal stresses at integration plane level.

The multilaminate model does not employ explicitly defined normal compression and critical state lines, which slightly complicates the calculation of the equivalent stress σ'_{ne}. However, at each stage the magnitude of the local pre-consolidation normal stress, σ'_{nc}, is known, which defines the intersection of the primary loading and the unloading/reloading line (Figure 68). Knowing the current normal stress and the unloading-reloading stiffness E_{ur}, the local normal strain related to elastic unloading from σ'_{nc} to σ'_n can be evaluated. Applying this strain increment to the hardening rule of the cap yield surface delivers the equivalent normal stress σ'_{ne}. The detailed derivation of the mathematical formulations for σ'_{ne} is given in Appendix C.

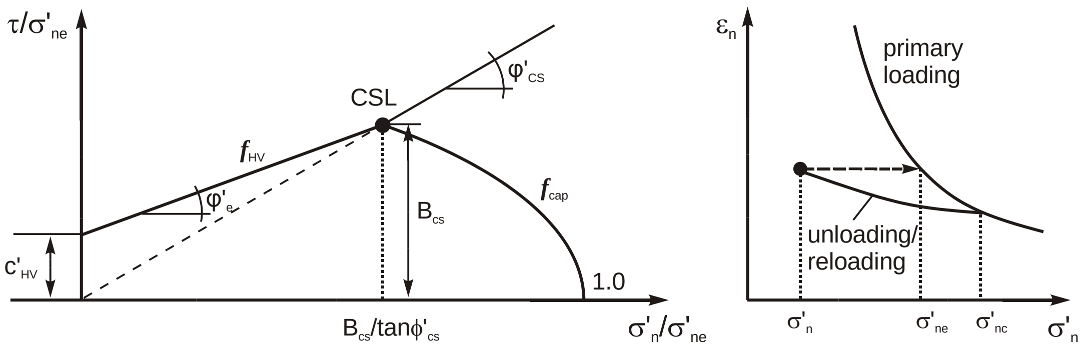

Fig. 68: Normalized Hvorslev yield surface on integration plane level

$$f_{HV} = \tau + \sigma'_n \cdot \tan\varphi'_e + c'_{HV} \cdot \sigma'_{ne} = 0 \tag{129}$$

$$\sigma'_{ne} = -\left[\left|\sigma'_{nc}\right|^{1-m} + \frac{3E_{oed,ref}}{E_{ur,ref}} \cdot \left(1 - 2\nu'_{ur}\right) \cdot \left(\left|\sigma'_n\right|^{1-m} - \left|\sigma'_{nc}\right|^{1-m} \right) \right]^{\frac{1}{1-m}} \tag{130}$$

$$c'_{HV} = B_{cs} \cdot \left(1 - \frac{\tan\varphi'_e}{\tan\varphi'_{CS}} \right) \tag{131}$$

The normalized intercept with the τ-axis, c'_{HV} is often treated as an independent material parameter (e.g. Burland et al. 1996). However, if the shape of the cap yield surface and the Hvorslev surface inclination φ'_e are known, also the intercept with the τ-axis is defined, as Hvorslev surface and cap yield surface intersect at the critical state line. The shape of the cap yield surface in the multilaminate model is determined by an iterative algorithm, which aims at reproducing realistic earth pressure coefficients K_{0nc} in primary oedometric loading (chapter 3.4). The auxiliary constant B_{cs} used in Equation 131 gives the ratio of local shear stress at critical state over σ'_{ne} and hence accounts for the shape of the cap yield surface.

As can easily be seen from Equation 130, σ'_{ne} decreases with reduction of the normal stress σ'_n, which means the Hvorslev yield surface f_{HV} is a curved line in the non-normalized $\tau - \sigma'_n$ plot of local yield surfaces (Figure 69). It is worth noting, that the Hvorslev yield surface serves as a strength boundary surface, which gets activated only once the local stress path reaches that surface. However, plastic strains are obtained also for stress states below the Hvorslev surface from the strain hardening deviatoric yield surface. This is a major difference to constitutive models like the Modified Cam Clay model (Roscoe and Burland 1968), and the Saniclay model (Dafalias et al. 2006), which assume purely elastic behaviour before peak shear strength is reached.

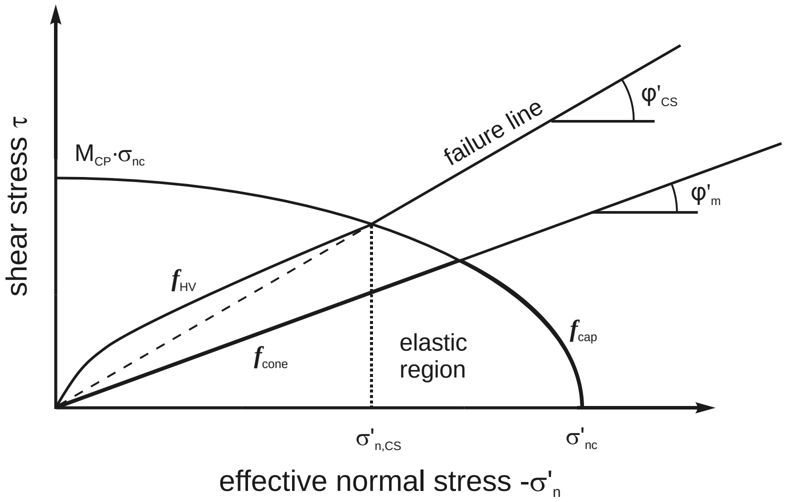

Fig. 69: Local yield surfaces

The position of the Hvorslev surface changes with the size of the cap yield surface and vice versa. For updating the local pre-consolidation stress σ'_{nc} in step k+1, normal plastic strain contributions from the cap and the Hvorslev yield surface are taken into account (Equation 132). Positive plastic normal strains, caused by dilatancy at the Hvorslev yield surface, reduce σ'_{nc}, whereas negative (compressive) plastic normal strains at the cap yield surface enlarge σ'_{nc}. The softening rule of the Hvorslev yield surface therefore equals the hardening rule of the cap yield surface:

$$\sigma'_{nc,k+1} = -\left[\left(-\sigma'_{nc,k}\right)^{1-m} + K \cdot \frac{(m-1)}{p_{ref}^{m-1}} \cdot \left(\Delta\varepsilon^{p}_{n,HV} + \Delta\varepsilon^{p}_{n,cap}\right)\right]^{\frac{1}{1-m}} \tag{132}$$

Equations 129-132 are in principle sufficient to describe the softening behaviour mathematically. However, numerical simulations at stress point level showed that plastic strains localize excessively in one or very few integration planes once softening commences. Consequently, post-peak behaviour is heavily influenced by the chosen integration rule (i.e. the number and orientation of integration planes). Furthermore, numerical calculations of boundary value problems tend to become unstable, if softening switches between different planes, which results in oscillatory stress-strain curves.

These effects have already been noted by Bažant (1984) and triggered the development of microplane models, which employ the kinematic constraint and hence introduce internal strain regularization at stress point level. Schuller (2000) utilized a scaling parameter in his multilaminate strain softening model, which relates the local softening modulus to the number of integration planes. In the present model a different approach is followed, which aims at distributing plastic strains from the Hvorslev surface over all integration planes currently in softening. Local plastic strain contributions of all integration planes are multiplied with their corresponding weight factors, w_i, to obtain the increment of the macroscopic damage strain, $\Delta\varepsilon_d$.

$$\Delta\varepsilon_d = \sum_i \Delta\varepsilon^{p}_{n,HV} \cdot w_i \tag{133}$$

$$\Delta\varepsilon_{di} = h_{soft} \cdot \Delta\varepsilon_d \cdot w_i \tag{134}$$

$\Delta\varepsilon_{n,HV}$ in Equation 132 is replaced by $\Delta\varepsilon_{di}$, which is the local proportion of the averaged macroscopic damage strain increment $\Delta\varepsilon_d$. The softening parameter h_{soft} controls the magnitude of softening for a given damage strain increment. The averaging of damage strains among the integration planes could be considered as a rough version of the kinematic constraint, where the global strain tensor is projected onto the various integration planes according to their respective orientation. However, here the strain averaging is limited to integration planes, whose stress paths have already reached the Hvorslev surface.

Figure 70 shows the macroscopic representation of the locally defined Hvorslev and cap yield surfaces, which has been obtained by the procedure described in section 3.5. Isotropic pre-consolidation of p'_c = -100 kPa is assumed. Material parameters are assumed as $\varphi'_{cs} = 30°$, $\varphi'_e = 24°$, $M_{CP} = 0.346$ and $m = 1$. Varying the ratio of E_{ur}/E_{oed} strongly influences the maximum shear strength in the heavily overconsolidated range. The higher the unloading-reloading stiffness E_{ur}, the more the Hvorslev yield surface resembles the straight Hvorslev line in the normalized plot (Figure 68), as volume changes in unloading diminish. The Hvorslev surface and the critical state line converge at low values of E_{ur}. Consequently, the model predicts more shear strength in the heavily overconsolidated range for soils which exhibit a large difference between primary loading and unloading/reloading stiffness.

The macroscopic cap and Hvorslev yield surface do not meet exactly at the critical state line (Figure 70). This might come as a surprise, as the local yield surfaces intersect the local critical state line at the same point (Figure 69). However, the point of intersection in the local τ-σ'_n diagram cannot be reached by any local stress path without activating cap yield surfaces on other integration planes, which represents macroscopic yielding. The Hvorslev surface still serves as a macroscopic shear strength envelope, but plastic strains will be produced by other integration planes before the stress path reaches the Hvorslev surface.

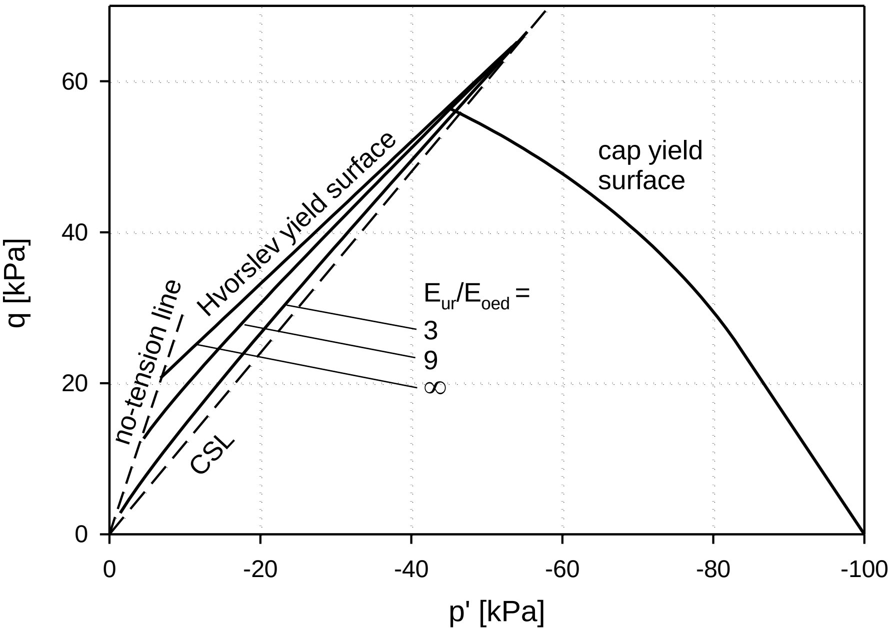

Fig. 70: Macroscopic Hvorslev and cap yield surface for different ratios of E_{ur}/E_{oed}, as predicted by the multilaminate model

6.2.2 Plastic potential functions

As in the basic version of the multilaminate model, plasticity resulting from the cap yield surface is assumed to be fully associated. Cone and Hvorslev yield surface are non-associated. The cone plastic potential function equals the cone yield function with the friction angle φ'_m being replaced by the mobilised angle of dilatancy ψ_m (Equation 135). Mobilisation of dilatancy below the critical state line equals the formulation in the basic version of the multilaminate model (chapter 3.1, Equations 42-48) and is modelled by a cubical function in dependency on the mobilised friction angle φ'_m. Above the critical state line, the maximum angle of dilatancy ψ_{max} is calculated from the difference between the critical state line and the Hvorslev surface at the current local stress state (Figure 72, Equation 136).

$$g_{cone} = \tau + \sigma'_n \cdot \tan\psi_m \tag{135}$$

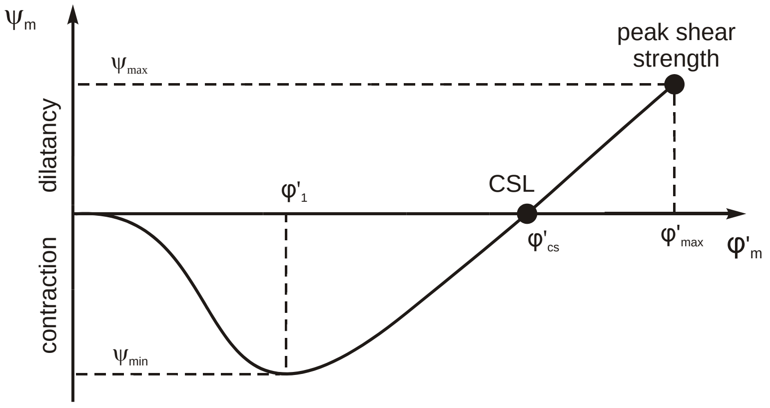

Fig. 71: Mobilisation of dilatancy

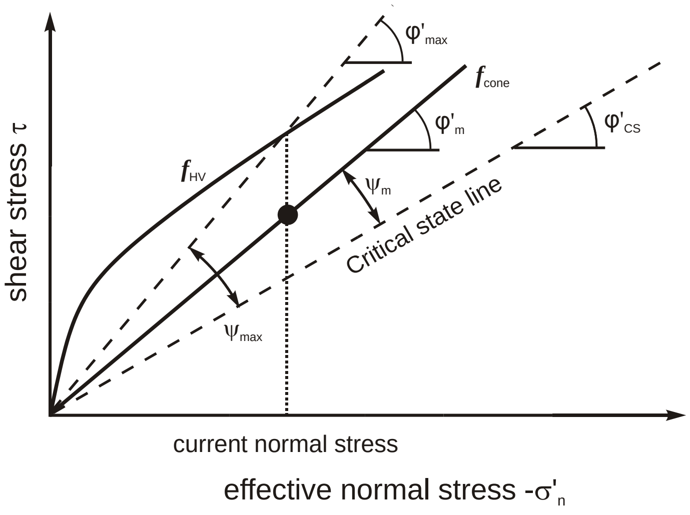

Fig. 72: Mobilised and maximum angle of dilatancy

The plastic potential of the Hvorslev surface equals the one of the cone yield surface at full mobilisation (Equation 137). With this approach a smooth transition from dilatant behaviour in the heavily overconsolidated to non-dilatant behaviour in the normally consolidated range is achieved. With increasing stress level and proceeding softening ψ_{max} reduces, eventually resulting in $\varphi'_m = \varphi'_{cs}$ and $\psi_{max} = \psi_{HV} = 0$ at critical state. It is worth noting, that the degree of dilatancy in the heavily overconsolidated range is an outcome of the model, not an input value.

$$\psi_{HV} = \psi_{max} = \varphi'_{max} - \varphi'_{cs} \tag{136}$$

$$g_{HV} = \tau + \sigma'_n \cdot \tan\psi_{HV} \tag{137}$$

6.3 Simulation of triaxial stress paths in clays

The Hvorslev surface model presented in previous sections has been primarily developed for fine grained soils. Validation is therefore focussed on comparing model predictions and experimental results for two different clays at different degrees of overconsolidation. Triaxial test simulations are carried out on stress point level for uniform deformation and do not account for the effects of strain localization, which is considered later on in this chapter. Still, such simplified test simulations are useful to evaluate the model behaviour in the pre-peak range and predicted peak strength.

Burland et al. (1996) reported the results of an extensive study on the strength properties of four overconsolidated clays, on both intact (natural) and reconstituted samples. The comparison here focusses on reconstituted samples of normally and overconsolidated Vallericca and Pietrafitta clay.

6.3.1 Vallericca clay

Vallericca clay was deposited in a marine environment and is heavily overconsolidated in its natural state with an estimated thickness of the previous overburden of about 220 m. The site from which the samples were excavated is located in the vicinity of Rome in the valley of the Tiber river.

The reconstituted, overconsolidated samples were compressed to an isotropic pre-consolidation pressure of -2000 kPa and then swelled isotropically to initial stresses of p'_0 = -100, -200 and -400 kPa. The intrinsic stiffness parameters λ =

0.145, $\kappa = 0.028$ and $e_{1kPa} = 1.68$ (Callisto & Rampello 2004) can be converted to multilaminate stiffness parameters according to Equations 138 and 139.

$$E_{oed,ref} = p_{ref} \cdot \frac{1+e_0}{\lambda} \tag{138}$$

$$E_{ur,ref} = 3(1-2\nu'_{ur}) \cdot p_{ref} \cdot \frac{1+e_0}{\kappa} \tag{139}$$

e_0 is taken as the void ratio in normal compression at $p' = -100$ kPa. While the choice of e_0 for the stiffness conversion is somewhat arbitrary, the overall influence of e_0 is small, if values within the range of applied stresses are chosen. The input parameters of the multilaminate model are summarized in Table 18. Normal consolidation and swelling lines are shown in Figure 73 for the intrinsic and the multilaminate parameters, as well as the starting points of the normally and overconsolidated experiments.

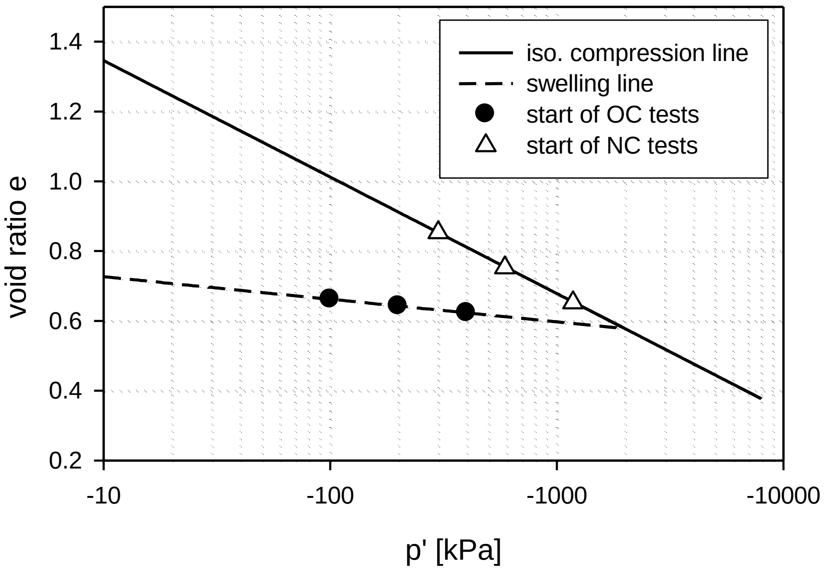

Fig. 73: Initial void ratio and stress states for the experiments on Vallericca clay

The undrained stress paths predicted by the multilaminate model are compared with the experimental results in Figure 74. It should be noted that normally and overconsolidated tests have been simulated with the same set of parameters (Table 18). The dilatant behaviour observed in the heavily overconsolidated tests after the stress path crosses the critical state stress ratio is in principle well predicted by the model.

Tab. 18: Input parameters for Vallericca clay

parameter		**value**	**unit**
oedometric stiffness	$E_{oed,ref}$	1 390	kPa
isotropic large strain Young’s modulus	$E_{ur,ref}$	12 930	kPa
isotropic large strain Poisson’s ratio	ν'_{ur}	0.20	--
shear hardening parameter	A_{mat}	0.010	--
critical state friction angle	φ'_{cs}	26.7	°
Hvorslev surface inclination	φ'_{e}	22.6	°
Initial pre-consolidation pressure	σ'_{nc}	-2000	kPa
reference pressure	p_{ref}	100	kPa
power index for stress dependency	m	1.0	--
softening scaling factor for plastic strains	h_{soft}	60	--

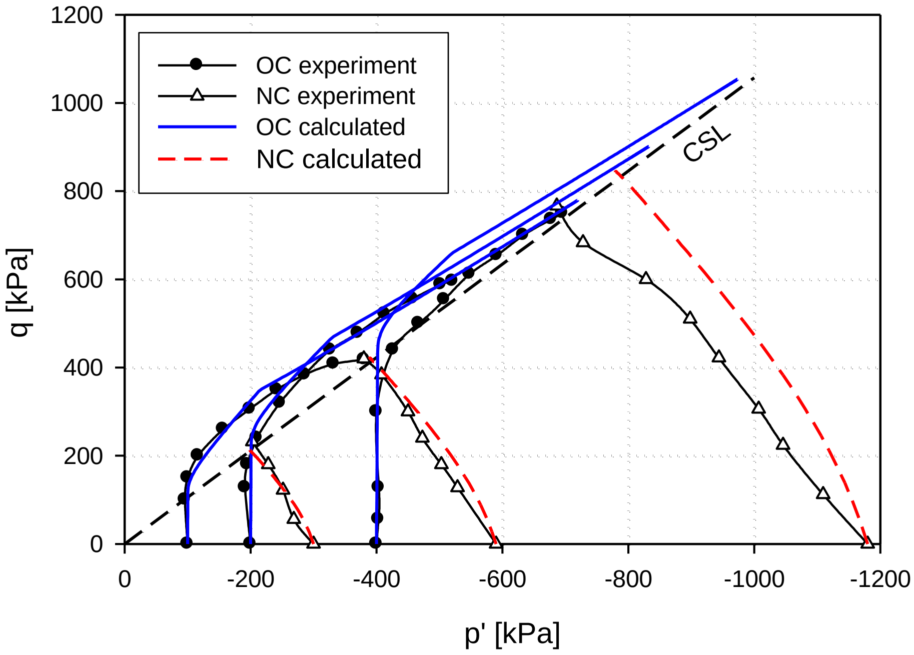

Fig. 74: Experimental and calculated effective stress paths of Vallericca clay

Development of excess pore pressures in the normally and overconsolidated test simulations is shown in Figure 75. Unfortunately, no experimental stress strain data have been published for the tests on reconstituted Vallericca clay. Excess pore pressures obtained in the reconstituted test simulations increase proportionally with the initial stress state p'_0. The overconsolidated test simulations show some compression at the start of the test due to elastic deformations, and consequently negative excess pore pressures develop in the early stage of the test. After about -2% of vertical strain, plastic volumetric strains due to dilation at the Hvorslev surface start to reduce the initial compression and result in positive excess pore pressures at the end of the test simulations.

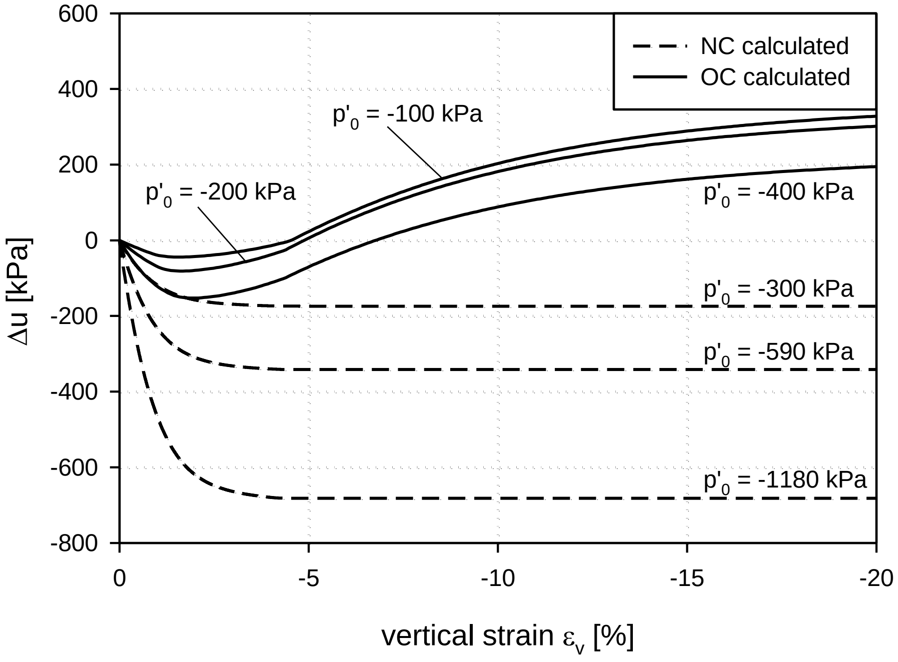

Fig. 75: Change of pore water pressure of reconstituted Vallericca clay in undrained triaxial compression

Undrained stress paths have been normalized by their respective equivalent pressure on the normal consolidation line in Figure 76. The experimental stress paths of the heavily overconsolidated samples approach the Hvorslev failure line, but do not travel along the Hvorslev surface long enough to reach the critical state at the initial equivalent pressure. That can be explained by loss of uniformity in the sample and local drainage within the shear band, which results in partially drained conditions and allows for localized changes in specific volume.

The numerical simulations, on the other hand, are carried out on a single stress point, which does not allow for such effects, and hence simulated stress paths reach the critical state line. However, due to the static constraint of the multilaminate framework, undrained conditions ($\Delta\varepsilon_{vol}$ = 0) are enforced on macroscopic level, but not individually for each integration plane. While the overall volume stays constant, local “volumes” (i.e. local normal strains $\varepsilon_{n,i}$) at integration plane level are allowed to change. Local equivalent pressures on planes reaching the Hvorslev surface reduce with the evolution of local dilatancy on these planes.

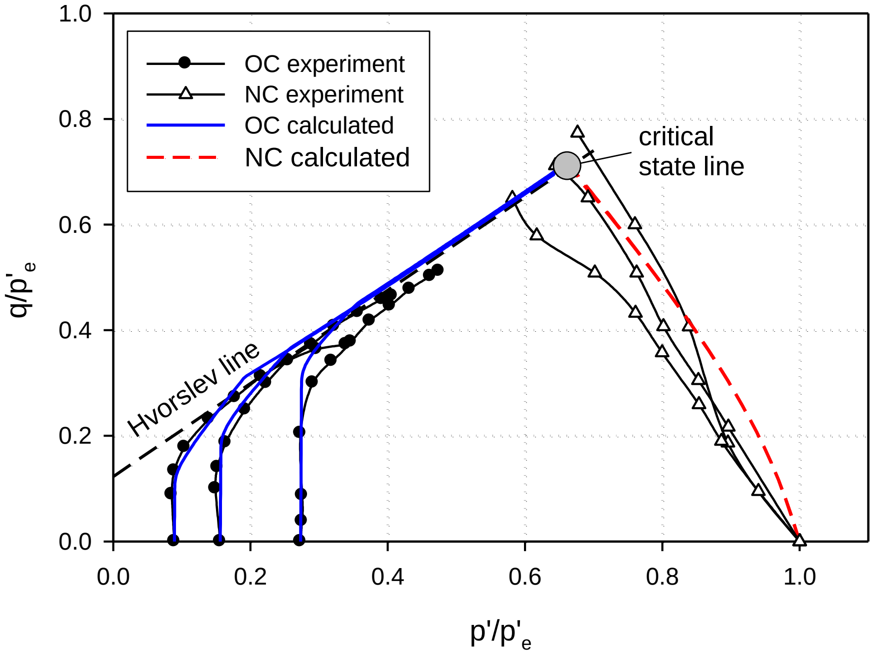

Fig. 76: Normalized effective stress paths of Vallericca clay

This is exemplified for test simulation 200 kPa OC in Figure 77, which shows the development of local equivalent normal pressures $\sigma'_{ne,i}$ with increasing vertical strain. All integration planes start at the same initial value of $p'_e = \sigma'_{ne,i} =$ -1281 kPa. Equivalent normal stresses on integration planes with inclination of $\alpha = 64.1°$ with regard to the horizontal (planes 22-25 and 30-33) drop significantly once local stress paths at these planes reach the Hvorslev surface and dilatancy commences. In order to fulfil the global constraint of $\Delta\varepsilon_{vol} = 0$, all the other integration planes compress elastically, which means equivalent pressures increase on these planes. This mechanism of strain redistribution among the integration planes can be considered as an additional degree of freedom in undrained conditions, which is a specific feature of multilaminate models.

The influence of h_{soft} on stress-strain behaviour and stress paths in undrained conditions is shown in Figure 78. High values of h_{soft} yield faster reduction of the pre-consolidation pressure σ'_{nc} with plastic volumetric strains, and thus less deviatoric stress can be mobilised. In boundary value problems, however, the influence of h_{soft} is coupled with the internal length parameter l_{cal}, as shown in chapter 6.5.3.

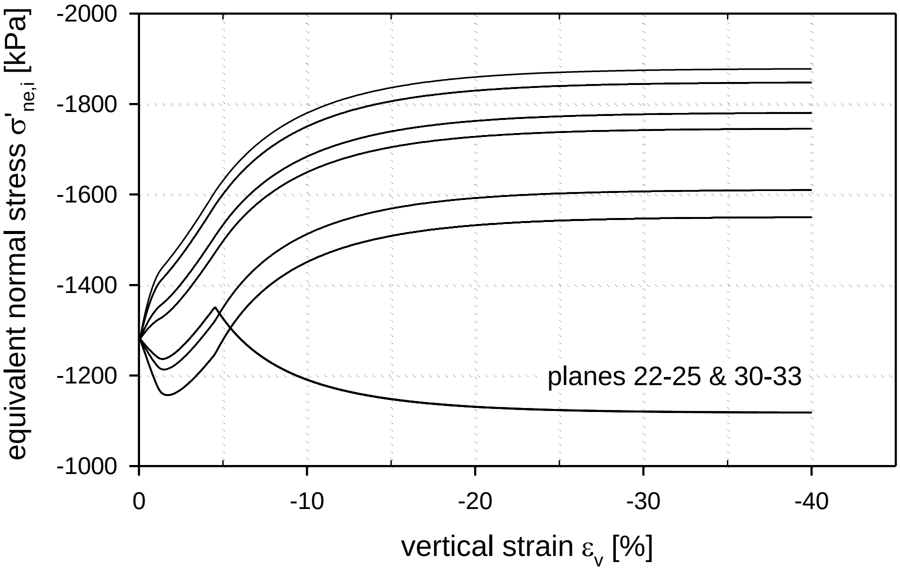

Fig. 77: Change of local equivalent normal stresses $\sigma'_{ne,i}$ during undrained test simulation 200 kPa OC

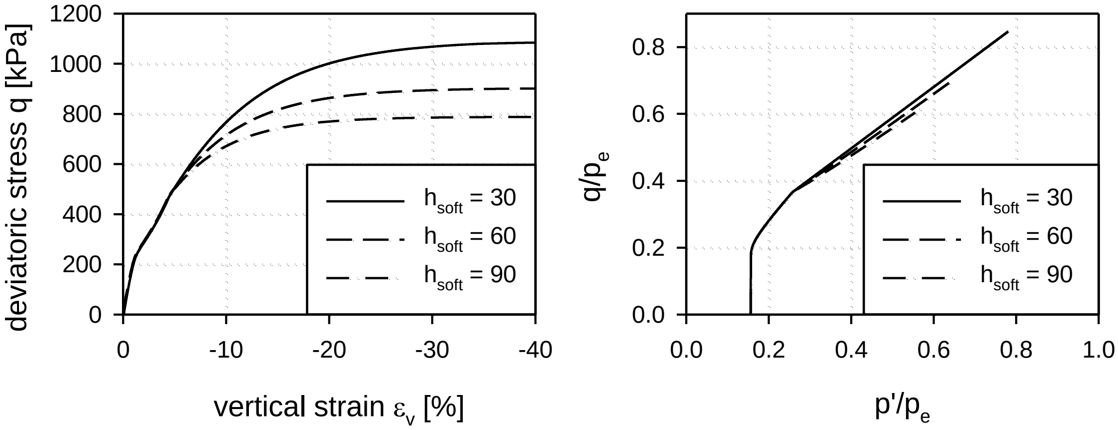

Fig. 78: Influence of h_{soft} on stress-strain curves and normalized undrained stress paths

6.3.2 Pietrafitta clay

Pietrafitta clay is a stiff, heavily overconsolidated clay of lacustrine origin from central Italy. It was deposited in the early Pleistocene age in the area that is today the western branch auf the Tiber basin. Previous overburden is estimated at about 150 m.

Undrained triaxial tests were reported by Burland et al. (1996) for both normally and overconsolidated reconstituted samples. Only test results obtained from reconstituted samples are considered here. The overconsolidated samples were consolidated to an isotropic pre-consolidation pressure of -2000 kPa and swelled isotropically to initial stresses of $p'_0 = -98$, -196 and -392 kPa, giving initial overconsolidation ratios OCR of about 20, 10 and 5, respectively. The tests on the normally consolidated samples started at initial pressures of $p'_0 = -294$, -588 and -1176 kPa.

The input parameters for the test simulations are summarized in Table 19. Intrinsic material parameters are reported as $\varphi'_{cs} = 28.6\text{-}33.0°$, $\varphi'_e = 23.8°$ (Burland et al. 1996), $\lambda = 0.227$, $\kappa = 0.0512$ and $e_{1kPa} = 2.362$ (Callisto & Rampello 2004). Shear strength parameters φ'_{cs} and φ'_e are used directly in the multilaminate model. Experimental variation of φ'_{cs} indicates curvature of the intrinsic failure line, with φ'_{cs} decreasing with increasing stress level. As the model employs a constant Mohr-Coulomb failure line at critical state, an intermediate value of 30° has been chosen for the numerical simulations. The stiffness parameters were converted to $E_{oed,ref}$ and $E_{ur,ref}$ according to Equations 138 and 139, with void ratio $e_0 = 1.32$ at $p'_0 = -100$ kPa. The deviatoric hardening parameter, A_{mat}, was obtained from calibration against triaxial stress-strain curves. Unfortunately, no small strain stiffness data have been available for the tests on reconstituted Pietrafitta clay. Isotropic small strain stiffness has therefore been estimated as $G_0 = 4.5 \cdot G_{ur}$. The stiffness degradation curve has been calibrated against test data on natural samples of Pietrafitta clay (Figure 79 left), as reported by Callisto & Rampello (2002).

Figure 79 compares experimental and calculated oedometric compression and swelling curves. For comparison a swelling curve assuming purely elastic, stress dependent material behaviour has been added. Experimental and numerical elastoplastic unloading curves differ slightly at low stress levels, as the numerical model predicts a larger elastic range in unloading and follows the elastic unloading line up to $\sigma'_v \approx -400$ kPa.

Tab. 19: Input parameters for Pietrafitta clay

parameter		**value**	**unit**
oedometric stiffness	$E_{oed,ref}$	1020	kPa
isotropic large strain Young’s modulus	$E_{ur,ref}$	8140	kPa
isotropic large strain Poisson’s ratio	ν'_{ur}	0.20	--
shear hardening parameter	A_{mat}	0.005	--
critical state friction angle	φ'_{cs}	30.0	°
Hvorslev surface inclination	φ'_{e}	23.8	°
initial pre-consolidation pressure	σ'_{nc}	-2000	kPa
reference pressure	p_{ref}	100	kPa
power index for stress dependency	m	1.0	--
Softening scaling factor for plastic strains	h_{soft}	60	--
Isotropic shear stiffness at very small strains	$G_{0,ref}$	15 000	kPa
threshold strain level for stiffness degradation	$\varepsilon_{deg,1}$	5e-6	--
transition to large strains	$\varepsilon_{deg,2}$	1e-2	--

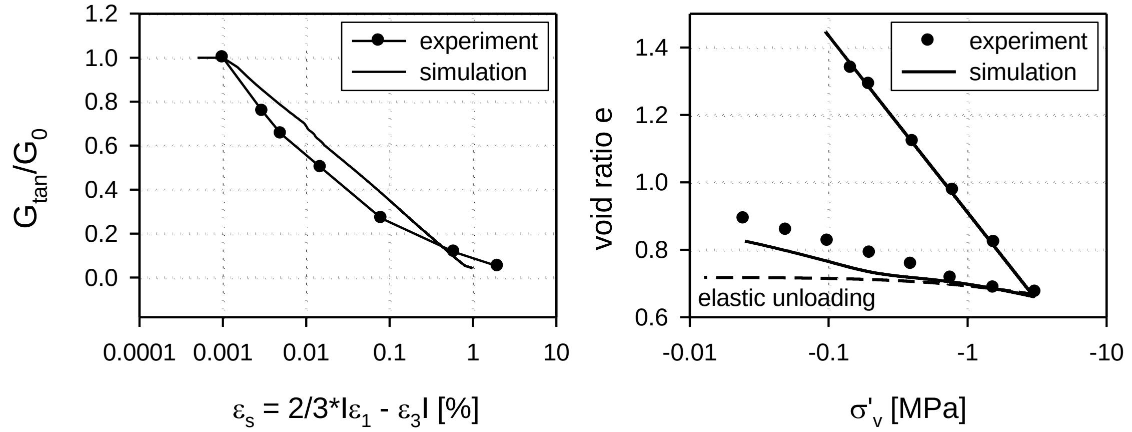

Fig. 79: Degradation of small strain stiffness of Pietrafitta clay (left) and deformation behaviour in oedeometric conditions (right)

The undrained stress paths predicted by the multilaminate model are compared with the experimental results in Figure 80. As for Vallericca clay, undrained shear strength is well predicted for the normally consolidated samples. The trend of the undrained stress paths of the heavily overconsolidated samples is in general also well captured. However, the tendency of experimental stress paths to curve to the right below the critical state line cannot be predicted by the model, which assumes dilatant behaviour only above the critical state stress ratio.

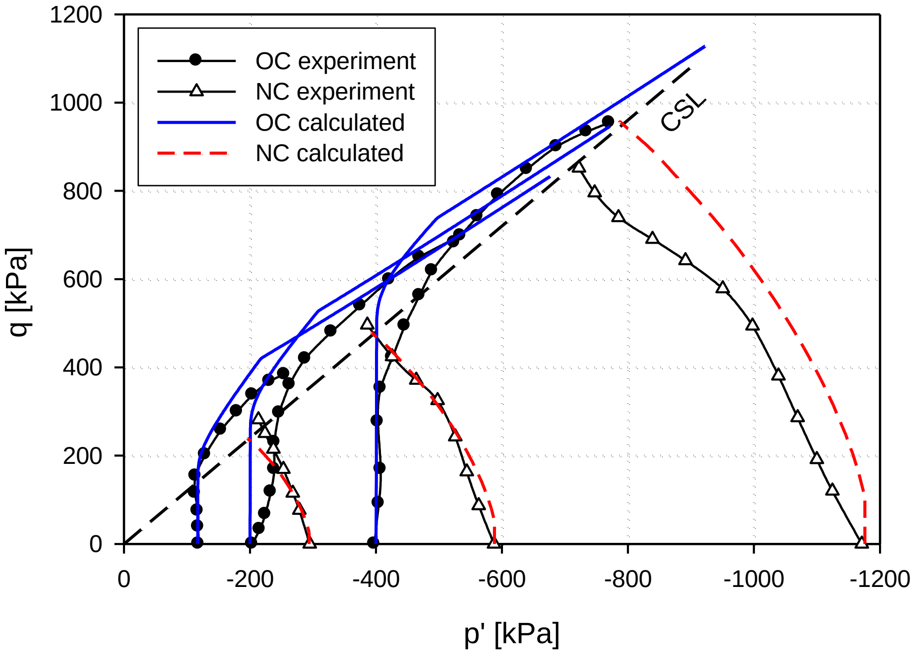

Fig. 80: Experimental and calculated undrained effective stress paths of Pietrafitta clay

Undrained effective stress paths have been normalized with the equivalent pressure on the normal consolidation line at the start of the test, p'_e, in Figure 81. The kink in the calculated stress paths of the heavily overconsolidated samples, indicating contact with the Hvorslev surface, plots slightly above the theoretical Hvorslev line. This is a result of the multilaminate integration rule, as the theoretical plane with the most critical stress ratio does in general not coincide with one of the predefined integration planes. The experimental stress paths do not reach the critical state line due to strain localization, as discussed before for Vallericca clay.

The experimental stress-strain curves of the overconsolidated samples (Figure 82) show a sharp drop of the deviatoric stress after reaching peak strength, which is related to the formation of shear bands and strain localization. Samples tested at higher initial stresses exhibited significant plastic yielding prior to failure, whereas the sample tested at p'_0 = -98 kPa failed in a rather brittle manner immediately after reaching peak strength. Such behaviour cannot be reproduced by undrained simulations on stress point level, and consequently calculated stress-strain curves progress steadily towards the maximum deviatoric stress. The high initial stiffness observed in the experiments is well captured by the simulations. Experimental results showed less contractancy at the start of the test than predicted by the model (Figure 83), and lower excess pore pressure at final state. The former can be attributed to the tendency of the experimental samples to dilate below the critical state line. The latter may be related to strain localization in the experiments, which leads to partially drained conditions and failure of the sample before critical state conditions are reached. Both effects are also notable in the normalized stress paths (Figure 81), as discussed before.

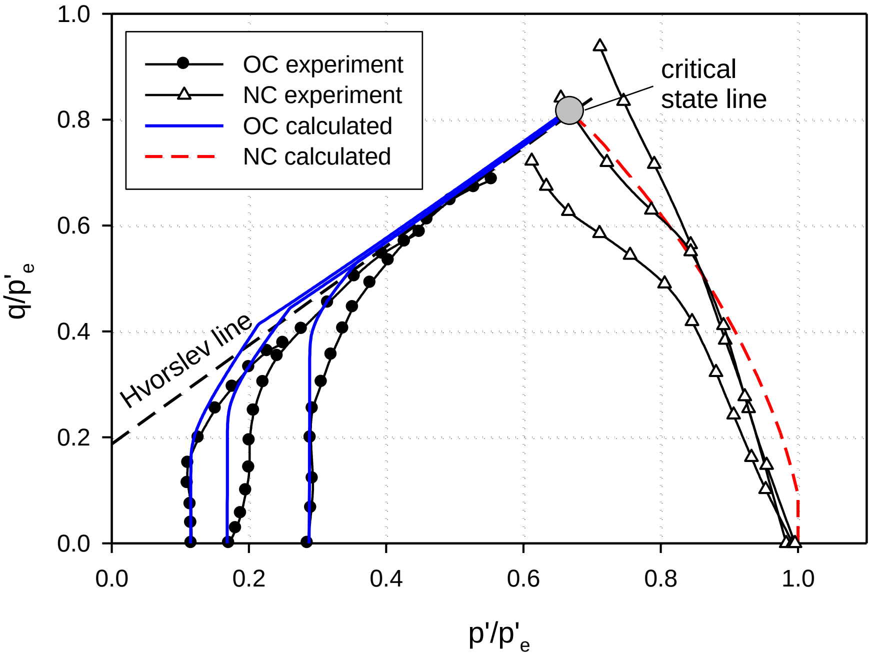

Fig. 81: Normalized undrained effective stress paths of Pietrafitta clay

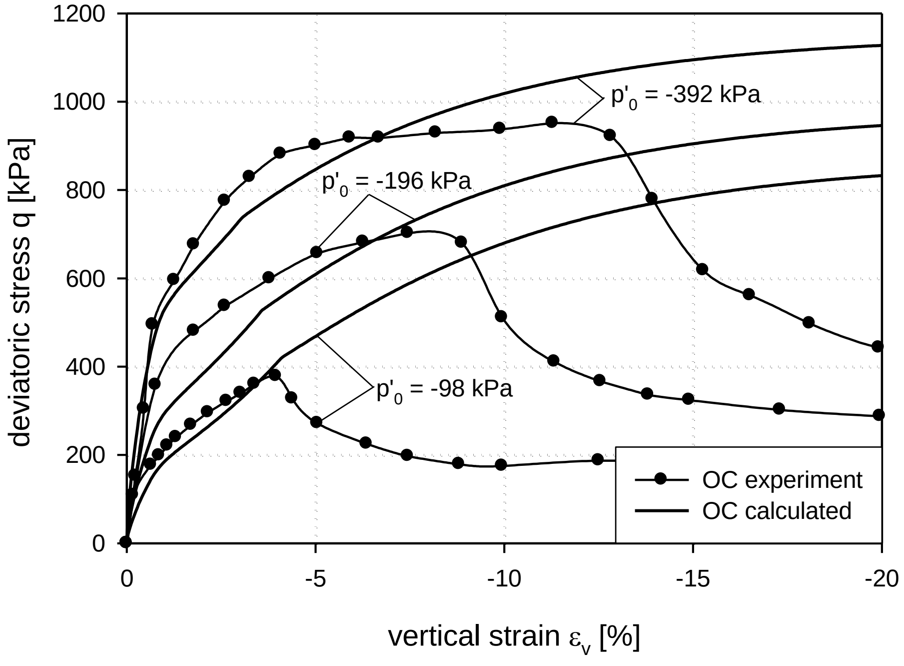

Fig. 82: Stress-strain curves of heavily overconsolidated Pietrafitta clay in undrained triaxial compression

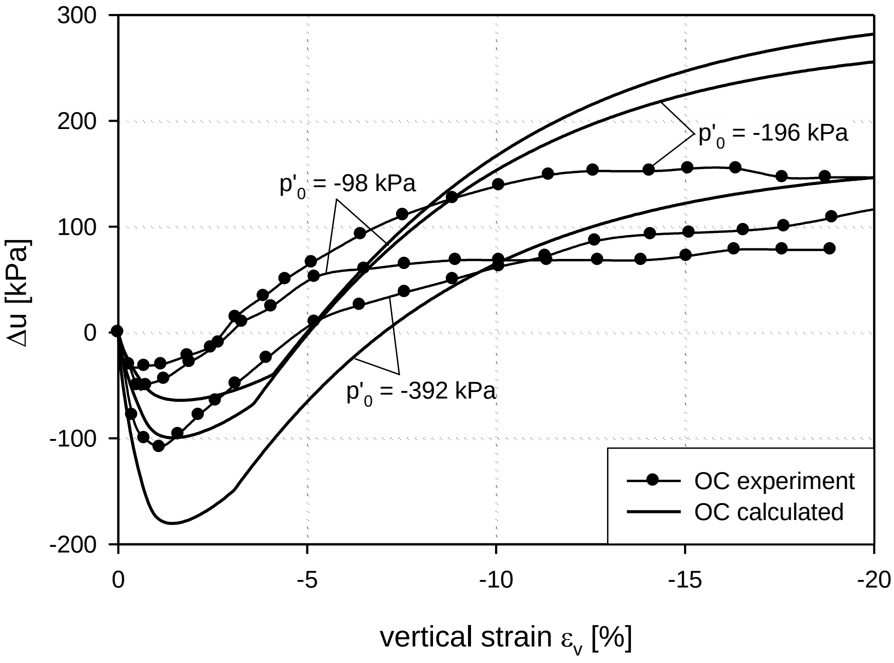

Fig. 83: Change of pore water pressure of heavily overconsolidated Pietrafitta clay in undrained triaxial compression

Stress-strain curves of normally consolidated samples show flat peaks, which indicates that critical state conditions have been reached (Figure 84, Figure 85). Due to introduction of small strain stiffness in the numerical simulations, the very stiff behaviour at the start of the experiments is again well captured.

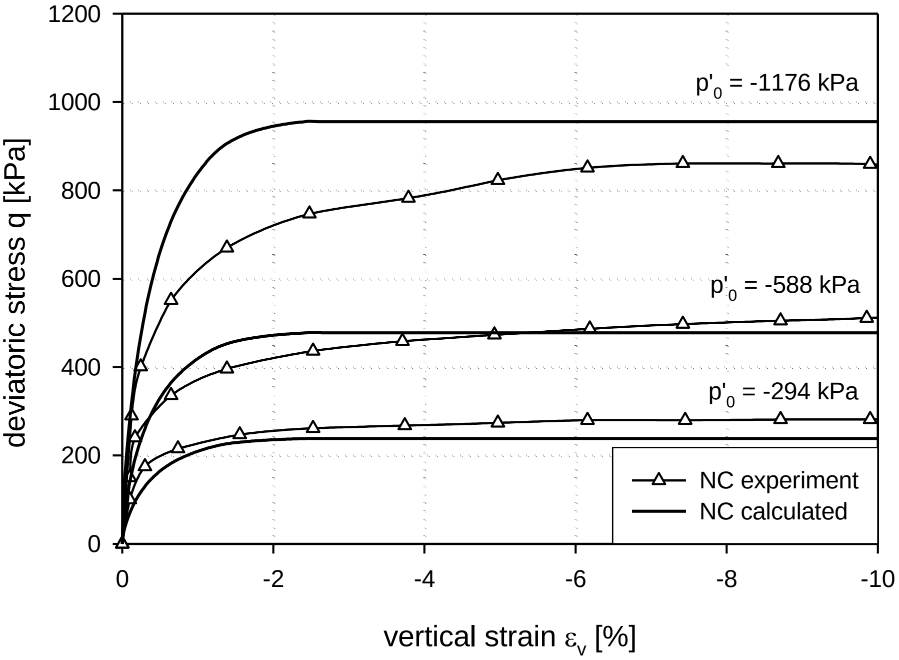

Fig. 84: Stress-strain curves of normally consolidated Pietrafitta clay in undrained triaxial compression

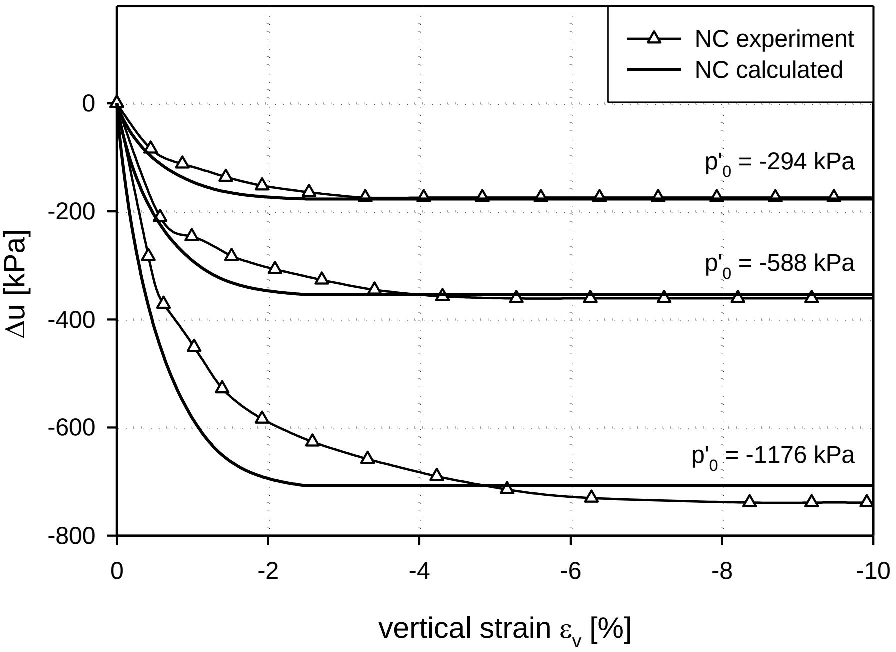

Fig. 85: Change of pore pressure of normally consolidated Pietrafitta clay in undrained triaxial compression

6.4 Mesh dependency and strain regularization

Numerical analyses of strain softening problems with rate-independent finite element techniques are severely dependent on discretisation. This is related to the localization of deformations in shear bands once peak soil strength is reached, and strain softening commences afterwards. While shear strength of the material within the shear band reduces, the continuum around the shear band unloads elastically as the overall load bearing capacity reduces.

The size of the shear band in granular materials is governed by micromechanical properties of the material, e.g. the average grain size (Vardoulakis 1980, Marcher 2003). In conventional finite element calculation, such micromechanical scale does not exist, but is however implicitly provided by the size of the finite elements. The magnitude of shear strain within the shear band can be roughly estimated by dividing the overall relative displacement by the thickness of the numerical shear band. If loss of shear strength is driven by plastic strains in the current stress point, strain softening will obviously take place faster in finer meshes, and will be delayed by increasing thickness of the numerical shear band. Consequently, both the thickness of the predicted shear band and the load-displacement behaviour in the post-peak range are strongly dependent on the finite element discretisation.

On a more mathematical scale the onset of shear banding represents a bifurcation point, after which several alternative deformation states are possible for a given stress state. Ellipticity of the governing partial differential equations gets lost locally, the tangential stiffness matrix becomes zero and the conventional iterative procedure ceases to converge to a unique solution.

Bifurcation analysis as proposed by Mandel (1966), Rice (1976) and Vardoulakis (1980) can be applied to study the conditions for the onset and the subsequent development of shear banding in frictional materials. These techniques are, however, rather challenging to implement in finite element codes. So called regularization techniques offer a more feasible alternative to overcome mesh dependency and have therefore gained widespread application in numerical strain softening analysis.

6.4.1 Regularization techniques

A condensed summary of the different regularization techniques is provided in the following. A more detailed description of these approaches has been given by Marcher (2003) and Galavi (2007).

1. Micropolar continua approach: Additional, rotational degrees of freedom are introduced on finite element level, which can account for the rotation of particles in shear bands, Mühlhaus & Vardoulakis (1987), de Borst (1991). The approach employs a Cosserat continuum and requires additional material parameters and boundary conditions.
2. Embedded discontinuity approach: The shape functions are enhanced to account for discontinuous displacement (strong discontinuity, Larsson et al. 1993, Simo et al. 1993) or discontinuous strains (weak discontinuity, Rudnicki 1977) within the finite element once bifurcation is detected. The method can be applied to relatively coarse meshes, but requires access to the calculation kernel of the FE-program.
3. Visco-plastic models: Artificial visco-plastic behaviour is introduced also for static problems, which implicitly provides an internal length scale. A viscous calculation step is performed after the static (non-softening) equilibrium analysis (Loret & Prevost 1991, Oka et al. 1995).
4. Length-scale approach: The softening rate is scaled by a factor which depends on the element size (Pietruszak & Mroz 1981).
5. Non-local approach: Local quantities (stresses and strains) are averaged over a predefined soil volume to obtain so called non-local or regularized quantities, Eringen (1972), Bažant & Gambarova (1984). The size of the averaging volume is defined by an internal length, which is an additional input parameter. Constitutive equations are then formulated in these “non-local”

quantities. A fully non-local approach involves regularization of both stresses and strains. In most constitutive models only softening state variables are treated as non-local quantities, which is known as the partially non-local approach, Brinkgreve (1994), Jirasek (1998).

6. Strain-gradient approach: The gradient of the strain tensor is taken into account in the constitutive equations. As a special case of the non-local approach, mesh independent results are obtained by introducing an internal length scale, but stresses and strains are kept as local quantities (Aifantis 1984, Vardoulakis & Aifantis 1989).

In the current multilaminate model a partially non-local approach is employed, in which regularization is applied only to plastic strains in strain softening. A similar approach has been successfully utilized by Galavi (2007) to model friction and cohesion softening within the multilaminate framework. The main advantage of the method is its relatively simple implementation without changes to the FE-calculation kernel, as all modifications can be carried out within the stress point algorithm.

6.4.2 Non-local approach

The non-local approach is based on the assumption that material behaviour does not only depend on local variables at the current stress point, but also on quantities averaged over a specific volume in the neighbourhood of the point. The fully non-local formulation of stresses and strains proposed by Eringen (1981) is given by Equations 140 and 141.

$$\sigma^*(x_n) = \frac{1}{V_w} \iiint \omega(x'_n)\sigma(x_n + x'_n)dx'_1 dx'_2 dx'_3 \tag{140}$$

$$\varepsilon^*(x_n) = \frac{1}{V_w} \iiint \omega(x'_n)\varepsilon(x_n + x'_n)dx'_1 dx'_2 dx'_3 \tag{141}$$

$\sigma(x_n)$ and $\varepsilon(x_n)$ are local stresses and strains at point x, which is defined by the global Cartesian coordinates x_1, x_2, x_3. The non-local stresses and strains at point x, $\sigma^*(x_n)$ and $\varepsilon^*(x_n)$, are found by integration over the local stresses and strains in the vicinity of x, for which the local coordinates x'_1, x'_2, x'_3 are introduced. The weight function $\omega(x'_n)$ accounts for the diminishing influence of points with increasing distance to the current stress point. The weighted volume V_w is used to normalise the integrals in Equations 140 and 141 and thus accounts for the smaller soil volume around stress points in the vicinity of model boundaries.

$$V_w = \iiint \omega(x'_n) dx'_1 dx'_2 dx'_3 \tag{142}$$

The weight function $\omega(x'_n)$ defines the soil volume over which averaging is carried out, and hence governs the predicted shear band thickness (Jostad & Grimstad 2011). Eringen (1981) proposed a Gaussian distribution function (Equation 143), which uses the internal length l to define the area of influence for the averaging. However, the Gaussian function still tends to deliver overly strain concentration in the centre of the shear band.

Brinkgreve (1994) therefore expanded the classical non-local approach by a linear combination of local and non-local contributions (Equation 144), while keeping the Gaussian distribution function as the weight function. An additional input parameter, α, is used to scale local and non-local quantities. Galavi (2007) kept the original formulation of strain integration (Equation 141), but introduced a weight function $\omega'(r)$ which is characterised by applying zero weight to the strain of the current stress point (Equation 145). Both weight functions are depicted in Figure 86 for an internal length of l = 1.

$$\omega(r) = \frac{1}{l\sqrt{\pi}} e^{-\left(\frac{r}{l}\right)^2} \tag{143}$$

$$\varepsilon^*(x_n) = (1-\alpha)\varepsilon(x_n) + \frac{\alpha}{V_w} \iiint \omega(x'_n)\varepsilon(x_n + x'_n) dx'_1 dx'_2 dx'_3 \tag{144}$$

$$\omega'(r) = \frac{r}{l^2} e^{-\left(\frac{r}{l}\right)^2} \tag{145}$$

The weight function proposed by Galavi (2007) is used in the current model, as it offers two major advantages:

1. The non-local strain is independent of the local strains at the current stress point. Plastic strains calculated within a calculation step therefore have no influence on the non-local strain, which is evaluated once at the start of the calculation step. This is particularly advantageous for multilaminate models, as the local strain distribution among the integration planes is only known at the end of the step. Employing a Gaussian distribution function would require an iterative scheme to update the non-local damage strain within the current calculation step, which requires additional computational effort.

2. Apart from the internal length *l*, no additional input parameters are required.

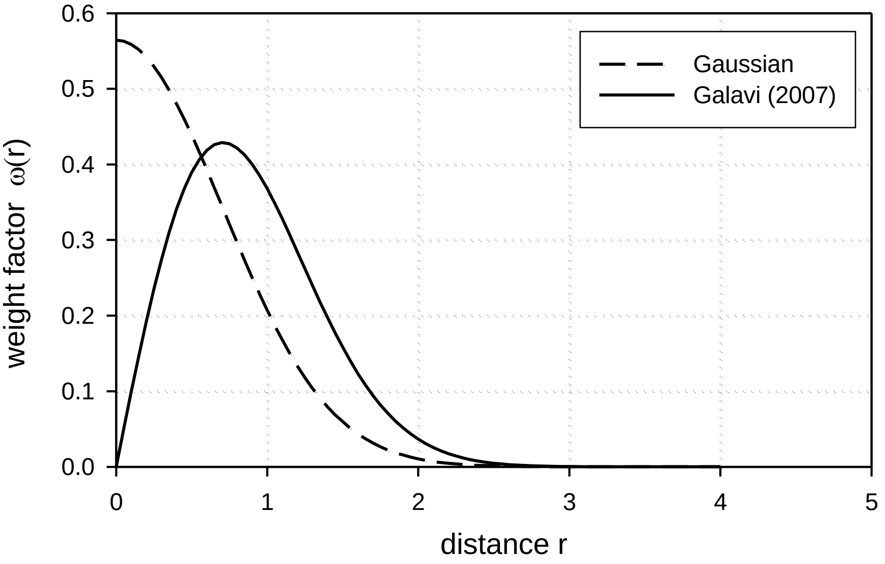

Fig. 86: Weight functions for $l = 1$

Jostad and Grimstad (2011) demonstrated that the modified weight function proposed by Galavi may result in non-smooth strain distributions over the shear band. However, mesh independence of results – which is seen as the major objective of strain regularization – was achieved even with the uneven strain distribution.

As pointed out by Galavi (2007) and Marcher (2003), the non-local approach is only applicable to shear bands which can be described as weak or no discontinuities. A weak discontinuity is characterised by a continuous displacement field, but exhibits a jump in the strain field. No discontinuity means that both strains and displacements within the shear band can be described by continuous, differentiable functions. Such shear bands are commonly observed in dense sands and overconsolidated clays, where softening is related to dilatant behaviour. Shear bands have a finite (albeit small) size, which allows for distribution of displacements over the shear band.

On the other hand, fractures in rock and concrete, or polished shear surfaces of clays at residual shear strength are so called strong discontinuities. Both strain and displacement fields are discontinuous, and formation of shear bands (or cracks) does not necessarily involve dilatancy. Consequently, infinitely small shear bands are observed which do not allow for distribution of displacements. The non-local approach, however, inevitably involves the assumption of shear bands of finite size, which does not reflect the softening behaviour of rocks and concrete.

6.4.3 Implementation

A partially non-local approach is implemented in the multilaminate model, which largely follows the procedure developed by Galavi (2007). The partially non-local formulation only treats softening state variables as non-local quantities, while stresses and strains in the hardening regime are kept as local values. Previous applications in geotechnical boundary value problems have demonstrated that sufficient regularization and mesh independence can be achieved with this approach (Brinkgreve 1994, Marcher 2003).

Regularization is carried out on the macroscopic damage strain ε_d, which is the weighted sum of plastic normal strains from local deviatoric and Hvorslev yield surfaces (Equation 146). The weight factors w_i and the number of integration planes i depend on the chosen integration rule.

$$\varepsilon_d = \sum_i \left(\varepsilon^p_{n,HV} + \varepsilon^p_{n,cone}\right) \cdot w_i \tag{146}$$

As the value of the weight function $\omega'(r)$ in the non-local approach rapidly diminishes with increasing distance to the current point, only stress points within a sphere of radius $2l$ are taken into account. The position of these points, their corresponding weights ω'_m and the size of the finite elements are written into external files at the start of the calculation. The non-local value of the global damage strain is then calculated separately for each stress point as

$$\varepsilon^*_d = \frac{1}{V_w} \cdot \sum_{m=1}^{m_{SP}} \varepsilon_{d,m} \cdot \omega'_m \cdot V_m \quad \text{with} \tag{147}$$

$$V_w = \sum_{m=1}^{m_{SP}} \omega'_m \cdot V_m \ . \tag{148}$$

V_w is the weighted volume within a sphere of radius $2l$ around the current stress point, V_m is the volume of influence of each stress point, m_{SP} is the number of stress points within a sphere of radius $2l$, l is the internal length parameter and ω'_m are the weight factors according to Equation 145. Global damage strains $\varepsilon_{d,m}$ must be known beforehand for all stress points. Non-local damage strains can therefore only be obtained at the start of a calculation step, as plastic strains and change of damage strain of neighbouring stress points are unknown within the current calculation step. The non-local damage strain ε^*_{di} for each integration plane is calculated by multiplying the non-local global damage strain with the weight factor w_i.

$$\varepsilon^*_{di} = \varepsilon^*_d \cdot w_i \tag{149}$$

Non-local softening is only considered after the local Hvorslev yield surface is activated for the first time. The non-local damage strain at first contact with the Hvorslev yield surface, $\varepsilon^*_{di,peak}$, is stored as a state variable for each integration plane, and only the difference between current and peak damage strain is used in the softening calculation. The local softening law (Equation 132) can therefore be rewritten as

$$\sigma'^*_{nc} = -\left[\left(-\sigma'_{nc}\right)^{1-m} + K \cdot \frac{(m-1)}{p_{ref}^{m-1}} \cdot h_{soft} \cdot \left(\varepsilon^*_{di} - \varepsilon^*_{di,peak}\right)\right]^{\frac{1}{1-m}} \tag{150}$$

σ'_{nc} is the local hardening pre-consolidation stress, which defines the size of the cap yield surfaces in strain hardening. The cap yield surface increases with plastic normal strains from the cap yield surface according to Equation 35. The softening parameter h_{soft} controls the magnitude of softening for a given damage strain increment. The non-local pre-consolidation stress σ'^*_{nc} is only calculated after strain softening started, and hence ε^*_{di} is always larger than $\varepsilon^*_{di,peak}$. K, m and p_{ref} are parameters of the basic model as described in chapter 3.1.

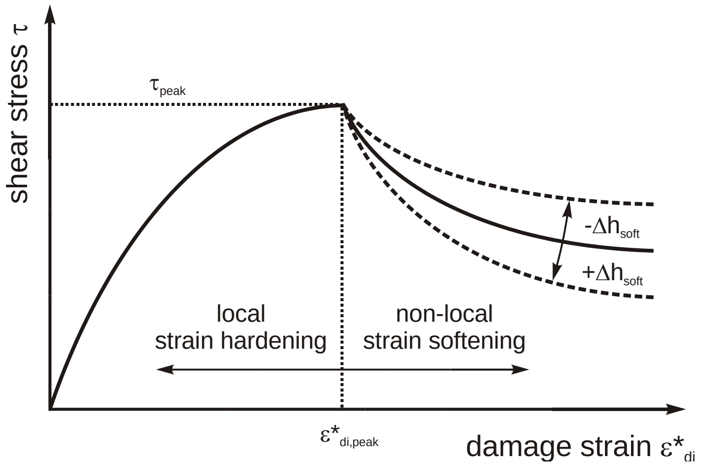

Fig. 87: Relation between mobilised shear stress and non-local damage strain on integration plane level

Even though contributions from the deviatoric yield surface are included in the macroscopic damage strain ε_d, dilatancy in deviatoric hardening does not result in reduction of σ'^*_{nc}, as non-local strain regularization only gets activated after peak strength has been mobilised. Strain softening in a neighbouring stress point only affects the current stress point if softening has already been initiated, i.e. the local Hvorslev yield surface has been reached. The impact of these assumptions on the evolution of shear bands will be discussed in section 6.5.4.

6.5 Numerical simulation of biaxial tests

The numerical biaxial test simulations reported in this chapter have been conducted to study the model behaviour in softening and to demonstrate the effectiveness of the non-local approach to obtain mesh independent results. These simulations are therefore not intended to reproduce specific experimental results.

Two different versions of the non-local approach are compared. Firstly, numerical simulations are presented which employ the “regular” approach described in previous sections of this chapter. In this approach, non-local strain regularization is only taken into account, once a stress point has reached its maximum shear strength. In another, “modified” version, non-local strain regularization is active from the onset of the simulation. The impact of these assumptions on the evolution of shear bands is discussed and results are compared with analytical solutions.

6.5.1 Numerical model and material properties

The test specimen is 1 m high and 0.5 m wide, with linear elastic, very stiff endplates at the top and the bottom of the specimen. Model symmetry is assumed in the standard calculations, and consequently only half of the biaxial specimen has been modelled in these simulations (Figure 88). In order to investigate the influence of boundary conditions, additional calculations have been performed with a full biaxial model, both with horizontally free and fixed top plate (Figure 89).

Plane strain, drained conditions are assumed in all calculations phases. The calculations are performed with small deformations, i.e. changes in model geometry and area of finite elements are not taken into account. Prescribed vertical displacements are transmitted to the specimen via the stiff endplates. Due to the restraint provided by the rough end plates, stress and strain distributions within the soil are non-uniform, which triggers the formation of shear bands without artificially introducing weak elements in the model. In order to enforce the formation of single shear bands in the full biaxial model with free top plate, a slight geometric shift of the top plate of 1 mm to the right has been applied.

Horizontal and vertical stresses of $\sigma'_h = \sigma'_v = -100$ kPa are applied at the start of the calculation, and horizontal stresses are kept constant during the simulation. The FE-meshes compared in this study contain 40, 86, 162 and 354 elements for the half model and 84, 156, 334 and 646 elements for the full biaxial model. 15-noded finite elements with forth-order shape functions and 12 Gauss points (stress points) per element are used.

Material parameters of reconstituted Pietrafitta clay (Table 19) are employed, with additional parameters for the non-local approach given in the corresponding sections of this chapter. Small strain stiffness effects have been neglected, as this study is focussed on post-peak behaviour.

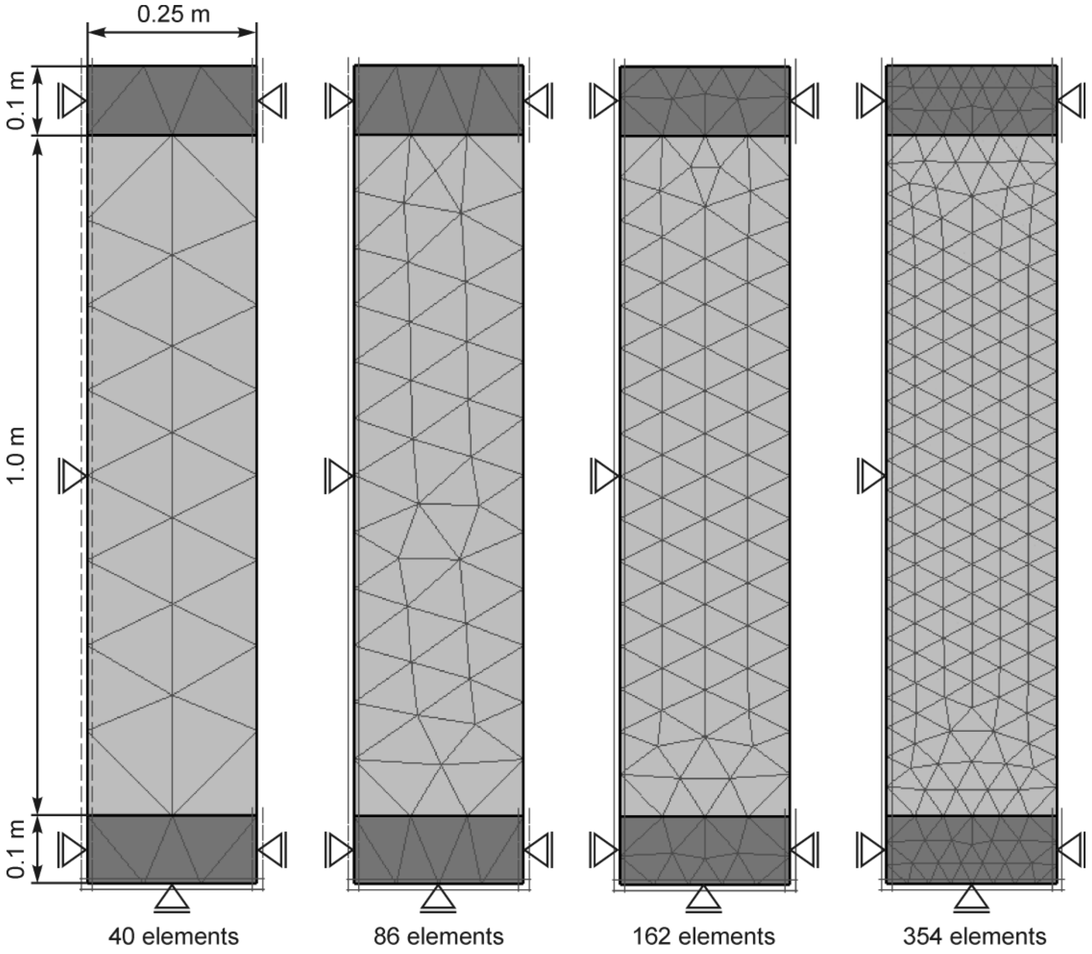

Fig. 88: Symmetric biaxial model and finite element meshes

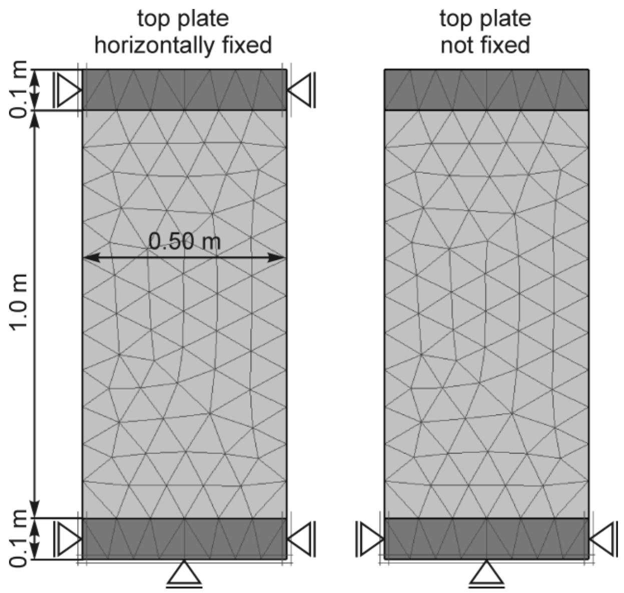

Fig. 89: Full biaxial model and boundary conditions

6.5.2 Results with regular approach

Mesh independence of load-displacement behaviour
Load-displacement curves of calculations without non-local strain regularization are shown in Figure 90 for the symmetric half model. A rather low softening rate of h_{soft} = 20 was used in these calculations to obtain numerically stable results with the finer FE-meshes. After peak strength is mobilised, results are strongly dependent on the coarseness of the FE-mesh. Finer meshes deliver faster strain softening and hence sharper decrease of vertical force than coarser meshes. Results obtained with the finest mesh show stepwise decrease of the vertical force, which indicates changes in the failure mechanism during softening.

Load displacement curves of the non-local calculations are shown in Figure 91 for the half model and in Figure 92 for the full biaxial model with free top plate. Simulations have been performed with an internal length of l_{cal} = 0.05 m and a softening parameter of h_{soft} = 40. Reasonable mesh independence is achieved up to u_y = 100 mm for both models, but curves diverge slightly at the residual load level in the half model. The difference between the coarsest and the finest mesh in the half model is about 10% at u_y = 200 mm. Post-peak softening proceeds at a significantly faster rate in the full biaxial model, if the top plate is allowed to move horizontally. Slightly better regularization is obtained with the full biaxial model. The meshes with 40 elements for the half model and 84 elements for the full appear to be slightly too coarse to achieve sufficient mesh independence at residual load level.

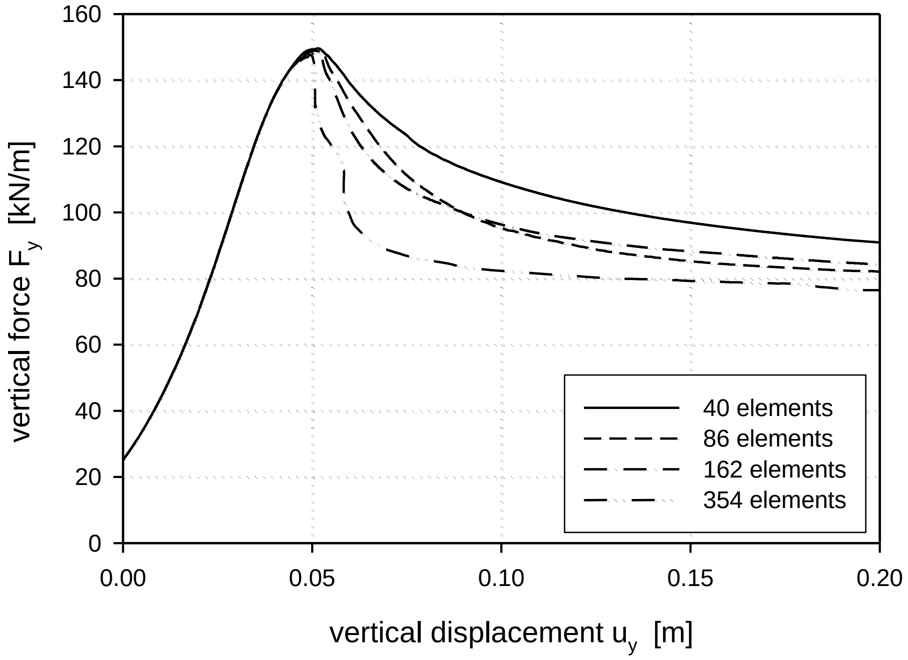

Fig. 90: Force-displacement curves of biaxial test simulations without strain regularization (h_{soft} = 20), half model

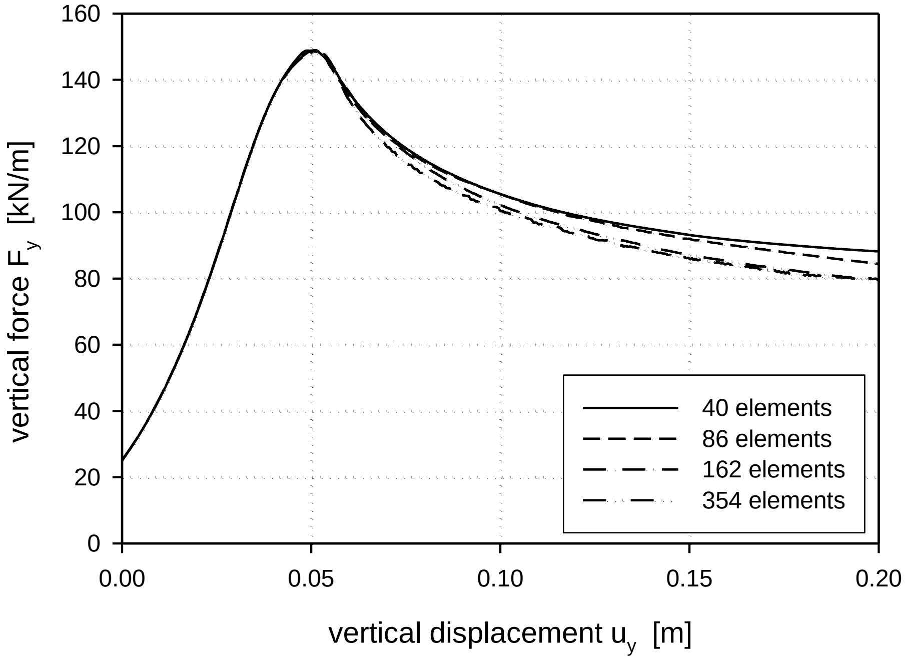

Fig. 91: Force-displacement curves of biaxial test simulations with strain regularization (l_{cal} = 0.05 m, h_{soft} = 40), half model

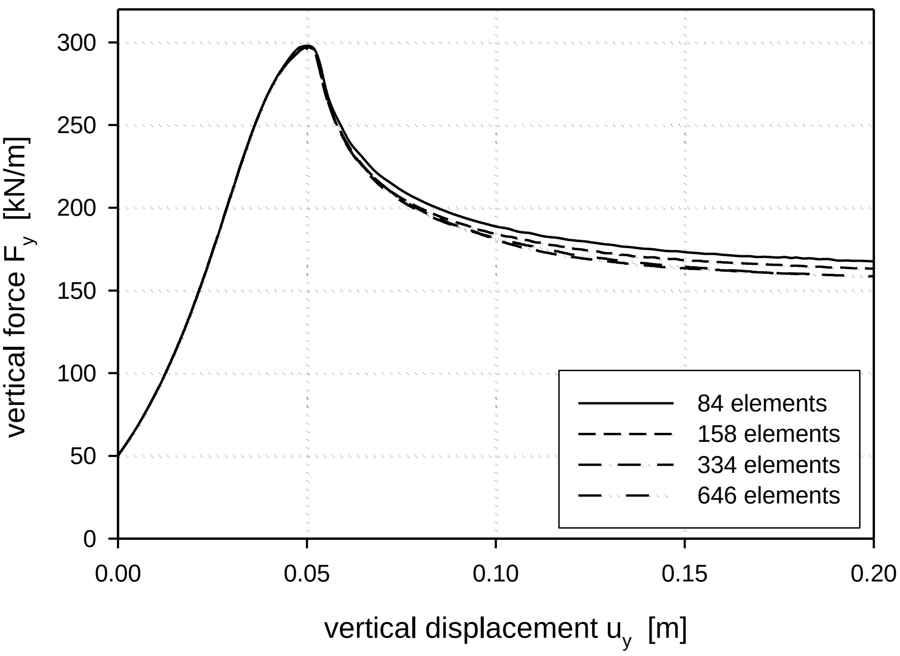

Fig. 92: Force-displacement curves of biaxial test simulations with strain regularization (l_{cal} = 0.05 m, h_{soft} = 40), full model

Evolution of shear bands

The distribution of accumulated shear strains at peak load is nearly symmetric and broadly similar for the various FE-meshes, with shear strains concentrated at mid height of the specimen and at the fixed end plates (Figure 93). Shortly after reaching the peak vertical force, shear strains start to concentrate in two narrow shear bands, which for the finer meshes are not symmetric.

The pattern of shear bands is very similar for the finer meshes (albeit in some cases mirrored to the horizontal), regardless whether non-local strain regularization is taken into account (Figure 95) or not (Figure 94). In both cases the inclination θ with respect to the horizontal is about 60-65° for the steep and about 35-40° for the shallow shear band. The steeper shear band develops first and is thicker than the shallow, secondary shear band.

This shear band pattern appears to be a result of the boundary conditions imposed by enforcing symmetry and consequently preventing any lateral movement of the top end plate. The simulations with a full biaxial model (Figure 96b, c) show, that strains concentrate in a single shear band, if the top plate is allowed to move laterally. Similar shear band patterns as with the half model are obtained, if the top plate is fixed laterally in the full biaxial model (Figure 96a).

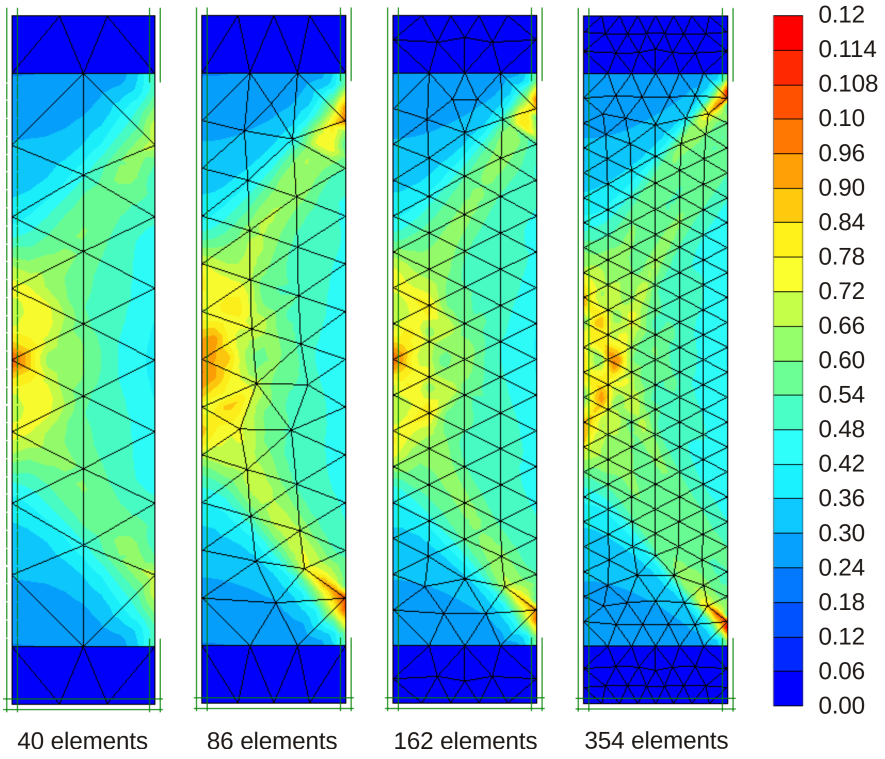

Fig. 93: Accumulated shear strains at peak vertical force, half model

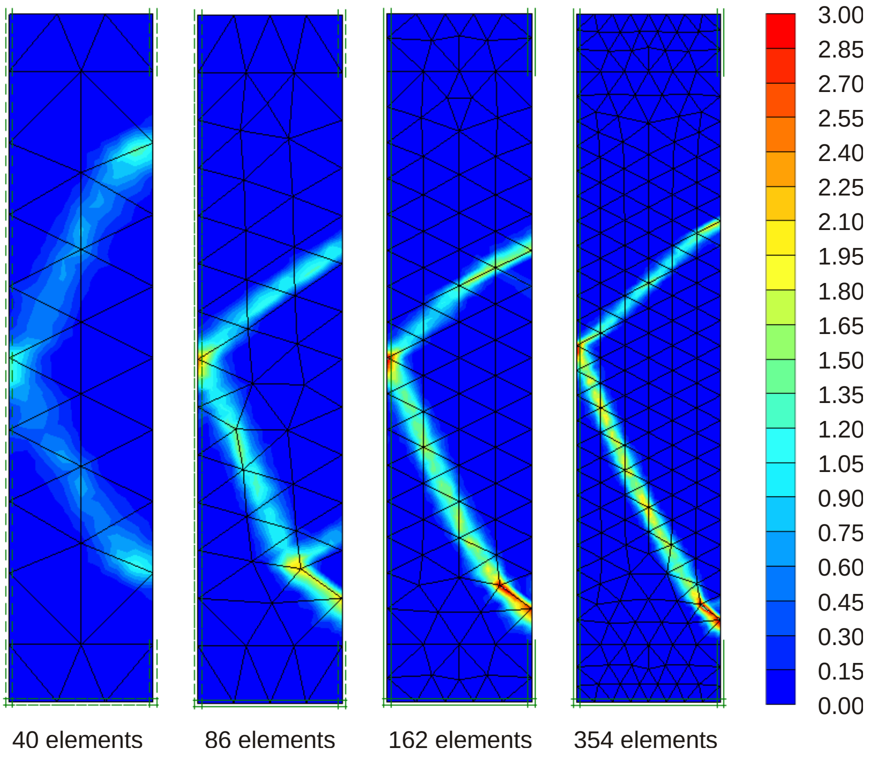

Fig. 94: Accumulated shear strains at u_y = 150 mm without strain regularization (h_{soft} = 20), half model

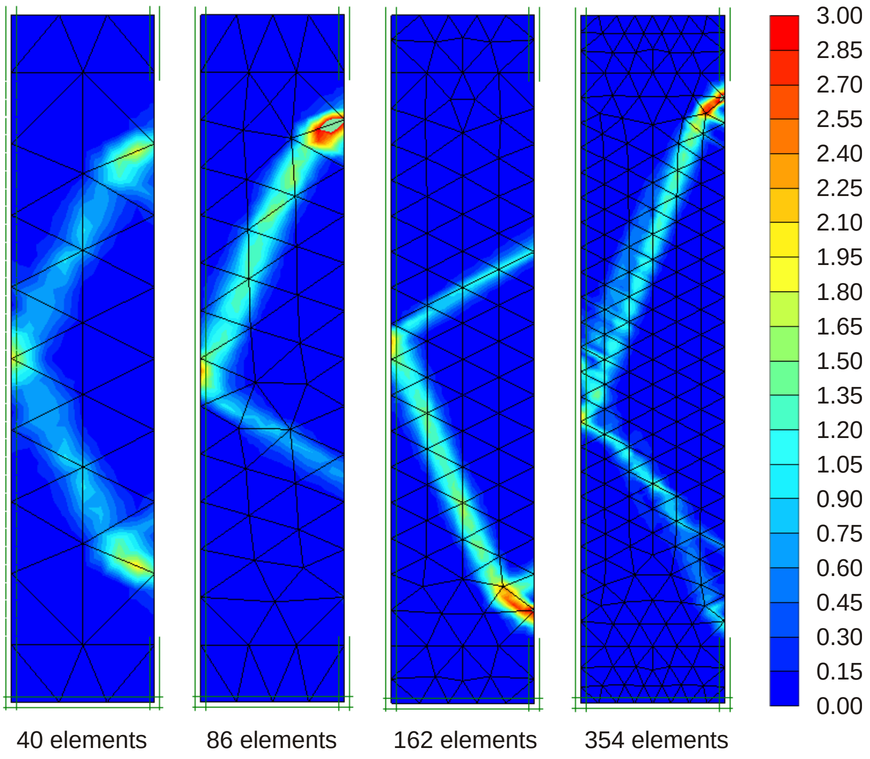

Fig. 95: Accumulated shear strains at u_y = 150 mm with non-local strain regularization (l_{cal} = 0.05 m, h_{soft} = 40), half model

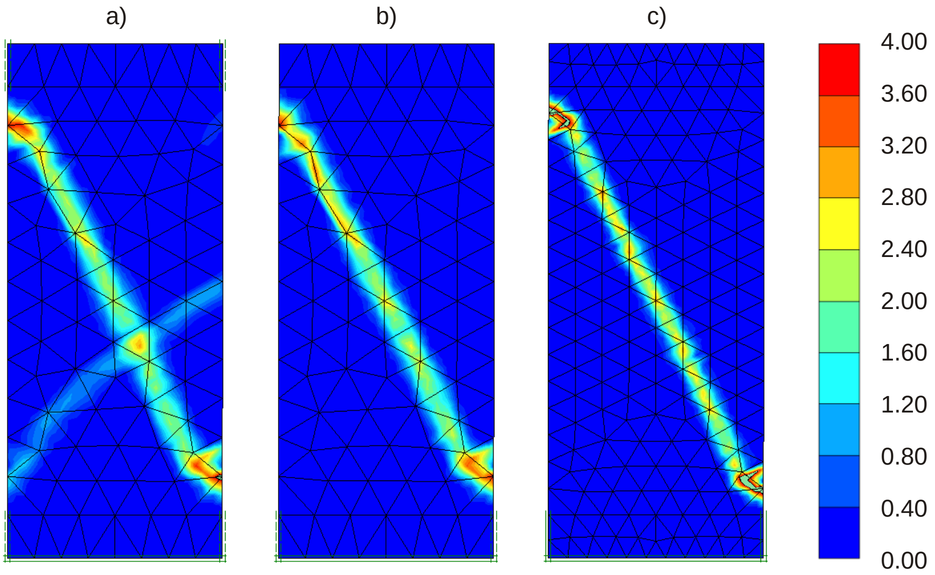

Fig. 96: Accumulated shear strains at u_y = 200 mm with non-local strain regularization in full biaxial model (l_{cal} = 0.05 m, h_{soft} = 40): a) both end plates horizontally fixed, 158 elements, b) top end plate horizontally free, 158 elements, c) top end plate horizontally free, 334 elements

The dependency of shear band patterns in biaxial tests on kinematic boundary conditions has also been observed experimentally. Desrues (1998) reported for dense sands, that two shear bands develop, if coaxiality of the end plates is enforced. The first shear band is the only mechanism for a long time, until the second shear band evolves shortly before the residual load level is reached.

The inclination of these two shear bands, however, is typically much closer to each other than in the numerical simulations presented here. Alshibli et al. (2003) found a difference of 3°-4° in biaxial tests on dense Ottawa sand. Comparable biaxial test results with horizontally restrained end plates are unfortunately not available for heavily overconsolidated clay. Most biaxial tests are carried out with testing equipment, in which one of the end plates is either free to move horizontally, or lubricated end plates are used (Vardoulakis & Goldscheider 1981, Drescher et al. 1990). In that case strains tend to localize into a single shear band (Mita 2002, Alshibli et al. 2007), as also observed in the numerical simulations here.

Two analytical solutions for the shear band inclination θ have been proposed: The Coulomb solution predicts the orientation of the plane in the Mohr's circle with the most critical stress ratio at failure and is therefore only related to φ' (Equation 151). Roscoe (1970) argued that the shear band at critical state is a line of zero extension, and θ is therefore related to the angle of dilatancy (Equation 152).

$$\theta_C = 45° + \frac{\varphi'_{max}}{2} \tag{151}$$

$$\theta_R = 45° + \frac{\psi_{max}}{2} \tag{152}$$

Experimental shear band inclinations plot between these bounds for most geomaterials, which led to the intermediate relationship proposed by Arthur et al. (1977):

$$\theta_A = 45° + \frac{\varphi'_{\max} + \psi_{\max}}{4} \tag{153}$$

In all three relationships the maximum friction angle at failure, φ'_{max}, and the maximum angle of dilatancy, ψ_{max}, are used. Based on experimental data Arthur & Dunstan (1982) reported that the shear band inclination changes from θ_C to θ_R with increasing particle size, which was later confirmed theoretically by Vermeer (1990). Desrues & Hammad (1989) showed experimentally for Hostun sand, that θ decreases slightly with increasing confining stress. Roscoe's solution, however, was out of the range of experimental results even at higher confining pressures.

Marcher (2003) compiled experimental data on coarse grained soils from various authors, which confirmed the trend observed by Desrues & Hammad. For fine grained, heavily overconsolidated Beaucaire marl, Marcher reported biaxial shear band inclinations of θ = 56-63° at low confining pressures of σ'_h = -100 kPa, which decreased to θ = 50-58° at σ'_h = -600 kPa.

Back calculating φ'_{max} in the numerical simulations from the overall effective stress ratio at peak delivers φ'_{max} = 45.3°, which according to the constitutive model yields ψ_{max} = 15.3°. The inclination of the numerical shear band in the full biaxial models (θ = 60-65°) is closer to the Coulomb (θ_C = 67.6°) than the Roscoe (θ_R = 52.7°) solution, and agrees reasonably well with experimental results on heavily overconsolidated Beaucaire marl at low confining pressure (Marcher 2003).

Stress level dependency of peak strength

One of the specific features of the multilaminate Hvorslev surface model is the dependency of peak strength and softening behaviour on stress level and degree of overconsolidation. Figure 97 shows the mobilisation of stress ratio σ'_v/σ'_h with increasing vertical displacement for different confining stresses σ'_h. Calculations have been performed with the full biaxial model with horizontally free top plate. The vertical stress σ'_v has been obtained by averaging the vertical force over the end plate length of 0.5 m.

With increasing confining stress, the peak stress ratio σ'_v/σ'_h reduces from 6.0 at σ'_h = -100 kPa to about 3.7 at σ'_h = -400 kPa. The softening rate directly after peak notably reduces with increasing confining stress, which compares well with experimental data (Burland et al. 1996, Callisto & Rampello 2004). Load displacement curves for the different confining stresses diverge slightly at residual load level, but plot close to the calculation without Hvorslev surface.

The analytical stress ratio at critical state is σ'_v/σ'_h = 3.0 (for φ'_{res} = 30°), which is about 7% less than the numerical results. This difference is a consequence of the multilaminate framework, which employs a set of predefined planes, whose orientation does not necessarily coincide with the plane of maximum stress obliquity.

The resultant overestimation of shear strength, which depends on the chosen integration rule, the friction angle and the stress state, has been investigated by Scharinger (2007), who found a maximum deviation of multilaminate prediction from the analytical result of ~9% for the integration rule with 2x33 planes. This is, however, not so critical in boundary value problems, as not all planes in all stress points deviate from the optimum orientation to the same degree.

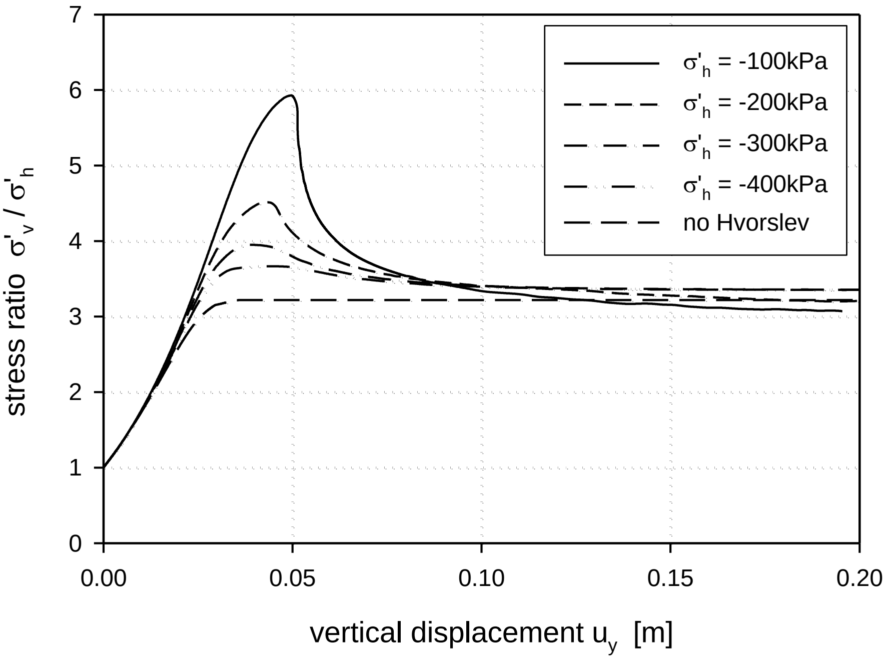

Fig. 97: Mobilisation of shear strength in biaxial test simulations for different confining stresses (l_{cal} = 0.05 m, h_{soft} = 80), full model

6.5.3 Softening scaling

The influence of the internal length parameter, l_{cal}, and the softening parameter, h_{soft}, on the post-peak load displacement behaviour has been studied in a series of biaxial test simulations. A full biaxial model with horizontally free top plate is used, as shown in Figure 89. Calculations have been performed with internal lengths l_{cal} = 0.05 m, 0.10 m and 0.20 m and with softening parameters h_{soft} = 20, 40 and 80. In all simulations finite element meshes with 158 15-noded elements have been utilized. Figure 98 shows the corresponding load-displacement curves for a horizontal confining pressure of -100 kPa. Reducing the internal length yields faster softening as strain regularization is confined to stress points closer to the shear band. A similar effect is obtained by increasing the local softening parameter.

It seems obvious, that an increase of the internal length can be compensated by a corresponding increase of the softening rate. Such a relation is particularly useful, as the non-local approach requires a sufficient number of stress points within the regularization area to work efficiently, which poses a lower limit for the internal length for a given finite element size. From the calculations of the previous section it is concluded that satisfactory regularization is obtained if the following condition is satisfied for 15-noded triangular elements:

$$l_{cal} \geq 0.5 \cdot L_{el} \tag{154}$$

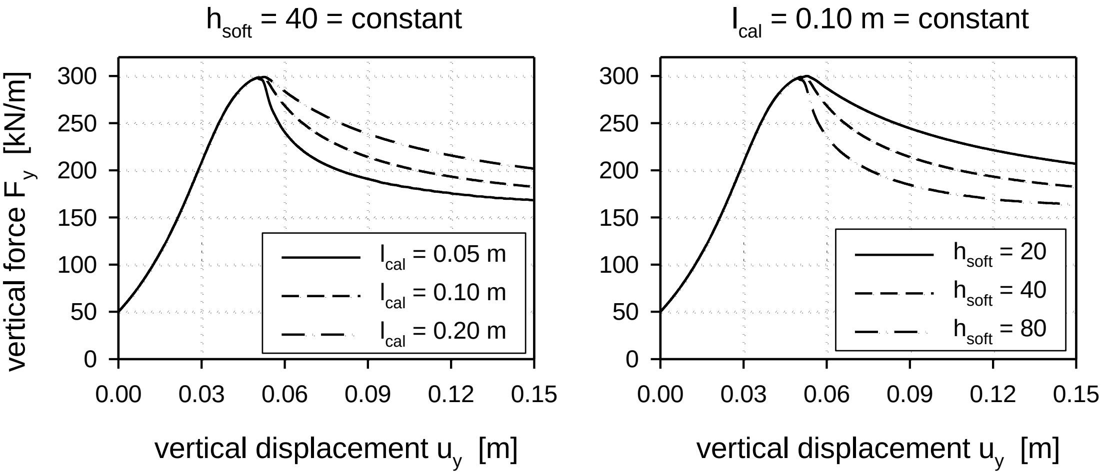

Fig. 98: Force-displacement curves of biaxial test simulations with varying internal length (left) and varying softening parameter (right)

L_{el} is the edge length of the triangular finite element. With that condition at least about 100 stress points are taken into account in strain regularization. If h_{soft} has been calibrated in back-calculations of small scale laboratory tests with a fine FE-mesh and a small internal length, h_{soft} can be scaled to coarser meshes and hence to a larger value of l_{cal} with the following linear relationship:

$$\frac{h_{soft,1}}{l_{cal,1}} = \frac{h_{soft,2}}{l_{cal,2}} \tag{155}$$

This scaling of the softening rate was suggested by Brinkgreve (1994), based on previous work by Pietruszczak & Mroz (1981), for a linear softening rate, i.e. for models in which the reduction of shear strength for a given plastic strain increment does not depend on the accumulated plastic strains. However, softening scaling also works reasonably well in the multilaminate Hvorslev surface model, which employs a non-linear softening rate. Figure 99 shows load-displacement curves of four biaxial test simulations with different combinations of h_{soft} and l_{cal}, but the same ratio of h_{soft}/l_{cal}. Finer meshes have been used for the simulations with l_{cal} = 0.05 m and 0.025 m in order to fulfil Equation 154. Very similar load-displacement curves are obtained for all cases, which demonstrates the applicability of linear softening scaling. It is therefore possible to carry out strain softening calculations with relatively coarse FE-meshes and fairly large internal lengths l_{cal}, if the softening parameter h_{soft} is adjusted according to Equation 155.

The experimental shear band thickness of a granular material – which can be regarded as the ‘real’ internal length – is related to the average grain diameter (~10…20·d_{50} for sand, Marcher 2003). A clear relationship between the internal length l_{cal} and the numerical shear band thickness obtained with the multilaminate model, however, could not be established. Calculations using the same FE-mesh but different internal lengths yield about the same numerical shear band thickness, while simulations with different meshes and the same value of l_{cal} show that the numerical shear band thickness varies with mesh coarseness (Figure 96).

A combination of non-local strain regularization and adaptive re-meshing in areas with high strain gradients could be used to ensure that a sufficient number of stress points are taken into account in the non-local approach while using a relatively coarse mesh outside the shear band area.

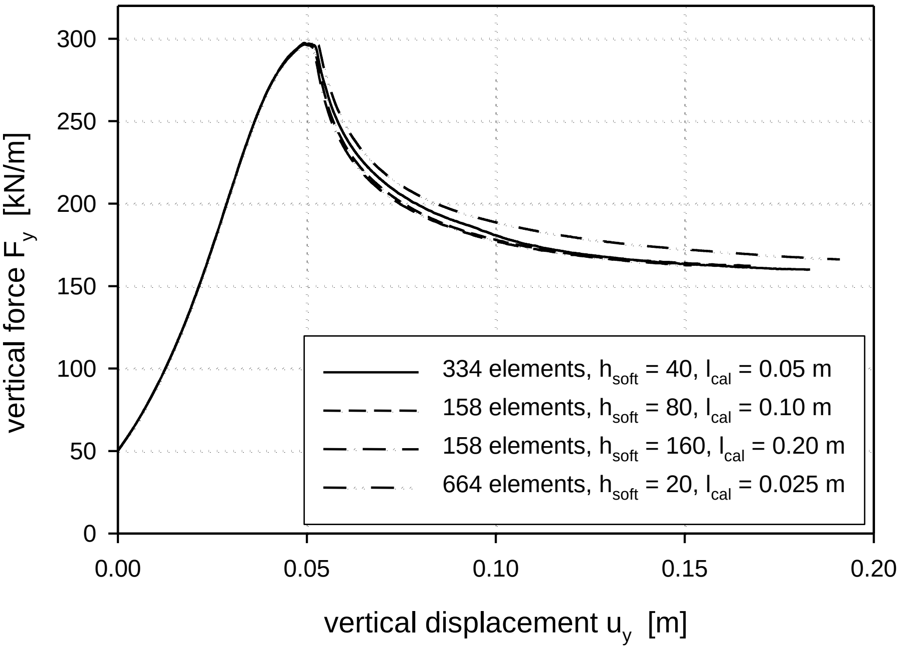

Fig. 99: Force-displacement curves of biaxial test simulations using softening scaling

6.5.4 Impact of non-local strain regularization in the pre-peak range

Non-local strain regularization is only activated in the regular model, once the stress point has mobilised its maximum shear strength, i.e. the stress path on at least one integration plane has reached the Hvorslev surface. Strain softening in neighbouring stress points therefore only affects stress points which have mobilised peak strength themselves. Consequently, the damage strain is distributed within the model, but does not necessarily induce strain softening in the vicinity of the existing shear band. Thereby the ability of the shear band to move within the numerical model is limited. The regular model differs in this aspect from other implementations of the non-local approach (Brinkgreve 1994, Marcher 2003, Tejchman 2004), which treat the softening state variable as a non-local quantity also before peak strength is reached.

In order to investigate the impact of pre-peak strain regularization, additional calculations have been performed with a slightly modified model, which employs non-local strain regularization from the start of the calculation (Figure 100). Dilatant plastic normal strains from the deviatoric yield surface cause a reduction of σ'_{nc} before the initial Hvorslev surface is reached. All constitutive equations at stress point level as well as the non-local weighting function are taken from the regular model.

Within boundary value problems, stress points outside the numerical shear band reduce in shear strength before any plastic strains might be generated by the stress point itself. Consequently, this modified implementation resembles the versions of the non-local approach mentioned above.

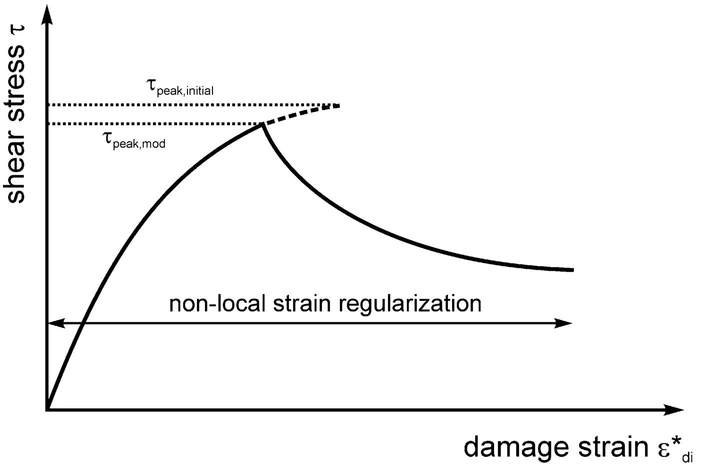

Fig. 100: Modified non-local strain regularization

Numerical biaxial simulations have been performed with the half model with enforced symmetry and with the full biaxial model with free top plate. In the full model, a slight geometric shift of the top plate of 1 mm to the right enforces strain localization into a single shear band. Calculations have been conducted with non-local softening parameters l_{cal} = 0.05 m and h_{soft} = 40.

Figure 101 shows load-displacement curves for the half model with four different FE-meshes and for one full biaxial test simulation with 158 finite elements. Load-displacement curves for the half model show good regularization and no significant mesh dependency. The peak vertical force of ~142 kN is slightly lower than obtained with the previous approach due to allowance for pre-peak reduction of the initial shear strength. To obtain comparability with the half model, the vertical force of the full biaxial model in Figure 101 has been halved.

As already seen with the previous approach, allowing the top plate to move horizontally in the full biaxial model yields slightly faster softening.

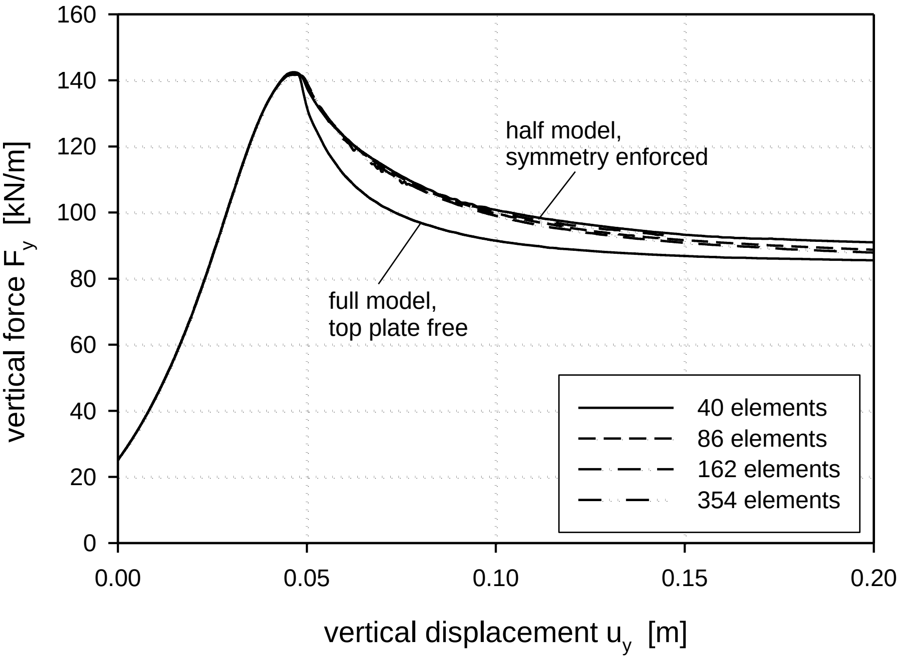

Fig. 101: Force-displacement curves of biaxial test simulations with modified non-local strain regularization (l_{cal} = 0.05 m, h_{soft} = 40), half model with four different FE-meshes, full model with 158 elements

While shear strain distributions at peak strength resemble those obtained with the regular model, shear bands at residual load show inclinations $\theta \approx 45°$ or even slightly below (Figure 102). The full biaxial model delivers essentially identical shear band inclinations (Figure 103). These flat shear bands are therefore not a result of the kinematic boundary condition imposed by assuming an axis of symmetry, or by preventing horizontal movement of the end plates in the half model.

Such low values of θ are rather unusual for frictional materials. They are, however, frequently observed in biaxial test simulations, when non-local strain regularization is employed. Shear band inclinations of less than 45° have been obtained by Grimstad and Jostad (2011) in biaxial simulations with the non-local NGI-ADPSOFT model for three different weighting functions. Tejchman (2004) reported inclinations of ~45° from drained biaxial test simulations using a hypoplastic model with Cosserat-continuum and a non-local hypoplastic model. Brinkgreve (1994) conducted drained biaxial test simulations with a non-local, strain softening Drucker-Prager model and found shear band inclinations of θ = 45° in purely cohesive material (no dilatancy), and $\theta = 45° + \psi/2$ for frictional material. Changing the friction angle φ' while holding dilatancy constant delivered identical values of θ. He therefore concluded, that the shear band inclination in plane strain is a result of his model, which enforces the Roscoe solution, $\theta = 45° + \psi/2$.

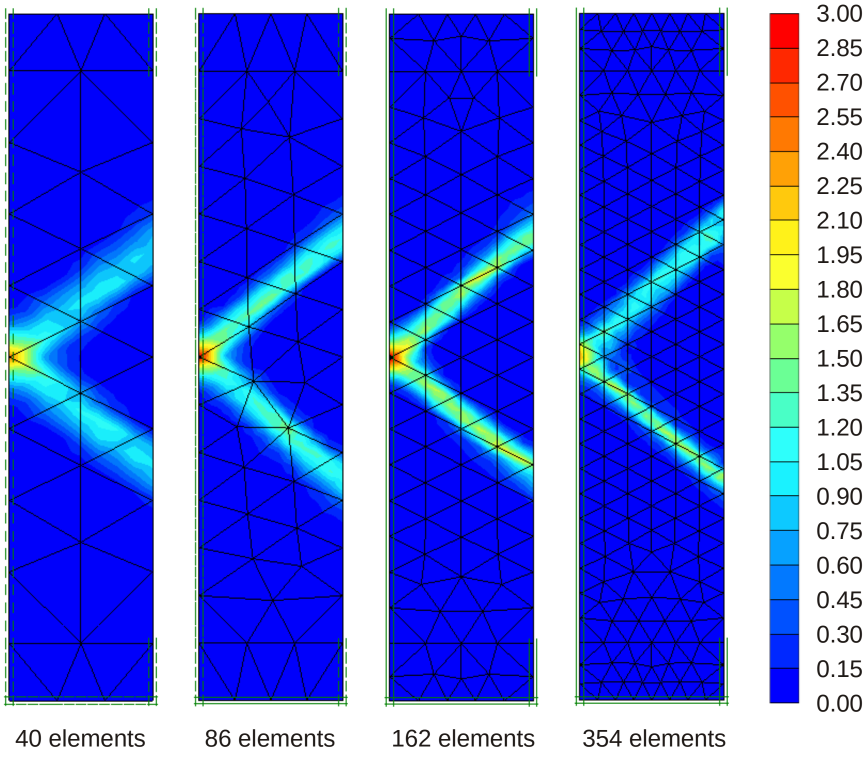

Fig. 102: Accumulated shear strains at residual vertical force with modified non-local strain regularization in half model (l_{cal} = 0.05 m, h_{soft} = 40)

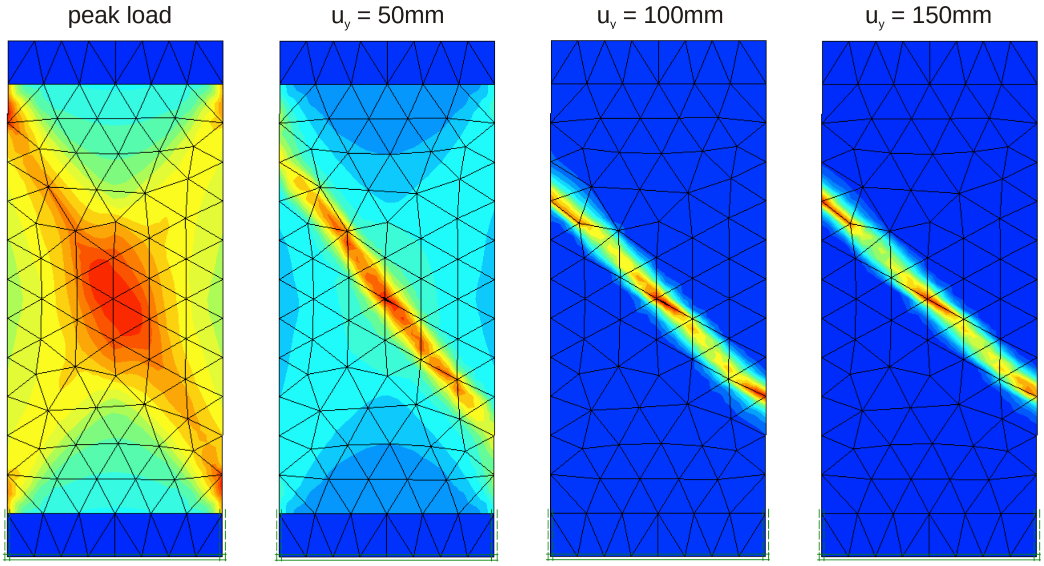

Fig. 103: Shear band evolution in full biaxial model with modified non-local strain regularization (l_{cal} = 0.05 m, h_{soft} = 40)

In view of published numerical studies employing various constitutive models, this appears to be a result of non-local strain regularization rather than the constitutive model. Tejchman's results (whose hypoplastic model emulated $\psi = 0$ at residual shear strength) and also the shear bands presented here with the modified softening model can be explained by the assumption of zero dilatancy at critical state. The various models may predict values of $\theta > 45°$ at peak strength, but as the non-local regularization allows the shear band to move, and $\psi = 0$ is assumed at critical state, eventually $\theta = 45°$ is obtained. The same effect is observed with the modified non-local multilaminate model. Figure 104 shows residual shear bands, obtained with the modified model for different values of φ'_{cs}. The inclination of the Hvorslev surface, φ'_{e}, has been varied with φ'_{cs}, such that $\varphi'_{\mathrm{cs}} - \varphi'_{\mathrm{e}}$ remained constant. Irrespective of the friction angle at critical state, shear band inclinations of about 45° are obtained in all three cases.

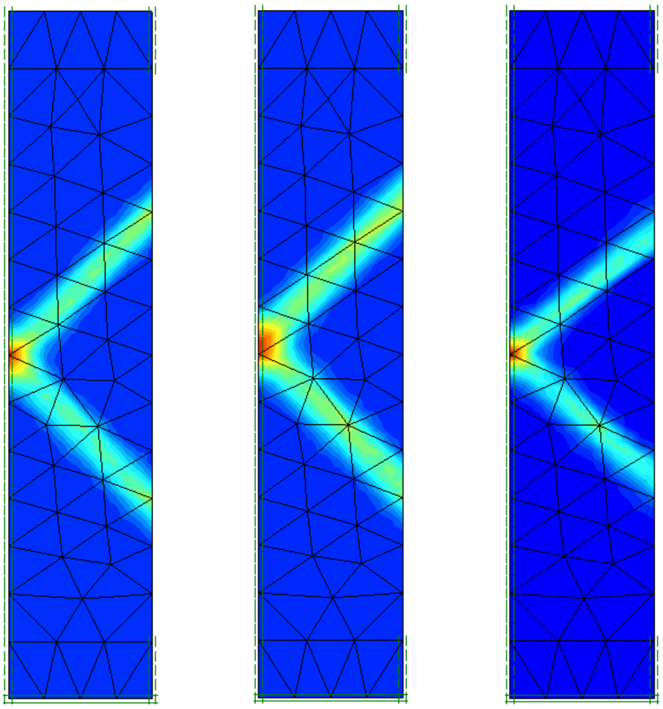

$\varphi'_{cs} = 20°$
$\varphi'_{e} = 13.8°$

$\varphi'_{cs} = 25°$
$\varphi'_{e} = 18.8°$

$\varphi'_{cs} = 30°$
$\varphi'_{e} = 23.8°$

Fig. 104: Accumulated shear strains with modified non-local regularization for different values of φ'_{cs} ($l_{cal} = 0.05$ m, $h_{soft} = 40$, half model)

However, no such rotation of shear bands is observed in laboratory tests. Shear bands typically develop at peak strength (or slightly before) with inclinations between the Roscoe and the Coulomb solution, but remain virtually constant in further loading (Arthur et al. 1977, Desrues & Viggiani 2004). The shear band inclination obtained with non-local strain regularization in the pre-peak range in strain hardening models therefore may not match the behaviour of typical geomaterials, if the constitutive model assumes $\psi = 0$ at critical state.

Only if the internal length parameter *l* comes close to the size of a realistic shear band thickness, inclinations $\theta > 45°$ are obtained. This is shown in Figure 105 for a very fine FE mesh of 2440 15-noded elements (l_{cal} = 1.0 cm, h_{soft} = 3). Thus, it appears that very fine FE-meshes (which facilitate low values of l_{cal} and thin numerical shear bands) are necessary to obtain realistic shear band orientations, if non-local strain regularization is applied in the pre-peak range.

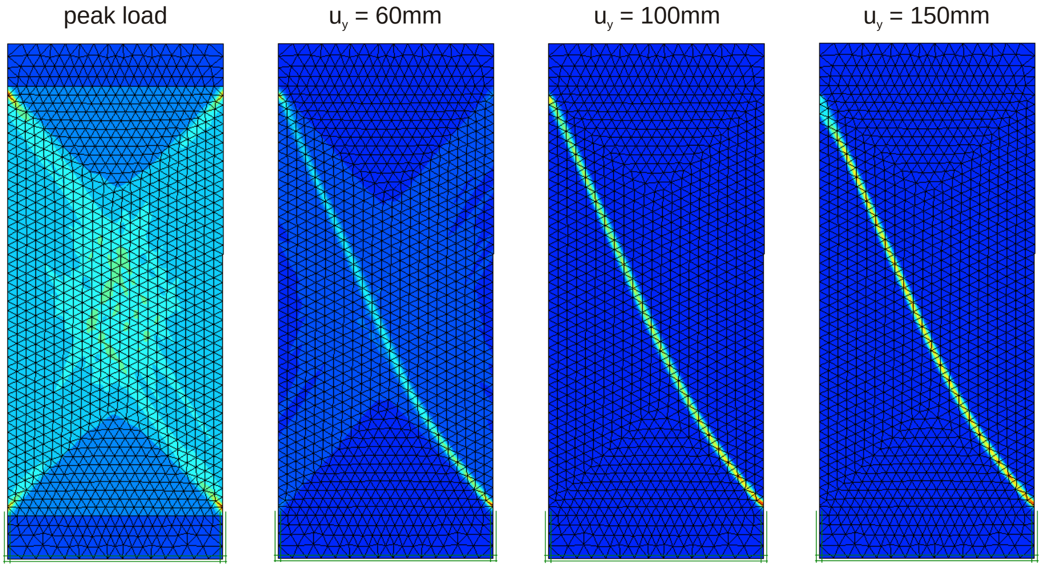

Fig. 105: Accumulated shear strains with modified non-local regularization for very small shear band thickness (l_{cal} = 0.01 m, h_{soft} = 3, full model)

The tendency of the non-local approach to predict Roscoe-type shear bands with coarse finite element meshes may be related to the kinematics of the numerical shear band. Unless very fine FE-meshes are used, the numerical shear band thickness is usually rather large compared to model dimensions (and much larger than observed in experiments). Implicitly, a very coarse grained material with a large shear band thickness is modelled, and consequently shear band inclination primarily depends on dilatancy, as shown analytically by Vermeer (1990). If shear bands are allowed to move within the numerical model, they therefore tend to evolve along lines of zero extension, as predicted by Roscoe's solution.

6.5.5 Conclusion for non-local approach

Two different implementations of the non-local approach have been presented:

1. The 'regular' version uses non-local strain regularization only once a stress point has reached its maximum shear strength. Softening is confined to the shear band itself, and the material around the shear band is not affected by plastic strains produced within the shear band. Consequently, the ability of the shear band to move within the numerical

model is limited, and the inclination of the shear band is primarily defined by conditions at peak strength.

2. In the ‘modified’ version, plastic damage strains are regularized also in the pre-peak range. The shear strength of stress points in the vicinity of a developing shear band reduces, even if these points have not fully mobilised their respective initial strength. The shear band can change its position within the model relatively easily.

Version 2 performs slightly better as far as mesh independent load-displacement curves are concerned. However, the tendency of shear bands to change their orientation in softening is problematic and does not agree with analytical solutions and experimental data. Apparently, shear bands level off at 45° to the horizontal, unless very small internal lengths and very fine FE-meshes are used.

Version 1 delivers reasonable (albeit not perfect) mesh independence of load-displacement behaviour. More importantly, the position of shear bands is defined at peak and agrees reasonably well with experimental results also for coarser meshes. Judging from the results of the biaxial test simulations, version 1 is therefore to be preferred over version 2.

However, the performance of these two versions in larger, more practical boundary value problems is hard to extrapolate from the biaxial simulations, as not all constraints of the biaxial test are practically relevant. In many cases, the position of shear bands is virtually fixed by geometrical constraints, which would prevent the unrealistic rotation of shear bands seen with 2.

Furthermore, shear band thickness is typically rather small compared to model dimensions in such problems, which reduces the impact of boundary conditions on shear band orientation. The two versions of the non-local approach should thus be finally evaluated after they have been applied to a variety of different boundary value problems.

7 Conclusion and further research

7.1 Conclusion

A constitutive model for heavily overconsolidated clay and dense sand for application in finite element calculations has been presented. The model is formulated within the multilaminate framework, which means that material behaviour is modelled on so called integration planes of varying orientation. Yield and plastic potential functions for the calculation of plastic strains are defined independently on the integration planes. The model can therefore account for strain induced anisotropy without additional input parameters. The macroscopic deformation is obtained by numerical integration over the integration planes according to a predefined integration rule, which governs the accuracy of model predictions. In this study 66 (2x33) integration planes have been used for carrying out the numerical integration.

The model presented in this thesis is based on previous work carried out at TU Graz. The non-linear stress dependency of stiffness parameters proposed by Scharinger (2007) has been combined with anisotropic shear strength and strain softening developed by Galavi (2007). Calculation speed was significantly improved by modifying the convergence criterion on stress point level without compromising on the accuracy of numerical results. Other improvements include the treatment of corner points in the yield surface and the automatic determination of the shape of the cap yield surface.

Two new features have been added to improve the predictive capabilities of the model for heavily overconsolidated clay and dense sand: Cross-anisotropic stiffness in the small strain range can be taken into account, and the shear strength of stiff clays on the dry side of the critical state line is defined by a Hvorslev yield surface with subsequent strain softening.

Modelling of stiffness anisotropy by a microstructure tensor has been compared with the spectral decomposition of the elastic compliance matrix. Better match with experimental data is obtained with the latter method, as the microstructure tensor approach cannot cover the whole range of cross-anisotropic stiffness characteristics. Degradation of small strain stiffness with accumulating strains is modelled by a logarithmic function. Stiffness recovery with changes in loading direction is governed by the evolution and removal of strain history contours, which are utilized to store the loading history of the integration plane. The model can account for the differences in stress dependency of small strain stiffness observed in experiments on fine and coarse grained soils.

The influence of cross-anisotropic stiffness in the small strain range has been studied in an excavation problem and a strip footing calculation. While deformations in the excavation problem were governed by the equivalent shear stiffness activated in the corresponding loading direction, footing settlements could be related to the mean axial stiffness of the soil at small strains.

To improve shear strength predictions for heavily overconsolidated clay, a Hvorslev yield surface has been introduced on integration plane level. An important feature of the model is the consideration of plastic strains before peak strength is mobilised. Comparison with experimental data on Vallericca and Pietrafitta clay shows good agreement in predicted shear strength and stress-strain behaviour. To avoid the numerical problems associated with strain softening in numerical analysis, non-local strain regularization is employed in the post-peak range. Biaxial test simulations demonstrated that mesh independent results are obtained. Scaling of the softening rate facilitates the application of the model in practical boundary value problems.

7.2 Further research

The multilaminate model presented in this thesis can account for various advanced facets of soil behaviour, like anisotropy in strength and stiffness, strain softening and non-linear small strain behaviour. It is recommended, that further research on the multilaminate model may focus on the following aspects:

- Development of a new deviatoric hardening rule to improve model predictions for varying confining stresses.
- Application of the Hvorslev surface model to geotechnical boundary value problems to assess numerical robustness and predictive capabilities.
- Evaluation of the impact of different assumptions in non-local strain regularization on the evolution of shear bands in geotechnical problems.
- Systematic investigation of the influence of anisotropy (both in strength and stiffness) and strain softening in geotechnical problems.
- Implementation of kinematic hardening in order to obtain more realistic results in large stress reversals and in cyclic loading.

8 Bibliography

Addenbrooke, T.I.; Potts, D.M.; Puzrin, A.M. (1997)
The influence of pre-failure soil stiffness on the numerical analysis of tunnel construction. Géotechnique, Vol. 47, No. 3, 693-712.

Aifantis, E.C. (1984)
Microscopic processes and macroscopic response. Mechanics of Engineering Materials, Desai & Gallagher (eds.), 1-22.

Alshibli, K.A.; Batiste, S.N.; Sture, S. (2003)
Strain localization in sand: plane strain versus triaxial compression. Journal of Geotechnical and Geoenvironmental Engineering, Vol. 129, No. 6, 483-494.

Alshibli, K.A.; Akbas, I.S. (2007)
Strain localization in clay: plane strain versus triaxial loading conditions. Geotechnical and Geological Engineering, Vol. 25, 45-55.

Al-Tabbaa, A.; Muir Wood, D. (1989)
An experimentally based “bubble” model for clay. Proc. 3rd International Symposium on Numerical Models in Geomechanics (NUMOG III), Pietruszczak & Pande (eds.), Niagara Falls, Canada, 91-99.

AnhDan, L.Q.; Koseki, J. (2005)
Small strain behaviour of dense granular soils by true triaxial tests. Soils and Foundations, Vol. 45, No. 3, 21-38.

Anhdan, L.Q.; Koseki, J.; Sato, T. (2006)
Evaluation of quasi-elastic properties of gravel using a large-scale true triaxial apparatus. Geotechnical Testing Journal, Vol. 29, No. 5, 374-384.

Arthur, J.R.F.; Menzies, B.K. (1972)
Inherent anisotropy in a sand. Géotechnique, Vol. 22, No. 1, 115-128.

Arthur, J.R.F.; Dunstan, T.; Al-Ani, Q.A.J.L.; Assadi, A. (1977)
Plastic deformation and failure in granular media. Géotechnique, Vol. 27, No. 1, 53-74.

Arthur, J.R.F.; Dunstan, T. (1982)
Rupture layers in granular materials. Proc. IUTAM Conference on Deformation and Failure of Granular Materials, Vermeer & Luger (eds.), Delft. Netherlands, 453-459.

Atkinson, J.H. (1975)
Anisotropic elastic deformations in laboratory tests on undisturbed London Clay. Géotechnique, Vol. 25, No. 2, 357-374.

Atkinson, J.H.; Sallfors, G. (1991)
Experimental determination of stress-strain-time characteristics in laboratory and in situ tests. Proc. 10th European Conference on Soil Mechanics and Foundation Engineering, Associazione Geotechnica Italiana (ed.), Florence, Italy, Vol. 3, 915-956.

Batdorf, S.B.; Budiansky, B. (1949)
A mathematical theory of plasticity based on the concept of slip. National Advisory Committee for Aeronautics, TN 1871.

Bažant, Z.P. (1984)
Microplane model for strain-controlled inelastic behaviour. Mechanics of Engineering Materials, Desai & Gallagher (eds.), 45-59.

Bažant, Z.P.; Gambarova, B. (1984)
Crack shear in concrete: crack band microplane model. Journal of Structural Engineering, Vol. 110, No. 9, 2015-2036.

Bažant, Z.P.; Oh, B.H. (1983)
Microplane model for fracture analysis of concrete structures. Proc. 1st International Symposium on the Interaction of Non-Nuclear Munitions With Structures, U.S. Air Force Academy, Colorado Springs, United States, 49–53.

Bažant, Z.P.; Oh, B.H. (1986)
Efficient Numerical Integration on the Surface of a Sphere. Zeitschrift für angewandte Mathematik und Mechanik (ZAMM), Vol. 66, 37-49.

Bažant, Z.P.; Prat, P.C. (1988)
Microplane model for brittle-plastic material. I. Theory, Journal of Engineering Mechanics, Vol. 114, No. 10, 1672-1688.

Bellotti, R.; Jamiolkowski, M.; Presti, D.C.F.; O'Neill, D.A. (1996)
Anisotropy of small strain stiffness in Ticino sand. Géotechnique, Vol. 40 No. 4, 115-131.

Benz, T. (2007)
Small-Strain Stiffness of Soils and its Numerical Consequences. Ph.D. Thesis, Mitteilungsheft Nr. 55, Institute for Geotechnical Engineering, University of Stuttgart.

Benz, T.; Vermeer, P.A.; Schwab, R. (2009)
A small-strain overlay model. International Journal for Numerical and Analytical Methods in Geomechanics, Vol. 33, No. 1, 25-44.

Brinkgreve, R.B.J. (1994)
Geomaterial models and numerical analysis of softening. Ph.D. thesis, Delft university press.

Brinkgreve, R.B.J.; Swolfs, W.M.; Engin, E. (2011)
PLAXIS 2D 2010 - Users Manual. Plaxis bv, Delft, The Netherlands.

Bolton, M. D. (1986)
The strength and dilatancy of sands. Géotechnique, Vol. 36, No. 1, 65-78.

de Borst, R. (1991)
Simulation of strain localization: A reappraisal of the Cosserat continuum. Engineering Computations, Vol. 8, No. 4, 317-332.

Burland, J.B. (1989)
Small is beautiful - the stiffness of soils at small strains. Ninth Laurits Bjerrum Memorial Lecture. Canadian Geotechnical Journal, Vol. 26, No. 4, 499–516.

Burland, J.B.; Rampello, S.; Georgiannou, V.N.; Calabresi, G. (1996)
A laboratory study of strength of four stiff clays. Géotechnique, Vol. 46, No. 3, 491-514.

Callisto, L.; Rampello, S. (2002)
Shear strength and small-strain stiffness of a natural clay under general stress conditions. Géotechnique, Vol. 52, No. 8, 547-560.

Callisto, L.; Rampello, S. (2004)
An interpretation of structural degradation for three natural clays. Canadian Geotechnical Journal, Vol. 41, No. 3, 392-407.

Carol, I.; Bažant Z.P. (1997)
Damage and plasticity in microplane models. International Journal of Solids and Structures, Vol. 34, No. 29, 3807-3835.

Carol, I.; Jirasek, M.; Bažant Z.P. (2001)
A thermodynamically consistent approach to microplane theory. Part I. Free energy and consistent microplane stresses. International Journal of Solids and Structures, Vol. 38, No. 9, 2921-2931.

Carol, I.; Prat, C.P.; Bažant Z.P. (1992)
New explicit microplane model for concrete: Theoretical aspects and numerical implementation. International Journal of Solids and Structures, Vol. 29, No. 9, 1173–1191.

Cole, K.W.; Burland, J.B. (1972)
Observations of retaining wall movements associated with a large excavation. Proc. 5th European Conference on Soil Mechanics and Foundation Engineering, Sociedad Espanola de Mecanica del Suelo y cimentaciones (ed.), Madrid, Spain, 1445-1453.

Cudny, M.; Vermeer, P.A. (2004)
On the modelling of anisotropy and destructuration of soft clays within the multi-laminate framework. Computers and Geotechnics, Vol. 31, 1-22.

Cundall, P.A.; Strack, O.D.L. (1979)
A discrete numerical model for granular assemblies. Géotechnique, Vol. 29 No. 1, 47-65.

Cusatis, G.; Beghini, A.; Bažant, Z.P. (2008)
Spectral stiffness microplane model for quasibrittle composite laminates - Part I: Theory. Journal of Applied Mechanics, ASME, Vol. 75, No. 2, 021009.

Cusatis, G.; Beghini, A.; Bažant, Z.P. (2008)
Spectral stiffness microplane model for quasibrittle composite laminates - Part II: Calibration and Validation. Journal of Applied Mechanics, ASME, Vol. 75, No. 2, 021009.

Dafalias, Y.F.; Manzari, M.T.; Papadimitriou, A.G. (2006)
SANICLAY: simple anisotropic clay plasticity model. International Journal for Numerical and Analytical Methods in Geomechanics, Vol. 30, No. 12, 1231-1257.

Desrues J. (1998)
Localization patterns in ductile and brittle geomaterials. Material Instabilities in Solids, Borst & van der Giessen (eds.), Wiley-Interscience-Europe, 137-158.

Desrues J.; Hammad, W. (1989)
Shear banding dependency on mean stress level in sand. Proc. 2nd International Workshop on Localisation and Bifurcation, Dembicki, Gudehus & Sikora (eds.), Gdansk, Poland, 57-68.

Desrues J.; Viggiani, G. (2004)
Strain localization in sand: an overview of the experimental results obtained in Grenoble using stereophotogrammetry. International Journal for Numerical and Analytical Methods in Geomechanics, Vol. 28, No. 4, 279–321.

Desrues, J.; Zweschper, B.; Vermeer, P.A. (2000)
Database for tests on Hostun RF Sand. Institutsbericht Nr. 13, Institute for Geotechnical Engineering, University of Stuttgart.

Drescher, A.; Vardoulakis, I.; Han, C. (1990)
A biaxial apparatus for testing soils. Geotechnical Testing Journal, Vol. 13, No. 3, 226–234.

Ehret, A.; Itskov, M.; Schmid, H. (2010)
Numerical integration on the sphere and its effect on the material symmetry of constitutive equations - A comparative study. International Journal for Numerical Methods in Engineering, Vol. 81, No. 2, 189–206.

Eringen, A.C. (1972)
Nonlocal polar elastic continua. International Journal of Engineering Science, Vol. 10, 1-16.

Federico, A.; Elia, G.; Murianni, A. (2009)
The at-rest earth pressure coefficient prediction using simple elasto-plastic constitutive models. Computers and Geotechnics, Vol. 36, 187–198.

Galavi, V. (2007)
A multilaminate model for structured clay incorporating inherent anisotropy and strain softening. Ph.D. thesis, Gruppe Geotechnik Graz, Graz University of Technology, Austria, Heft 32.

Gasparre A. (2005)
Advanced laboratory characterisation of London Clay. Ph.D. Thesis, Imperial College, London, U.K.

Gasparre, A.; Nishimura, S.; Minh, N.A.; Coop, M.R.; Jardine, R.J. (2007)
The stiffness of natural London Clay. Géotechnique, Vol. 57, No. 1, 33-47.

Gautam, R.; Wong, R.C.K. (2006)
Transversely isotropic stiffness parameters and their measurement in Colorado shale. Canadian Geotechnical Journal, Vol. 43, No. 12, 1290-1305.

Hardin, B.O.; Richart, F.E. (1963)
Elastic wave velocities in granular soils. Journal of the Soil Mechanics and Foundations Division, ASCE, Vol. 89, No. SM1, 33-65.

Hicher, P.Y.; Chang, C.S. (2006)
Anisotropic nonlinear elastic model for particulate materials. Journal of Geotechnical and Geoenvironmental Engineering, ASCE, Vol. 132, No. 8, 1052-1061.

Hoque, E.; Tatsuoka, F. (2004)
Effects of stress ratio on small-strain stiffness during triaxial shearing. Géotechnique, Vol. 54, No. 7, 429-439.

Hvorslev, M.J. (1937)
Über die Festigkeitseigenschaften gestörter bindiger Böden. Ingeniørvidenskabelige Skrifter A, No. 45, Copenhagen

Jiang, G.L.; Tatsuoka, F.; Flora, A.; Koseki, J. (1997)
Inherent and stress-state-induced anisotropy in very small strain stiffness of a sandy gravel. Géotechnique, Vol. 47, No. 3, 509-521.

Jirasek, M. (1998)
Nonlocal models for damage and fracture: Comparison of approaches. International Journal of Solids and Structures, Vol. 35, No. 31-32, 4133-4145.

Jostad, H.P.; Grimstad, G. (2011)
Comparison of distribution functions for the nonlocal strain approach. Proc. 2nd International Symposium on Computational Geomechanics, (COMGEO II), Pietruszczak & Pande (eds.), Cavtat-Dubrovnik, Croatia, 212-223.

Jovičić, V.; Coop, M.R. (1998)
The measurement of stiffness anisotropy in clays with bender element tests in the triaxial apparatus. Geotechnical Testing Journal, Vol. 21, No. 1, 3-10.

Karstunen, M. (1999)
Numerical modelling of strain localization in dense sands. Acta Polytechnica Scandinavia, The Finnish Academy of Technology, Espoo, Finland, No. 113.

Krajewski, W. (1986)
Mathematisch-numerische und experimentelle Untersuchung zur Bestimmung der Tragfähigkeit von in Sand gegründeten, vertikal belasteten Pfählen. Veröff. des Institutes für Grundbau, Bodenmechanik, Felsmechanik und Verkehrswasserbau der RWTH Aachen, Germany, Vol. 13.

Kuhl E.; Ramm E. (2000)
Microplane modelling of cohesive frictional materials. European Journal of Mechanics – A/Solids; Vol. 19, 121-143.

Kuwano R. (1999)
The stiffness and yielding anisotropy of sand. Ph.D. Thesis, Imperial College, London, U.K.

Kuwano, R.; Jardine, R.J. (2002)
On the applicability of cross-anisotropic elasticity to granular materials at very small strains. Géotechnique, Vol. 52, No. 10, 727-749.

Larsson, R.; Runesson, K.; Ottosen, N.S. (1993)
Discontinuous displacement approximation for capturing plastic localization. International Journal of Numerical Methods in Engineering, Vol. 36, 2087-2105.

Leukart, M. (2005)
Kombinierte anisotrope Schädigung und Plastizität bei kohäsiven Reibungsmaterialien. Ph.D. Thesis, Bericht Nr. 45, Institute for Structural Mechanics, University of Stuttgart.

Lings, M.L.; Pennington, D.S.; Nash, D.F.T. (2000)
Anisotropic stiffness parameters and their measurements in a stiff natural clay. Géotechnique, Vol. 50, No. 2, 109-125.

Loret, B.; Prevost, J.H. (1991)
Dynamic strain localization in fluid-saturated porous media. Journal of Engineering Mechanics, ASCE, Vol. 117, 907-922.

Mandel, J. (1966)
Conditions de stabilité et postulat de Drucker. Proceeding of the IUTAM Symposium on Rheology and soil Mechanics. Springer, Berlin, 58-68.

Marcher, T. (2003)
Nichtlokale Modellierung der Entfestigung dichter Sande und steifer Tone. Ph.D. thesis, University of Stuttgart, Stuttgart, Germany.

Maudlin, P.J.; Wright, S.I.; Kocks, U.F.; Sahota, M.S. (1996)
An application of multisurface plasticity theory: yield surfaces of textured materials. Acta Materialia, Vol. 44, No. 10, 4027–4032.

Mita, K.A. (2002)
Constitutive testing of soil on the dry side of critical state. Ph.D. thesis, National University of Singapore, Singapore.

Mühlhaus, H.-B.; Vardoulakis, I. (1987)
The thickness of shear bands in granular materials. Géotechnique, Vol. 37, 271-283.

Muir Wood, D. (1990)
Soil behaviour and critical state soil mechanics. Cambridge University Press.

Nash, D.F.T.; Lings, M.L.; Pennington, D.S. (1999)
The dependence of anisotropic G0 shear moduli on void ratio and stress state for reconstituted Gault clay. Proc. 2nd International Symposium on Pre-failure Deformation Characteristics of Geomaterials, Jamiolkowski, Lancellotta & Lo Presti (eds.), Torino, Italy, Vol. 1, 229-238.

Ng, C.W.W.; Leung, E.H.Y.; Lau, C.K. (2004)
Inherent anisotropic stiffness of weathered geomaterial and its influence on ground deformations around deep excavations. Canadian Geotechnical Journal, Vol. 41, No. 1, 12-24.

Niemunis, A.; Herle, I. (1997)
Hypoplastic model for cohesionless soils with elastic strain range. Mechanics of Cohesive-Frictional Materials, Vol. 2, No. 4, 279–299

Nishimura S. (2005)
Laboratory study on anisotropy of natural London clay. Ph.D. Thesis, Imperial College, London, U.K.

Oka, F.; Adachi, T.; Yashima, A. (1995)
A strain localization analysis of clay using a strain softening viscoplastic model. International Journal of Plasticity, Vol. 11, No. 5, 523-545.

Pande, G.N.; Sharma, K.G. (1983)
Multilaminate model of clays – a numerical evaluation of the influence of rotation of principal stress axes. International Journal for Numerical and Analytical Methods in Geomechanics, Vol. 7, No. 4, 397-418.

Parry, R.H.G. (1960)
Triaxial compression and extension tests on remoulded saturated clay. Géotechnique, Vol. 10, No. 4, 166 –180.

Pennington, D.S.; Nash, D.F.T.; Lings, M.L.; (1997)
Anisotropy of G0 shear stiffness in Gault Clay. Géotechnique, Vol. 47, No. 3, 391-398.

Pietruszczak, S.; Mroz, Z. (1981)
Finite element analysis of deformation of strain-softening materials. International Journal for Numerical Methods in Engineering, Vol. 17, 327-334.

Pietruszczak, S.; Mroz, Z. (2000)
Formulation of anisotropic failure criteria incorporating a microstructure tensor. Computers and Geotechnics, Vol. 26, 105-112.

Pietruszczak, S.; Pande, G.N. (1987)
Multi-laminate framework of soil models – plasticity formulation. International Journal for Numerical and Analytical Methods in Geomechanics, Vol. 11, 651-658.

Piriyakul, K. (2007)
Anisotropic stress-strain behaviour of Belgian Boom clay in the small strain region. Ph.D. Thesis, Ghent University, Ghent, Belgium

Potts, D.M.; Zdravković, L. (1999)
Finite element analysis in geotechnical engineering, Theory. London: Telford.

Puzrin, A.M.; Burland, J.B. (1998)
Non-linear model of small-strain behaviour of soils. Géotechnique, Vol. 48, No. 2, 217-233.

Pyke, R. (1979)
Nonlinear soil models for irregular cyclic loadings. Journal of the Geotechnical Engineering Division, ASCE, Vol. 105, No. 6, 715–726.

Rice, J.R. (1976)
The localization of plastic deformation. Theoretical and Applied Mechanics, North-Holland: Amsterdam, 207-220.

Richardson, D. (1988)
Investigations of threshold effects in soil deformations. PhD-thesis, City University, London, UK.

Roesler, S.K. (1979)
Anisotropic shear modulus due to stress anisotropy. Journal of the Geotechnical Engineering Division, ASCE, Vol. 105, No. 7, 871-880.

Roscoe, K. H. (1970)
The influence of strains in soil mechanics. Géotechnique, Vol. 20, No. 2, 129-170.

Roscoe, K.H.; Burland, J.B. (1968)
On the generalized stress-strain behaviour of ‘wet’ clay. Engineering Plasticity, Heyman & Leckie (eds.), Cambridge University Press, 535-609.

Rudnicki, J.W. (1977)
The inception of failure in a rock mass with a weakened zone. Journal of Geophysical Research, Vol. 82, No. 5, 844-854.

Sadek, T.; Lings, M.L.; Dihoru, L.; Muir Wood, D. (2007)
Wave transmission in Hostun sand: multiaxial experiments. Rivista Italiana di Geotecnica, Vol. 41, No. 2, 69-84.

Sadrnejad, S.A.; Pande, G.N. (1989)
A multilaminate model for sands. Proc. 3rd International Symposium on Numerical Models in Geomechanics (NUMOG), Pietruszczak & Pande (eds.), Niagara Falls, Canada, 17-27. London: Elsevier.

Sánchez, F.; Prat, P.C. (2008)
A multiple plane plasticity model for rock materials. Part I: definitions of

strength. Proc. 12th International Conference of the International Association of Computer Methods and Advances in Geomechanics (IACMAG), Singh (ed.), Goa, India. 669-677

Sanders, J.L. (1955)
Plastic stress-strain relations based on linear loading functions. Proc. 2nd United States National Congress on Applied Mechanics, ASME, 455-460.

Schanz, T; Vermeer, P.A. (1996)
Angles of Friction and Dilatancy of Sand. Géotechnique, Vol. 46, No. 1, 145-151.

Scharinger, F. (2007)
A multilaminate model for soil incorporating small strain stiffness. Ph.D. thesis, Gruppe Geotechnik Graz, Graz University of Technology, Austria, Heft 31.

Schofield, A.N.; Wroth, C.P. (1968)
Critical state soil mechanics. London: McGraw Hill.

Schuller, H. (2000)
A multilaminate model for soils and its application to numerical analysis of tunnel excavation. PhD thesis, Graz University of Technology, Graz, Austria.

Schweiger, H.F.; Wiltafsky, C.; Scharinger, F.; Galavi, V. (2009)
A multilaminate framework for modelling induced and inherent anisotropy of soils. Géotechnique, Vol. 59, No. 2, 87-101.

Seed, H.B.; Idriss, I.M. (1970)
Soil moduli and damping factors for dynamic response analyses. Earthquake Engineering Research Center, Berkeley, California, USA, Report No. 70-10.

Sharma, K.G. (1980)
Numerical models of soils under monotonic and cyclic loading. Ph.D. thesis, University of Wales Swansea, UK.

Simo, J.C.; Oliver, J.; Armero, F. (1993)
An analysis of strong discontinuities induced by strain-softening in rate-independent inelastic solids. Computational Mechanics, Vol. 12, 277-296.

Simpson, B. (1992)
Retaining structures: displacement and design. Géotechnique, Vol. 42, No. 4, 541-576.

Simpson B.; O'Riordan, N.J.; Croft, D.D. (1979)
A computer model for the analysis of ground movements in London Clay. Géotechnique, Vol. 29, No. 2, 149-175.

Taylor, G.I. (1938)
Plastic strain in metals. Journal of the Institute of Metals, Vol. 62, 307-324. Reprinted in: The Scientific Papers of G.I. Taylor 1, 1958, Cambridge University Press, Cambridge, UK.

Tejchman, J. (2004)
Comparative FE-studies of shear localizations in granular bodies within a polar and non-local hypoplasticity. Mechanics Research Communications, Vol. 31, No. 1, 341–354.

Theocaris, P.S.; Philippidis, T. P. (1991)
Spectral decomposition of compliance and stiffness fourth-rank tensors suitable for orthotropic materials. Zeitschrift für angewandte Mathematik und Mechanik (ZAMM), Vol. 71, No. 3, 161-171.

Theocaris, P.S.; Sokolis, D.P. (2000)
Spectral decomposition of the compliance fourth-rank tensor for orthotropic materials. Archive of Applied Mechanics, Vol. 70, No. 4, 289-306.

Varadarajan, A.; Sharma, K.G.; Pande, G.N. (1990)
Prediction of anisotropic behaviour of clays by the multilaminate model. Proc. 2nd European Conference on Numerical Methods in Geomechanics, Santander, Spain.

Vardoulakis, I. (1980)
Shear band inclination and shear modulus of sand in biaxial tests. International Journal for Numerical and Analytical Methods in Geomechanics, Vol. 4, 103-119.

Vardoulakis, I.; Aifantis, E.C. (1989)
Gradient dependent dilatancy and its implications in shear banding and liquefaction. Ingenieur Archiv, Vol. 59, 197-208.

Vardoulakis, I.; Goldscheider, M. (1981)
Biaxial apparatus for testing shear bands in soils. Proc. 10th International

Conference of Soil Mechanics and Foundation Engineering, Flodin (ed.), Stockholm, Sweden, Vol. 4, 819-824

Verdugo, R.; Ishihara, K. (1996)
The steady state of sandy soils. Soils and Foundations, Vol. 36, No. 2, 81-91.

Vermeer, P.A. (1990)
The orientation of shear bands in biaxial tests. Géotechnique, Vol. 40, No. 2, 223-236.

Wiltafsky Ch. (2003)
A multilaminate model for normally consolidated clay. PhD thesis, Gruppe Geotechnik Graz, Heft 18, Graz University of Technology, Austria.

Yimsiri, S.; Soga, K. (2000)
Micromechanics-based stress-strain behaviour of soils at small strains. Géotechnique, Vol. 50, No. 5, 559-571.

Yimsiri, S.; Soga, K. (2011)
Cross-anisotropic elastic parameters of two natural stiff clays. Géotechnique, Vol. 61, No. 9, 809–814.

Zienkiewicz, O.C.; Pande, G.N. (1977)
Time-dependent multilaminate model of rocks - A numerical study of deformation and failure of rock masses. International Journal for Numerical and Analytical Methods in Geomechanics, Vol. 1, No. 3, 219-247.

Appendix A

The following appendix provides some further details on the spectral decomposition of the global compliance matrix, which is employed in the model to derive local compliance matrices on integration plane level. The equations are valid for a cross-anisotropic material with a vertical axis of symmetry, in which case the material behaviour is isotropic in the horizontal plane. The vertical axis coincides with the Cartesian y-direction. Material behaviour is defined by five elastic constants, E'_v, E'_h, G'_{vh}, ν'_{hv}, ν'_{hh},. The spectral decomposition is based on Kelvin notation of the macroscopic compliance matrix **C**, which is required to preserve the sum of the components of the stress and strain tensor.

Eigenvalues of cross anisotropic compliance matrix **C**:

$$\lambda_1 = \frac{\nu'_{hh}+1}{E'_h} \tag{A.1a}$$

$$\lambda_2 = \frac{1-\nu'_{hh}}{2E'_h} + \frac{1}{2E'_v} - \sqrt{\left(\frac{1-\nu'_{hh}}{2E'_h} - \frac{1}{2E'_v}\right)^2 + \frac{2\nu'^{\,2}_{hv}}{E'^{\,2}_h}} \tag{A.1b}$$

$$\lambda_3 = \frac{1-\nu'_{hh}}{2E'_h} + \frac{1}{2E'_v} + \sqrt{\left(\frac{1-\nu'_{hh}}{2E'_h} - \frac{1}{2E'_v}\right)^2 + \frac{2\nu'^{\,2}_{hv}}{E'^{\,2}_h}} \tag{A.1c}$$

$$\lambda_4 = \frac{1}{2G_{vh}} \tag{A.1d}$$

Eigenangle of cross-anisotropic compliance matrix:

$$\tan 2\omega = \frac{-2\cdot\sqrt{2}\cdot\dfrac{\nu'_{hv}}{E'_v}}{\dfrac{1-\nu'_{hh}}{E'_h} + \dfrac{1}{E'_v}} \tag{A.2}$$

Idempotent matrices of **C**:

$$\mathbf{E}_1 = \begin{pmatrix} 1/2 & 0 & -1/2 & 0 & 0 & 0 \\ 0 & 0 & 0 & 0 & 0 & 0 \\ -1/2 & 0 & 1/2 & 0 & 0 & 0 \\ 0 & 0 & 0 & 0 & 0 & 0 \\ 0 & 0 & 0 & 0 & 0 & 0 \\ 0 & 0 & 0 & 0 & 0 & 1 \end{pmatrix} \tag{A.3a}$$

$$\mathbf{E}_2 = \begin{pmatrix} \frac{\cos^2\varpi}{2} & \frac{\cos\varpi\cdot\sin\varpi}{\sqrt{2}} & \frac{\cos^2\varpi}{2} & 0 & 0 & 0 \\ \frac{\cos\varpi\cdot\sin\varpi}{\sqrt{2}} & \sin^2\varpi & \frac{\cos\varpi\cdot\sin\varpi}{\sqrt{2}} & 0 & 0 & 0 \\ \frac{\cos^2\varpi}{2} & \frac{\cos\varpi\cdot\sin\varpi}{\sqrt{2}} & \frac{\cos^2\varpi}{2} & 0 & 0 & 0 \\ 0 & 0 & 0 & 0 & 0 & 0 \\ 0 & 0 & 0 & 0 & 0 & 0 \\ 0 & 0 & 0 & 0 & 0 & 0 \end{pmatrix} \tag{A.3b}$$

$$\mathbf{E}_3 = \begin{pmatrix} \frac{\sin^2\varpi}{2} & \frac{\cos\varpi\cdot\sin\varpi}{-\sqrt{2}} & \frac{\sin^2\varpi}{2} & 0 & 0 & 0 \\ \frac{\cos\varpi\cdot\sin\varpi}{-\sqrt{2}} & \cos^2\varpi & \frac{\cos\varpi\cdot\sin\varpi}{-\sqrt{2}} & 0 & 0 & 0 \\ \frac{\sin^2\varpi}{2} & \frac{\cos\varpi\cdot\sin\varpi}{-\sqrt{2}} & \frac{\sin^2\varpi}{2} & 0 & 0 & 0 \\ 0 & 0 & 0 & 0 & 0 & 0 \\ 0 & 0 & 0 & 0 & 0 & 0 \\ 0 & 0 & 0 & 0 & 0 & 0 \end{pmatrix} \tag{A.3c}$$

$$\mathbf{E}_4 = \begin{pmatrix} 0 & 0 & 0 & 0 & 0 & 0 \\ 0 & 0 & 0 & 0 & 0 & 0 \\ 0 & 0 & 0 & 0 & 0 & 0 \\ 0 & 0 & 0 & 1 & 0 & 0 \\ 0 & 0 & 0 & 0 & 1 & 0 \\ 0 & 0 & 0 & 0 & 0 & 0 \end{pmatrix} \tag{A.3d}$$

Appendix B

The model has been implemented as a user-defined soil model (UDSM) for the finite element code PLAXIS 2D 2010 and is linked as a Dynamic Link Library (DLL) to the calculation kernel of the finite element code. In each calculation step, information about the previous stress state, previous state variables and the current strain increment is provided by PLAXIS, while the UDSM returns the current stress state and changes in state variables according to the constitutive model. The FORTRAN source code of the model is given in Appendix D. The model has been developed as a full three-dimensional model and can also be used in a three-dimensional version of PLAXIS.

The UDSM performs four main functionalities:

- Provide information about the type of calculation to be performed (e.g. undrained, time dependent)
- Initialisation of state variables at the start of the calculation in elastoplastic constitutive models
- Return of constitutive stresses and new state variables for the current strain increment
- Return effective stiffness matrix
- Return elastic stiffness matrix

The following chapter provides an overview on the implementation of the Multilaminate Model for Stiff Soil with respect to these tasks.

B.1 Parameters exchanged between PLAXIS and UDSM

The parameters exchanged by the UDSM and the finite element code at each iteration are listed in Table B.1. The parameter *IDTask* identifies the task the UDSM is requested to perform. *IDTask* can take values from 1 to 6, with

IDTask = 1: Initialisation of state variables
2: Calculation of constitutive stresses
3: Formation of effective stiffness matrix
4: Return of number of state variables
5: Return of matrix attributes
6: Formation of elastic stiffness matrix

Tab. B.1: Property variables of UDSM

parameter		**description**
IDTask	*IDTask*	identification number of the task
iMod	*iMod*	soil model number
IsUndr	*IsUndr*	drained (0) or undrained (1) conditions
iStep	*iStep*	current calculation step number within current calculation phase
iter	*Iter*	current iteration number
Iel	*iEl*	current element number
Int	*Int*	current local stress point number
X,Y,Z	*X, Y, Z*	global coordinates of current stress point
Time0	not used	time at the start of the current step
dTime	not used	time increment of current step
Props	**Props**	array (1..50) of model input parameters
Sig0	$\boldsymbol{\sigma}'_0$	array (1..20) of previous effective stress state in current stress point, could include suction stresses
Swp0	$p_{w,0}$	previous excess pore pressure in current stress point
StVar0	$\mathbf{StVar}_0$	array (1..nstat) of previous values of state variables of the current stress points
dEps	$\mathbf{d\varepsilon}$	total strain increment of the current step
D	**D**	effective material stiffness matrix
BulkW	K_e	bulk modulus of pore fluid
Sig	$\boldsymbol{\sigma}'$	resulting constitutive stress state
Swp	p_w	resulting excess pore pressure
StVar	**StVar**	resulting values of state variables
ipl	*ipl*	plasticity indicator (for output purposes)
nStat	*nStat*	number of state variables
NonSym	*NonSym*	symmetry indicator of material stiffness matrix
iStrsDep	*iStrsDep*	stress-dependency of material stiffness matrix
iTimeDep	*iTimeDep*	time-dependency of material stiffness matrix
iTang	*iTang*	indicator for type of stiffness matrix
iPrjDir	*iPrjDir*	project directory name
iPrjLen	*iPrjLen*	length of project directory name
iAbort	Not used	parameter forcing the calculation to stop

B.2 Files for non-local strain regularization

The UDSM facility provided by PLAXIS only delivers information about the current stress point, but not about the neighbouring stress points in the finite element mesh. Non-local strain regularization as employed in the presented model requires information about the position and strains of neighbouring stress points, which needs to be stored in external files. Table B.2 gives a list of the files created during the calculation process. Info.sft and Geometry.sft are only used at the start of the calculation to obtain information about the position of the stress points within the finite element mesh and assign non-local weighting factors, which are then stored in Weights.sft. Point_index.sft contains the address of the neighbouring stress points within the softening files for all stress points of the model. Stresspoint.sft stores the maximum number of stress points considered for strain regularization at any single stress point. Step.nr, Element.nr and StartPhase.nr monitor the position of the current calculation step and iteration within the calculation process.

Tab. B.2: I/O files for non-local strain regularization

File name	**Contents**	**description**
Info.sft & Geometry.sft	*iEl*	element number
	Int	local stress point number
	X	X coordinate of stress point
	Y	Y coordinate of stress point
	Z	Z coordinate of stress point
StartPhase.nr	*StartPhase*	number of previous calculation phase
Step.nr	*iStep*	calculation step number at current phase
	iS	total calculation step number
	InSPoint	total number of stress points in domain
Phasexxxx & Iter.xxxx	*AE*	area of element
	ε_d	local damage strain on the level of stress point
Null.sft	*iNull*	0: if element is inactive and 1: if element exists
Weights.sft	*weights*	non-local weighting factors of neighbouring stress points
Point_index.sft	*point_index*	address of the neighbouring stress points in softening files
Stresspoint.sft	*stresspoint*	maximum number of stress points within domain of any stress point
Element.nr	*iEl*	element number
	Iter	iteration number

B.3 Return the number of state variables (IDTask=4)

The number of required state variables is requested by PLAXIS at the beginning of each calculation phase to allocate the necessary data storage. To optimize calculation speed, only the number of state variables essential for the current type of calculation is returned, as listed in Table B.3. *NUMCP* is the number of planes taken into account in the integration rule, which is an input parameter of the model. As the full functionality of the model is not required in all types of calculations, the amount of data stored and transferred by PLAXIS can be significantly reduced.

Tab. B.3: Number of state variables required by the available models

Model	***nStat***	**description**
Basic	3**NUMCP*+3	no softening, no small strain stiffness
MMSS	7**NUMCP*	Hvorslev surface shear strength and softening, no small strain stiffness
MMSC	8* *NUMCP*	strain softening according to Galavi (2007), no small strain stiffness
Basic_sss MMSS_sss MMSC_sss	12* *NUMCP*	any of the aforementioned models with small strain stiffness, no stiffness recovery
Basic_sss_lh MMSS_sss_lh MMSC_sss_lh	32* *NUMCP*	any of the aforementioned models with small strain stiffness and stiffness recovery

B.4 Return matrix attributes (IDTask=5)

In order to store the global stiffness matrix properly, PLAXIS requests information about the attributes of stress point stiffness matrices at the beginning of each calculation phase. The multilaminate model employs a stiffness matrix which is stress-dependent (*iStrDep*=1), symmetric (*NonSym*=0), not tangent (*iTang*=0) and time-independent (*iTimeDep*=0).

B.5 Initialisation of state variables (IDTask=1)

The initial position of yield surfaces and thus the initial values of state variables are defined in *IDTask* = 1 according to the initial stress state and possible overconsolidation for each stress point. The shape of the volumetric yield surface is determined by an iterative subroutine which aims at reproducing the input lateral earth pressure coefficient in primary loading, K_{0nc}. The initial stresses are transferred from PLAXIS to the UDSM, as well as the input model parameters. Pre-overburden pressure (*POP*) and overconsolidation ratio (*OCR*) have to be defined as input model parameters in the UDSM and are taken into account in the calculation of stress history as detailed in Equations B.1 to B.4.

$$\sigma'_{pv} = \sigma'_{v,0} + POP \tag{B.1}$$

$$\sigma'_{pv} = \sigma'_{v,0} \cdot OCR \tag{B.2}$$

$$\sigma'_{ph} = \left(\sigma'_{v,0} + POP\right) \cdot K_{0nc} \tag{B.3}$$

$$\sigma'_{ph} = \left(\sigma'_{v,0} \cdot OCR\right) \cdot K_{0nc} \tag{B.4}$$

$\sigma'_{v,0}$ is the initial vertical stress delivered by PLAXIS according to bulk unit weight and model geometry as specified in the input program. The modified vertical stress, σ'_{pv} is adjusted for the stress history defined by *OCR* and *POP*. The modified horizontal stress σ'_{ph} is obtained from σ'_{pv} and the lateral earth coefficient in primary loading, K_{0nc}, which is assumed as $K_{0nc} = 1 - \sin\varphi'$ if not specified otherwise.

Both the macroscopic initial stress, $\boldsymbol{\sigma}'_0$, and the maximum previous stress state, $\boldsymbol{\sigma}'_p$, are transformed to the integration planes to obtain local stresses τ and σ'_n. The initial position of the cap and cone yield surface is determined independently for each integration plane according to Equations B.5 and B.6.

$$\sigma'_{nc,i} = \sqrt{{\sigma'_n}^2 + \frac{\tau^2}{{M_{CP}}^2}} \tag{B.5}$$

$$\tan\varphi'_m = \frac{\tau}{c' / \tan\varphi'_{max} - \sigma'_n} \tag{B.6}$$

In the case of the Hvorslev surface model, cohesion $c' = 0$ and thus the initially mobilised friction angle φ'_m is derived from the stress ratio τ / σ'_n. Both $\boldsymbol{\sigma}'_0$ and $\boldsymbol{\sigma}'_p$ are considered in the determination of initial yield surfaces to ensure that the initial stress state does not violate the yield condition $f_i = 0$.

B.6 Model input parameters

The input parameters of the multilaminate model presented in this thesis are listed in Tables B.4 to B.7. Maximum friction angle φ'_{max}, effective cohesion c' and dilation angle ψ are only used if the Hvorslev surface model is not activated ($\varphi'_e = 0$). The default value of K_{0nc} is calculated from the critical state angle φ'_{cs} if the Hvorslev surface is activated. The isotropic shear modulus at small strains, $G_{0,ref}$, is not used once input values for cross-anisotropic small strain stiffness are defined.

Tab. B.4: Basic input parameters

symbol	Dim.	description
φ'_{max}	°	maximum effective friction angle
E_{oed}^{ref}	stress	reference stiffness for primary oedometer loading
E_{ur}^{ref}	stress	elastic stiffness for un- and reloading at reference stress
ν'_{ur}	-	drained Poisson’s ratio for un- and reloading
p_{ref}	stress	reference stress
A_{mat}	-	parameter to control deviatoric hardening
σ'_t	stress	maximum tensile strength
R_f	-	failure ratio
m	-	power for stress-dependency of stiffness
φ'^{*}_{mob}	°	mobilised friction angle at min. mobilised dilatancy
$\psi_{mob,min}$	°	minimum of mobilised dilatancy
c'	stress	effective cohesion
ψ	°	dilation angle

Tab. B.5: Input parameters for initialisation

symbol	Dim.	default	description
φ'_0	°	1.0	minimum initial effective friction angle
$\sigma'_{nc,0}$	stress	-1.0	minimum initial preconsolidation pressure
K_{0nc}	-	1-sinφ'_{cs}	K_0 value for normally consolidated conditions
POP	stress	0.0	pre-overburden pressure
OCR	-	1.0	over-consolidation ratio

Tab. B.6: Input parameters for small strain stiffness

symbol	**Dim.**	**description**
$G_{0,ref}$	stress	isotropic shear stiffness at very small strains
$\varepsilon_{deg,1}$	-	threshold strain level for stiffness degradation
$\varepsilon_{deg,2}$	-	local strain at transition to large strains
$E'_{v0,ref}$	stress	vertical stiffness at very small strains
$E'_{h0,ref}$	stress	horizontal stiffness at very small strains
$G_{vh0,ref}$	stress	cross-anisotropic shear modulus at very small strains
ν'_{vh0}	-	cross-anisotropic Poisson's ratio ν'_{vh} at very small strains
ν'_{hh0}	-	cross-anisotropic Poisson's ratio ν'_{hh} at very small strains

Tab. B.7: Input parameters for Hvorslev surface and softening

symbol	**Dim.**	**description**
φ'_e	°	inclination of Hvorslev surface in τ-σ' diagram
φ'_{cs}	°	critical state friction angle
h_{soft}	-	Hvorslev surface softening parameter
l_{cal}	-	internal length for non-local approach

B.6 Determination of stiffness matrix (IDTask = 3)

The multilaminate model does not utilise a tangent stiffness matrix (*iTang*=0), which means that *IDTask* = 3 and *IDTask* = 6 both return the elastic stiffness matrix of the current stress point.

B.6.1 Non-linear stiffness at very small strains

The modified Newton-Raphson iteration scheme employed in the multilaminate model requires the elastic stiffness matrix at the start of the iteration. If elastic stiffness is allowed to change with strain level, the global elastic stiffness matrix depends on strain history and hence on the strain increment of the current iteration. However, the next strain increment is evaluated by the finite element code based on information provided by *IDTask* = 3, and consequently information on the next strain increment is not available at the start of this task. A lower stiffness than actually present (e.g. at load reversals) leads to no convergence of the iteration process at stress point level and must therefore be avoided. As the stiffness matrix given by *IDTask* = 3 is only used to determine the size of the next strain increment, the high initial stiffness at very small strains is used. For calculation of constitutive stresses in *IDTask* = 2, the stiffness matrix is updated according to the strain history, which takes changes in loading direction into account. As mentioned by Scharinger (2007), this approach increases the number of iterations per calculation step proportional to the ratio of G_0/G_{ur}, which is however inevitable with the current version of the UDSM interface in PLAXIS.

B.6.2 Equivalent bulk modulus of pore fluid

Changes in pore water pressure, dp_w, during undrained analysis are calculated from the equivalent bulk stiffness of the pore fluid, K_e, and the volumetric strain increment $d\varepsilon_{vol}$ according to Equation B.7.

$$dp_w = K_e \cdot d\varepsilon_{vol} \tag{B.7}$$

$$K_e = K_u - K' = \frac{2 \cdot G}{3} \cdot \left(\frac{1+\nu_u}{1-2\nu_u} - \frac{1+\nu'_{ur}}{1-2\nu'_{ur}} \right) \tag{B.8}$$

K_e is obtained from the elastic shear stiffness G, the effective Poisson's ratio ν'_{ur} and the undrained Poisson's ratio ν_u. In case of anisotropic small strain stiffness, G is the average of the anisotropic small strain shear moduli. K_e approaches infinity for an incompressible fluid with $\nu_u = 0.5$, which can be avoided by using a slightly smaller value of $\nu_u = 0.495$ (Potts & Zdravković, 1999).

B.7 Calculation of constitutive stresses (IDTask=2)

This task delivers the new stress state at the end of the given strain increment and hence forms the main part of the USDM. The flowchart for this task is shown in Figure B.1 and Figure B.2.

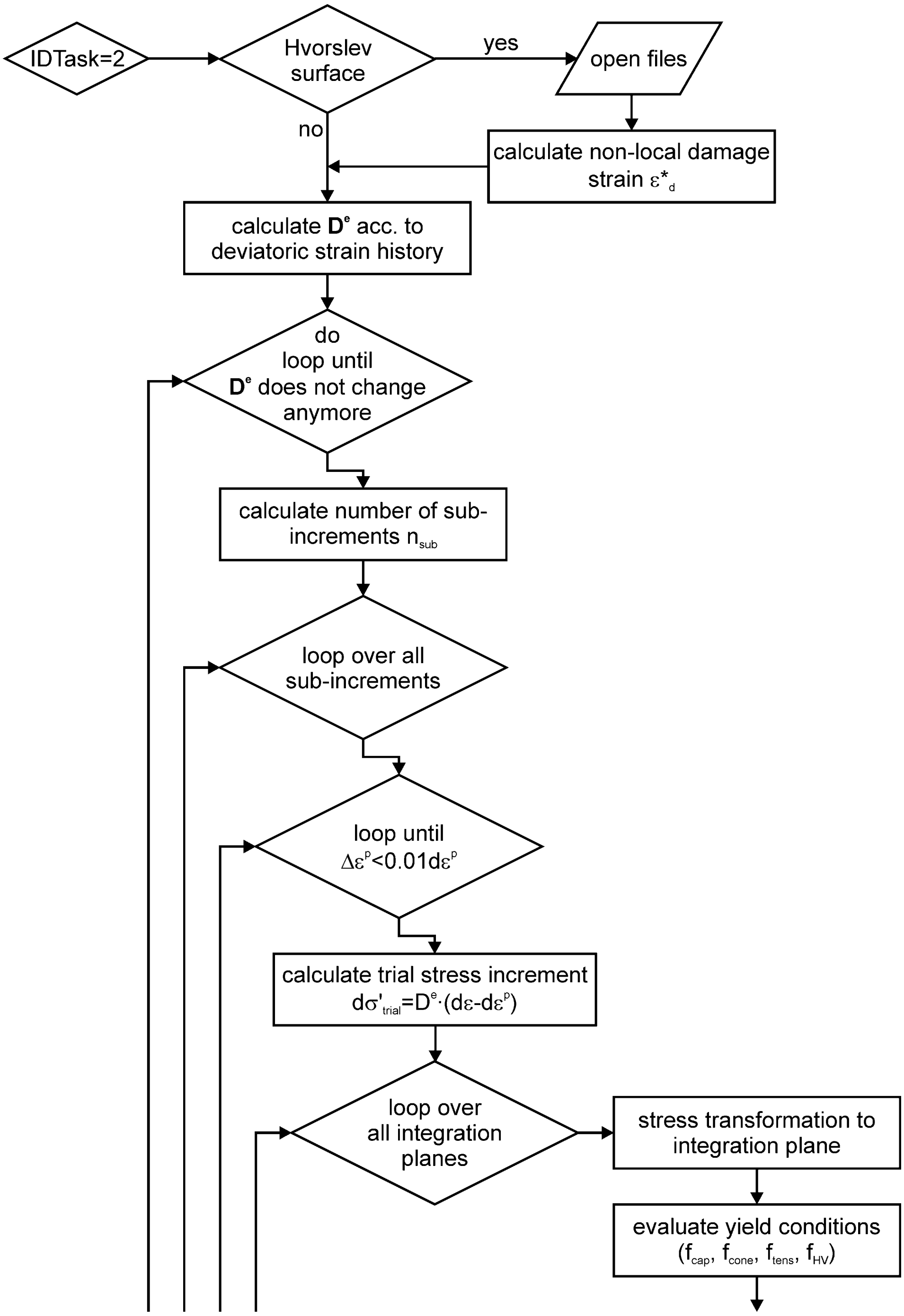

Fig. B.1: Flowchart of IDTask 2, part 1

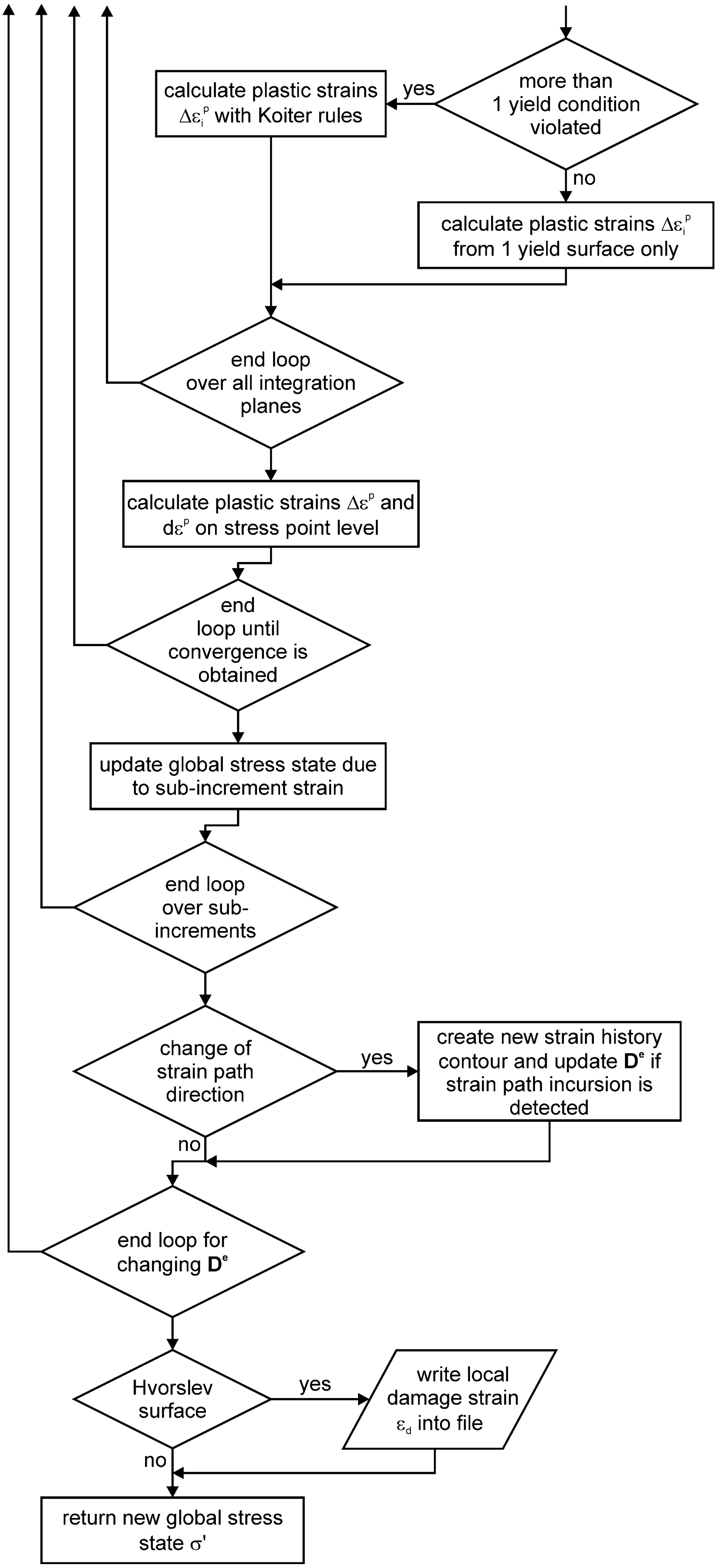

Fig. B.2: Flowchart of IDTask 2, part 2

B.7.1 Determination of elastic stiffness matrix

The elastic stiffness matrix $\mathbf{D^e} = \mathbf{C}^{-1}$ calculated in *IDTask*=3=6 assumes a full return of the strain path on all integration planes and thus represents the stiffness of the material at very small strain, adjusted for the current stress level. For calculating the constitutive stresses in *IDTask*=2, the actual elastic stiffness according to current strain history is required. The current elastic material stiffness is governed by two aspects: The local degradation strain ε_{deg} from previous calculation steps needs to be determined for all integration planes, resulting in corresponding increase of local compliances $\mathbf{C}_i$, which are then summed up to obtain the elastic compliance matrix $\mathbf{C}$. This compliance matrix, however, is only valid for a monotonic loading path.

In case of changes in loading direction, material stiffness also depends on the current strain increment $\mathbf{d\varepsilon}$, as deviation from the previous loading path may result in partial or full recovery of the initial stiffness. Such change in loading direction on integration plane level cannot be detected a priori, as the double constraint (enabling projection of both stresses and strains) is only valid before any stiffness degradation occurred on any of the integration planes. As generally the distribution of strains among the various integration planes is only known at the end of the stress point algorithm, an iterative scheme is employed to work out the current elastic stiffness. The first run of the stress point algorithm assumes a monotonic loading path, i.e. no change in local deviatoric strain direction and thus no recovery of small strain stiffness. If the current strain increment yields the creation or the erasure of a strain sphere on at least one of the integration planes, the stress point algorithm is repeated with an updated global elastic stiffness assuming stiffness recovery on that plane. This procedure is repeated until no further change of the global elastic stiffness matrix is detected.

Recovery of small strain stiffness is confined to the area below the critical state line, $\varphi'_m < \varphi'_{cs}$, to avoid spurious changes in stiffness if the stress point is close to or at failure.

B.7.2 Sub-stepping algorithm

A larger distance between $\boldsymbol{\sigma}'_{trial}$ and the yield surface may not be severely problematic in macroscopic constitutive models with fully implicit return algorithms, which employ second order derivatives of yield and plastic potential functions. In multilaminate models, however, too large strain increments yield incorrect local plastic strain distributions, as already pointed out by Schuller (2000). Scharinger (2007) proposed a sub-stepping procedure to ensure that the elastic trial stress $\boldsymbol{\sigma}'_{trial}$ is never excessively outside of the current yield surface, which is also employed in the current multilaminate model. The input parameter *StepSize* determines the maximum distance between $\boldsymbol{\sigma}'_{trial}$ and the yield surface closest to $\boldsymbol{\sigma}'_{trial}$. If the elastic trial stress, calculated from $\mathbf{D}^{\mathbf{e}}$ and $\mathbf{d}\boldsymbol{\varepsilon}$, is larger than permitted by *StepSize*, the strain increment $\mathbf{d}\boldsymbol{\varepsilon}$ is split into n_{sub} sub-increments, which are then calculated one after another. All sub-increments are calculated with the same elastic stiffness matrix $\mathbf{D}^{\mathbf{e}}$. Typically, values of *StepSize* = 5…10 kPa ensure sufficiently accurate results

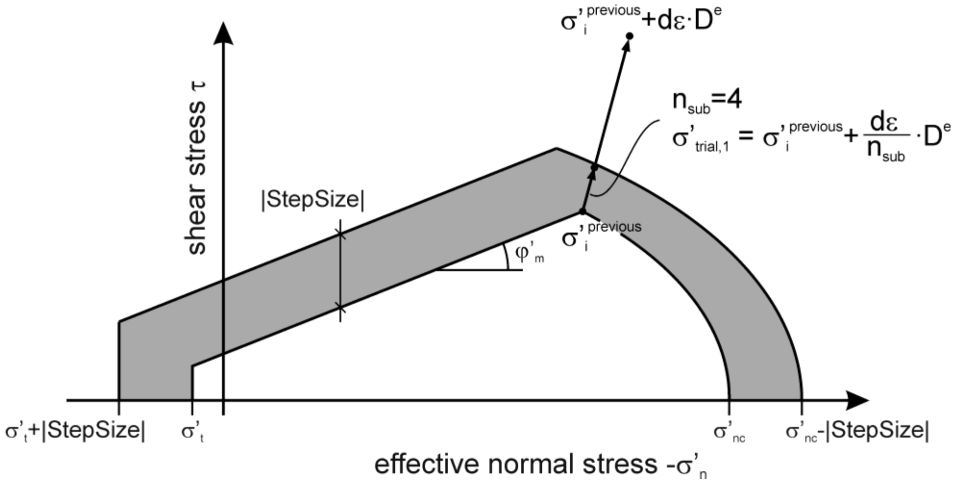

Fig. B.3: Sub-stepping procedure (Scharinger 2007)

B.7.3 Stress point return algorithm

Various solution strategies are available to solve the constitutive equations of a non-linear constitutive model at stress point level for a given strain increment. Wiltafsky (2003) implemented a modified Newton-Raphson scheme in combination with an implicit return stress point algorithm in the basic version of the multilaminate model. This approach is also employed in the model presented in this thesis. In implicit return algorithms, plastic strains are calculated for the stress state at the end of the increment, which is obviously not known at the start of the stress point iteration. The elastic trial stress $\boldsymbol{\sigma}'_{trial}$ is used as a predictor for the stress state $\boldsymbol{\sigma}'$ at the end of the increment (Equation B.9). In subsequent stress point iterations, plastic strain increments $\mathbf{d}\boldsymbol{\varepsilon}^{\mathbf{p}}$ and hardening of yield surfaces reduce the distance between $\boldsymbol{\sigma}'_{trial}$ and the updated yield surfaces, until the convergence criterion is satisfied. In previous multilaminate models the condition $f_i \leq 1\cdot10^{-15}$ has been enforced individually for all integration planes (Scharinger 2007, Galavi 2007). In the current multilaminate model the convergence criterion relates to the change of macroscopic plastic strains in consecutive iterations in order to increase calculation speed, as described in chapter 3.2.

$$\boldsymbol{\sigma}'_{trial} = \boldsymbol{\sigma}'_{previous} + \mathbf{C}^{-1} \cdot \left(\frac{\mathbf{d\varepsilon}}{n_{sub}} - \mathbf{d\varepsilon}^{p} \right) \tag{B.9}$$

$$\mathbf{d\varepsilon}^{p} = 3 \cdot \sum_{i} d\Lambda_i \mathbf{T}_i \frac{\partial g_i}{\partial \boldsymbol{\sigma}'_i} w_i \tag{B.10}$$

$\boldsymbol{\sigma}'_{previous}$ is the stress state at the end of the previous increment, $\mathbf{d\varepsilon}$ is the strain increment given by PLAXIS, and $d\Lambda_i$ is the increment of the local plastic multiplier of the integration planes. $d\Lambda_i$ is calculated from Equation B.11 separately for each of the yield surfaces (tension cut off, cap yield surface, cone yield surface, Hvorslev surface). Local cap and cone yield surfaces do not interact in hardening (independent multi-surface plasticity), but Hvorslev surface and cap yield surface shrink and expand together, as they are defined to intersect at the critical state line.

$$d\Lambda_i = \frac{f_i^{trial}}{\dfrac{\partial f_i}{\partial \boldsymbol{\sigma}'_{i,trial}} \mathbf{C}_i^{-1} \dfrac{\partial g_i}{\partial \boldsymbol{\sigma}'_{i,trial}} - \dfrac{\partial f_i}{\partial \boldsymbol{\varepsilon}_i^{p}} \dfrac{\partial g_i}{\partial \boldsymbol{\sigma}'_{i,trial}}} \tag{B.11}$$

$$\boldsymbol{\sigma}'_{i,trial} = \begin{pmatrix} \sigma'_{n,trial} \\ \tau_{trial} \end{pmatrix} \qquad \boldsymbol{\varepsilon}_i^{p} = \begin{pmatrix} \varepsilon_n^{p} \\ \gamma^{p} \end{pmatrix} \tag{B.12}$$

f_i^{trial} is the value of the yield function at the local trial stress $\boldsymbol{\sigma}'_{i,trial}$ on the integration plane. As $\boldsymbol{\sigma}'_{i,trial}$ is outside of the yield surface as long as the consistency condition (B.13) is not fulfilled, f_i^{trial} takes values larger than 0.

$$\frac{\partial f_i}{\partial \boldsymbol{\sigma}'_{i,trial}} \mathbf{d}\boldsymbol{\sigma}'_{i,trial} + \frac{\partial f_i}{\partial \boldsymbol{\varepsilon}_i^{p}} \mathbf{d\varepsilon}_i^{p} = 0 \tag{B.13}$$

The local elastic compliance matrix $\mathbf{C}_\mathrm{i}$ is given in Equation B.14. Yield surfaces are formulated in local tangential stress τ and local normal stress σ'_n. $\mathbf{C}_\mathrm{i}$ is therefore the elastic compliance found for the normal-tangential split of local stresses, as described in chapter 2.4.

$$\mathbf{C}_i = \begin{bmatrix} \dfrac{1-2\nu'_{ur}}{E'_{ur}} & 0 \\ 0 & \dfrac{1+3\nu'_{ur}}{E'_{ur}} \end{bmatrix} \tag{B.14}$$

Softening of the Hvorslev surface is driven by non-local strains (chapter 6.4.3), which are calculated once at the start of *IDTask*=2 from the damage strains of the neighbouring stress points and cannot be updated within the stress point iteration. Local strains of the current stress point hence have no direct influence on the position of the Hvorslev surface, and the model is consequently explicit in softening. This is a slight disadvantage of the current implementation, as small load steps are required in the post-peak range to obtain accurate results.

The partial derivatives of the local yield and plastic potential functions are given in the following equations. For clarity of the equations local trial stresses $\sigma'_{n,trial}$ and τ_{trial} have been replaced by σ'_n and τ.

- **Tension yield surface:**

$$\frac{\partial f_{tens}}{\partial \sigma'_n} = \frac{\partial g_{tens}}{\partial \sigma'_n} = 1 \tag{B.15}$$

$$\frac{\partial f_{tens}}{\partial \tau} = \frac{\partial g_{tens}}{\partial \tau} = 0 \tag{B.16}$$

$$\frac{\partial f_{tens}}{\partial \varepsilon_n^p} = \frac{\partial f_{tens}}{\partial \gamma^p} = 0 \tag{B.17}$$

- **Cone yield surface:**

$$\frac{\partial f_{cone}}{\partial \sigma'_n} = \tan\varphi'_m \tag{B.18}$$

$$\frac{\partial f_{cone}}{\partial \tau} = 1 \tag{B.19}$$

$$\frac{\partial g_{cone}}{\partial \sigma'_n} = \tan\psi_m \tag{B.20}$$

$$\frac{\partial g_{cone}}{\partial \tau} = 1 \tag{B.21}$$

$$\frac{\partial f_{cone}}{\partial \varepsilon^{p}_{n,cone}} = 0 \tag{B.22}$$

$$\frac{\partial f_{cone}}{\partial \gamma^{p}_{cone}} = \frac{\partial f_{cone}}{\partial \tan\varphi'_m} \cdot \frac{\partial \tan\varphi'_m}{\partial \gamma^{p}_{cone}}$$

$$= \left(\sigma'_n - \frac{c'}{\tan\varphi'_{max}}\right) \cdot \frac{3 \cdot \left(\tan\varphi'_m - \tan\varphi'_{mod}\right)^2}{A_{mat} \cdot \left(\tan\varphi'_{mod} - \tan\varphi'_0\right)} \tag{B.23}$$

- **Cap yield surface:**

$$\frac{\partial f_{cap}}{\partial \sigma'_n} = \frac{\partial g_{cap}}{\partial \sigma'_n} = \frac{2\sigma'_n}{{\sigma'_{nc}}^2} \tag{B.24}$$

$$\frac{\partial f_{cap}}{\partial \tau} = \frac{\partial g_{cap}}{\partial \tau} = \frac{2\tau}{\left(M_{CP} \cdot \sigma'_{nc}\right)^2} \tag{B.25}$$

$$\frac{\partial f_{cap}}{\partial \varepsilon^{p}_{n,cap}} = \frac{\partial f_{cap}}{\partial \sigma'_{nc}} \cdot \frac{\partial \sigma'_{nc}}{\partial \varepsilon^{p}_{n,cap}}$$

$$= -2 \cdot \left|\sigma'_{nc}\right|^m \cdot {p_{ref}}^{1-m} \cdot K \cdot \frac{\left({\sigma'_n}^2 + \frac{\tau^2}{{M_{CP}}^2}\right)}{{\sigma'_{nc}}^3} \tag{B.26}$$

$$\frac{\partial f_{cap}}{\partial \gamma^{p}_{cap}} = 0 \tag{B.27}$$

- **Hvorslev yield surface:**

$$\frac{\partial f_{HV}}{\partial \sigma'_n} = \tan\varphi'_e + B_{cs} \cdot \frac{3E_{oed} \cdot \left(2\nu'_{ur} - 1\right)}{E_{ur}} \cdot \left(\frac{\tan\varphi'_e}{\tan\varphi'_{cs}} - 1\right) \cdot \left(\frac{\sigma'_{ne}}{\sigma'_n}\right)^m \tag{B.28}$$

$$\frac{\partial f_{HV}}{\partial \tau} = 1 \tag{B.29}$$

$$\frac{\partial g_{HV}}{\partial \sigma'_n} = \tan \psi_{HV} \tag{B.30}$$

$$\frac{\partial g_{HV}}{\partial \tau} = 1 \tag{B.31}$$

$$\frac{\partial f_{HV}}{\partial \varepsilon^{p}_{n,HV}} = \frac{\partial f_{HV}}{\partial \gamma^{p}_{HV}} = 0 \tag{B.32}$$

σ'_{ne} in Equation B.28 is the equivalent stress on the local normal consolidation line at the trial stress $\sigma'_{n,trial}$. B_{cs} is a scalar material parameter defining the ratio τ/σ'_n at the intersection of cap yield surface and critical state line, which is determined automatically by the model at the initialisation of the stress point.

Appendix C

The following section gives the transformation of the Hvorslev yield function f_{HV} from the normalized τ-σ'_{ne} space to the local stress space τ-σ'_n, which simplifies the calculation of plastic strains.

The Hvorslev yield function is defined in the normalized stress space according to Figure C.1 and as given in Equation C.1. Due to normalization with σ'_{ne} (equivalent stress on the normal consolidation line at the current normal strain), Figure C.1 (left) represents a cross section through the state boundary surface.

$$f_{HV} = \tau + \sigma'_n \cdot \tan\varphi'_e + c'_{HV} \cdot \sigma'_{ne} = 0 \tag{C.1}$$

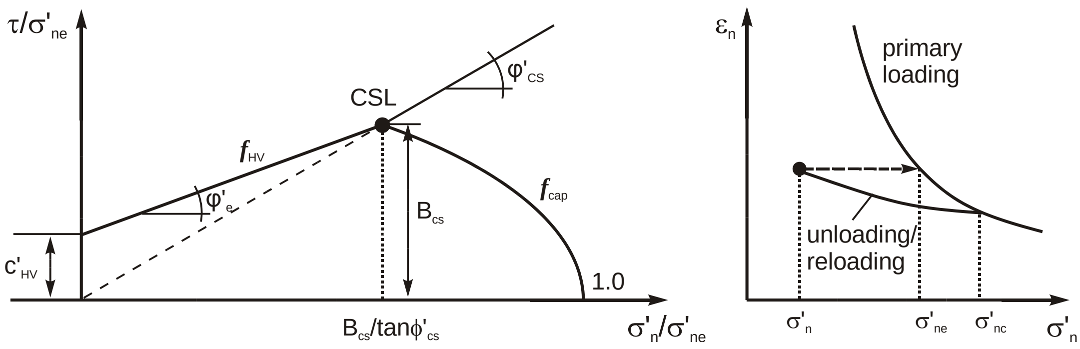

Fig. C.1: Normalized Hvorslev yield surface

For calculation of plastic strains, however, a cut along the “elastic wall” (i.e. along the unloading/reloading line) is more appropriate. For this end, σ'_{ne} needs to be replaced by σ'_{nc}, which can be achieved by considering the shape of the unloading/reloading and normal consolidation line and the current normal stress σ'_n. Elastic unloading from σ'_{nc} to σ'_n yields elastic normal strains $\Delta\varepsilon_n$:

$$\Delta\varepsilon_n = \int_{\sigma'_{nc}}^{\sigma'_n} C_n \cdot d\sigma'_n = \int_{\sigma'_{nc}}^{\sigma'_n} \frac{1-2\nu'_{ur}}{E_{ur,ref}} \left(\frac{p_{ref}}{\sigma'_n}\right)^m \cdot d\sigma'_n$$

$$= \frac{1-2\nu'_{ur}}{E_{ur,ref}} \cdot \frac{p_{ref}{}^m \left(\left|\sigma'_n\right|^{1-m} - \left|\sigma'_{nc}\right|^{1-m}\right)}{m-1} \tag{C.2}$$

Applying $\Delta\varepsilon_n$ to the hardening rule of the cap yield surface, change of σ'_{nc} along the normal compression line delivers σ'_{ne} as a function of σ'_{nc} and the current normal stress σ'_n:

$$\sigma'_{ne} = -\left[\left|\sigma'_{nc}\right|^{1-m} + \frac{3E_{oed,ref}}{{p_{ref}}^{m}} \cdot (m-1) \cdot \Delta\varepsilon_n\right]^{\frac{1}{1-m}}$$

$$= -\left[\left|\sigma'_{nc}\right|^{1-m} + \frac{3E_{oed,ref}}{E_{ur,ref}} \cdot (1 - 2\nu'_{ur}) \cdot \left(\left|\sigma'_{n}\right|^{1-m} - \left|\sigma'_{nc}\right|^{1-m}\right)\right]^{\frac{1}{1-m}} \qquad \text{(C.3)}$$

The normalized cohesion intercept c'_{HV} of the normalized yield function is defined by the shape of the cap yield surface and the difference between φ'_e and φ'_{cs}.

$$c'_{HV} = B_{cs} \cdot \left(1 - \frac{\tan\varphi'_e}{\tan\varphi'_{CS}}\right) \qquad \text{(C.4)}$$

The material parameter B_{cs} gives the ratio of shear stress τ_{cs} and equivalent normal stress $\sigma'_{n,cs}$ at critical state and thus defines the position of the critical state line.

$$B_{cs} = \frac{\tau_{cs}}{\sigma'_{ne,cs}} = \frac{\sigma'_{n,cs} \cdot \tan\varphi'_{cs}}{\sigma'_{ne,cs}} \qquad \text{(C.5)}$$

$$\sigma'_{n,cs} = \frac{M_{CP} \cdot \sigma'_{nc}}{\sqrt{{M_{CP}}^2 + {\tan\varphi'_{cs}}^2}} \qquad \text{(C.6)}$$

$$\sigma'_{ne,cs} = -\left[\left|\sigma'_{nc}\right|^{1-m} + \frac{3E_{oed,ref}}{E_{ur,ref}} \cdot (1 - 2\nu'_{ur}) \cdot \left(\left|\sigma'_{n,cs}\right|^{1-m} - \left|\sigma'_{nc}\right|^{1-m}\right)\right]^{\frac{1}{1-m}} \qquad \text{(C.7)}$$

While it is possible to derive analytical relationships for B_{cs} independent of σ'_{nc}, it is more appropriate to assume a random value of σ'_{nc} and calculate the values of $\sigma'_{n,cs}$ and $\sigma'_{ne,cs}$ according to Equations C.6 and C.7.

Appendix D

The following chapter provides the source code of the Multilaminate Model for Stiff Soil. The model is written in FORTRAN programming language to serve as a user-defined soil model (UDSM) for the finite element code PLAXIS 2010. The subroutines for storing information about the finite element mesh have been omitted for clarity. A detailed description of the structure of the source code, including the derivatives of the yield and plastic potential functions is given in Appendix B.

```
! --------------------------------------------------------------------------------------
! 'Multilaminate Model for OC Clay': user-defined soil model, Bert Schädlich (2012)
! --------------------------------------------------------------------------------------

   Subroutine MMS_G0_spec(IDTask, iMod, IsUndr, iStep, iTer, iEl, Int, &
                           X, Y, Z, Time0, dTime, Props, Sig0, Swp0, StVar0, &
                           dEps, D, BulkW, Sig, Swp, StVar, ipl, &
                           nStat, NonSym, iStrsDep, iTimeDep, iTang, &
                           iPrjDir, iPrjLen,iAbort )
! --------------------------------------------------------------------------------------
! User-defined soil model: multilaminate model
!
!  Depending on IDTask, 1: Initialize state variables
!                       2: calculate stresses
!                       3: calculate material stiffness matrix
!                       4: return number of state variables
!                       5: inquire matrix properties
!                       6: calculate elastic material stiffness matrix
!
!  Argument I/O Type
!  -------- --- ----
!  IDTask   I   I    : see above
!  iMod     I   I    : model number (1..10)
!  IsUndr   I   I    : =1 for undrained, 0 otherwise
!  iStep    I   I    : Global step number in current phase (reset to 1 in each phase)
!  iter     I   I    : Global iteration number (reset to 1 in each step)
!  iel      I   I    : Global element number
!  Int      I   I    : Global integration point number
!  X        I   R    : X-Position of integration point
!  Y        I   R    : Y-Position of integration point
!  Z        I   R    : Z-Position of integration point
!  Time0    I   R    : Time at start of step
!  dTime    I   R    : Time increment
!  Props    I   R()  : List with model parameters
!  Sig0     I   R()  : Stresses at start of step
!  Swp0     I   R    : Excess pore pressure start of step
!  StVar0   I   R()  : State variable at start of step
!  dEps     I   R()  : Strain increment
!  D       I/O  R(,) : Material stiffness matrix
!  BulkW   I/O  R    : Bulkmodulus for water (undrained only)
!  Sig      O   R()  : Resulting stresses
!  Swp      O   R    : Resulting excess pore pressure
!  StVar    O   R()  : Resulting values state variables
!  ipl      O   I    : Plasticity indicator
!  nStat    O   I    : Number of state variables
!  NonSym   O   I    : Non-Symmetric D-matrix ?
!  iStrsDep O   I    : =1 for stress dependent D-matrix
!  iTimeDep O   I    : =1 for time dependent D-matrix
!  iPrjDir  I   I    : Project directory (ASCII numbers)
!  iPrjLen  I   I    : Length of project directory name
!  iAbort   O   I    : =1 to force stopping of calculation
! --------------------------------------------------------------------------------------
  USE DFLIB
  Implicit None
  Integer         iPrjLen, nstat, iPrjLen_short
  Integer         iPrjDir(iPrjLen)
  Integer         iStep
```

```
  Integer            iTer
  Double Precision   StVar(nStat)
  Double Precision   Sig(6)
  Double Precision   Sig0(6)
  Double Precision   StVar0(nStat)
  Double Precision   dEps(6)
  Double Precision   D(6,6)
  Double Precision   Props(50)

! --------------------------------------------------------------------------------------
! Expected contents of Props(1..50)
!
!  1 : Eoed_ref      reference stiffness for primary oedometer loading
!  2 : Eur_ref       elastic refference stiffness for un- and reloading
!  3 : p_ref         reference stress
!  4 : m_power       power for stress dependency of stiffness
!  5 : NYUR          Poisson's ratio
!  6 : AMAT          material parameter for deviatoric hardening
!  7 : switch_HV     0-no Hvorslev, 1-Hvorslev with non-local, 2-Hvorslev w/o non-local
!  8 : COH           cohesion
!  9 : PHI           ultimate friction angle
! 10 : PSI           dilatancy angle
! 11 : TENS          value of sig_n for tension cut-off
! 12 : POP           pre-overburden pressure
! 13 : OCR           overconsolidation ratio
! 14 : Rf            failure ratio
! 15 : K0nc          lateral earth pressure coefficient for normal consolidation
! 16 : NUMCP         number of contact planes
! 17 : phi1          mobilised friction angle at psimin (new dev. flow rule)
! 18 : psimin        minimum of mobilised dilatancy (new dev. flow rule)
! 19 : F_Amat        factor on Amat above CSL (research use only)
! 20 : F_psi         factor on psi above CSL (research use only)
! 21 : G0ref         isotropic shear modulus at very small strains
!                    at reference pressure
! 22 : sw_pdash_SN0  switch for stress dependency of stiffness: 0-on p', 1-on sig_n,
!                    2-on sig_h0 and sig_v0
! 23 : eps_deg_1     parameter for stiffness degradation (small-strain stiffness)
! 24 : eps_deg_2     parameter for stiffness degradation (small-strain stiffness)
! 25 : phi_e         inclination of Hvorslev surface in tau-sign-space
! 26 : SIG_I(1)      optional initial stress state (first component)
! 27 : SIG_I(2)      optional initial stress state (second component)
! 28 : SIG_I(3)      optional initial stress state (third component)
! 29 : SIG_I(4)      optional initial stress state (forth component)
! 30 : SIG_I(5)      optional initial stress state (fifth component)
! 31 : SIG_I(6)      optional initial stress state (sixth component)
! 32 : STEPSIZE      for subincrementing (determines max. size of dEps)
! 33 : PHI_NULL      minimum value for mobilised friction angle (for initialization)
! 34 : SIGN_NULL     minimum value for preconsolidation stress (for initialization)
! 35 : Ev0           Small strain stiffness - Vertical axial E-modulus
! 36 : Eh0           Small strain stiffness - Horizontal axial E-modulus
! 37 : Gvh0          Small strain stiffness - Independent anisotropic shear modulus
! 38 : nuhh0         Small strain stiffness - Poison's ratio within plane of symmetry
! 39 : nuvh0         Small strain stiffness - Poison's ratio out of plane of symmetry
! 40 : Ar            Ratio of anisotropy with regard to shear strength
! 41 : Theta         Angle of rotation between the primary axis of anisotropy
!                    (shear strength) and vertical axis, rotation in xy-plane only,
!                    clockwise rotation = positiv Theta
! 42 : phi_res       critical state phi in Hvorslev model
!                    /residual phi in Galavis softening model
! 43 : coh_res       residual cohesion in Galavis softening model
! 44 : h_phi         softening rate for friction angle (Galavis softening model)
! 45 : h_coh         softening rate for cohesion (Galavis softening model)
! 46 : Length        Internal length in non-local approach
! 47 : A             gives proportion of dev. / normal plastic strains
!                    in Galavis softening approach
! 48 : MaxPoint      limits number of stresspoints considered in non-local approach,
!                    should be checked with value in stresspoint.sft
! 49 : sss_recovery  switch for sss recovery, 0 - no recovery,
!                    1 - sss recovery activated
! 50 : h_soft        softening rate in Hvorslev softening model
! --------------------------------------------------------------------------------------

Double Precision  ::    Eoed_ref
Double Precision  ::    Eur_ref
Double Precision  ::    p_ref
Double Precision  ::    m_power
Double Precision  ::    NYUR
Double Precision  ::    AMAT, Amat_ref, F_amat, F_psi
```

```
Double Precision  ::    ACAP
Double Precision  ::    COH, COH_i
Double Precision  ::    PHI, PHI_i, tan_phi, tan_phi_i
Double Precision  ::    PSI, psi_HV
Double Precision  ::    POWER
Double Precision  ::    TENS
Double Precision  ::    POP
Double Precision  ::    OCR
Double Precision  ::    Rf
Double Precision  ::    K0nc
Integer           ::    NUMCP, numpoint
Double precision  ::    phi1
Double precision  ::    psimin
Double Precision  ::    SIG_I(6)
Double Precision  ::    STEPSIZE
Double Precision  ::    PHI_NULL, tan_phi_Null
Double Precision  ::    SIGN_NULL
Double Precision  ::    G0ref
Integer           ::    sw_pdash_SN0
Double Precision  ::    gamma_1, gamma_2
Double Precision  ::    phi_e, tan_phi_e
Double Precision  ::    CONVERGE    ! for convergence control
Double Precision  ::    crit        ! for convergence control
Double Precision  ::    SIGNC, TPHIM
Double precision  ::    xNu_U       ! undrained Poisson's ratio
Double precision  ::    BulkW       ! Bulk modulus of water in undrained calculation
Double precision  ::    phicv       ! critical state frictio angle
Double Precision  ::    tan_PHI_MOD ! corresponding to Rf
Double Precision  ::    MCP         ! cap shape parameter
Double Precision  ::    L(3)        ! for stress transformation
Double Precision  ::    P(3), t(3), tt(3), s(3) ! for stress transformation
Double Precision  ::    SN          ! normal stress on contact plane
Double Precision  ::    TAU         ! shear stress on contact plane
Double Precision  ::    iTAU        ! check value for negative TAU
Double Precision  ::    SN0         ! normal stress from sig0 on contact plane
Double Precision  ::    TAU0        ! shear stress from sig0 on contact plane
Double Precision  ::    SIGMA0(3,3), sigma_nc0 ! symmetric stress matrix sigma0
Double Precision  ::    SIGMA0_mod(3,3)! symmetric stress matrix sigma0_mod
Double Precision  ::    SIGMA(3,3)  ! symmetric stress matrix
Integer,Dimension(3)::  V1,V2,V3    ! for assembling stress matrix
Double Precision  ::    dsig(6)     ! stress increment
Double Precision  ::    Sig0_mod(6) ! modified initial stress state due to POP/OCR
Double Precision  ::    Sig_trial(6)! trial stress state
Double Precision  ::    dSig_trial(6)  ! trial stress increment
Double Precision  ::    dEps_trial(6)  ! target global strain increment
Double Precision  ::    dEps_plastic(6)! global plastic strain increment

! difference of global plastic strain increments of subsequent iterations
Double Precision  ::    dEps_vol_pl, SumdEps_vol_pl, dGamma_pl, SumdGamma_pl

! subincrementing variables
Double Precision  ::    SIGNC_s, ITAU_0
Integer           ::    n_sub, n_sub_cone, n_sub_cap, n_sub_tens, n_sub_HV
Double Precision  ::    dSig_check(6)  ! stress increment for calculating n_sub
Double Precision  ::    Sig_check(6)   ! stress state for calculating n_sub
Double Precision  ::    SIGMA_check(3,3), SN_CHECK, TAU_check
Double Precision  ::    dEps_sub(6)      ! global strain increment for subincrementing
Double Precision  ::    dEps_norm        ! norm of dEps for subincementing
Double Precision  ::    Sig0_sub(6)      ! global stress state at start of subincr.
Double Precision  ::    SIGMA_0(3,3), SN_0, TAU_0  ! stresses at start of step
Double Precision  ::    DSN, DTAU        ! local stress change due to deps
Logical           ::    converged_cp     ! convergence for iteration over cp's
Logical           ::    failure_mode     ! correct mode of failure
Integer           ::    ipl_cp(5)        ! state of plasticity during one sub-iteration
Integer           ::    ipl_gl(5)        ! state of plasticity within integration point
Double Precision  ::    corr_val         ! min. value of local normal stress
Character         ::    fname*255        ! file name for debugging
Logical           ::    IsOpen           ! file status
Logical(4)        ::    dirpath          ! path of current directory
Double Precision  ::    Cnn_ref, Cnn, Ctt, CNNCTT ! Local normal and shear stiffness
Double Precision  ::    facCnn           ! stress dependency of local stiffness
Double Precision  ::    TiT_spec(6,6), Tj_spec(6,6), TiT_spec_inv(6,6), TiT(3,6),
Tj(6,3) ! Transformation matrices
Double Precision  ::    Sig0_cp(3), Sig_cp(3), Sig_cp_spec(6), Sig0_cp_spec(6),
Sig0_sub_cp(6)    !Local stress vectors
Double Precision  ::    C_cp(6,6), LE(6,6), LExTiT_inv(6,6), TjxC_cp(6,6), C_gl_cp(6,6),
C_gl(6,6)   ! local compliance matrices
```

```
Double Precision  ::    D_loc(2,2)     !Local elastic stiffness matrix for plastic strain
calculation (N-T-split)

 ! For local plastic strain calculation
Double Precision  ::    f_cap, f_cone, f_tens, f_HV      ! values of yield functions
Double Precision  ::    Lambda_cone, Lambda_cap, Lambda_HV  ! Local plastic multipliers
Double Precision  ::    epsNcone, epsGcone, epsG1cone, epsG2cone, eps_cone(3)
Double Precision  ::    epsNcap, epsGcap, epsG1cap, epsG2cap, eps_cap(3)
Double Precision  ::    epsNHV, epsGHV, eps_HV(3)
Double Precision  ::    epsNtens, epsGtens, eps_tens(3)
Double Precision  ::    Dloc_x_dgconedsig(2), Dloc_x_dgcapdsig(2), Dloc_x_dgHVdsig(2)

! Derivatives of yield functions
Double Precision  ::    dFcap_dsig(2), dGcap_dsig(2), dFcap_depspl(2)
Double Precision  ::    dFcone_dsig(2), dGcone_dsig(2), dFcone_depspl(2)
Double Precision  ::    dFHV_dsig(2), dGHV_dsig(2), dFHV_depspl(2)
Double Precision  ::    dGTdSN, dGTdTau, dFTdSN, dFTdTau

 ! Variables for plastic strain calculation with Koiter rules
Logical           ::    cap_active, cone_active, HV_active, failure, Hvorslev
Double Precision  ::    L11, L22, L33, L12, L21, L13, L31, L23, L32
Double Precision  ::    Lambda_cone_1, Lambda_cone_12, Lambda_cap_1, Lambda_cap_12
Double Precision  ::    Lambda_HV_1, Lambda_HV_13, Lambda_HV_23, Lambda_cap_23,
Lambda_cone_13

! Small strain stiffness parameters
Double Precision  ::    deg_par     ! stiffness degradation parameters
Logical           ::    stiff_low, smallstrain, anisotropic_el
Double Precision  ::    sss_indicator_cp, sss_indicator_gl, FLOH_GAMMA

! Modification of strain hardening due to small strain stiffness
Double Precision  ::    x_stiff
Double Precision  ::    TPHIM_SSS, SIGNC_SSS, SIGNC_Sig_trial, TPHI_Sig_trial
Double Precision  ::    SIGNC_sub0, TPHIM_sub0

! Anisotropic small strain stiffness
Double Precision  ::    Ev0, Eh0, Gvh0, nu_hh_0, nu_vh_0, nu_hv_0 ! initial stiffness
Double Precision  ::    Ev, Eh, Gvh, nu_hh, nu_vh, nu_hv ! current tangential stiffness
Double Precision  ::    lambda_1, lambda_2, lambda_3, lambda_4, omega
Double Precision  ::    sig_h0, sig_v0    ! initial horizontal and vertical stresses

! calculation of stress/strain direction and stiffness recovery
Double Precision  ::    dSig_el_cp_spec(6)
Logical           ::    stiffness, recovery, existing
Integer           ::    iterStiff, sss_recovery
Double Precision  ::    n_bubble_old
Double Precision, ALLOCATABLE ::   eps_cp_gamma(:,:), deps_cp_gamma(:,:), gamma_cp(:)
Double Precision, ALLOCATABLE ::   dEps_cp_pl(:,:), dEps_cp_el(:,:), dEps_cp(:,:)
Double Precision, ALLOCATABLE ::   dEps_cp_el_spec(:,:), eps_gamma_return_1 (:)
Double Precision, ALLOCATABLE ::   eps_gamma_return_2 (:), eps_gamma_return_3 (:),
Double Precision, ALLOCATABLE ::   eps_cp_gamma_centre_1(:,:), n_bubble (:)
Double Precision, ALLOCATABLE ::   eps_cp_gamma_centre_2(:,:), gamma_bubble(:,:)
Double Precision, ALLOCATABLE ::   eps_cp_gamma_centre_3(:,:)

! Hvorslev surface variables
Double Precision  ::    sig_ve, sigS, tauS, B_cs, tau_max, sig_ve0, sig_ve_check
Double Precision  ::    tan_phi_HV, switch_HV, h_soft

! Parameters of Scharingers dilatancy formulation
Double Precision  ::    a1, b1, c1, a2, b2, c2, d2, k1_nSDT, k2_nSDT

! For correction of plastic strain calculation at tension cut off and Hvorslev surface
Double Precision, ALLOCATABLE ::   epsn_t_step(:), epsn_HV_step(:), gamma_HV_step(:)

! Anisotropic shear strength
Double Precision  ::    Ar, Theta, Nv, Norm_t, rot(3)

! Parameters for strain softening calculation
Double Precision  ::    Damage_strain, X, Y, Z, Length, Volume
Double Precision  ::    XX,YY,ZZ, LL, GLD_strain
Integer           ::    iPhase, inSPoint, MaxPoint
Double Precision  ::    Phi_res, tan_phi_res, C_res, eps_damage, eps_damage_old
Double Precision  ::    hPhi, hCoh, Eps_non_local, Eps_non_local_old
Logical           ::    Softening, Hard_Soft, Eps_non_local_cal
Double Precision::dSt, WdSt, Vol
Double Precision, ALLOCATABLE    :: weights(:)
Integer, ALLOCATABLE             :: point_index(:)
```

```
Double Precision  ::    pdash, Pi, Rad, DUM1, DUM2, DUM, EXPRESSION1, EXPRESSION2,
EXPRESSION
Double Precision  ::    Eur, facE, Hardcap, phim, psim, SWP0, Time0, DTIME, A
Double Precision  ::    dEpsV, SWp, dSwp, Gur, f1, f2, eps_cp_plastic(3), eps_cp_gl(6)
Integer           ::    IDTask, i, ii, k, j, m, iel, iter_cp, INT, ipl, Isundr, Nonsym
Integer           ::    ISTRSDEP, ITANG, ITIMEDEP, IMod, Iabort, NUMSTV, iSt, IREC
Double Precision, ALLOCATABLE ::    n1(:,:), s1(:,:), t1(:,:), WEIGHT(:)

Data Pi/3.141592653589793238462643383279502884197169399d0/
Rad  = 180d0 / Pi

Eoed_ref    = Props(1)
Eur_ref     = Props(2)
p_ref       = Props(3)
m_power     = Props(4)
NYUR        = Props(5)
AMAT        = Props(6) / 1000
switch_HV   = Props(7)
COH         = Props(8)
PHI         = Props(9) / Rad
PSI         = Props(10) / Rad
TENS        = Props(11)
POP         = Props(12)
OCR         = Props(13)
Rf          = Props(14)
K0nc        = Props(15)
NUMCP       = Props(16)
phi1        = Props(17) / Rad
psimin      = Props(18) / Rad
F_Amat      = Props(19)
F_psi       = Props(20)
G0ref       = Props(21)
sw_pdash_SN0= Props(22)
gamma_1     = Props(23)
gamma_2     = Props(24)
phi_e       = Props(25) / Rad
SIG_I(1)    = Props(26)
SIG_I(2)    = Props(27)
SIG_I(3)    = Props(28)
SIG_I(4)    = Props(29)
SIG_I(5)    = Props(30)
SIG_I(6)    = Props(31)
STEPSIZE    = Props(32)
PHI_NULL    = Props(33) / Rad
SIGN_NULL   = Props(34)
Ev0         = Props(35)
Eh0         = Props(36)
Gvh0        = Props(37)
nu_hh_0     = Props(38)
nu_vh_0     = Props(39)
Ar          = Props(40)
Theta       = Props(41) / Rad
Phi_res     = Props(42) / Rad
C_res       = Props(43)
hPhi        = Props(44)
hCoh        = Props(45)
Length      = Props(46)
A           = Props(47)
MaxPoint    = Props(48)
sss_recovery= Props(49)
h_soft      = Props(50)

CONVERGE = 1.0d-7
corr_val = -1.0d0

! open storage for parameters with variable field length
Allocate (eps_cp_gamma(3,numcp), deps_cp_gamma(3,numcp), gamma_cp(numcp),
dEps_cp_pl(3,numcp))
Allocate (dEps_cp_el(3,numcp), dEps_cp(3,numcp), epsn_t_step(numcp),
epsn_HV_step(numcp), gamma_HV_step(numcp))
Allocate (dEps_cp_el_spec(6,numcp), n1(numcp,3), s1(numcp,3),t1(numcp,3), WEIGHT(numcp))
Allocate (eps_gamma_return_1(numcp), eps_gamma_return_2(numcp),
eps_gamma_return_3(numcp),n_bubble (numcp))
Allocate (eps_cp_gamma_centre_1(numcp,4), eps_cp_gamma_centre_2(numcp,4),
eps_cp_gamma_centre_3(numcp,4), gamma_bubble(numcp,4))

smallstrain =.true.
anisotropic_el =.true.
```

```
! In case of isotropy in small strain range calculate local compliance from G0ref input
If (Eh0.le.Eur_ref.and.Ev0.le.Eur_ref) then
   If (G0ref.gt.(Eur_ref/(2.0d0+2.0d0*NYUR)))  then  ! isotropic small strain stiffness
         Gvh0 = G0ref
         Ev0 = G0ref*2*(1+NYUR)
         Eh0 = Ev0
         nu_vh_0 = NYUR
         nu_hh_0 = NYUR
         anisotropic_el =.false.
   Else                 ! small strain stiffness == large strain elastic stiffness
         Gvh0 = Eur_ref/(2.0d0+2.0d0*NYUR)
         Ev0 = Eur_ref
         Eh0 = Eur_ref
         nu_vh_0 = NYUR
         nu_hh_0 = NYUR
         smallstrain =.false.
         anisotropic_el =.false.
         If (sw_pdash_SN0 == 2)  sw_pdash_SN0 = 0
      End if
End if

nu_hv_0     =  nu_vh_0*Eh0/Ev0

! set default values if no user input
if (Rf==0)              Rf=0.9
if (K0nc==0)            K0nc=1-dsin(PHI)
if (p_ref==0)           p_ref=100.0d0
if (m_power.ge.1.0d0)   m_power = 0.9999d0
if (Ar==0)              Ar = 1.0d0
if (gamma_1 == 0)       gamma_1 = 0.00000001
if (gamma_2 == 0)       gamma_2 = 0.000002
if (gamma_2.le.gamma_1) gamma_2 = gamma_1 + 0.000001d0
if (MaxPoint == 0)      MaxPoint = 200
if (NUMCP == 0)         NUMCP = 33
if (F_amat ==0)         F_amat = 1
if (F_psi ==0)          F_psi = 1

! check whether stiffness recovery is required
if (sss_recovery == 1)  then
   recovery = .true.
Else
   recovery = .false.
End if

! check whether Hvorslev softening calculation is required
if (switch_HV == 1.or.switch_HV == 2) then
   Hvorslev = .true.
   psi = 0.0d0
   coh = 0.0d0
   phi = phi_res
else
   Hvorslev = .false.
End if

Hard_Soft=.True.     ! check whether Galavi softening calculation is required
if ((Phi_res>=0.999999d0*PHI).and.(C_res>=0.999999d0*Coh)) Hard_Soft=.False.

! get direction cosines and weight factors
call DIRCOS3D (NUMCP, n1, s1, t1, WEIGHT, anisotropic_el, sw_pdash_SN0)
rot(1) = dsin(Theta)
rot(2) = dcos(Theta)
rot(3) = 0.0d0
tan_phi = dtan(phi)
tan_phi_e = dtan(phi_e)
k1_nSDT = 0.0d0
k2_nSDT = 0.0d0

! --------------------------------------------------------------------------------------
! Initialize state variables
! --------------------------------------------------------------------------------------
If (IDTask .Eq. 1) Then
   ! do IDTask1 only once
   If (StVar0(3*ABS(NUMCP)+2)==123.) then
      if (Hard_Soft) close (34)  ! close file startphase.sft if softening calculation
      Return
   end if
```

```
! get length of project directory, specific for Plaxis 2D 2010!
iPrjLen_short = iPrjLen - 9
StVar0(3*ABS(NUMCP)+13) = iPrjLen_short

! get cap shape parameter
Call GetAcap   (iel,int,ACAP,NUMCP,NYUR,p_ref,Eur_ref,Eoed_ref,AMAT,phi_res,coh,&
               m_power,tens,Rf,K0nc,phi1,psimin,k1_nSDT,k2_nSDT,sw_pdash_SN0,&
               PHI_NULL,SIGN_NULL,anisotropic_el,iPrjDir, iPrjLen_short)

StVar0(3*ABS(NUMCP)+3) = ACAP
tan_phi_Null = dtan(phi_null)
tan_phi_res = dtan(phi_res)

! open files to put information of stress point
if (hard_Soft.or.switch_HV == 1) then
   ! create subdirectory "softening_files" in current directory
   Do i=1,iPrjLen_short
      fname(i:i) = Char( iPrjDir(i) )
   End Do
   fname= fname(:iPrjLen_short)//'softening_files'
   dirpath = MAKEDIRQQ(fname)
   ! write point ccordinates to file 31 ==> Info.sft
   Inquire(Unit= 31, Opened= IsOpen)
   If (.not.IsOpen) Then
      fname=' '
      Do i=1,iPrjLen_short
         fname(i:i) = Char( iPrjDir(i) )
      End Do
      fname= fname(:iPrjLen_short) //'softening_files'//'/'//'Info.sft'
      Open(Unit= 31, File= fname, Position='Append')
   End If
   write (31,*) Iel, Int, X, Y, Z
   close (31)
   iPhase=0
   fname=' '
   Do i=1,iPrjLen_short
      fname(i:i) = Char( iPrjDir(i) )
   End Do
   fname= fname(:iPrjLen_short)//'softening_files'//'/'//'StartPhase.nr'

   Inquire (file = fname, Exist= existing)
   if (.not.existing) then
      Open(Unit= 34, File= fname, Position='rewind')
      write (34,*) iPhase     ! write phase number to file "StartPhase.nr"
      inSPoint=0
      Inquire(Unit= 30, Opened= IsOpen)
      If (.not.IsOpen) Then
         fname=' '
         Do i=1,iPrjLen_short
            fname(i:i) = Char( iPrjDir(i) )
         End Do
         fname = fname(:iPrjLen_short)//'softening_files'//'/'//'Step.nr'
         Open  (Unit= 30, File= fname, RECL=15, Form='FORMATTED', access='Direct'&
               ,action='readwrite')
         iSt=1
         write (30,'(I5, I7)',rec=1) iSt, inSPoint
      End If
   End if
end if   ! hard_Soft.or.Hvorslev

! adjust Sig0 due to input values
if (sum(SIG_I)==0.) SIG_I=Sig0 ! no modification due to Props(21..26)
  Sig0_mod = Sig0

   ! adjust Sig0(1:3) due to OCR
   if (OCR.gt.1.) then
      Sig0_mod(1)=(SIG_I(1)*OCR)
      Sig0_mod(2)=SIG_I(2)*OCR
      Sig0_mod(3)=(SIG_I(3)*OCR)
      Sig0_mod(4)=0d0
      Sig0_mod(5)=0d0
      Sig0_mod(6)=0d0
   end if

   ! adjust Sig0(1:3) due to POP
   if (POP.ne.0.) then
      Sig0_mod(1)=(SIG_I(2)-dabs(POP))*K0nc
      Sig0_mod(2)=SIG_I(2)-dabs(POP)
```

```
   Sig0_mod(3)=(SIG_I(2)-dabs(POP))*K0nc
   Sig0_mod(4)=0d0
   Sig0_mod(5)=0d0
   Sig0_mod(6)=0d0
end if

! prepare data
V1= (/1,4,6/); V2= (/4,2,5/); V3= (/6,5,3/)
SIGMA0_mod(:,1)= Sig0_mod(V1)      ! assembling symm.stress matrix SIGMA0_mod
SIGMA0_mod(:,2)= Sig0_mod(V2)      ! from stress vector Sig0_mod dim(6)
SIGMA0_mod(:,3)= Sig0_mod(V3)

SIGMA0(:,1)= Sig_I(V1)             ! assembling symm.stress matrix SIGMA0 dim(3,3)
SIGMA0(:,2)= Sig_I(V2)             ! from stress vector Sig_I dim(6)
SIGMA0(:,3)= Sig_I(V3)

StVar0(0*ABS(NUMCP)+1:ABS(NUMCP)*1)=SIGN_NULL     ! sigma_n_preconsolidation
StVar0(1*ABS(NUMCP)+1:ABS(NUMCP)*2)=tan_phi_null  ! tan_phi_mob in hardening
StVar0(2*ABS(NUMCP)+1:ABS(NUMCP)*3)=SIGN_NULL     ! sigma_n_preconsolidation

If (smallstrain.or.Hard_soft.or.Hvorslev) then
   StVar0(3*ABS(NUMCP)+4)=0.d0     ! record number of current stress point
   StVar0(3*ABS(NUMCP)+5)=1.d0     ! sss_indicator
   StVar0(3*ABS(NUMCP)+8)=0.d0     ! non_local damage factor
   StVar0(3*ABS(NUMCP)+9)=0.d0     ! Value of macroscopic local damage strain
   StVar0(3*ABS(NUMCP)+10)=0.d0    ! Number of stress points within 2*Length
   StVar0(4*ABS(NUMCP)+1:ABS(NUMCP)*5)=0.d0    ! Local damage strain
   StVar0(5*ABS(NUMCP)+1:ABS(NUMCP)*6)=0.d0    ! eps_gamma_cone_Peak
   StVar0(6*ABS(NUMCP)+1:ABS(NUMCP)*7)=tan_phi ! Tan_Phi_mobilised  in softening
   If (Hvorslev) StVar0(6*ABS(NUMCP)+1:ABS(NUMCP)*7)=0.d0   ! previous non_local
                                                  !damage strain Hvorslev softening
   If (Hard_soft) StVar0(7*ABS(NUMCP)+1:ABS(NUMCP)*8)=coh   ! cohesion
End if ! smallstrain.or.hardsoft.or.Hvorslev

if (smallstrain)  then
   StVar0(8*ABS(NUMCP)+1:(ABS(NUMCP)*9))=0.d0     ! shear strain component 1
    StVar0(9*ABS(NUMCP)+1:(ABS(NUMCP)*10))=0.d0   ! shear strain component 2
   StVar0(10*ABS(NUMCP)+1:(ABS(NUMCP)*11))=0.d0   ! shear strain component 3
    StVar0(11*ABS(NUMCP)+1:(ABS(NUMCP)*12))=0.d0     ! gamma_cp
   If (recovery == .true.) then
      StVar0(12*ABS(NUMCP)+1:ABS(NUMCP)*15)=0.d0  ! Coordinates of return point
      StVar0(15*ABS(NUMCP)+1:ABS(NUMCP)*16)=1.d0  ! number of active bubbles
      StVar0(16*ABS(NUMCP)+1:ABS(NUMCP)*32)=0.d0  ! Bubble coordinates and radii
   End if   ! smallstrain & recovery
End if ! smallstrain

   ! transformation of Sig0_mod -> sigma_n, tau
DO i=1,ABS(NUMCP) !loop over all cps
   L(1:3)= n1(i,1:3)                     ! unit normal vector of plane, dim(3)
   P= MATMUL (SIGMA0_mod,L)              ! traction P, dim(3)
   SN=  DOT_PRODUCT (L,P)                ! sigma_n on c.p.
   TAU= DOT_PRODUCT (P,P)- SN**2
   iTAU= -0.01*dabs(SN)
   IF (iTAU.le.0.01) iTAU=0.01d0
   IF (TAU < 0.and.TAU>-iTAU) TAU= 0.0   ! adjust small differences
   IF (TAU > 0.and.TAU<iTAU) TAU= 0.0    ! adjust small differences
   IF (TAU <= -iTAU) STOP 'ERROR - MYMOD_ML: tau negative on cp'
   TAU= dsqrt(TAU)                       ! tau on c.p.
   ! transformation of Sig0 -> sigma_n0, tau0
   P= MATMUL (SIGMA0,L)                  ! traction P, dim(3)
   SN0=  DOT_PRODUCT (L,P)               ! sigma_n0 on c.p.
   TAU0= DOT_PRODUCT (P,P)- SN0**2
   iTAU= -0.01*dabs(SN)
   IF (iTAU.le.0.01) iTAU=0.01d0
   IF (TAU0 < 0.and.TAU0>-iTAU) TAU0= 0.0 ! adjust small differences
   IF (TAU0 > 0.and.TAU0<iTAU) TAU0= 0.0
   IF (TAU0 <= -iTAU) then
      STOP 'ERROR - MYMOD_ML: tau negative on cp'
   end if
   TAU0= dsqrt(TAU0)                     ! tau0 on c.p.

   s(1)=SN0*L(1)
   s(2)=SN0*L(2)
   s(3)=SN0*L(3)

   t(1)=P(1)-S(1)
   t(2)=P(2)-S(2)
   t(3)=P(3)-S(3)
```

```
      tt(1)=dcos(Theta)*t(1)-dsin(Theta)*t(2)
      tt(2)=dSin(Theta)*t(1)+dcos(Theta)*t(2)

      Norm_t=dSqrt(tt(1)**2+tt(2)**2+t(3)**2)

      if (Norm_t/=0) then
         Nv=dabs(tt(2))/Norm_t
         tan_Phi_i= tan_phi*(1-(Ar-1)/(Ar+2)*(1-3*(Nv**2)))
         COH_i=COH*(1-(Ar-1)/(Ar+2)*(1-3*(Nv**2)))
      else
         tan_Phi_i = tan_phi
         COH_i = COH
      endif

      ! initial stress state: cone - tanphi_mob_i
      DUM1= (TAU*tan_phi_i) / (COH_i-SN*tan_phi_i)
      IF ((COH_i-SN*tan_phi_i).eq.0) DUM1=0.0d0
      DUM2= (TAU0*tan_phi_i) / (COH_i-SN0*tan_phi_i)
      IF ((COH_i-SN0*tan_phi_i).eq.0) DUM2=0.0d0
      DUM= MAXVAL((/DUM1,DUM2,tan_phi_null/))

      if (.not.Hvorslev) then
         IF (DUM.gt.tan_phi_i) DUM=tan_phi_i
      End if

      StVar0(1*ABS(NUMCP)+i) = DUM        ! tan_phi_mob_initial

      ! initial cap position: signc_mob_i
      IF (tan_PHI_i==0.0) STOP 'ERROR - PHI=0 not possible' ! to avoid division by 0
       MCP= ACAP*tan_phi_res
      EXPRESSION1= -dsqrt((SN*SN)+(TAU*TAU)/(MCP*MCP))
      EXPRESSION2= -dsqrt((SN0*SN0)+(TAU0*TAU0)/(MCP*MCP))
      EXPRESSION= MINVAL((/EXPRESSION1,EXPRESSION2/))
      sigma_nc0= MINVAL((/SIGN_NULL,-tan_phi_null*coh/(MCP*tan_phi_i)/))
      IF (SIGN_NULL > EXPRESSION) then
         StVar0(2*ABS(NUMCP)+i)= EXPRESSION
      else
         StVar0(2*ABS(NUMCP)+i)= sigma_nc0
      end if
      StVar0(0*ABS(NUMCP)+i)= StVar0(2*ABS(NUMCP)+i)  ! set value of signc_0
   END DO ! loop over all cps

   ! get Hvorslev surface parameter B_cs
   signc = -1000                 ! test signc, only used for getting B_cs
   sigS = MCP*signc/dsqrt(MCP**2 + tan_phi_res**2) ! intersection of cap and CSL
   tauS = -tan_phi_res*sigS      ! intersection of cap and CSL
   ! equivalent normal stress at the normal consolidation line
   sig_ve = -((-signc)**(1-m_power)+Eoed_ref/Eur_ref*3*(1-2*NYUR)*((-sigS)**&
                (1-m_power)-(-signc)**(1-m_power)))**(1/(1-m_power))
   B_cs = tauS / -sig_ve         ! ratio of shear stress vs. equivalent pressure
   StVar0(3*ABS(NUMCP)+12) = B_cs

   ! Initial anisotropic stiffness due to initial stress ratio
   if (smallstrain.and.sw_pdash_SN0 == 2) then
      sig_v0 = Sig0(2)
      sig_h0 = 0.5d0*(Sig0(1)+Sig0(3))
      pdash = (Sig0(1) + Sig0(2) + Sig0(3))/3
      Eh0 = Eh0*(-sig_h0/-pdash)**m_power
      Ev0 = Ev0*(-sig_v0/-pdash)**m_power
      Gvh0 = Gvh0*(dsqrt(sig_v0*sig_h0)/-pdash)**m_power
      nu_hv_0     =  nu_vh_0*Eh0/Ev0
      StVar0(3*ABS(NUMCP)+14) =  Eh0
      StVar0(3*ABS(NUMCP)+15) =  Ev0
      StVar0(3*ABS(NUMCP)+16) =  Gvh0
      StVar0(3*ABS(NUMCP)+17) =  nu_hv_0
   End if

   StVar0(3*ABS(NUMCP)+2)=123. ! initialization is done
End If  !IDTask = 1

! --------------------------------------------------------------------------------------
! calculate stresses
! --------------------------------------------------------------------------------------
If (IDTask .Eq. 2) Then

   C_gl = 0.0d0

   ! calculate ratio Cnn/Ctt from NYur
```

```
   CnnCtt = (1d0-2d0*NYur)/(1d0+3d0*NYur)
   Cnn_ref=(1.0d0-2.0d0*NYur)/Eur_ref
   Amat_ref = Amat

   ACAP = StVar0(3*ABS(NUMCP)+3)       ! cap shape parameter
   B_cs = StVar0(3*ABS(NUMCP)+12)      ! Hvorslev surface parameter
   tan_phi_Null = dtan(phi_null)
   tan_phi_res = dtan(phi_res)
   MCP      = ACAP*tan_phi_res         ! M_cap_shape (M=alpha*tan_phi)

   iterStiff=0
   stiffness=.false.

   iPrjLen_short = IDint(StVar0(3*ABS(NUMCP)+13)) ! get length of project directory path

   ! get anisotropic small strain stiffness if dependency on axial stresses
   if (smallstrain.and.sw_pdash_SN0 == 2) then
      Eh0 = StVar0(3*ABS(NUMCP)+14)
      Ev0 = StVar0(3*ABS(NUMCP)+15)
      Gvh0 = StVar0(3*ABS(NUMCP)+16)
      nu_hv_0 = StVar0(3*ABS(NUMCP)+17)
   End if

   ! initialize StVar
   StVar = StVar0

! Creating files with strain softening information
!***********************************************************************************
   If (switch_HV == 2)  GLD_strain = StVar(3*ABS(NUMCP)+9)

   If (Hard_Soft.or.switch_HV == 1) then
      Call Open_DamageFile (iStep, iter, iel, iPrjDir, iPrjLen_short, iPhase, &
                            StVar, nStat, NumCP)
      iRec=IDint(StVar0(3*ABS(NUMCP)+4))
      If (iRec==0) then
         Call FileOrganize(iPrjDir, iPrjLen_short, Iel, Int, Length, StVar, NumCP, &
                            X, Y, Z,nStat,iPhase, MaxPoint)
         iRec=IDint(StVar(3*ABS(NUMCP)+4))
      end if

!     call Weight_Strain(StVar, nStat, Weight, NUMCP, GLD_strain)
      GLD_strain = StVar(3*ABS(NUMCP)+9)
      Vol= StVar(3*ABS(NUMCP)+7)
      NumPoint = IDint(StVar(3*ABS(NUMCP)+10))

      Allocate (point_index (NumPoint), weights(NumPoint))

      ! open file which contains point indices in vicinity of current stress point
      Inquire(Unit= 40, Opened= IsOpen)
      If (.not.IsOpen) Then
         fname=' '
         Do i=1,iPrjLen_short
            fname(i:i) = Char( iPrjDir(i) )
         End Do
         fname= fname(:iPrjLen_short)//'softening_files'//'/'//'point_index.sft'
         Open(Unit= 40, File= fname, RECORDTYPE='Fixed', RECL=4*MaxPoint, &
              Form='Binary', access='Direct', action='readwrite')
      End If

      ! open file which contains point weights in vicinity of current stress point
      Inquire(Unit= 41, Opened= IsOpen)
      If (.not.IsOpen) Then
         fname=' '
         Do i=1,iPrjLen_short
            fname(i:i) = Char( iPrjDir(i) )
         End Do
         fname= fname(:iPrjLen_short)//'softening_files'//'/'//'weights.sft'
         Open(Unit= 41, File= fname, RECORDTYPE='Fixed', RECL=8*MaxPoint, &
              Form='Binary', access='Direct', action='readwrite')
      End If

      ! get point indices and weights from files "point_index.sft" and "weights.sft"
      Read (40, Rec=IDint(StVar(3*ABS(NUMCP)+4))) point_index
      Read (41, Rec=IDint(StVar(3*ABS(NUMCP)+4))) weights

   end if   ! (Hard_Soft.or.switch_HV == 1)
!***********************************************************************************
```

```
Eps_non_local_cal=.False.

Do while (.not.stiffness)  !loop until elastic matrix D does not change any more

 iterStiff=iterStiff+1
 stiffness=.true. !gets false if D-matrix changes

 ! get deviatoric degradation strain
 If (smallstrain.and.iterStiff.eq.1) then
   Do i=1,abs(NUMCP)
      gamma_cp(i) = StVar0(11*ABS(NUMCP)+i)
   Enddo
 End if !small strain

 pdash = (sig0(1)+sig0(2)+sig0(3))/3d0
 if (pdash.gt.corr_val) pdash = corr_val       ! to avoid zero stiffness

 facCnn = (p_ref/dabs(pdash))**m_power
 facE = (dabs(pdash)/p_ref)**m_power

 Eur = Eur_ref*facE

 ! get stiffness matrix according to gamma_cp - anisotropic case
 !***********************************************************************************
 if ((smallstrain ==.true..and.anisotropic_el ==.true.).or.sw_pdash_SN0 == 2) then
   C_gl = 0.0d0
   D = 0.0d0
   Do i=1,ABS(NUMCP)

      LE = 0.0D0
      Tj_spec = 0.0D0

      !form transformation matrix Tj_spec(6,6)
      Tj_spec(1,1) = 1.0d0/3.0d0
      Tj_spec(2,1) = 1.0d0/3.0d0
      Tj_spec(3,1) = 1.0d0/3.0d0
      Tj_spec(1,2) = n1(i,1)**2 - 1.0d0/3.0d0
      Tj_spec(2,2) = n1(i,2)**2 - 1.0d0/3.0d0
      Tj_spec(3,2) = n1(i,3)**2 - 1.0d0/3.0d0
      Tj_spec(4,2) = 2.0d0*n1(i,1)*n1(i,2)
      Tj_spec(5,2) = 2.0d0*n1(i,2)*n1(i,3)
      Tj_spec(6,2) = 2.0d0*n1(i,3)*n1(i,1)
      Tj_spec(1,3) = n1(i,1)*s1(i,1)
      Tj_spec(2,3) = n1(i,2)*s1(i,2)
      Tj_spec(3,3) = n1(i,3)*s1(i,3)
      Tj_spec(4,4) = n1(i,1)*s1(i,2)+n1(i,2)*s1(i,1)
      Tj_spec(5,4) = n1(i,3)*s1(i,2)+n1(i,2)*s1(i,3)
      Tj_spec(6,4) = n1(i,3)*s1(i,1)+n1(i,1)*s1(i,3)
      Tj_spec(1,5) = n1(i,1)*t1(i,1)
      Tj_spec(2,5) = n1(i,2)*t1(i,2)
      Tj_spec(3,5) = n1(i,3)*t1(i,3)
      Tj_spec(4,6) = n1(i,2)*t1(i,1)+n1(i,1)*t1(i,2)
      Tj_spec(5,6) = n1(i,2)*t1(i,3)+n1(i,3)*t1(i,2)
      Tj_spec(6,6) = n1(i,1)*t1(i,3)+n1(i,3)*t1(i,1)

      !get transposed transformation matrix TiT_spec(6,6)
      TiT_spec= Transpose(Tj_spec)

      !get inverse of transposed transformation matrix TiT_spec_inv(6,6)
      Call MatInvPiv(TiT_spec,TiT_spec_inv,6)

      Sig0_cp_spec= MATMUL (TiT_spec,Sig0)
      SN0=Sig0_cp_spec(1)+Sig0_cp_spec(2)
      If (SN0.gt.corr_val) SN0 = corr_val

      if(gamma_cp(i).le.gamma_1) then
         deg_par = 0.0d0
      elseif (gamma_cp(i).ge.gamma_2) then
         deg_par = 1.0d0
      else
         deg_par = (dlog(gamma_cp(i))-dlog(gamma_1))/(dlog(gamma_2)-dlog(gamma_1))
      end if

      Eh = Eh0 - (Eh0 - Eur_ref)*deg_par
      Ev = Ev0 - (Ev0 - Eur_ref)*deg_par
      Gvh = Gvh0 - (Gvh0 - Eur_ref/(2.0d0+2.0d0*nyur))*deg_par
      nu_hv = nu_hv_0 - (nu_hv_0 - nyur)*deg_par
      nu_hh = nu_hh_0 - (nu_hh_0 - nyur)*deg_par
```

```
         ! Calculate eigenvalues and eigenangle of global anisotropic compliance matrix
         lambda_1 = (1.0d0+nu_hh)/Eh
         lambda_2 = (1.0d0-nu_hh)/(2.0d0*Eh) + 1.0d0/(2.0d0*Ev) - dsqrt(((&
                  1.0d0-nu_hh)/(2.0d0*Eh)-1.0d0/(2.0d0*Ev))**2+((2.0d0*nu_hv**2)/Eh**2))
         lambda_3 = (1.0d0-nu_hh)/(2.0d0*Eh) + 1.0d0/(2.0d0*Ev)+ dsqrt(((&
                  1.0d0-nu_hh)/(2.0d0*Eh)-1.0d0/(2.0d0*Ev))**2+((2.0d0*nu_hv**2)/Eh**2))
         lambda_4 = 1.0d0/(2.0d0*Gvh)

         If (((1.0d0-nu_hh)/Eh - 1.0d0/Ev)==0.0d0.AND.nu_hv.gt.0.0d0) then
            omega = Pi/4.d0
         Else If (((1.0d0-nu_hh)/Eh - 1.0d0/Ev)==0.0d0.AND.nu_hv.le.0.0d0) then
            omega = -Pi/4.d0
         Else
            If (((1.0d0-nu_hh)/Eh - 1.0d0/Ev).gt.0) then
               omega = Pi/2.0d0 + 1.0d0/2.0d0*datan((-2.0d0*dsqrt(2.0d0)*((nu_hv)/Eh))&
                       /((1.0d0-nu_hh)/Eh - 1.0d0/Ev))
            Else
               omega = 1.0d0/2.0d0*datan((-2.0d0*dsqrt(2.0d0)*((nu_hv)/Eh))/&
                       ((1.0d0-nu_hh)/Eh - 1.0d0/Ev))
            End If
         End if

         ! Get components of matrix Sum(lambda_i*E_i)
         LE(1,1) = 1.0d0/2.0d0*lambda_1 + lambda_2*(dcos(omega))**2/2.0d0 + &
                   lambda_3*(dsin(omega))**2/2.0d0
         LE(2,1) = lambda_2*(dcos(omega)*dsin(omega))/dsqrt(2.0d0) + &
                   lambda_3*(-dcos(omega)*dsin(omega))/dsqrt(2.0d0)
         LE(3,1) = -1.0d0/2.0d0*lambda_1 + lambda_2*(dcos(omega))**2/2.0d0 + &
                   lambda_3*(dsin(omega))**2/2.0d0
         LE(1,2) = LE(2,1)
         LE(2,2) = lambda_2*(dsin(omega))**2 + lambda_3*(dcos(omega))**2
         LE(3,2) = LE(1,2)
         LE(1,3) = LE(3,1)
         LE(2,3) = LE(3,2)
         LE(3,3) = LE(1,1)
         LE(4,4) = lambda_4
         LE(5,5) = lambda_4
         LE(6,6) = lambda_1

         ! get C_cp at reference pressure
         LExTiT_inv = MATMUL (LE,TiT_spec_inv)
         C_cp= MATMUL (TiT_spec,LExTiT_inv)

         if(sw_pdash_SN0==0.or.sw_pdash_SN0==2) then
            C_cp = C_cp * facCnn
         Else if(sw_pdash_SN0==1) then
            C_cp = C_cp * (p_ref/dabs(SN0))**m_power
         End if

         TjxC_cp = Matmul(Tj_spec,C_cp)
         C_gl_cp = Matmul(TjxC_cp,TiT_spec)
         C_gl = C_gl + 3.0d0*C_gl_cp*Weight(i)

      End Do   !loop over all cp's

      Call MatInvPiv(C_gl,D,6)

   End If ! (smallstrain ==.true..and.anisotropic_el ==.true.).or.sw_pdash_SN0 == 2
!************************************************************************************

! get stiffness matrix according to gamma_cp - isotropic case
!************************************************************************************
   if (smallstrain ==.true..and.anisotropic_el ==.false..and.sw_pdash_SN0.ne.2) then
        C_gl = 0.0d0
        D = 0.0d0
        Do i=1,ABS(NUMCP)
         !Call GetVec(i,NUMCP,s1,t1,anisotropic_el)

         C_cp = 0.0d0
         Tj_spec = 0.0d0

         !form transformation matrix Tj_spec(6,6)
         Tj_spec(1,1) = 1/3.0d0
         Tj_spec(2,1) = 1/3.0d0
         Tj_spec(3,1) = 1/3.0d0
         Tj_spec(1,2) = n1(i,1)**2 - 1/3.0d0
         Tj_spec(2,2) = n1(i,2)**2 - 1/3.0d0
```

```
         Tj_spec(3,2) = n1(i,3)**2 - 1/3.0d0
         Tj_spec(4,2) = 2.0d0*n1(i,1)*n1(i,2)
         Tj_spec(5,2) = 2.0d0*n1(i,2)*n1(i,3)
         Tj_spec(6,2) = 2.0d0*n1(i,3)*n1(i,1)
         Tj_spec(1,3) = n1(i,1)*s1(i,1)
         Tj_spec(2,3) = n1(i,2)*s1(i,2)
         Tj_spec(3,3) = n1(i,3)*s1(i,3)
         Tj_spec(4,4) = n1(i,1)*s1(i,2)+n1(i,2)*s1(i,1)
         Tj_spec(5,4) = n1(i,3)*s1(i,2)+n1(i,2)*s1(i,3)
         Tj_spec(6,4) = n1(i,3)*s1(i,1)+n1(i,1)*s1(i,3)
         Tj_spec(1,5) = n1(i,1)*t1(i,1)
         Tj_spec(2,5) = n1(i,2)*t1(i,2)
         Tj_spec(3,5) = n1(i,3)*t1(i,3)
         Tj_spec(4,6) = n1(i,2)*t1(i,1)+n1(i,1)*t1(i,2)
         Tj_spec(5,6) = n1(i,2)*t1(i,3)+n1(i,3)*t1(i,2)
         Tj_spec(6,6) = n1(i,1)*t1(i,3)+n1(i,3)*t1(i,1)

         !get transposed transformation matrix TiT_spec(6,6)
         TiT_spec= Transpose(Tj_spec)

         Sig0_cp_spec= MATMUL (TiT_spec,Sig0)
         SN0=Sig0_cp_spec(1)+Sig0_cp_spec(2)
         If (SN0.gt.corr_val) SN0 = corr_val

         if(gamma_cp(i).le.gamma_1) then
            deg_par = 0.0d0
         elseif (gamma_cp(i).ge.gamma_2) then
            deg_par = 1.0d0
         else
            deg_par = (dlog(gamma_cp(i))-dlog(gamma_1))/(dlog(gamma_2)-dlog(gamma_1))
         end if

         Eh = Eh0 - (Eh0 - Eur_ref)*deg_par
         Gvh =  Eh/(2.0d0+2.0d0*NYUR)

         ! Calculate eigenvalues and eigenangle of global anisotropic compliance matrix
         lambda_1 = (1.0d0+NYUR)/Eh
         lambda_2 = (1.0d0-2d0*NYUR)/Eh

         ! get C_cp at reference pressure                  ! schä 301109
         C_cp(1,1)= lambda_2
         Do m=2,6
            C_cp(m,m) = lambda_1
         End Do

         if(sw_pdash_SN0==0) then
            C_cp = C_cp * facCnn
         else if(sw_pdash_SN0==1) then
            C_cp = C_cp * (p_ref/dabs(SN0))**m_power
         End if

         TjxC_cp = Matmul(Tj_spec,C_cp)
         C_gl_cp = Matmul(TjxC_cp,TiT_spec)

         C_gl = C_gl + 3.0d0*C_gl_cp*Weight(i)

        End Do !loop over all cp's

        Call MatInvPiv(C_gl,D,6)

     End if !(smallstrain ==.true..and.anisotropic_el ==.false..and.sw_pdash_SN0.ne.2)
!***********************************************************************************

     ! cap hardening parameter
     HARDCAP   = 3.0d0/(p_ref*(1.0d0/Eoed_ref-(3.0d0*(1.0d0-2.0d0*NYUR))/Eur_ref))

     ! reset matrix with local strains
     dEps_cp = 0.

     ! reset plasticity indicators
     ipl_gl = 0
     failure_mode=.true.  ! one or no plane is in failure mode
     ipl = 0

! subincrementing
!***********************************************************************************
     n_sub=1 ! at least one subincrement
```

```
IF (StepSize.lt.0.) then
  dEps_norm=dsqrt(dEps(1)**2+dEps(2)**2+dEps(3)**2+dEps(4)**2+dEps(5)**2+dEps(6)**2)
  n_sub=ceiling(dEps_norm/dabs(stepsize)) ! get number of subincrements
End If

IF (StepSize.gt.0.) Then     ! get number of subincrements
  dSig_check = Matmul(D,dEps)
  !Call MatVec(D,6,dEps,6,dSig_check)
  Sig_check=Sig0+dSig_check
  ! prepare data
  V1= (/1,4,6/); V2= (/4,2,5/); V3= (/6,5,3/)
  SIGMA_check(:,1)= Sig_check(V1)    !  assembling symm.stress matrix SIGMA_check
  SIGMA_check(:,2)= Sig_check(V2)    !  from stress vector Sig_check dim(6)
  SIGMA_check(:,3)= Sig_check(V3)

  SIGMA_0(:,1)= Sig0(V1)    !  assembling symm.stress matrix SIGMA_0 dim(3,3)
  SIGMA_0(:,2)= Sig0(V2)    !  from stress vector Sig0 dim(6)
  SIGMA_0(:,3)= Sig0(V3)

  Do m=1,ABS(NUMCP) !loop over all cp's
     ! transformation of stresses -> sigma_n, tau
     L(1:3)= n1(m,1:3)                 ! unit normal vector of plane, dim(3)
     P= MATMUL (SIGMA_check,L)         ! traction P, dim(3)
     SN_check=  DOT_PRODUCT (L,P)      ! sigma_n on cp
     TAU_check= DOT_PRODUCT (P,P)- SN_check**2
     iTAU= -0.01d0*dabs(SN_check)
     IF (iTAU.le.0.01) iTAU=0.01d0
     IF (TAU_check < 0.and.TAU_check>-iTAU) TAU_check= 0.0d0
     IF (TAU_check > 0.and.TAU_check<iTAU) TAU_check= 0.0d0
     IF (TAU_check <= -iTAU) then
        STOP 'ERROR - MYMOD_ML: tau negative on cp'
     end if
     TAU_check= dsqrt(TAU_check)       ! new tau on cp

     If (Ar/=1.0d0) then
        s(1)=SN_check*L(1)
        s(2)=SN_check*L(2)
        s(3)=SN_check*L(3)
        t(1)=P(1)-S(1)
        t(2)=P(2)-S(2)
        t(3)=P(3)-S(3)
        TAU=Sqrt(t(1)**2+t(2)**2+t(3)**2)
        tt(1)=dcos(Theta)*t(1)-dsin(Theta)*t(2)
        tt(2)=dSin(Theta)*t(1)+dcos(Theta)*t(2)
        Norm_t=dSqrt(tt(1)**2+tt(2)**2+t(3)**2)
        if (Norm_t/=0.0d0) then
           Nv=dabs(tt(2))/Norm_t
        else
           Nv=1.0d0
        endif
        tan_Phi_i= tan_phi*(1.0d0-(Ar-1.0d0)/(Ar+2.0d0)*(1.0d0-3.0d0*(Nv**2)))
        COH_i=COH*(1.0d0-(Ar-1.0d0)/(Ar+2.0d0)*(1.0d0-3.0d0*(Nv**2)))
     Else
        tan_Phi_i= tan_phi
        COH_i=COH
     End if

     tan_PHI_MOD=tan_phi_i/Rf

     ! transformation of stresses -> sigma_0, tau_0 -> initial stress state
     P= MATMUL (SIGMA_0,L)                ! traction P, dim(3)
     SN_0=  DOT_PRODUCT (L,P)                   ! sigma_n on cp
     TAU_0= DOT_PRODUCT (P,P)- SN_0**2
     iTAU_0= -0.01d0*dabs(SN_0)
     IF (iTAU_0.le.0.01) iTAU_0=0.01d0
     IF (TAU_0 < 0.and.TAU_0>-iTAU) TAU_0= 0.0d0      ! adjust small differences
     IF (TAU_0 > 0.and.TAU_0<iTAU) TAU_0= 0.0d0       ! adjust small differences
     IF (TAU_0 <= -iTAU) then
        STOP 'ERROR - MYMOD_ML: tau negative on cp'
     end if
     TAU_0= dsqrt(TAU_0)                        ! new tau on cp
     DSN = SN_check-SN_0
     DTAU = TAU_check-TAU_0

     ! get state variables at start of step for actual contact plane m
     SIGNC = StVar0(2*ABS(NUMCP)+m)    ! sigma_n_preconsolidation for cap
     TPHIM = StVar0(1*ABS(NUMCP)+m)
     if (TPHIM.gt.tan_phi_i.and..not.Hvorslev) TPHIM=tan_phi_i
```

```
         If (Hvorslev) then         ! get non-local value of preconsolidation pressure
            SIGNC =  StVar0(0*ABS(NUMCP)+m)
         Else if (Hard_soft) then ! potential friction softening analysis
            EpsDamPeak=StVar(5*ABS(NUMCP)+m) ! check whether peak shear strength reached
            if(EpsDamPeak.gt.0.000000000001) then
               TPHIM=StVar0(6*ABS(NUMCP)+m)        !Gal 190106
               Coh_i=StVar0(7*ABS(NUMCP)+m)           !Gal 190106
            end if
         End if

         SIGNC_s  = SIGNC-STEPSIZE  ! maximal new admissible yield surface on cap side

         ! calculate number of substeps
         n_sub_cone = 1
         n_sub_tens = 1
         n_sub_cap = 1
         n_sub_HV = 1

         f_cone   = TAU_check + SN_check*TPHIM - COH_i*TPHIM/tan_phi_i
         f_cap = (SN_check**2)/(SIGNC**2) + (TAU_check**2)/((MCP*SIGNC)**2) - 1.0d0
         f_tens   = SN_check-TENS

         If(f_cone.gt.0.and.f_tens.lt.0)  n_sub_cone = CEILING((DTAU*tan_phi_i + &
               TPHIM*DSN*tan_phi_i)/(COH_i*TPHIM + stepsize*tan_phi_i &
               - TAU_0*tan_phi_i - SN_0*TPHIM*tan_phi_i))
         If (tphim.gt.tan_phi_res.and.Hvorslev) n_sub_cone = 1

         If(f_cap.gt.0.and.f_tens.lt.0)   n_sub_cap = CEILING(-(MCP*dsqrt(MCP**2*&
            SIGNC_s**2*DSN**2 + SIGNC_s**2*DTAU**2 - (SN_0*DTAU - TAU_0*DSN)**2) + &
            TAU_0*DTAU + MCP**2*SN_0*DSN)/(MCP**2*SN_0**2 - MCP**2*SIGNC_s**2 + &
            TAU_0**2))
         If(f_tens.gt.0)    n_sub_tens = CEILING(DSN / (TENS + stepsize - SN_0))

         If (Hvorslev) then
            sig_ve_check = -((-signc)**(1-m_power)+Eoed_ref/Eur_ref*3*(1-2*NYUR)*&
                  ((-SN_check)**(1-m_power)-(-signc)**(1-m_power)))**(1/(1-m_power))
            f_HV = TAU_check + SN_check*tan_phi_e - sig_ve_check*B_cs*&
                  (tan_phi_e/tan_phi_res - 1.0d0)
            If (SN_check.ge.0.0d0) f_HV = 0
            Do while (f_HV.gt.stepsize)
               n_sub_HV = n_sub_HV + 1
               SN_check = SN_0 + DSN/n_sub_HV
               TAU_check = TAU_0 + DTAU/n_sub_HV
               sig_ve_check =   -((-signc)**(1-m_power)+Eoed_ref/Eur_ref*3*(1- &
                     2*NYUR)*((-SN_check)**(1-m_power)-(-signc)**(1-m_power)))**&
                     (1/(1-m_power))
               f_HV = TAU_check + SN_check*tan_phi_e - sig_ve_check*B_cs*&
                     (tan_phi_e/tan_phi_res - 1.0d0)
            End do
         End if

         IF (MAXVAL((/n_sub_cone,n_sub_cap,n_sub_tens,n_sub_HV/)).gt.n_sub)
            n_sub=MAXVAL((/n_sub_cone,n_sub_cap,n_sub_tens,n_sub_HV/))
       End Do  !loop over all cp's
     End If ! StepSize.gt.0
!***********************************************************************************

     dEps_sub=dEps/n_sub   ! subincrement
     Sig0_sub=Sig0         ! stress state at start of subincrementing

     Do ii=1,n_sub
      dEps_trial=dEps_sub  ! first trial for each substep (elastic)

      ! reset variables
      dEps_plastic=0.
      dEps_cp_pl = 0.
      converged_cp=.false. ! do at least one loop over all cp's
      SumdEps_vol_pl = 0.
      SumdGamma_pl = 0.
      epsn_t_step = 0.
      epsn_HV_step = 0.
      gamma_HV_step = 0.
      iter_cp=0

      ! loop until convergence is reached
       Do While (.not.converged_cp)
```

```
converged_cp=.true. ! gets false again during iteration when plasticity occurs

! increase iteration counter
  iter_cp=iter_cp+1

 ! reset plasticity indicators
 ipl_cp = 0

! reset small-strain stiffness indicator for output
if (ii==n_sub) sss_indicator_gl = 0.0d0

dEps_cp_el = 0.

! new trial strain increment
dEps_trial=dEps_trial-dEps_plastic

! calculate new trial stress increment dSig_trial=dEps_trial*D
dSig_trial = MatMul(D,dEps_trial)

dEps_plastic = 0.0d0

! get new trial stress state
Sig_trial=Sig0_sub+dSig_trial

  ! prepare data for stiffness-calculation
if (Sig0(1)==0.and.Sig0(2)==0.and.Sig0(3)==0.and.Sig0(4)==0.and.Sig0(5)==0  &
    .and.Sig0(6)==0) then
   Sig0(1)= corr_val
   Sig0(2)= corr_val
   Sig0(3)= corr_val
endif

Cnn = Cnn_ref * facCnn
Ctt = Cnn / CnnCtt

!loop over all cps
DO i=1,ABS(NUMCP)

  ! reset plastic strain vectors of cp's
  epsNcone = 0.
  epsGcone = 0.
  epsNcap = 0.
  epsGcap = 0.
  epsNtens = 0.
  epsGtens = 0.
  epsNHV = 0.
  epsGHV = 0.

  eps_cone = 0.0d0
  eps_cap = 0.0d0
  eps_tens = 0.0d0
  eps_HV = 0.0d0
  eps_cp_plastic = 0.0d0

  Lambda_cone = 0.0d0
  Lambda_cap = 0.0d0
  Lambda_HV = 0.0d0
  Lambda_cap_1 = 0.0d0
  Lambda_cap_12 = 0.0d0
  Lambda_cap_23 = 0.0d0
  Lambda_cone_1 = 0.0d0
  Lambda_cone_12 = 0.0d0
  Lambda_cone_13 = 0.0d0
  Lambda_HV_1 = 0.0d0
  Lambda_HV_13 = 0.0d0
  Lambda_HV_23 = 0.0d0

  ! get transformation matrices
  Tj = 0.0d0

  !form transformation matrix Tj(6,3) (old split)
  Tj(1,1) = n1(i,1)**2
  Tj(1,2) = n1(i,1)*s1(i,1)
  Tj(1,3) = n1(i,1)*t1(i,1)
  Tj(2,1) = n1(i,2)**2
  Tj(2,2) = n1(i,2)*s1(i,2)
  Tj(2,3) = n1(i,2)*t1(i,2)
  Tj(3,1) = n1(i,3)**2
```

```
        Tj(3,2) = n1(i,3)*s1(i,3)
        Tj(3,3) = n1(i,3)*t1(i,3)
        Tj(4,1) = 2.0d0*n1(i,1)*n1(i,2)
        Tj(4,2) = n1(i,1)*s1(i,2)+n1(i,2)*s1(i,1)
        Tj(4,3) = n1(i,2)*t1(i,1)+n1(i,1)*t1(i,2)
        Tj(5,1) = 2.0d0*n1(i,2)*n1(i,3)
        Tj(5,2) = n1(i,3)*s1(i,2)+n1(i,2)*s1(i,3)
        Tj(5,3) = n1(i,2)*t1(i,3)+n1(i,3)*t1(i,2)
        Tj(6,1) = 2.0d0*n1(i,3)*n1(i,1)
        Tj(6,2) = n1(i,3)*s1(i,1)+n1(i,1)*s1(i,3)
        Tj(6,3) = n1(i,3)*t1(i,1)+n1(i,1)*t1(i,3)

        ! old stress state
        TiT= Transpose(Tj)
        Sig0_cp= MATMUL (TiT,Sig0)
        SN0=Sig0_cp(1)
        Tau0 = dsqrt(Sig0_cp(2)**2 + Sig0_cp(3)**2)
        If (SN0.gt.corr_val) SN0 = corr_val

        ! get non-local state variables for Hvorslev surface
        !*******************************************************************************
        signc  = StVar(2*ABS(NUMCP)+i)    ! sigma_n_preconsolidation from hardening

        If (Hvorslev) then       ! get non-local value of preconsolidation pressure

            EpsDamPeak = StVar0(5*ABS(NUMCP)+i)
            If (EpsDamPeak.ge.0.000000000001d0) then
               ! update non-local correction factor once at the beginning of each step
               if (.not.Eps_non_local_cal.and.switch_HV == 1) then
                  call Non_Local (StVar, nStat, NumCP, GLD_strain, iStep, numpoint, &
                                  point_index, weights, Hvorslev)
                  Eps_non_local_cal=.True.
               end if
               Eps_non_local=StVar(3*ABS(NUMCP)+8)    ! non-local macro damage strain
               Eps_Damage = Eps_Non_Local*weight(i) - EpsDamPeak
               If (switch_HV == 2) Eps_Damage = StVar0(3*ABS(NUMCP)+9)*weight(i)-  &
                                                EpsDamPeak
            Else
               Eps_Damage = 0.0d0
            End if

            ! non_local damage strain in previous calculation step
            Eps_Damage_old = StVar0(6*ABS(NUMCP)+i)

            ! check that damage strain is not decreasing
            If (Eps_Damage.lt.Eps_Damage_old) Eps_Damage = Eps_Damage_old
            StVar(6*ABS(NUMCP)+i) = Eps_Damage

            ! non-local signc
            SIGNC = -((-signc)**(1.0d0-m_power)+HARDCAP*(m_power-1.0d0) &
                   *p_ref**(1.0d0-m_power)*(h_soft*Eps_Damage))**(1.0d0/(1.0d0-m_power))
            StVar(0*ABS(NUMCP)+i) = SIGNC    ! store non-local preconsolidation pressure

            sig_ve0 = -((-signc)**(1-m_power)+Eoed_ref/Eur_ref*3*(1-2*NYUR)*((-SN0)**   &
                       (1-m_power)-(-signc)**(1-m_power)))**(1/(1-m_power))
            tau_max = -tan_phi_e*SN0 + sig_ve0*B_cs*(tan_phi_e/tan_phi_res - 1.0d0)
            tan_phi_HV = -tau_max / SN0      ! max. phi at Hvorslev surface
            If (tan_phi_HV.gt.1.73d0) tan_phi_HV = 1.73d0

            ! use phi_HV for cone if old stress state is left of cap cone intersection
            If (SN0.gt.sigS) then
               tan_phi = tan_phi_HV
            Else
               tan_phi = tan_phi_res
            End if
         End if !  (Hvorslev)
!************************************************************************************

         if (smallstrain ==.false.) then
            Sig_cp = MATMUL (TiT,Sig_trial)
            SN=  Sig_cp(1)          ! sigma_n on c.p.
            TAU= dsqrt(Sig_cp(2)**2 + Sig_cp(3)**2)
            iTAU= -0.01*dabs(SN)
            IF (iTAU.le.0.01) iTAU=0.01d0
            IF (TAU < 0.and.TAU>-iTAU) TAU= 0.0    ! adjust small differences
            IF (TAU > 0.and.TAU<iTAU) TAU= 0.0     ! adjust small differences
            IF (TAU <= -iTAU) then
               STOP 'ERROR - MYMOD_ML: tau negative on cp'
```

```
            end if

            ! get anisotropic shear strength according to stress path direction
            If (Ar/=1.0d0) then
               tt = Sig_cp(2)*s1(i,1:3) + Sig_cp(3)*t1(i,1:3)

               if (TAU/=0) then
                  Nv=dabs(DOT_PRODUCT(tt,rot)/TAU)
                  tan_Phi_i= tan_phi*(1.0d0-(Ar-1.0d0)/(Ar+2.0d0)*(1.0d0-3.0d0*(Nv**2)))
                  COH_i=COH*(1.0d0-(Ar-1.0d0)/(Ar+2)*(1.0d0-3.0d0*(Nv**2)))
               else
                  tan_Phi_i= tan_phi
                  COH_i=COH
               endif
            Else
               tan_Phi_i= tan_phi
               COH_i=COH
            End if

            tan_PHI_MOD=tan_phi_i/Rf
            MCP   = ACAP*tan_phi_res

            !calculate local spectral stiffness parameters (with Sig0_cp)
            if(sw_pdash_SN0==1) then
               Cnn = Cnn_ref * (p_ref/dabs(SN0))**m_power
               Ctt = Cnn / CnnCtt
            End if
         end if ! smallstrain ==.false.

!**********************************************************************************

         if (smallstrain ==.true.) then

            Tj_spec = 0.0d0
            !form transformation matrix Tj(6,6)
            Tj_spec(1,1) = 1/3.0d0
            Tj_spec(2,1) = 1/3.0d0
            Tj_spec(3,1) = 1/3.0d0
            Tj_spec(1,2) = n1(i,1)**2 - 1/3.0d0
            Tj_spec(2,2) = n1(i,2)**2 - 1/3.0d0
            Tj_spec(3,2) = n1(i,3)**2 - 1/3.0d0
            Tj_spec(4,2) = 2.0d0*n1(i,1)*n1(i,2)
            Tj_spec(5,2) = 2.0d0*n1(i,2)*n1(i,3)
            Tj_spec(6,2) = 2.0d0*n1(i,3)*n1(i,1)
            Tj_spec(1,3) = n1(i,1)*s1(i,1)
            Tj_spec(2,3) = n1(i,2)*s1(i,2)
            Tj_spec(3,3) = n1(i,3)*s1(i,3)
            Tj_spec(4,4) = n1(i,1)*s1(i,2)+n1(i,2)*s1(i,1)
            Tj_spec(5,4) = n1(i,3)*s1(i,2)+n1(i,2)*s1(i,3)
            Tj_spec(6,4) = n1(i,3)*s1(i,1)+n1(i,1)*s1(i,3)
            Tj_spec(1,5) = n1(i,1)*t1(i,1)
            Tj_spec(2,5) = n1(i,2)*t1(i,2)
            Tj_spec(3,5) = n1(i,3)*t1(i,3)
            Tj_spec(4,6) = n1(i,2)*t1(i,1)+n1(i,1)*t1(i,2)
            Tj_spec(5,6) = n1(i,2)*t1(i,3)+n1(i,3)*t1(i,2)
            Tj_spec(6,6) = n1(i,1)*t1(i,3)+n1(i,3)*t1(i,1)

            !get transposed transformation matrix TiT_spec(6,6)
            TiT_spec= Transpose(Tj_spec)

            ! stress transformation with 6 local stress components
            Sig_cp_spec = MATMUL (TiT_spec,Sig_trial)
            Sig0_sub_cp= MATMUL (TiT_spec,Sig0_sub)

            Sig_cp(1) = Sig_cp_spec(1) + Sig_cp_spec(2)
            Sig_cp(2) = Sig_cp_spec(3) + Sig_cp_spec(4)
            Sig_cp(3) = Sig_cp_spec(5) + Sig_cp_spec(6)

            SN=  Sig_cp(1)                   ! sigma_n on c.p.
            TAU= dsqrt(Sig_cp(2)**2 + Sig_cp(3)**2)
            iTAU= -0.01*dabs(SN)
            IF (iTAU.le.0.01) iTAU=0.01d0
            IF (TAU < 0.and.TAU>-iTAU) TAU= 0.0    ! adjust small differences
            IF (TAU > 0.and.TAU<iTAU) TAU= 0.0     ! adjust small differences
            IF (TAU <= -iTAU) then
               STOP 'ERROR - MYMOD_ML: tau negative on cp'
            end if
```

```
! get anisotropic shear strength according to local stress path direction
If (Ar/=1.0d0) then
   tt = Sig_cp(2)*s1(i,1:3) + Sig_cp(3)*t1(i,1:3)
   if (TAU/=0) then
      Nv=dabs(DOT_PRODUCT(tt,rot)/TAU)
      tan_Phi_i= tan_phi*(1.0d0-(Ar-1.0d0)/(Ar+2.0d0)*(1.0d0-3.0d0*(Nv**2)))
      COH_i=COH*(1.0d0-(Ar-1.0d0)/(Ar+2)*(1.0d0-3.0d0*(Nv**2)))
   else
      tan_Phi_i= tan_phi
      COH_i=COH
   endif
Else
   tan_Phi_i= tan_phi
   COH_i=COH
End if

tan_PHI_MOD=tan_phi_i/Rf
MCP      = ACAP*tan_phi_res

!calculate local spectral stiffness matrix
stiff_low=.false.

LE = 0.0d0
C_cp = 0.0d0

if(gamma_cp(i).le.gamma_1) then
   deg_par = 0.0d0
elseif (gamma_cp(i).ge.gamma_2) then
   deg_par = 1.0d0
else
   deg_par = (dlog(gamma_cp(i))-dlog(gamma_1))/(dlog(gamma_2)-dlog(gamma_1))
end if

! anisotropic spectral stiffness
if (anisotropic_el ==.true..or.sw_pdash_SN0 == 2) then
   Eh = Eh0 - (Eh0 - Eur_ref)*deg_par
   Ev = Ev0 - (Ev0 - Eur_ref)*deg_par
   Gvh = Gvh0 - (Gvh0 - Eur_ref/(2.0d0+2.0d0*NYUR))*deg_par
   nu_hv = nu_hv_0 - (nu_hv_0 - NYUR)*deg_par
   nu_hh = nu_hh_0 - (nu_hh_0 - NYUR)*deg_par
   if (deg_par==1.0d0)  stiff_low=.true.

   ! Calculate eigenvalues and eigenangle
   lambda_1 = (1.0d0+nu_hh)/Eh
   lambda_2 = (1.0d0-nu_hh)/(2.0d0*Eh) + 1.0d0/(2.0d0*Ev) - dsqrt(((1.0d0- &
            nu_hh)/(2.0d0*Eh)-1.0d0/(2.0d0*Ev))**2+((2.0d0*nu_hv**2)/Eh**2))
   lambda_3 = (1.0d0-nu_hh)/(2.0d0*Eh) + 1.0d0/(2.0d0*Ev)+ dsqrt(((1.0d0- &
            nu_hh)/(2.0d0*Eh)-1.0d0/(2.0d0*Ev))**2+((2.0d0*nu_hv**2)/Eh**2))
   lambda_4 = 1.0d0/(2.0d0*Gvh)

   If (((1.0d0-nu_hh)/Eh - 1.0d0/Ev)==0.0d0.AND.nu_hv.gt.0.0d0) then
      omega = Pi/4.d0
   Else If (((1.0d0-nu_hh)/Eh - 1.0d0/Ev)==0.0d0.AND.nu_hv.le.0.0d0) then
      omega = -Pi/4.d0
   Else
      If (((1.0d0-nu_hh)/Eh - 1.0d0/Ev).gt.0) then
         omega = Pi/2.0d0 + 1.0d0/2.0d0*datan((-2.0d0*dsqrt(2.0d0)*   &
                 ((nu_hv)/Eh))/((1.0d0-nu_hh)/Eh - 1.0d0/Ev))
      Else
         omega = 1.0d0/2.0d0*datan((-2.0d0*dsqrt(2.0d0)*   &
                 ((nu_hv)/Eh))/((1.0d0-nu_hh)/Eh - 1.0d0/Ev))
      End If
   End if

   ! Get components of matrix Sum(lambda_i*E_i)
   LE(1,1) = 1.0d0/2.0d0*lambda_1 + lambda_2*(dcos(omega))**2/2.0d0 +    &
             lambda_3*(dsin(omega))**2/2.0d0
   LE(2,1) = lambda_2*(dcos(omega)*dsin(omega))/dsqrt(2.0d0) + lambda_3*(- &
             dcos(omega)*dsin(omega))/dsqrt(2.0d0)
   LE(3,1) = -1.0d0/2.0d0*lambda_1 + lambda_2*(dcos(omega))**2/2.0d0 +    &
             Lambda_3*(dsin(omega))**2/2.0d0
   LE(1,2) = LE(2,1)
   LE(2,2) = lambda_2*(dsin(omega))**2 + lambda_3*(dcos(omega))**2
   LE(3,2) = LE(1,2)
   LE(1,3) = LE(3,1)
   LE(2,3) = LE(3,2)
   LE(3,3) = LE(1,1)
   LE(4,4) = lambda_4
```

```
   LE(5,5) = lambda_4
   LE(6,6) = lambda_1

   !get inverse of transposed transformation matrix TiT_spec_inv(6,6)
   Call MatInvPiv(TiT_spec,TiT_spec_inv,6)

   ! get local C_cp at reference pressure                   ! schä 301109
   LExTiT_inv = MATMUL (LE,TiT_spec_inv)
   C_cp= MATMUL (TiT_spec,LExTiT_inv)

! isotropic small strain stiffness
Else if (anisotropic_el ==.false..and.sw_pdash_SN0.ne.2) then
   Eh = Eh0 - (Eh0 - Eur_ref)*deg_par

   if (deg_par==1.0d0)  stiff_low=.true.

   ! Calculate eigenvalues of local compliance matrix
   lambda_1 = (1.0d0+NYUR)/Eh
   lambda_2 = (1.0d0-2d0*NYUR)/Eh

   ! get C_cp at reference pressure                   ! schä 301109
   C_cp(1,1)= lambda_2
   Do m=2,6
      C_cp(m,m) = lambda_1
   End Do
End if  ! isotropic small strain stiffness

if(sw_pdash_SN0==0) then         ! approach 1
   C_cp = C_cp * facCnn
   Cnn = Cnn_ref * facCnn
   Ctt = Cnn / CnnCtt
Else if(sw_pdash_SN0==1) then    !approach 2
   C_cp = C_cp * (p_ref/dabs(SN0))**m_power
   Cnn = Cnn_ref * (p_ref/dabs(SN0))**m_power
   Ctt = Cnn / CnnCtt
Else if(sw_pdash_SN0==2) then    ! approach 3
   C_cp = C_cp * facCnn
   Cnn = Cnn_ref * (p_ref/dabs(SN0))**m_power
   Ctt = Cnn / CnnCtt
End if

! set small-strain stiffness indicator for output
if (ii==n_sub) sss_indicator_cp = 1.0d0 - deg_par

! accumulate global value of small-strain stiffness indicator
if (ii==n_sub) sss_indicator_gl = sss_indicator_gl + sss_indicator_cp * &
                                  Weight(i)

! SSS-influenced hardening - shift of yield surfaces
if (iter_cp==1.and.stiff_low==.false.) then
   x_stiff = 1.0d0   - deg_par   ! acc. to degradation of stiffness

   ! CONE: change (increase) of TPHIM
   TPHIM_sub0 = StVar(1*ABS(NUMCP)+i)
   TPHI_Sig_trial = TAU*tan_phi_i/(COH_i-SN*tan_phi_i)
   TPHIM_SSS = TPHIM_sub0+x_stiff*(TPHI_Sig_trial-TPHIM_sub0)

   If (TPHIM_SSS.gt.tan_phi_i)   TPHIM_SSS = tan_phi_i

   f_cone = TAU + SN*TPHIM_sub0 - COH_i*TPHIM_sub0/tan_phi_i
   if (TPHIM_sub0.lt.TPHIM_SSS.and.f_cone.Gt.CONVERGE.and.SN.lt.TENS) then
      ! update StVar
      StVar(1*ABS(NUMCP)+i) = TPHIM_SSS
   endif

   ! CAP: change (increase) of SIGNC
   SIGNC_sub0 = signc
   SIGNC_Sig_trial = -dsqrt((SN*SN)+(TAU*TAU)/(MCP*MCP))
   SIGNC_SSS = SIGNC_sub0+x_stiff*(SIGNC_Sig_trial-SIGNC_sub0)
   f_cap = (SN**2)/(SIGNC_sub0**2) + (TAU**2)/((MCP*SIGNC_sub0)**2) - 1
   if (dabs(SIGNC_sub0).lt.dabs(SIGNC_SSS).and.f_cap.Gt.CONVERGE) then
      ! update StVar
      StVar(2*ABS(NUMCP)+i) = SIGNC_SSS
      SIGNC = SIGNC_SSS
      If (Hvorslev)  then
         ! reduction of signc
         SIGNC = -((-signc)**(1.0d0-m_power)+HARDCAP*(m_power-1.0d0) &
                  *p_ref**(1.0d0-m_power)*(h_soft*Eps_Damage))**  &
```

```
                             (1.0d0/(1.0d0-m_power))
                 End if
              endif
           endif ! SSS-influenced hardening - shift of yield surfaces

           ! calculate deviatoric elastic strains on cp
           dSig_el_cp_spec = Sig_cp_spec - Sig0_sub_cp
           dEps_cp_el_spec(:,i) = Matmul(C_cp,dSig_el_cp_spec)
           dEps_cp_el(1,i) = dEps_cp_el_spec(2,i)
           dEps_cp_el(2,i) = dEps_cp_el_spec(3,i) + dEps_cp_el_spec(4,i)
           dEps_cp_el(3,i) = dEps_cp_el_spec(5,i) + dEps_cp_el_spec(6,i)

        endif !  smallstrain==.true.
!***************************************************************************************

        ! local compliance matrix for plastic strain calculation
        D_loc(1,1)  = 1.0d0 / Cnn
        D_loc(1,2)  = 0.0d0
        D_loc(2,1)  = 0.0d0
        D_loc(2,2)  = 1.0d0 / Ctt

        ! get equivalent pressure on NCL at trial normal stress
        sig_ve =   -((-signc)**(1-m_power)+Eoed_ref/Eur_ref*3*(1-2*NYUR)*((-SN)**(1- &
                     m_power)-(-signc)**(1-m_power)))**(1/(1-m_power))

        !Variation of phi with damage strain - Galavi softening model
        !*****************************************************************************
        ! calculate tan(phi_mob)
        If (.not.Hard_Soft) then                  ! no strain softening calculation
           TPHIM = StVar(1*ABS(NUMCP)+i)
           if (TPHIM.gt.tan_PHI_i.and..not.Hvorslev) TPHIM=tan_phi_i
           Softening   =.false.
        else  !  strain softening calculation
           EpsDamPeak=StVar(5*ABS(NUMCP)+i)       ! non-local damage strain
           if(EpsDamPeak<=0.000000000001) then    ! peak strength not reached yet
              Softening =.false.
              TPHIM = StVar(1*ABS(NUMCP)+i)
              if (TPHIM.ge.tan_PHI_i) then
                 if (.not.Eps_non_local_cal) then
                    call Non_Local (StVar, nStat, NumCP, GLD_strain, iStep, numpoint, &
                                    point_index, weights, Hvorslev)
                    Eps_non_local_cal=.True.
                 end if
                 ! Correction factor for non-local damage strain
                 Eps_non_local = StVar(3*ABS(NUMCP)+8)
                 Eps_Damage = StVar(4*ABS(NUMCP)+i)  !Local damage strain

                 ! non-local damage strain at peak friction angle
                 StVar(5*ABS(NUMCP)+i) = Eps_Non_Local * Eps_Damage
                 TPHIM=tan_PHI_i
                 StVar(6*ABS(NUMCP)+i) = TPHIM
                 StVar(7*ABS(NUMCP)+i) = Coh_i
              end if
           else  ! strain softening calculation beyond peak shear strength
              Softening   =.true.
              if (.not.Eps_non_local_cal) then
                 call Non_Local (StVar, nStat, NumCP, GLD_strain, iStep, numpoint, &
                             point_index, weights, Hvorslev)
                 Eps_non_local_cal=.True.
              end if

              if (StVar(6*ABS(NUMCP)+i)>1.0000001*tan_phi_res) then
                 Eps_non_local=StVar(3*ABS(NUMCP)+8)
                 Eps_Damage=StVar(4*ABS(NUMCP)+i)
                 TPHIM=(-hPhi)*(Eps_Non_Local * Eps_Damage -EpsDamPeak)+tan_phi_i
                 if (TPHIM>StVar(6*ABS(NUMCP)+i)) TPHIM=StVar(6*ABS(NUMCP)+i)
                 if (TPHIM<=tan_phi_res) Then
                    TPHIM=tan_phi_res
                 end if
              else
                 TPHIM=tan_phi_res
              end if

              StVar(6*ABS(NUMCP)+i)=TPHIM

              if (StVar(7*ABS(NUMCP)+i) >1.0000001*C_res) then
                 Eps_non_local=StVar(3*ABS(NUMCP)+8)
                 Eps_Damage=StVar(4*ABS(NUMCP)+i)
```

```
         Coh_i  = (-hCoh)*(Eps_Non_Local*Eps_Damage-EpsDamPeak)+Coh_i
         if (Coh_i>StVar(7*ABS(NUMCP)+i)) Coh_i=StVar(7*ABS(NUMCP)+i)
         if (Coh_i<C_res)  Coh_i=C_res
      else
         Coh_i=C_res
      end if
      StVar(7*ABS(NUMCP)+i)=Coh_i
   end if
end if   !  .not.Hard_soft
!*****************************************************************************

! check yield criteria
f_cone   = TAU + SN*TPHIM - COH_i*TPHIM/tan_phi_i
If (softening) f_cone   = TAU + SN*TPHIM - COH_i
   f_cap    = (SN**2)/(SIGNC**2) + (TAU**2)/((MCP*SIGNC)**2) - 1.0d0
f_tens   = SN-TENS
f_HV =   TAU + SN*tan_phi_e - sig_ve*B_cs*(tan_phi_e/tan_phi_res - 1.0d0)
If (tphim.le.tan_phi_res.or..not.Hvorslev) f_HV = 0.0d0

! increase Amat above CSL
If (tphim.gt.tan_phi_res.and.Hvorslev) then
   Amat = Amat_ref + Amat_ref*((tphim-tan_phi_res)/tan_phi_res)*F_amat
else
   Amat = Amat_ref
End if

! plastic strains on tensile side
If (F_tens .gt. 0.0d0) then ! associated flow for SN>TENS
   ! gt = sn - tens
   ! sn is negative for compression

   dGTdSN   = 1.0d0
   dGTdTAU  = 0.0d0

   dFTdSN   = dGTdSN
   dFTdTAU  = dGTdTAU

   ! set plasticity indicator
   ipl_cp(2) = ipl_cp(2)+1 ! increase counter for tension cut off

   ! calculate plastic strain contribution of contact plain
   epsNtens = f_tens*Cnn*dGTdSN  ! normal strains of cp from tension hardening
   epsGtens = f_tens*Cnn*dGTdTAU ! shear strains of cp from tension hardening

   epsn_t_step(i) = epsn_t_step(i) + epsNtens

   eps_tens(1) = epsNtens
   eps_tens(2) = 0.0d0
   eps_tens(3) = 0.0d0
End If  !(F_tens .gt. 0.0d0)

! correction of plastic tensile strains for negative values of yield function
If (F_tens.lt.0d0.and.epsn_t_step(i).gt.0d0) then
   epsNtens = f_tens*Cnn
   epsGtens = 0.0d0

   If (abs(epsNtens).gt.epsn_t_step(i)) then
      epsNtens = -epsn_t_step(i)
   End if

   epsn_t_step(i) = epsn_t_step(i) + epsNtens

   eps_tens(1) = epsNtens
   eps_tens(2) = 0.0d0
   eps_tens(3) = 0.0d0
 End If  !(F_tens.lt.0d0.and.epsn_t_step(i).gt.0d0)

If (F_cone.gt.0.0d0.and.SN.le.TENS) then
   ! Cone hardening - derivatives, mobilized phi etc.
   ! g = tau + sn*tan(psim) - coh*tan(phim)/tan(phi)
   ! sn is negative for compression

   PHIM = datan(TPHIM)        ! get phi_mob
   Phi_i = datan(tan_phi_i)

   ! new stress dilatancy theory´acc. Scharinger
   If (.not.Hvorslev) then
      ! get critical state friction angle
```

```
      PHIcv = Asin((dsin(PHI_i)-dsin(PSI))/(1.0d0-dsin(PHI_i)*dsin(PSI)))
      ! get inclination for PHIm.gt.PHIcv
      if (PSI.ne.0) k2_nSDT = PSI/(PHI_i-PHIcv)
   Else
      Phicv = phi_res
      If (psimin.ne.0) k2_nSDT = 1
   End if

   a1 = -((-(k1_nSDT*phi1)+2*psimin)/phi1**3)
   b1 = -((2*k1_nSDT*phi1-3*psimin)/phi1**2)
   c1 = k1_nSDT

   a2 = -((-(k2_nSDT*phi1) + k2_nSDT*phicv + 2*psimin)/(phi1 - phicv)**3)
   b2 = -((2*k2_nSDT*phi1**2 - k2_nSDT*phi1*phicv - k2_nSDT*phicv**2 - &
           3*phi1*psimin- 3*phicv*psimin)/(phi1 - phicv)**3)
   c2 = (phi1*(k2_nSDT*phi1**2 + k2_nSDT*phi1*phicv - 2*k2_nSDT*phicv**2 - &
         6*phicv*psimin))/(phi1 - phicv)**3
   d2 = -((k2_nSDT*phi1**3*phicv - k2_nSDT*phi1**2*phicv**2 -   &
         3*phi1*phicv**2*psimin + phicv**3*psimin)/(phi1 - phicv)**3)

   if (phim.le.phi1) then
      psim = a1*phim**3+b1*phim**2+c1*phim
   elseif (phim.gt.phi1.and.phim.le.phicv) then
      psim = a2*phim**3+b2*phim**2+c2*phim+d2
   else
      psim = (datan(tphim)-phicv)*F_psi
   endif

   !calculate derivatives for cone hardening
   dFcone_dsig(1) =  TPHIM
   dFcone_dsig(2) =  1.0d0
   dGcone_dsig(1) =  dtan(PSIM)
   dGcone_dsig(2) =  1.0d0
   If (.not.softening) then
      dFcone_depspl(1)  =  0.0d0
      dFcone_depspl(2)  =  (SN-COH_i/tan_phi_i)*3*(tan_phi_mod-  &
                            TPHIM)**2/(AMAT*(tan_phi_mod-tan_phi_null))
      If (tphim.eq.tan_phi_i) dFcone_depspl(2)  =  0.0d0
   Else   ! Galavi softening model in post peak range
      dFcone_depspl(1)  =  (SN-COH_i/tan_phi_i)* (-hPhi)* (Eps_non_local*(1-A))&
                           + (-TPHIM/tan_phi_i)*(-hCoh)* (Eps_non_local*(1-A))
      dFcone_depspl(2)  =  (SN-COH_i/tan_phi_i)* (-hPhi)* (Eps_non_local*A) + &
                        (-TPHIM/tan_phi_i)*(-hCoh)* (Eps_non_local*A)
   End if

   Dloc_x_dgconedsig(1) =  D_loc(1,1)*dGcone_dsig(1)
   Dloc_x_dgconedsig(2) =  D_loc(2,2)*dGcone_dsig(2)

   L11 = DOT_PRODUCT(dFcone_dsig,Dloc_x_dgconedsig)-  &
         DOT_PRODUCT(dFcone_depspl,dGcone_dsig)

   Lambda_cone_1 = f_cone / L11
   Lambda_cone = Lambda_cone_1

   ! set plasticity indicator for cone hardening
   If (Hard_soft) then
      if (softening) then
         ipl_cp(1) = ipl_cp(1)+1 ! peak friction angle reached => failure
      else
         ipl_cp(5) = ipl_cp(5)+1 ! friction hardening
      end if
   Else
      if (TPHIM.gt.0.99*tan_PHI_i) then
         ipl_cp(1) = ipl_cp(1)+1 ! max. friction angle reached => failure
      else
         ipl_cp(5) = ipl_cp(5)+1 ! friction hardening
      end if
   End if
End if ! cone hardening

If (F_cap.gt.0.0d0.and.SN.le.TENS) then
   ! Cap hardening - derivatives etc.
   ! g_cap = f_cap = sn**2/signc**2 + tau**2/(mcp*signc)**2 - 1
   ! sn is negative for compression

   ! derivatives
   dFcap_dsig(1)  =  2.0d0*SN/(SIGNC**2)
   dFcap_dsig(2)  =  2.0d0*TAU/((MCP*SIGNC)**2)
```

```
   dGcap_dsig(1)  =  dFcap_dsig(1)
   dGcap_dsig(2)  =  dFcap_dsig(2)
   dFcap_depspl(1)   =  (-2.0d0*(SN**2+(TAU**2.0d0/MCP**2))/SIGNC**3) &
                  *(p_ref**(1.0d0-m_power)*HARDCAP*(dabs(SIGNC))**m_power)
   dFcap_depspl(2)   =  0.0d0

   Dloc_x_dgcapdsig(1)     =  D_loc(1,1)*dGcap_dsig(1)
   Dloc_x_dgcapdsig(2)     =  D_loc(2,2)*dGcap_dsig(2)

   ! Local plastic multiplier
   L22   =  DOT_PRODUCT (dFcap_dsig,Dloc_x_dgcapdsig)   &
            - DOT_PRODUCT (dFcap_depspl,dGcap_dsig)
   Lambda_cap_1 = f_cap / L22
   Lambda_cap = Lambda_cap_1

   ! set plasticity indicator for cap hardening
   ipl_cp(3) = ipl_cp(3)+1
End if ! cap hardening

! Hvorslev yield surface
If (F_HV.gt.0.0d0.and.SN.le.TENS) then
   If (tan_phi_i.gt.tphim) then
      psi_HV = (datan(tphim)-phi_res)*F_psi
   Else
      psi_HV = (datan(tan_phi_i)-phi_res)*F_psi
   End if

   !calculate derivatives for Hvorslev surface
   dFHV_dsig(1)   =  tan_phi_e + B_cs*Eoed_ref/Eur_ref*(tan_phi_e/tan_phi_res &
                      - 1.0d0)*3d0*(2d0*NYUR - 1.0d0)*(sig_ve/SN)**m_power
   dFHV_dsig(2)   =  1.0d0
   dGHV_dsig(1)   =  dtan(PSI_HV)
   dGHV_dsig(2)   =  1.0d0
   dFHV_depspl(1) =  0.0d0 ! explicit in softening
   dFHV_depspl(2) =  0.0d0

   Dloc_x_dgHVdsig(1)   =  D_loc(1,1)*dGHV_dsig(1)
   Dloc_x_dgHVdsig(2)   =  D_loc(2,2)*dGHV_dsig(2)

   L33   = DOT_PRODUCT (dFHV_dsig,Dloc_x_dgHVdsig) -   &
           DOT_PRODUCT (dFHV_depspl,dGHV_dsig)

   Lambda_HV_1 = f_HV / L33
   Lambda_HV = Lambda_HV_1

   ipl_cp(1) = ipl_cp(1)+1 ! Hvorslev surface equals failure in MC terms

End if ! Hvorslev surface

! Plastic strain correction for f_HV < 0
If (F_HV.lt.0.0d0.and.gamma_HV_step(i).gt.0d0) then

   If (tan_phi_i.gt.tphim) then
      psi_HV = (datan(tphim)-phi_res)*F_psi
   Else
      psi_HV = (datan(tan_phi_i)-phi_res)*F_psi
   End if

   !calculate derivatives for Hvorslev surface
   dFHV_dsig(1)   =  tan_phi_e + B_cs*Eoed_ref/Eur_ref*(tan_phi_e/tan_phi_res &
                     - 1.0d0)*3d0*(2d0*NYUR - 1.0d0)*(sig_ve/SN)**m_power
   dFHV_dsig(2)   =  1.0d0
   dGHV_dsig(1)   =  dtan(PSI_HV)
   dGHV_dsig(2)   =  1.0d0
   dFHV_depspl(1) =  0.0d0
   dFHV_depspl(2) =  0.0d0
   Dloc_x_dgHVdsig(1)   =  D_loc(1,1)*dGHV_dsig(1)
   Dloc_x_dgHVdsig(2)   =  D_loc(2,2)*dGHV_dsig(2)

   ! Local plastic multiplier
   L33   = DOT_PRODUCT (dFHV_dsig,Dloc_x_dgHVdsig) -   &
           DOT_PRODUCT (dFHV_depspl,dGHV_dsig)
   Lambda_HV = f_HV / L33

   ipl_cp(1) = ipl_cp(1)+1          ! Hvorslev surface equals MC failure

   epsNHV = Lambda_Hv * dGHV_dsig(1)   ! normal strains from Hvorslev surface
   epsGHV = Lambda_HV * dGHV_dsig(2)   ! shear strains from Hvorslev surface
```

```
         If (abs(epsGHV).gt.gamma_HV_step(i)) then
            epsNHV = -epsn_HV_step(i)
            epsGHV = -gamma_HV_step(i)
         End if

         epsn_HV_step(i) = epsn_HV_step(i) + epsNHV
         gamma_HV_step(i) = gamma_HV_step(i) + epsGHV

         eps_HV(1) = epsNHV

         if (TAU==0) then
            eps_HV(2) = 0.0d0
            eps_HV(3) = 0.0d0
         else
            eps_HV(2) = epsGHV*Sig_cp(2)/TAU
            eps_HV(3) = epsGHV*Sig_cp(3)/TAU
         endif
      End if ! Hvorslev surface

      ! check if cap and cone are active
      If (f_cone.Gt.0.0d0.and.SN.le.TENS.and.f_cap.Gt.0.0d0.and.f_HV.le.0.0d0) then

         L12   =  DOT_PRODUCT (dFcone_dsig,Dloc_x_dgcapdsig)
         L21   =  DOT_PRODUCT (dFcap_dsig,Dloc_x_dgconedsig)

         Lambda_cone_12 =  (L22*f_cone - L12*f_cap)/ (L11*L22 - L12*L21)

         Lambda_cap_12  =  (L11*f_cap - L21*f_cone)/ (L11*L22 - L12*L21)

         If (Lambda_cone_12.gt.0.0d0) then
            cone_active =  .true.
         else
            cone_active =  .false.
         endif

         If (Lambda_cap_12.gt.0.0d0) then
            cap_active  =  .true.
         else
            cap_active  =  .false.
         endif

         If (cap_active ==.false.) then
            Lambda_cone =  Lambda_cone_1
            Lambda_cap  =  0.0d0
         else if (cone_active ==.true..and.cap_active ==.true.) then
            Lambda_cone =  Lambda_cone_12
            Lambda_cap  =  Lambda_cap_12
         else if (cone_active ==.false.) then
            Lambda_cone =  0.0d0
            Lambda_cap  =  Lambda_cap_1
         endif
      End if !(f_cone.Gt.0.0d0.and.f_cap.Gt.0.0d0)

      ! check if cone and Hvorslev surface are active
      If (f_cone.Gt.0.0d0.and.SN.le.TENS.and.f_HV.gt.0.0d0) then

         If (PSIM.gt.psi_HV) then
            L13   =  DOT_PRODUCT (dFcone_dsig,Dloc_x_dgHVdsig)
            L31   =  DOT_PRODUCT (dFHV_dsig,Dloc_x_dgconedsig)

            Lambda_cone_13 =  (L33*f_cone - L13*f_HV)/ (L11*L33 - L13*L31)

            Lambda_HV_13      =  (L11*f_HV - L31*f_cone)/ (L11*L33 - L13*L31)

            If (Lambda_cone_13.gt.0.0d0) then
               cone_active =  .true.
            else
               cone_active =  .false.
            endif

            If (Lambda_HV_13.gt.0.0d0) then
               HV_active   =  .true.
            else
               HV_active   =  .false.
            endif

            If (HV_active ==.false.) then
```

```
         Lambda_cone =  Lambda_cone_1
         Lambda_HV   =  0.0d0
      else if (cone_active ==.true..and.HV_active ==.true.) then
         Lambda_cone =  Lambda_cone_13
         Lambda_HV   =  Lambda_HV_13
      else if (cone_active ==.false.) then
         Lambda_cone =  0.0d0
         Lambda_HV   =  Lambda_HV_1
      endif
   Else
      If (Lambda_cone_1.ge.Lambda_HV_1) then
         Lambda_cone =  Lambda_cone_1
         Lambda_HV   =  0.0d0
      else
         Lambda_cone =  0.0d0
         Lambda_HV   =  Lambda_HV_1
      endif
   End if
End if !(f_cone.Gt.0.0d0.and.f_HV.Gt.0.0d0)

! check if cap and Hvorslev surface are active
If (SN.le.TENS.and.f_cap.gt.0.0d0.and.f_HV.gt.0.0d0) then
   L23   =  DOT_PRODUCT (dFcap_dsig,Dloc_x_dgHVdsig)
   L32   =  DOT_PRODUCT (dFHV_dsig,Dloc_x_dgcapdsig)
   Lambda_cap_23  =  (L33*f_cap - L23*f_HV)/ (L22*L33 - L23*L32)
   Lambda_HV_23   =  (L22*f_HV - L32*f_cap)/ (L22*L33 - L23*L32)

   If (Lambda_cap_23.gt.0.0d0) then
      cap_active  =  .true.
   else
      cap_active  =  .false.
   end if

   If (Lambda_HV_23.gt.0.0d0) then
      HV_active   =  .true.
   else
      HV_active   =  .false.
   End if

   If (HV_active ==.false.) then
      Lambda_cap  =  Lambda_cap_1
      Lambda_HV   =  0.0d0
   else if (cap_active.and.HV_active) then
      Lambda_cap  =  Lambda_cap_23
      Lambda_HV   =  Lambda_HV_23
   else if (cap_active ==.false.) then
      Lambda_cap  =  0.0d0
      Lambda_HV   =  Lambda_HV_1
   End if
End if !(f_cap.Gt.0.0d0.and.f_HV.Gt.0.0d0)

! check whether cone, cap and Hvorslev surface are active if trial stress
!is outside of all 3 yield surfaces
If (f_cone.gt.0.0d0.and.SN.le.TENS.and.f_cap.gt.0.0d0.and.f_HV.gt.0.0d0) then

   ! cone more mobilized than what corresponds to Hvorslev surface
   If (PSIM.gt.(psi_HV+0.001)) then
      ! check if cap and HV are active
      If (Lambda_cap_23.gt.0.0d0) then
         cap_active  =  .true.
         If (Lambda_HV_23.gt.0.0d0) then
            HV_active   =  .true.
         else
            HV_active   =  .false.
         endif ! Lambda_HV_23.gt.0.0d0
      else ! Lambda_cap_23 < 0
         cap_active  =  .false.
         ! check if cone and HV are active
         If (Lambda_HV_13.gt.0.0d0) then
            HV_active   =  .true.
         else
            HV_active   = .false.
         endif

         If (Lambda_cone_13.gt.0.0d0) then
            cone_active =  .true.
         else
            cone_active =  .false.
```

```
         endif
      endif !Lambda_cap_23.gt.0.0d0

   Else ! PSIM=psi_HV==>special return necessary due to non-convex yield surf.
      ! check if cap and HV are active
      If (Lambda_cap_23.gt.0.0d0) then ! cap active
         cap_active  = .true.
         cone_active = .false.   ! cone cannot be active if Hvor. Surf. exists
                                 ! and cap is active
         If (Lambda_HV_23.gt.0.0d0) then ! Hvorslev surface active
            HV_active = .true.
         else
            HV_active = .false.
         endif
      else ! cap not active
         cap_active  =  .false.

         ! cone return delivers longer return path ==> cone active
         If (Lambda_cone_1.ge.Lambda_HV_1) then
            cone_active =  .true.
            HV_active   =  .false.
         else  ! cone not active
            cone_active =  .false.
            HV_active   =  .true.
         endif
      endif !Lambda_cap_23.gt.0.0d0
   End if   ! PSIM.gt.psi_HV

   If (.not.HV_active) then
      Lambda_HV   =  0.0d0
      If (cone_active) then
         Lambda_cone =  Lambda_cone_1
         Lambda_cap  =  0.0d0
      else if (cap_active) then
         Lambda_cone =  0.0d0
         Lambda_cap  =  Lambda_cap_1
      End if
   Else if (HV_active) then
      If (cone_active) then
         Lambda_cone =  Lambda_cone_13
         Lambda_HV   =  Lambda_HV_13
         Lambda_cap  =  0.0d0
      else if (cap_active) then
         Lambda_cone =  0.0d0
         Lambda_HV   =  Lambda_HV_23
         Lambda_cap  =  Lambda_cap_23
      else
         Lambda_cone =  0.0d0
         Lambda_HV   =  Lambda_HV_1
         Lambda_cap  =  0.0d0
      End if
   End if
End if !(f_cone.gt.0.0d0.and.SN.lt.TENS.and.f_cap.gt.0.0d0.and.f_HV.gt.0.0d0)

If (F_cone.gt.0.0d0.and.SN.le.TENS) then
   ! calculate plastic strain contribution  - cone hardening
   epsNcone = Lambda_cone * dGcone_dsig(1)      ! normal strains from cone
   epsGcone = Lambda_cone * dGcone_dsig(2)      ! shear strains from cone
   if (TAU==0) then
      epsG1cone = 0.0d0
      epsG2cone = 0.0d0
   else
      epsG1cone = epsGcone*Sig_cp(2)/TAU
      epsG2cone = epsGcone*Sig_cp(3)/TAU
   endif

   eps_cone(1) = epsNcone
   eps_cone(2) = epsG1cone
   eps_cone(3) = epsG2cone

   ! update state variables: mobilized friction angle for cone hardening
   StVar(1*ABS(NUMCP)+i)=  tphim + epsGcone*(tan_phi_mod-tphim) /   &
      (Amat/3.0d0*(tan_phi_mod-tan_phi_null)/(tan_phi_mod-tphim) + epsGcone)
End if !f_cone.Gt.0.0d0

If (F_cap.gt.0.0d0.and.SN.le.TENS) then

   ! calculate plastic strain contribution - cap hardening
```

```
            epsNcap = Lambda_cap * dGcap_dsig(1)   ! normal strains from cap hardening
            epsGcap = Lambda_cap * dGcap_dsig(2)   ! shear strains from cap hardening

            if (TAU==0) then
               epsG1cap = 0.0d0
               epsG2cap = 0.0d0
            else
               epsG1cap = epsGcap*Sig_cp(2)/TAU
               epsG2cap = epsGcap*Sig_cp(3)/TAU
            endif

            eps_cap(1) = epsNcap
            eps_cap(2) = epsG1cap
            eps_cap(3) = epsG2cap

         End if !f_cap.Gt.0.0d0


         If (F_HV.gt.0.0d0.and.SN.le.TENS) then

            ! calculate plastic strain contribution - Hvorslev surface
            epsNHV = Lambda_Hv * dGHV_dsig(1)   ! normal strains from Hvorslev surface
            epsGHV = Lambda_HV * dGHV_dsig(2)   ! shear strains from Hvorslev surface
            eps_HV(1) = epsNHV

            if (TAU==0) then
               eps_HV(2) = 0.0d0
               eps_HV(3) = 0.0d0
            else
               eps_HV(2) = epsGHV*Sig_cp(2)/TAU
               eps_HV(3) = epsGHV*Sig_cp(3)/TAU
            endif

            epsn_HV_step(i) = epsn_HV_step(i) + epsNHV
            gamma_HV_step(i) = gamma_HV_step(i) + epsGHV

         End if !f_HV.Gt.0.0d0

         if (smallstrain==.true.) then
            ! form matrix with local plastic strains
            If(SN.ne.0d0) then
               dEps_cp_pl(1,i) = dEps_cp_pl(1,i) + (eps_tens(1)+eps_cone(1)+eps_cap(1) &
                                 +eps_HV(1))*(Sig_cp_spec(2) / SN)
            Else
               dEps_cp_pl(1,i) = dEps_cp_pl(1,i)
            End if

            dEps_cp_pl(2,i) = dEps_cp_pl(2,i)+(eps_tens(2)+eps_cone(2)+ &
                              eps_cap(2)+eps_HV(2))
            dEps_cp_pl(3,i) = dEps_cp_pl(3,i)+(eps_tens(3)+ eps_cone(3)+ &
                              eps_cap(3)++eps_HV(3))
         End if

!       Updating of sig_nc in hardening
        StVar(2*ABS(NUMCP)+i) = -((dabs(StVar(2*ABS(NUMCP)+i)))**(1.0d0-m_power)+ &
                              HARDCAP*(m_power-1.0d0)*p_ref**(1.0d0-m_power)*epsNcap) &
                              **(1.0d0/(1.0d0-m_power))

!       Updating of damage strain for softening calculation
!*****************************************************************************************
        if (hard_Soft) then
            dSt = (1.0d0-A)*dabs(epsNtens + epsNcap + epsNcone)+A*dabs(epsGtens +   &
                  epsGcap + epsGcone)
            StVar(4*ABS(NUMCP)+i)= StVar(4*ABS(NUMCP)+i) + dSt
            GLD_strain=GLD_strain+Weight(i)*dSt !Damage Strain Storage
        else if (Hvorslev) then
            If (epsNcone.gt.0.0d0) then
               dSt= epsNHV + epsNcone  ! cone&Hvorslev plast. strain in Hvorslev soft.
            Else
               dSt= epsNHV ! only Hvorslev plastic strains in Hvorslev softening
            End if

            ! local plastic normal strain
            StVar(4*ABS(NUMCP)+i)= StVar(4*ABS(NUMCP)+i) + dSt
            GLD_strain=GLD_strain+Weight(i)*dSt !Damage Strain Storage

            ! first contact with Hvorslev surface
            If (epsNHV.gt.0.0d0.and.StVar(5*ABS(NUMCP)+i)==0.0d0) then
```

```
               if(.not.Eps_non_local_cal.and.switch_HV == 1) then
                  call Non_Local (StVar, nStat, NumCP, GLD_strain, iStep, numpoint, &
                                  point_index, weights, Hvorslev)
                  Eps_non_local_cal=.True.
               end if

               ! non local macro. damage strain
               Eps_non_local=StVar(3*ABS(NUMCP)+8)

               ! store non-local EpsDamPeak as state variable
               StVar(5*ABS(NUMCP)+i) = Eps_non_local*weight(i)

               ! store local EpsDamPeak as state variable
               If (switch_HV == 2) StVar(5*ABS(NUMCP)+i) = StVar0(3*ABS(NUMCP)+9)* &
                                                            weight(i)
            End if
        End if
!*************************************************************************************

        eps_cp_plastic = eps_tens + eps_cone + eps_cap + eps_HV
        eps_cp_gl = MATMUL (Tj,eps_cp_plastic)
        dEps_plastic = dEps_plastic + 3.0d0*eps_cp_gl*Weight(i)

      END DO !loop over all integration planes

      ! calculate plastic strains on global level
      !plastic volumetric strain of current iteration
      dEps_vol_pl = dEps_plastic(1) + dEps_plastic(2) + dEps_plastic(3)

      ! Sum of plastic volumetric strain of current step along strain path
      SumdEps_vol_pl = SumdEps_vol_pl + dabs(dEps_vol_pl)

      !plastic octrahedral shear strain of current iteration
      dGamma_pl = 2.0d0/3.0d0*dsqrt((dEps_plastic(1)-dEps_plastic(2))**2 +   &
                  (dEps_plastic(2)-dEps_plastic(3))**2 + (dEps_plastic(3)-  &
                  dEps_plastic(1))**2 + 1.5d0*dEps_plastic(4)**2 +     &
                  1.5d0*dEps_plastic(5)**2 + 1.5d0*dEps_plastic(6)**2)

      ! Sum of plastic octahedral shear strain of current step along strain path
      SumdGamma_pl = SumdGamma_pl + dGamma_pl

      ! check convergence criterion
      crit = 0.001d0
      If (dabs(SumdEps_vol_pl).gt.1d-15.or.SumdGamma_pl.gt.1d-15) then
         If (dabs(dEps_vol_pl/SumdEps_vol_pl)>crit.or.dabs(dGamma_pl/SumdGamma_pl)>crit)
            converged_cp=.false.
      End if

      ! set plasticity indicator
      if (ipl_cp(1)>1) failure_mode=.false. ! more than one plane is in failure mode
      ipl_gl= ipl_gl + ipl_cp

     End Do ! While not converged

     ! form matrix with local strain components (accumulation for each substep)
     dEps_cp = dEps_cp + (dEps_cp_el + dEps_cp_pl)

     ! Update global stress state
     dEps_trial=dEps_trial-dEps_plastic

     dSig_trial = MatMul(D,dEps_trial)

     Sig_trial=Sig0_sub+dSig_trial

     ! calculate new global stress state
     Sig0_sub = Sig_trial

     End Do ! Subincrementing

     ! set plasticity indicator
     if (ipl_gl(5).ne.0.and.ipl_gl(5).ge.ipl_gl(3)) ipl=5
     if (ipl_gl(3).ne.0.and.ipl_gl(5).lt.ipl_gl(3)) ipl=3
     if (ipl_gl(2).ne.0) ipl=2
     if (ipl_gl(1).ne.0) ipl=1


     ! calculate new D-Matrix acc. to direction of local shear strains
     if (smallstrain.and.iterStiff.lt.11) then
```

```
failure = .false.
Do i=1,ABS(NUMCP)    ! Check for planes which are in failure ==>
                     ! then no stiffness recovery at load reversal
   If (StVar(1*ABS(NUMCP)+i).ge.(0.99d0*tan_phi_res)) failure = .true.
End do

Do i=1,ABS(NUMCP) ! Small strain stiffness recovery with Bubble Model
   ! check strain path direction
   ! round strain increments to avoid numerical problems if dEps_cp close to 0
   if (abs(dEps_cp(1,i)).lt.1d0-12) dEps_cp(1,i)=0d0
   if (abs(dEps_cp(2,i)).lt.1d0-12) dEps_cp(2,i)=0d0
   if (abs(dEps_cp(3,i)).lt.1d0-12) dEps_cp(3,i)=0d0

   deps_cp_gamma(1,i) = dEps_cp(1,i)
   deps_cp_gamma(2,i) = dEps_cp(2,i)
   deps_cp_gamma(3,i) = dEps_cp(3,i)

   ! get accumulated deviatoric strain path direction
   eps_cp_gamma(1,i) = StVar0(8*ABS(NUMCP)+i) + deps_cp_gamma(1,i)
   eps_cp_gamma(2,i) = StVar0(9*ABS(NUMCP)+i) + deps_cp_gamma(2,i)
   eps_cp_gamma(3,i) = StVar0(10*ABS(NUMCP)+i) + deps_cp_gamma(3,i)

   If (recovery == .false.)   then  ! no stiffness recovery
      gamma_cp(i) = dsqrt(eps_cp_gamma(1,i)**2 + eps_cp_gamma(2,i)**2 + &
                     eps_cp_gamma(3,i)**2)
   Else
      eps_gamma_return_1(i) = StVar0(12*ABS(NUMCP)+i)
      eps_gamma_return_2(i) = StVar0(13*ABS(NUMCP)+i)
      eps_gamma_return_3(i) = StVar0(14*ABS(NUMCP)+i)

      ! get number of bubbles of previous round of stiffness iteration
      If (iterStiff.gt.1)  n_bubble_old = n_bubble(i)
      If (iterStiff.eq.1)  n_bubble_old = StVar0(15*ABS(NUMCP)+i)

      n_bubble(i) = StVar0(15*ABS(NUMCP)+i)           !

      Do k=1,n_bubble(i)   ! Get properties of active bubbles
         !Get centre coordinates of active bubbles
         eps_cp_gamma_centre_1(i,k) = StVar0((16+4*(k-1))*ABS(NUMCP)+i)
         eps_cp_gamma_centre_2(i,k) = StVar0((17+4*(k-1))*ABS(NUMCP)+i)
         eps_cp_gamma_centre_3(i,k) = StVar0((18+4*(k-1))*ABS(NUMCP)+i)
         ! Get size of active bubbles
         gamma_bubble(i,k) = StVar0((19+4*(k-1))*ABS(NUMCP)+i)
      End Do

      Do k=1,n_bubble(i)   ! Check all existing bubbles for active bubbles
         gamma_cp(i) =  dsqrt((eps_cp_gamma(1,i)-eps_cp_gamma_centre_1(i,k))**2 &
                        + (eps_cp_gamma(2,i)-eps_cp_gamma_centre_2(i,k))**2 + &
                        (eps_cp_gamma(3,i)-eps_cp_gamma_centre_3(i,k))**2)
         !innermost bubble is active bubble, updating of centre and bubble size
         If (gamma_cp(i).ge.gamma_bubble(i,k).and. &
            k==n_bubble(i).and.gamma_cp(i).gt.1*1d-15) then
            If (k.gt.1) then
               eps_cp_gamma_centre_1(i,k) = (eps_cp_gamma(1,i) +   &
                                              eps_gamma_return_1(i)) / 2d0
               eps_cp_gamma_centre_2(i,k) = (eps_cp_gamma(2,i) +   &
                                             eps_gamma_return_2(i)) / 2d0
               eps_cp_gamma_centre_3(i,k) = (eps_cp_gamma(3,i) +   &
                                             eps_gamma_return_3(i)) / 2d0
            Else
               eps_cp_gamma_centre_1(i,k) = eps_cp_gamma_centre_1(i,k)
               eps_cp_gamma_centre_2(i,k) = eps_cp_gamma_centre_2(i,k)
               eps_cp_gamma_centre_3(i,k) = eps_cp_gamma_centre_3(i,k)
            End If
            gamma_cp(i) = dsqrt((eps_cp_gamma(1,i)-eps_cp_gamma_centre_1(i,k))**2&
                          + (eps_cp_gamma(2,i)-eps_cp_gamma_centre_2(i,k))**2 + &
                         (eps_cp_gamma(3,i)-eps_cp_gamma_centre_3(i,k))**2)
            gamma_bubble(i,k) = gamma_cp(i)
         End If

         ! Strain path reaches one of the outer bubble boundaries
         If (gamma_cp(i).ge.gamma_bubble(i,k).and.k.lt.n_bubble(i). &
             and.gamma_cp(i).gt.1*1d-15) then
            Do m=k+1,n_bubble(i) ! Erase strain history of inner bubbles
               eps_cp_gamma_centre_1(i,m) = 0.0d0
               eps_cp_gamma_centre_2(i,m) = 0.0d0
               eps_cp_gamma_centre_3(i,m) = 0.0d0
```

```
                  gamma_bubble(i,m) = 0.0d0
               End Do
               eps_gamma_return_1(i) = eps_cp_gamma(1,i) +   &
                              2d0*(eps_cp_gamma_centre_1(i,k) - eps_cp_gamma(1,i))
               eps_gamma_return_2(i) = eps_cp_gamma(2,i) +   &
                              2d0*(eps_cp_gamma_centre_2(i,k) - eps_cp_gamma(2,i))
               eps_gamma_return_3(i) = eps_cp_gamma(3,i) +   &
                              2d0*(eps_cp_gamma_centre_3(i,k) - eps_cp_gamma(3,i))

               If (k==1) then
                  eps_gamma_return_1(i) = 0.0d0
                  eps_gamma_return_2(i) = 0.0d0
                  eps_gamma_return_3(i) = 0.0d0
               End If

               ! Enter small strain stiffness loop if change in bubbles
               ! is detected in first loop
               If (iterStiff == 1) stiffness=.false.
               n_bubble(i) = k
               gamma_bubble(i,k) = gamma_cp(i)
               Exit
            End If
         End do   !loop over all existing bubbles

         ! If strain path turns inside active bubble ==> create new strain contour
         If (failure==.false..and.istep.le.1.and.gamma_cp(i).lt. &
                  gamma_bubble(i,n_bubble(i)).and.n_bubble(i).le.3.and.  &
                  gamma_bubble(i,n_bubble(i)).gt.1*1d-15) then
            n_bubble(i) = n_bubble(i) + 1
            eps_gamma_return_1(i) = eps_cp_gamma(1,i) - deps_cp_gamma(1,i)
            eps_gamma_return_2(i) = eps_cp_gamma(2,i) - deps_cp_gamma(2,i)
            eps_gamma_return_3(i) = eps_cp_gamma(3,i) - deps_cp_gamma(3,i)
            eps_cp_gamma_centre_1(i,n_bubble(i)) = eps_gamma_return_1(i) +   &
                                                    deps_cp_gamma(1,i)/2d0
            eps_cp_gamma_centre_2(i,n_bubble(i)) = eps_gamma_return_2(i) +   6
                                                    deps_cp_gamma(2,i)/2d0
            eps_cp_gamma_centre_3(i,n_bubble(i)) = eps_gamma_return_3(i) +   6
                                                    deps_cp_gamma(3,i)/2d0
            gamma_cp(i) = dsqrt((eps_cp_gamma(1,i)-eps_cp_gamma_centre_1  &
                        (i,n_bubble(i)))**2 + (eps_cp_gamma(2,i)-  &
                        eps_cp_gamma_centre_2(i,n_bubble(i)))**2 + &
                        (eps_cp_gamma(3,i)-eps_cp_gamma_centre_3(i,n_bubble(i)))**2)
            gamma_bubble(i,n_bubble(i)) = gamma_cp(i)
            ! Enter small strain stiffness loop if change in bubbles
            !is detected in first loop
            If (iterStiff == 1) stiffness=.false.
         End If ! Strain path turns inward

         If (iterStiff.gt.1.and.n_bubble(i).ne.n_bubble_old) then
            Stiffness=.false.
         End If

         ! no stiffness recovery if failure line is reached on any plane
         If (failure) stiffness=.true.
      End if ! (recovery == .false.)
   End do   !loop over all cp's
  End if ! small strain == .true.
Enddo ! loop until stiffness = .true.

! Update of small strain stiffness state variables
!*********************************************************************
If (smallstrain) then
   ! update state variables: gamma_cp
   floh_gamma=0.
   Do i=1,abs(NUMCP)
      StVar(8*ABS(NUMCP)+i) = eps_cp_gamma(1,i)
      Star(9*ABS(NUMCP)+i) = eps_cp_gamma(2,i)
      StVar(10*ABS(NUMCP)+i) = eps_cp_gamma(3,i)
      StVar(11*ABS(NUMCP)+i) = gamma_cp(i)

      If (recovery == .true.) then
         StVar(12*ABS(NUMCP)+i)  = eps_gamma_return_1(i)
         StVar(13*ABS(NUMCP)+i)  = eps_gamma_return_2(i)
         StVar(14*ABS(NUMCP)+i)  = eps_gamma_return_3(i)
         StVar(15*ABS(NUMCP)+i)  = n_bubble(i)
         Do k=1,n_bubble(i)
            StVar((16+4*(k-1))*ABS(NUMCP)+i) = eps_cp_gamma_centre_1(i,k)
            StVar((17+4*(k-1))*ABS(NUMCP)+i) = eps_cp_gamma_centre_2(i,k)
```

```
               StVar((18+4*(k-1))*ABS(NUMCP)+i) = eps_cp_gamma_centre_3(i,k)
               StVar((19+4*(k-1))*ABS(NUMCP)+i) = gamma_bubble(i,k)
            End Do
         End if ! (recovery == .true.)

         floh_gamma = floh_gamma + gamma_cp(i)
      Enddo

      StVar(3*ABS(NUMCP)+6) = floh_gamma
      ! update state variables: indicator for small-strain stiffness
      StVar(3*ABS(NUMCP)+5) = sss_indicator_gl
   End if !small strain

   !************************************************************************
   !  Update strain softening data
   !************************************************************************
   If (switch_HV == 2)  StVar(3*ABS(NUMCP)+9)=GLD_strain

   if (Hard_Soft.or.switch_HV == 1) then
      ! store global damage strain of current stresspoint in file ITERXXXX
      write (37, rec=iRec) Vol, GLD_strain
      StVar(3*ABS(NUMCP)+9)=GLD_strain

      ! open and read file to get information on element and iteration number
      Inquire(Unit= 39, Opened= IsOpen)
      If (IsOpen) then
         rewind (39)
      else
         fname=' '
         Do i=1,iPrjLen_short
            fname(i:i) = Char( iPrjDir(i) )
         End Do
         fname= fname(:iPrjLen_short)//'softening_files'//'/'//'Element.nr'
         Open(Unit= 39, File= fname, Position='rewind')
      End If
      write (39,*) iel, iter
      rewind (39)
   end if
   !************************************************************************

   ! Update and return new global stress state
   sig(1:6) = Sig_trial

   ! calculate change of volumetric strains
   dEpsV = dEps(1) + dEps(2) + dEps(3)

   ! calculate pore water pressure
   If (IsUndr.Eq.1) Then
      dSwp  = BulkW * dEpsV
      Swp   = Swp0 + dSwp
   Else
      Swp = Swp0
   End If

   If (Hard_Soft.or.switch_HV == 1) then
      Deallocate (point_index, weights)
   End if

End If  ! IDTask = 2

! -------------------------------------------------------------------------------------
! calculate material stiffness matrix (D-matrix)
! -------------------------------------------------------------------------------------
If ( IDTask .Eq. 3 .Or. IDTask .Eq. 6 ) Then

   pdash = (sig0(1)+sig0(2)+sig0(3))/3d0
   if (pdash.gt.corr_val) pdash = corr_val
   facCnn = (p_ref/dabs(pdash))**m_power

   C_gl = 0.0d0

!  stiffness depends on p', isotropic material
   if(sw_pdash_SN0==0.and.anisotropic_el ==.false.) then
      F1  = 2.0d0*Gvh0*(1.0d0-NYUR)/(1.0d0-2.0d0*NYUR)
      F2  = 2.0d0*Gvh0*( NYUR )/(1.0d0-2.0d0*NYUR)
      D = 0.0d0
      Do i=1,3
         Do j=1,3
```

```
            D(i,j) = F2
         End Do
         D(i,i) = F1
         D(i+3,i+3) = Gvh0
         C_gl(i+3,i+3) = 1.0d0 / Gvh0
      End Do
      D = D / facCnn
      C_gl = C_gl * facCnn
   End if      !sw_pdash_SN0==0.and.anisotropic_el ==.false.

!  stiffness depends on p', cross anisotropic material
   if((sw_pdash_SN0==0.and.anisotropic_el ==.true.).or.sw_pdash_SN0 == 2) then
      if (sw_pdash_SN0 == 2) then
         Eh0 = StVar0(3*ABS(NUMCP)+14)
         Ev0 = StVar0(3*ABS(NUMCP)+15)
         Gvh0 = StVar0(3*ABS(NUMCP)+16)
      End if
      C_gl(1,1) = 1.0d0/Eh0
      C_gl(2,2) = 1.0d0/Ev0
      C_gl(3,3) = 1.0d0/Eh0
      C_gl(1,2) = -nu_vh_0/Ev0
      C_gl(1,3) = -nu_hh_0/Eh0
      C_gl(2,1) = C_gl(1,2)
      C_gl(3,1) = C_gl(1,3)
      C_gl(2,3) = -nu_vh_0/Ev0
      C_gl(3,2) = C_gl(2,3)
      C_gl(4,4) = 1.0d0/Gvh0
      C_gl(5,5) = 1.0d0/Gvh0
      C_gl(6,6) = 2*(1.0d0+nu_hh_0)/Eh0
      C_gl = C_gl*facCnn
      Call MatInvPiv(C_gl,D,6)
   End if   !  (sw_pdash_SN0==0.and.anisotropic_el ==.true.).or.sw_pdash_SN0 == 2

!  stiffness depends on plane normal stress
   if(sw_pdash_SN0==1) then

      ! Calculate eigenvalues and eigenangle of global anisotropic compliance
      ! matrix without stiffness degradation
      lambda_1 = (1.0d0+nu_hh_0)/Eh0
      lambda_2 = (1.0d0-nu_hh_0)/(2.0d0*Eh0) + 1.0d0/(2.0d0*Ev0) - dsqrt(((1.0d0 &
         -nu_hh_0)/(2.0d0*Eh0)-1.0d0/(2.0d0*Ev0))**2+((2.0d0*nu_hv_0**2)/Eh0**2))
      lambda_3 = (1.0d0-nu_hh_0)/(2.0d0*Eh0) + 1.0d0/(2.0d0*Ev0)+ dsqrt(((1.0d0 &
         -nu_hh_0)/(2.0d0*Eh0)-1.0d0/(2.0d0*Ev0))**2+((2.0d0*nu_hv_0**2)/Eh0**2))
      lambda_4 = 1.0d0/(2.0d0*Gvh0)

      ! Get components of matrix Sum(lambda_i*E_i)
      LE = 0.0d0
      If (anisotropic_el ==.true.) then
         If (((1.0d0-nu_hh_0)/Eh0 - 1.0d0/Ev0)==0.0d0.AND.nu_hv_0.gt.0.0d0) then
            omega = Pi/4.d0
         Else If (((1.0d0-nu_hh_0)/Eh0 - 1.0d0/Ev0)==0.0d0.AND.nu_hv_0.le.0.0d0) then
            omega = -Pi/4.d0
         Else
            If (((1.0d0-nu_hh_0)/Eh0 - 1.0d0/Ev0).gt.0) then
               omega = Pi/2.0d0 + 1.0d0/2.0d0*datan((-2.0d0*dsqrt(2.0d0)* &
                      ((nu_hv_0)/Eh0))/((1.0d0-nu_hh_0)/Eh0 - 1.0d0/Ev0))
            Else
               omega = 1.0d0/2.0d0*datan((-2.0d0*dsqrt(2.0d0)*((nu_hv_0)/Eh0)) &
                       /((1.0d0-nu_hh_0)/Eh0 - 1.0d0/Ev0))
            End If
         End if

         LE(1,1) = 1.0d0/2.0d0*lambda_1 + lambda_2*(dcos(omega))**2/2.0d0 +  &
                   lambda_3*(dsin(omega))**2/2.0d0
         LE(2,1) = lambda_2*(dcos(omega)*dsin(omega))/dsqrt(2.0d0) + lambda_3*(- &
                   dcos(omega)*dsin(omega))/dsqrt(2.0d0)
         LE(3,1) = -1.0d0/2.0d0*lambda_1 + lambda_2*(dcos(omega))**2/2.0d0 +  &
                   lambda_3*(dsin(omega))**2/2.0d0
         LE(1,2) = LE(2,1)
         LE(2,2) = lambda_2*(dsin(omega))**2 + lambda_3*(dcos(omega))**2
         LE(3,2) = LE(1,2)
         LE(1,3) = LE(3,1)
         LE(2,3) = LE(3,2)
         LE(3,3) = LE(1,1)
         LE(4,4) = lambda_4
         LE(5,5) = lambda_4
         LE(6,6) = lambda_1
      End if
```

```
      ! do loop over all cp's
      Do i=1,ABS(NUMCP)

         ! get transformation matrices (TiT_spec)
         Tj_spec = 0.0d0
         C_cp = 0.0d0

         !form transformation matrix Tj_spec(6,6)
         Tj_spec(1,1) = 1/3.0d0
         Tj_spec(2,1) = 1/3.0d0
         Tj_spec(3,1) = 1/3.0d0

         Tj_spec(1,2) = n1(i,1)**2 - 1/3.0d0
         Tj_spec(2,2) = n1(i,2)**2 - 1/3.0d0
         Tj_spec(3,2) = n1(i,3)**2 - 1/3.0d0
         Tj_spec(4,2) = 2.0d0*n1(i,1)*n1(i,2)
         Tj_spec(5,2) = 2.0d0*n1(i,2)*n1(i,3)
         Tj_spec(6,2) = 2.0d0*n1(i,3)*n1(i,1)

         Tj_spec(1,3) = n1(i,1)*s1(i,1)
         Tj_spec(2,3) = n1(i,2)*s1(i,2)
         Tj_spec(3,3) = n1(i,3)*s1(i,3)

         Tj_spec(4,4) = n1(i,1)*s1(i,2)+n1(i,2)*s1(i,1)
         Tj_spec(5,4) = n1(i,3)*s1(i,2)+n1(i,2)*s1(i,3)
         Tj_spec(6,4) = n1(i,3)*s1(i,1)+n1(i,1)*s1(i,3)

         Tj_spec(1,5) = n1(i,1)*t1(i,1)
         Tj_spec(2,5) = n1(i,2)*t1(i,2)
         Tj_spec(3,5) = n1(i,3)*t1(i,3)

         Tj_spec(4,6) = n1(i,2)*t1(i,1)+n1(i,1)*t1(i,2)
         Tj_spec(5,6) = n1(i,2)*t1(i,3)+n1(i,3)*t1(i,2)
         Tj_spec(6,6) = n1(i,1)*t1(i,3)+n1(i,3)*t1(i,1)

         !get transposed transformation matrix TiT_spec(6,6)
         TiT_spec= Transpose(Tj_spec)

         !-----------------------------------------------------------------------------
         ! stress transformation acc. to spectral stiffness method
         !-----------------------------------------------------------------------------
         Sig0_cp_spec= MATMUL (TiT_spec,Sig0)

         !-----------------------------------------------------------------------------
         !calculate local stiffness matrix (with Sig0_cp)
         !-----------------------------------------------------------------------------
         ! get local normal stress at start of step (SN0)
         SN0 = Sig0_cp_spec(1) + Sig0_cp_spec(2)
         If (SN0.gt.corr_val) SN0 = corr_val

         If (anisotropic_el ==.true.) then
            !get inverse of transposed transformation matrix TiT_spec_inv(6,6)
            Call MatInvPiv(TiT_spec,TiT_spec_inv,6)
            LExTiT_inv = MATMUL (LE,TiT_spec_inv)
            C_cp= MATMUL (TiT_spec,LExTiT_inv)
         Else if (anisotropic_el ==.false.) then
            C_cp(1,1)= lambda_2
            Do m=2,6
               C_cp(m,m) = lambda_1
            End Do
         End if

         C_cp = C_cp * (p_ref/dabs(SN0))**m_power

         ! back transformation of compliance matrix
         TjxC_cp = Matmul(Tj_spec,C_cp)
         C_gl_cp = Matmul(TjxC_cp,TiT_spec)

         C_gl = C_gl + 3.0d0*C_gl_cp*Weight(i)

      End Do   !loop over all cp's

      Call MatInvPiv(C_gl,D,6)

   End if      !sw_pdash_SN0==1
```

```
   ! calculate bulk modulus of water
      If (IsUndr.Eq.1) Then
       Gur = (1.0d0/C_gl(4,4)+1d0/C_gl(5,5)+1d0/C_gl(6,6))/3.0d0
      If (BulkW==0) Then
         xNu_U=0.495d0
           BulkW = 2.0d0*Gur/3.0d0*((1.0d0+xNu_U)/(1.0d0-2.0d0*xNu_U) - &
                  (1.0d0+NYUR)/(1.0d0-2.0d0*NYUR))
        End If
     End If

   End If  ! IDTask = 3, 6


! ---------------------------------------------------------------------------------------
! get number of state parameters
! ---------------------------------------------------------------------------------------
 If (IDTask .Eq. 4) Then

      nStat = 3*ABS(NUMCP)+3  ! Basic model

      if (Hvorslev)  then  ! Hvorslev surface model
         nStat = 7*ABS(NUMCP)
      else if (Hard_Soft) then   ! Galavi softening model
         nStat = 8*ABS(NUMCP)
      End if

      If (smallstrain) then   ! Small strain model
         If (recovery == .false.) nStat = 12*ABS(NUMCP)
         If (recovery == .true.) nStat = 32*ABS(NUMCP)
      End if

! state variables on integration planes in array StVar0/StVar

! StVar(0*ABS(NUMCP)+1:ABS(NUMCP)*1)      sigma_nc with Hvorslev softening
! StVar(1*ABS(NUMCP)+1:ABS(NUMCP)*2)      tan_phi mobilized in hardening
! StVar(2*ABS(NUMCP)+1:ABS(NUMCP)*3)      sigma_nc for hardening only
! StVar(3*ABS(NUMCP)+2)                   initialization indicator
! StVar(3*ABS(NUMCP)+3)                   ACAP (cap shape parameter)
! StVar(3*ABS(NUMCP)+4)                   record number of current stress point
! StVar(3*ABS(NUMCP)+5)                   sss_indicator
! StVar(3*ABS(NUMCP)+6)                   floh_gamma
! StVar(3*ABS(NUMCP)+7)                   Volume (area in 2D) of Finite Element
! StVar(3*ABS(NUMCP)+8)                   Correction factor for non-local damage strain
! StVar(3*ABS(NUMCP)+9)                   Global damage strain
! StVar(3*ABS(NUMCP)+10)                  Number of stress points within radius 2*Length
! StVar(3*ABS(NUMCP)+12)                  Hvorslev surface parameter B_cs
! StVar(3*ABS(NUMCP)+13)                  length of project directory path
! StVar(3*ABS(NUMCP)+14)                  Eh0_ref at initial stress ratio
! StVar(3*ABS(NUMCP)+15)                  Ev0_ref at initial stress ratio
! StVar(3*ABS(NUMCP)+16)                  Gvh0_ref at initial stress ratio
! StVar(3*ABS(NUMCP)+17)                  nu_hv0 at initial stress ratio
! StVar(4*ABS(NUMCP)+1:ABS(NUMCP)*5)      Local damage strain
! StVar(5*ABS(NUMCP)+1:ABS(NUMCP)*6)      non-local damage strain at peak
! StVar(6*ABS(NUMCP)+1:ABS(NUMCP)*7)      Tan_Phi_mobilised (in friction softening) /
!                       non_local damage strain of previous step in Hvorslev model
! StVar(7*ABS(NUMCP)+1:ABS(NUMCP)*8)      mobilised cohesion ci
! StVar(8*ABS(NUMCP)+1:(ABS(NUMCP)*9))    local shear strain history component 1
! StVar(9*ABS(NUMCP)+1:(ABS(NUMCP)*10))   local shear strain history component 2
! StVar(10*ABS(NUMCP)+1:(ABS(NUMCP)*11))  local shear strain history component 3
! StVar(11*ABS(NUMCP)+1:(ABS(NUMCP)*12))  length of Gamma-path abs(Gamma)
! StVar(12*ABS(NUMCP)+1:ABS(NUMCP)*13)    Return point, first shear strain component
! StVar(13*ABS(NUMCP)+1:ABS(NUMCP)*14)    Return point, second shear strain component
! StVar(14*ABS(NUMCP)+1:ABS(NUMCP)*15)    Return point, second shear strain component
! StVar(15*ABS(NUMCP)+1:ABS(NUMCP)*16)    number of active bubbles per plane
! StVar(16*ABS(NUMCP)+1:ABS(NUMCP)*17)    Bubble centre 1, shear strain component 1
! StVar(17*ABS(NUMCP)+1:ABS(NUMCP)*18)    Bubble centre 1, shear strain component 2
! StVar(18*ABS(NUMCP)+1:ABS(NUMCP)*19)    Bubble centre 1, shear strain component 3
! StVar(19*ABS(NUMCP)+1:ABS(NUMCP)*20)    Bubble 1, maximum shear strain (radius)
! StVar(20*ABS(NUMCP)+1:ABS(NUMCP)*21)    Bubble centre 2, shear strain component 1
! StVar(21*ABS(NUMCP)+1:ABS(NUMCP)*22)    Bubble centre 2, shear strain component 2
! StVar(22*ABS(NUMCP)+1:ABS(NUMCP)*23)    Bubble centre 2, shear strain component 3
! StVar(23*ABS(NUMCP)+1:ABS(NUMCP)*24)    Bubble 2, maximum shear strain (radius)
! StVar(24*ABS(NUMCP)+1:ABS(NUMCP)*25)    Bubble centre 3, shear strain component 1
! StVar(25*ABS(NUMCP)+1:ABS(NUMCP)*26)    Bubble centre 3, shear strain component 2
! StVar(26*ABS(NUMCP)+1:ABS(NUMCP)*27)    Bubble centre 3, shear strain component 3
! StVar(27*ABS(NUMCP)+1:ABS(NUMCP)*28)    Bubble 3, maximum shear strain (radius)
```

```
! StVar(28*ABS(NUMCP)+1:ABS(NUMCP)*29)    Bubble centre 4, shear strain component 1
! StVar(29*ABS(NUMCP)+1:ABS(NUMCP)*30)    Bubble centre 4, shear strain component 2
! StVar(30*ABS(NUMCP)+1:ABS(NUMCP)*31)    Bubble centre 4, shear strain component 3
! StVar(31*ABS(NUMCP)+1:ABS(NUMCP)*32)    Bubble 4, maximum shear strain (radius)

End If  ! IDTask = 4

! ---------------------------------------------------------------------------------------
! get matrix attributes
! ---------------------------------------------------------------------------------------
If (IDTask .Eq. 5) Then
   NonSym   = 0  ! 1 for non-symmetric D-matrix
   iStrsDep = 1  ! 1 for stress dependent D-matrix
   iTang    = 0  ! 1 for tangent D-matrix
   iTimeDep = 0  ! 1 for time dependent D-matrix
End If  ! IDTask = 5

Deallocate (eps_cp_gamma, deps_cp_gamma, gamma_cp, dEps_cp_pl, dEps_cp_el, dEps_cp, &
            epsn_t_step, epsn_HV_step, gamma_HV_step)
Deallocate (dEps_cp_el_spec, n1, s1, t1, WEIGHT)
Deallocate (eps_gamma_return_1, eps_gamma_return_2, eps_gamma_return_3, n_bubble, &
            eps_cp_gamma_centre_1, eps_cp_gamma_centre_2)
Deallocate (eps_cp_gamma_centre_3, gamma_bubble)

Return

End Subroutine
```